THE PHOTOCHEMISTRY OF SULFURIC ACID AEROSOLS

A thesis
submitted in partial fulfillment of the requirements for the degree
of

Doctor of Philosophy in Chemistry

in the

University of Canterbury

by

Glenn Anthony Rowland

University of Canterbury
2001

To my wife,

Jing Zhang Rowland

Acknowledgments

There are many people without whose assistance this work could never have been completed. First and foremost, I must thank my supervisor, Professor Leon F. Phillips, for his guidance and considerable patience during the past few years. I am also grateful to Drs. Colin Freeman and Richard Hartshorn, and Professor Murray McEwan for valuable suggestions throughout the course of this research, and to Professor Laurie Butler of the University of Chicago for *ab initio* calculations on sulfuric acid.

I also wish to thank the talented members of the Department's technical staff for their contribution to the success of this research. Special thanks go to Dave MacDonald, Rob McGregor, Sandy Ferguson, John Davis, Russell Gillard and Wayne Mackay for their willingness to come to my rescue on a number of occasions!

I am grateful to the Chemistry Department for a Teaching Assistant Scholarship, and to the Marsden Fund for supporting this research.

Thankyou to Clinton Mills, Chris Knox, Christian Neilsen, Sumith Withanage and Julian Browne, fellow researchers whose friendship and encouragement over the past years have made this work a pleasure.

Finally, I wish to thank my family – my parents Pam and Chris, my sister Katrina, and my wife Jing – for their unconditional love and support throughout the course of my studies.

G.A. Rowland

Table of Contents

Abstract

We report here the experimental investigation of several photochemical reactions that may occur in concentrated sulfuric acid droplets in the clouds of the planet Venus.

It was found that the irradiation of 80-100wt.% sulfuric acid aerosol with 193nm light in the presence of carbon monoxide resulted in the formation of carbon dioxide and either the formation or destruction of sulfur dioxide. The measured quantum yield for carbon dioxide formation is 0.011±0.010.

Various instrumental techniques for determining the size and number density of aerosol droplets were utilised in an attempt to generate a stable, monodisperse sulfuric acid aerosol.

Concentrated sulfuric acid solutions were irradiated with 178.3nm, 184.9nm, 193.3nm and 253.7nm light in order to investigate the UV photochemistry of the bulk liquid. No significant photochemistry was observed. The reactions occurring in sulfuric acid aerosol at 193nm were attributed to multiphoton processes, permitted by the optical focussing effects observed in small droplets.

Irradiation of solutions of Fe(II) in 98wt.% sulfuric acid solution with 193nm or 248nm light results in the formation of Fe(III). Under the same conditions, the reduction of Fe(III) is also observed. The presence of sulfur dioxide increases the initial rate of the reaction, and dissolved oxygen is consumed in the initial stages.

A qualitative mechanism for the photochemical interconversion of Fe(II) and Fe(III) in concentrated sulfuric acid is proposed, which incorporates the effect of sulfur dioxide and oxygen on the reaction.

Chapter 1

Chemistry of the Atmosphere of Venus

Chapter 1

Chemistry of the Atmosphere of Venus

1.1 General Introduction and Scope of the Present Work

The clouds of Venus have long been responsible for drawing the attention of terrestrial observers to our nearest neighbouring planet. When close to the Earth, Venus appears as the second brightest object in the night sky – second only to the moon – due to reflection of the Sun's light from the clouds that blanket the planet's surface. Unlike Earth's other neighbours, the moon and Mars, the surface of Venus is completely hidden from sight by the dense cloud layer, contributing to the sense of mystery surrounding Venus. Although an extensive series of interplanetary space probes have traveled to Venus, providing a considerable volume of scientific information regarding the planet, the clouds still remain a source of mystery.

Over the past thirty years, it has become apparent that heterogeneous reactions play a critical role in the atmospheric chemistry of Earth, and have been the subject of extensive research. Heterogeneous reactions – occurring either on the surface of solid aerosol particles or in solution within liquid droplets – have been implicated in areas of major contemporary concern, such as polar ozone depletion and the chemical transformation of anthropogenic emissions.

To date, attempts to model the chemistry of Venus have been restricted to gas-phase reactions and physical transport processes. These have been unable to explain the stability of the carbon dioxide atmosphere against photochemical reduction or account for the extremely low partial pressure of oxygen that has been observed. In order to improve on present models, it will be necessary to include the contribution of heterogeneous and liquid phase reactions, just as it has been on Earth. Until now, there have been few experimental studies which have direct relevance to the cloud chemistry of Venus, since the droplets are made up of concentrated sulfuric acid and

are unlike the clouds that occur on Earth. The objective of this thesis is to explore some of the photochemical reactions that may occur within the sulfuric acid clouds of Venus.

In this chapter, the current knowledge of the atmosphere of Venus – its reported composition and the gas-phase reactions that form the basis of the current chemical and dynamic model of the stratosphere – is reviewed. The composition of the cloud layers is still a matter of debate, due to inconsistencies in the *in situ* observations made by interplanetary landing probes. However, there is strong evidence to support the presence of concentrated sulfuric acid droplets containing dissolved iron salts in the cloud layer. The chapter concludes with a brief review of the role of iron in aqueous aerosols in Earth's troposphere, which has been the subject of extensive study, and of the known photochemistry of iron salts in aqueous solution.

The second chapter of this thesis describes an experiment in which concentrated sulfuric acid aerosols are generated and irradiated with 193nm light in the presence of carbon monoxide. The results from this experiment show that carbon dioxide is formed during the irradiation, which supports the proposition that heterogeneous chemistry may play an important role in reversing the carbon dioxide photolysis in the upper atmosphere of Venus. However, the experimental results were not reproducible, in that on some occasions sulfur dioxide was also observed as a reaction product, while on others the reaction was found to consume sulfur dioxide.

In order to account for the results obtained for the experiment described in Chapter two, we sought to reduce the number of variable factors in the experimental system. The two areas of greatest uncertainty were the physical composition of the sulfuric acid aerosol, and the photochemical reactivity of bulk sulfuric acid liquid. Chapter Three of this thesis concerns the generation and characterisation of aerosols under laboratory conditions. The objective was to develop a method for producing a sulfuric acid aerosol with known particle size and number density, in order to determine the effect that these physical properties had on the observed photochemical reaction. However, it is concluded that the corrosive nature and hydroscopic properties of concentrated sulfuric acid solutions made it impossible to produce such an aerosol with the available equipment.

Chapter Four discusses several experimental investigations into the photochemical reactions of bulk liquid solutions of concentrated sulfuric acid at 253.7, 193.3 and 178.3nm. The chapter concludes by presenting the results of a recently completed *ab initio* study of the electronically excited states of sulfuric acid, which effectively rules out photo-dissociation of sulfuric acid molecules by single-photon absorption at any of the wavelengths studied. Alternative explanations for the observed photochemical reactivity of sulfuric acid solutions and aerosols are advanced.

In Chapters Five and Six, attention is turned to the photochemical reactions of iron salts in concentrated sulfuric acid solution, as there is strong evidence for the presence of iron in the clouds of Venus. Transition metal complexes are widely reported to participate in the photochemistry of aqueous aerosols in Earth's troposphere, and have been the subject of extensive investigation, but little is known of the reactions of iron salts in liquids other than water. Chapter Five describes the results of an investigation into the photochemical interconversion of Fe(II) and Fe(III) in concentrated sulfuric acid, and the effects of dissolved sulfur dioxide and oxygen on the reaction. Finally, in Chapter Six, several reaction mechanisms are proposed which account for the results observed in Chapter Five, and the significance of these reactions for the cloud chemistry of Venus is discussed.

1.2 Composition of the Atmosphere of Venus

1.2.1 History of the exploration of Venus

While Venus has been observed by astronomers for around 5000 years, it is only recently that information about conditions on the planet has become available. In 1761, a halo was observed around Venus during its transit across the disk of the sun, providing the first evidence that Venus possessed an atmosphere. Telescopic observations revealed a featureless surface, and observers concluded that the planet was completely and continually covered with clouds. By the 1920's, UV photography had revealed dark markings in the clouds that were short-lived, constantly changing and invisible to the naked eye. In the 1930's, the first spectroscopic measurements of Venus were made, revealing CO_2 absorption bands in the spectrum. For the next thirty years, Earth-based measurements provided the only available information about the chemical nature of Venus' atmosphere. Since the cloud cover prevented any spectroscopic probing of the lower atmosphere, its composition was completely unknown. Popular literature imagined a warm, wet jungle – and possibly life – on the surface of Venus, hidden by the clouds.

With the advent of rocketry in the 1950's, new possibilities for the scientific study of Venus emerged. Both the U.S. and Soviet space programs targeted Venus as the destination for their first interplanetary missions. The first successful contact with Venus was a flyby by Mariner 2 in 1962, followed in 1967 by the insertion of instrument-bearing entry probes from Venera 4. A summary of the successful missions to Venus is given in Figure 1.2. The *in situ* measurements made by these satellites and entry probes have provided the majority of current information about the chemical composition of Venus, and are the only source of direct knowledge we have about the lower atmosphere. The most recent entry probes were Vega 1 and 2, which contacted Venus in 1984. Since this date, there has been no new chemical data for Venus.

Mission	Launch Date	Mission Type
Mariner 2	27 August, 1962	Flyby
Venera 4	12 June, 1967	4 × Entry Probes/hard-landing
Mariner 5	14 June, 1967	Flyby
Venera 5	5 January, 1969	Entry Probe/hard-landing
Venera 6	10 January, 1969	Entry Probe/hard-landing
Venera 7	17 August, 1970	Entry Probe/soft landing. First Successful Landing
Venera 8	27 March, 1972	Entry Probe/soft landing
Mariner 10	4 November, 1973	Flyby
Venera 9	8 June, 1975	Orbiter
Venera 10	14 June, 1975	Orbiter
Pioneer Venus 1	20 May, 1978	Orbiter
Pioneer Venus 2	8 August, 1978	4 × Entry Probes/hard-landing
Venera 11	9 September, 1978	Entry Probe/soft landing
Venera 12	14 September, 1978	Entry Probe/soft landing
Venera 13	30 October, 1981	Entry Probe/soft landing
Venera 14	4 November, 1981	Entry Probe/soft landing
Venera 15	2 June, 1983	Orbiter
Venera 16	7 June, 1983	Orbiter
Vega 1	15 December, 1984	Soft Landing and Balloon
Vega 2	21 December, 1984	Soft Landing and Balloon
Magellan	4 May, 1989	Orbiter – Radar Mapping of Surface
Galileo	18 October, 1989	Flyby *en route* to Jupiter
Cassini	15 October, 1997	Flyby *en route* to Saturn

Figure 1.2 Summary of Interplanetary Missions to Venus

1.2.2 Physical Structure

1.2.2.1 Physical Structure of the Atmosphere of Venus

Detailed information about the pressure and temperature on Venus was obtained from infrared radiometer measurements by the Pioneer Venus orbiter. The standard reference model was published by Seiff in 1983[1] (Fig. 1.3). The surface temperature is 720K– much higher than that of Earth – with little latitudinal variation. Likewise, the pressure at the surface is greater than that of Earth, at just under 100 bar.

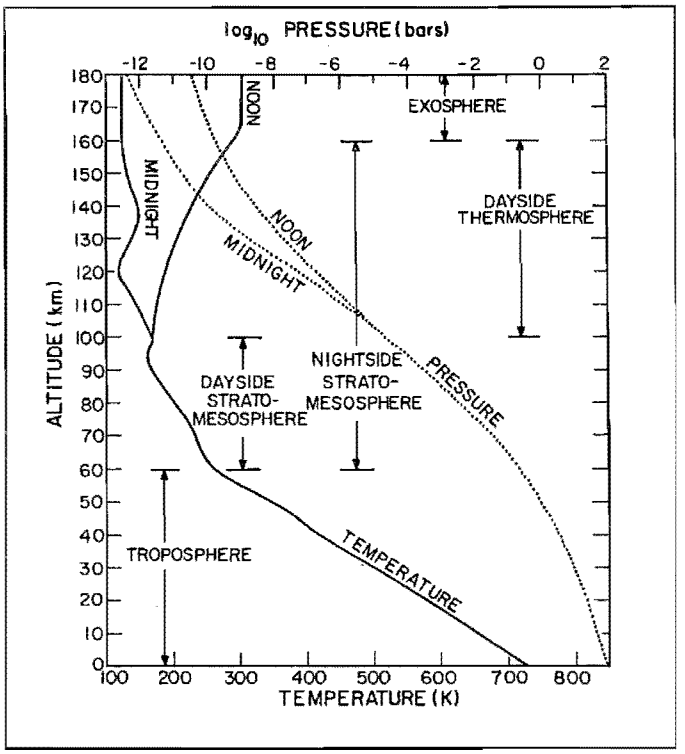

Figure 1.3 Variation of temperature and pressure with altitude at 30° latitude on Venus[1].

Significant variations between day and night measurements were observed due to the effects of photochemistry in the upper atmosphere.

1.2.2.2 *Physical Structure of the Clouds*

Several entry modules have studied the physical properties of the clouds. Particle size and number density was measured as a function of altitude by a particle size spectrometer on the Pioneer Venus descent probe as it descended through the atmosphere. The Pioneer Venus data, as well as that from the later Venera and Vega missions, showed that significant variation occurred within the clouds. The clouds were found to exist in several semi-separate layers, ranging from 46 – 70 km in altitude. Each layer contained particles from up to three different size distributions, denoted as Modes 1, 2 and 3 from smallest to largest. Table 1.4 summarises the mass and size distribution properties of the different types of particle in each cloud layer[2]. The mass density of aerosols in the clouds as a function of altitude[3] is presented in Fig. 1.5.

Cloud Layer	Altitude, km	mode	r, μm	σ, μm	n, cm^{-3}	M, $g.cm^{-2}$
Upper haze	90-70	1	0.13	2.16	0.1-100	3×10^{-6}
Upper cloud layer	70-57	1	0.18	2.16	600	1.1×10^{-4}
		2	1.1	0.4	70	9.5×10^{-4}
Middle cloud layer	57-50	1	0.15	1.9	70-120	2×10^{-5}
		2	1.36	0.28	30-55	4.7×10^{-4}
		3	3.7	1.26	40	4×10^{-3}
Lower cloud layer	50-47.5	1	0.2	1.8	150	2×10^{-5}
		2	1.3	0.33	70	3.8×10^{-4}
		3	3.6	1.29	150	1.5×10^{-3}
Precloud layer	48-46	1	0.15	1.9	300	10^{-5}
		2	1.25	0.5	60	6×10^{-5}
Lower haze	48-30	1	0.13	1.57	45	10^{-5}
		0	0.06	-	8000	10^{-5}

Table 1.4 Physical Properties of Aerosols in Venus' Clouds. r is the modal radius; σ is its variance; n is the number density of particles; M is the columnar mass. Modes 1 and 3 have log-normal distribution; Mode 2 has Gaussian distribution

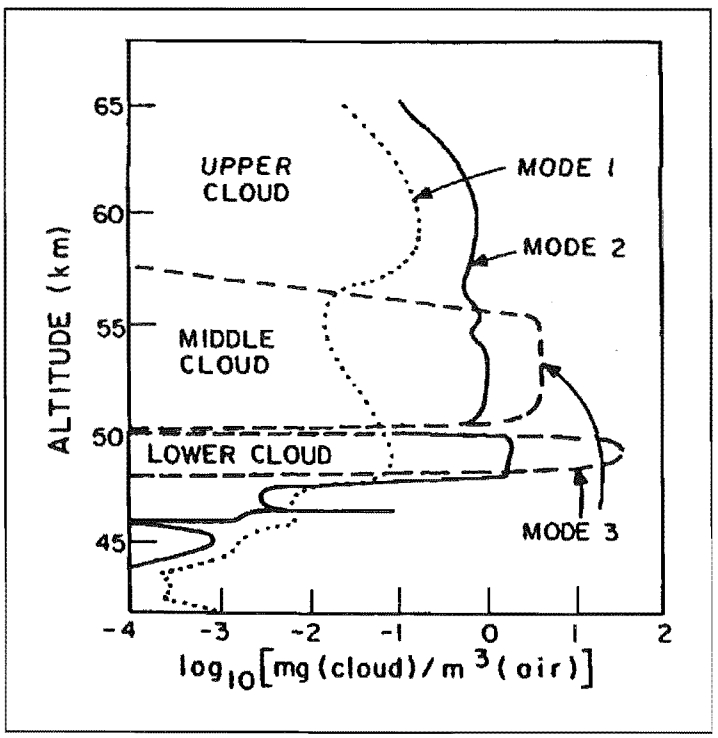

Figure 1.5 Smoothed profile of aerosol mass density as a function of altitude, using data from Pioneer Venus[3]

The greatest mass of aerosol is made up of the large Mode 3 particles, despite their being low in number. Mode 1 particles are numerous, but they represent only a small fraction of the total mass due to their small size.

The division of particles into different modes is based solely on the particles' size. Consideration of the altitude distribution of the different modes indicates that not all particles in a mode have the same origin. For instance, the altitude profile of Mode 1 particles shows density maxima occurring at 46km and 57km, which suggests that there are two kinds of particles, formed by separate processes, which are probably of different chemical composition.

The rotation of Venus is slow compared with Earth, with one Venusian day equalling 243 Earth days. However, observations of the UV markings in the clouds show that the clouds are circulating rapidly, completing a full circuit of the planet in a period of just 4-5 Earth days. This ensures that the full cloud cover receives frequent periods of solar irradiation, despite the slow rotation of the planet's surface.

1.2.3 Reported Composition of the Atmosphere of Venus

The chemical composition of Venus' upper atmosphere is well reported, with extensive data coming from spectroscopic measurements by instruments on Earth and on satellites in orbit around Venus. At altitudes below 60km, the composition is less well known. The only measurements for this region come from instruments mounted on entry probes during the descent. The most comprehensive data comes from mass spectrometry and gas chromatography instruments mounted on the Pioneer Venus lander and on the Venera 11-14 entry probes. However, results from these experiments were often inconsistent, and lacked the ability to measure altitudinal variations.

Table 1.6 is a summary of the experimental data for the composition of the troposphere and the instrumental techniques used for the measurements, taken from Krasnopolsky[2] and Yung and DeMore[4]. The atmospheric composition is described in

terms of mixing ratio (in ppm, part-per-million) rather than concentration, to allow for the variation of pressure with altitude. Key features are the high proportion of CO_2, low CO, and the strong altitude dependence of SO_2 and H_2O. The upper limit for the mixing ratio of O_2 is determined by spectroscopic measurement, and is a strict limit for the observable region above the clouds[5]. Gas chromatographs aboard Pioneer Venus and the Venera landers indicated that there may be up to 44ppm of oxygen at 50km – the base of the clouds – falling to 16ppm at 42km and undetectable by 22km.

Component	Recommended Value	Data Source
CO_2	96.5%	
N_2	3.4%	PV GC
Ar	90	V MS + PV MS average
Ne	7	V MS
He	12	PV MS
Kr	0.04	V MS
Xe	≤0.02	V MS
HCl	0.6	S
HF	5×10^{-3}	S
CO	50(60km)	S
	30 (40km)	V GC
	15(0km)	V GC
SO_2	0.02(70km)	S
	2(66km)	S
	10 (57km)	V OS
	20 (54 km)	V OS
	50(50km)	V OS
	150(<40km)	V GC + PV GC average
H_2O	10(63km)	S
	30(58km)	S
	200(50km)	V OS high error
	20(0km)	V OS
O_2	<0.3(63km)	S
SO	0.02	
COS	0.3	

Table 1.6 Summary of chemical composition of Venus' troposphere, in ppm. Data sources: PV – Pioneer Venus entry probe, V – Venera 11-14 entry probes, S – Spectroscopy from orbiter, GC – Gas Chromatography instrument, MS – Mass spectrometry, OS – Optical spectroscopy on V11-14 entry probe.

1.2.4 Reported Composition of the Clouds of Venus

1.2.4.1 Sulfuric Acid

Sulfuric acid has been proposed as one of the major constituents of the clouds since the early 1970's[6,7]. The identification was originally made on the basis of measurements of the polarisation of reflected light in the visible and near-infrared regions of the spectrum, as observed from Earth. These optical properties suggested that the outer layers of Venus' clouds – primarily consisting of Mode 2 particles – were made up of a 75wt% sulfuric acid/water solution. Since the Pioneer Venus observations indicate that the physical properties of the Mode 2 particles are stable throughout the cloud layers, all Mode 2 particles are thought to consist of concentrated sulfuric acid.

The distribution of Mode 1 particles in the upper cloud layers mimics that of Mode 2. Combined with the refractive index of the upper haze, this suggests that the upper Mode 1 particles are also concentrated sulfuric acid.

Krasnopolsky[8,9] has argued that a substantial portion – between 50-100% – of the Mode 3 particles in the middle cloud layer are also sulfuric acid, based on (i) calculations on the flux of water vapour and (ii) the column mass of sulfur, as measured by the X-ray fluorescence spectrometer (XFS) carried on Venera 14. Other suggestions[10,11] for the composition of Mode 3 are H_3PO_4 and $HClO_4$. No conclusive identification has been made.

1.2.4.2 Iron and other Minor Constituents in the Clouds

Before any direct measurements were performed, a variety of species were proposed for Venus' clouds. In 1969, Kuiper[12] suggested that the UV absorbance observed in the clouds of Venus could be explained by the presence of $FeCl_2$. The presence of heavy elements like Fe in the atmosphere is plausible due to the high temperatures

occurring at the surface of the planet. The chemistry of the lower atmosphere is believed to be thermochemically governed by interactions at the surface, due to the high pressure and therefore sluggish gas movement that occurs near the surface. In 1970, Lewis[13] proposed a thermodynamic equilibrium model for reactions at the surface between minerals and atmospheric gases, based on the spectroscopically observed gases in the upper atmosphere and the composition of minerals found on Earth. In his study, he noted that $FeCl_2$ and $FeCl_3$ vapour would be generated at the surface, by the action of HCl on Fe_3O_4 (magnetite) and $FeMgSiO_4$ (olivine + enstatite), if these minerals were present. Because of the low volatility of $FeCl_2$ (which has a vapour pressure of only 5×10^{-12} bar at 500K), Lewis concluded that $FeCl_2$ should not be a major component of the clouds, as almost all $FeCl_2$ would condense and precipitate out of the atmosphere at lower altitudes. No further mention was made in his analysis of $FeCl_3$ as a component of the cloud system.

In 1981, researchers at the Space Research Institute of the USSR Academy of Science [14] again proposed that the lower cloud layer contains approximately 1% $FeCl_3$, in order to explain the decreased planetary albedo in the range 300-500nm. The absence of spectral band structure implied that the absorbing species occurred in a condensed phase, and unpublished experiments showed that the absorbance of a solution of 1% $FeCl_3$ in 75wt% sulfuric acid solution matched the observed absorption in the clouds to within experimental uncertainty. They suggested that the source of $FeCl_3$ was condensation from Fe_2Cl_6 vapour generated at the surface and present in the hot lower atmosphere. At higher altitudes, the temperature drops and $FeCl_3$ condenses into small particles, which act as nuclei for the condensation of H_2SO_4 generated in gas phase reactions.

The composition of the clouds was directly probed during the descent of Veneras 12 and 14 (1978, 1981) using an X-ray fluorescence (XFS) spectrometer which performed an elemental analysis on samples from the clouds[15,16]. Initial results from V12 showed that Cl, S, Ar, Al and Ti were present; instrument design prevented the detection of elements with $Z<13$. The Al and Ti were attributed to material from the measuring cell rather than from the clouds. The XFS instrument on V12 used ^{55}Fe and ^{109}Cd as sources of ionising photons. Since all of the elements identified by V12

could be detected using the ^{55}Fe source alone, the ^{109}Cd source was omitted from the instrument on V14. Further examination of the V12 data[17] showed that Fe was also present – but this could only be detected by using the ^{109}Cd source. Thus, the instrument on V14 was incapable of detecting Fe, even if it were present in the clouds. V14 again showed that Cl and S were present, though the concentrations reported were somewhat different to V12. Table 1.7 shows the elemental composition of the clouds as determined by XFS experiments aboard V12 and V14. Both V12 and V14 may have underestimated the amount of some components, especially S, due to the evaporation of volatile gases from the aerosol during sampling[8].

	Venera 12 [15]	**Venera 14** [16]	**Vega 2** [18]
Sulfur	0.17±0.03 mg/m^3	1.10±0.13 mg/m^3	1.5mg/m^3 (63-51.5 km)
Chlorine	2.1±0.06 mg/m^3	0.16±0.04 mg/m^3	1.5mg/m^3 (63-51.5 km)
Argon	200±100ppm	-	-
Mercury	<5×10^{-2} mg/m^3	-	-
Iron	0.22 mg/m^3 [17]	-	0.2±0.1 mg/m^3 (52-47 km)
Phosphorus	<0.1 mg/m^3	<0.1 mg/m^3	6mg/m^3 (51-47km)

Table 1.7 Elemental Composition of Venus' Clouds determined by XFS on Venera 12, Venera 14 and Vega 2

In 1985, Krasnopolsky[8] showed that the observed mass loading profile of the Mode 1 particles in the lower and middle layers of cloud closely matched a calculated condensation profile for $FeCl_3$. This assumed that ferric chloride vapour – which exists as Fe_2Cl_6 dimers – was present in the lower atmosphere as a result of thermochemical reactions at the surface. Mode 1 particles in the upper cloud have a different origin, as shown by the sudden increase in mass loading at 57km, and are probably H_2SO_4. (Section 1.2.4.1)

In addition, Krasnopolsky calculated that the ratio of the upward flux of Mode 1 $FeCl_3$ particles to the downward flux of Mode 2 H_2SO_4 particles is 1% which is the concentration of $FeCl_3$ dissolved in sulfuric acid that is required to explain the UV albedo of Venus. Upwardly mobile $FeCl_3$ particles are incorporated into the sulfuric acid droplets, either by collision or condensation of H_2SO_4 vapour onto $FeCl_3$ nuclei.

The most recent direct investigation of the cloud composition was carried out by Vega 1 and 2 in 1984. Each of the Vega landing probes carried instruments to study the chemical composition of the clouds using mass spectrometry, gas chromatography and X-ray spectroscopy as part of their payload. The results of these experiments have been summarised by Krasnopolsky[10]. Gas chromatography showed 1mg/m^3 of H_2SO_4 and 0.1 mg/m^3 of S_x in the aerosol, while the mass spectrometer indicated 6±4 mg/m^3 of H_2SO_4 and >0.3 mg/m^3 of Cl. The most unexpected results came from the X-ray fluorescence spectroscopy. The instrument was designed for increased resolution and higher detection limits than instruments used on Veneras 12 and 14, and was set up to detect Cl, S, P, Fe, elements lighter than P ($Z<15$) and elements heavier than Fe ($Z>26$). Unfortunately, statistical errors in the data and unstable instrument characteristics meant that the XFS information was incomplete. No information was gathered about Fe at altitudes greater than 52km, or about elements with atomic number less than 15. The big surprise, however, was the discovery of significant amounts of phosphorus in the clouds, something that had not previously been observed. Krasnopolsky's revised tabulation of the most likely composition of the cloud particles, as indicated by the Vega experiments, is also shown in Fig. 1.7. The most notable feature is the change in the clouds at 52km (roughly matching the separation between the lower and the middle/upper clouds observed by Pioneer Venus). The clouds above 52 km are H_2SO_4, S_8 and Al_2Cl_6, while the lower clouds are H_3PO_4 and Fe_2Cl_6. Al_2Cl_6 was proposed as a chlorine-bearing aerosol on the basis of vapour pressure calculations, despite the presence of Al in the clouds being experimentally unverified. It must be remembered that no data was available for Fe in the upper clouds, and that there is no evidence from other experimental techniques to support the identification of phosphoric acid in the lower clouds.

The three XFS experiments, which were intended to provide direct evidence for the composition of Venus' clouds, each returned significantly different results – in turn identifying Cl, S and P as the major elemental component of the clouds. There is some question as to the validity of these experimental identifications. The energy of an elemental peak in an XFS experiment is dependent on the atomic number. Since P, S and Cl have consecutive atomic numbers, their XFS peaks are very close together, and can only be resolved mathematically. As the results from the Vega 2 instrument

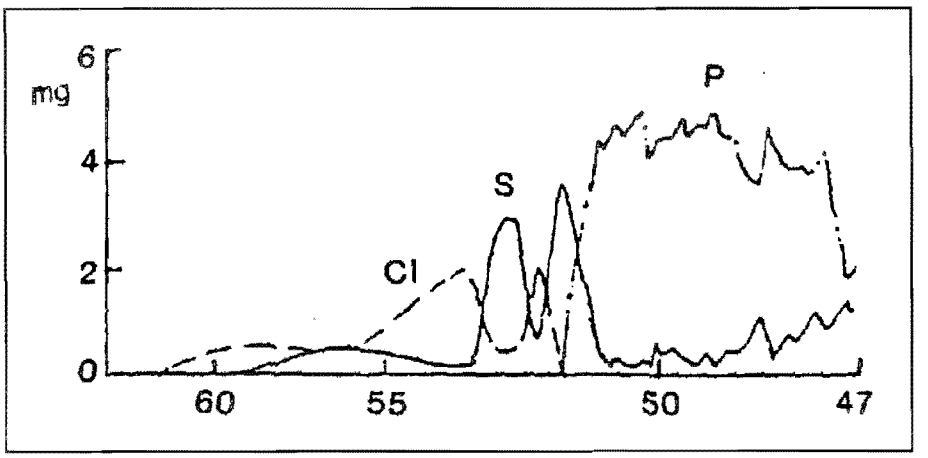

Figure 1.8 Accumulation of Cl, S and P on the XFS filter on Vega-2

show (Fig 1.8)[18], there is a strong anticorrelation between the elements, although the total mass of the aerosol varies quite slowly. The most likely explanation is that the data quality is inadequate to solve the equations separating the three chemical components, rather than that a genuine stratification exists between layers of chlorine, sulfur and phosphorus in the clouds on Venus.

Cloud Region	**h, km**	**1985 (Venera 14)**			**1988 (Vega 2)**
		Mode 1	Mode 2	Mode 3	
Upper Haze	70-90	H_2SO_4 (~85%)	-	-	H_2SO_4 (~85%)
Upper Layer	57-70	H_2SO_4 (~85%), S_8	H_2SO_4 (~85%) + $FeCl_3$(~1%) + S_8	-	H_2SO_4 (~5mg/m^3) S_8 (~0.5mg/m^3)
Middle Layer	50-57	$FeCl_3$	H_2SO_4 (~85%) + $Fe_2(SO_4)_3$ (~1%) + S_8	H_2SO_4 (~85%)	Al_2Cl_3 (~3mg/m^3)
Lower Layer	48-50	$FeCl_3$	H_2SO_4 (~95%) + $Fe_2(SO_4)_3$ (~1%) + S_8	H_2SO_4 (~85%)	H_3PO_4 (~5mg/m^3)
Pre-cloud Layer	46-48	$FeCl_3$	H_2SO_4 (~95%) + $Fe_2(SO_4)_3$ (~1%)	-	Fe_2Cl_6 (~1%)
Lower Haze	30-48	$Fe_2(SO_4)_3$	-	-	

Table 1.9 Probable Cloud Composition of Venus – Comparison of Venera14 and Vega 2 Analyses by Krasnopolsky

In later publications, the possible presence of H_3PO_4 in the lower clouds has been ignored. In 1994, Krasnopolsky and Pollack published a study on the formation of H_2SO_4 and the H_2O-H_2SO_4 equilibrium at the base of the clouds[9]. Yung and DeMore's book Photochemistry of Planetary Atmospheres (1999)[2] makes no mention of phosphoric acid or phosphorus-containing gases in their discussion of Venus.

In conclusion, it can be said that the clouds on Venus include aerosols of concentrated sulfuric acid, ferric chloride and other chlorine-containing compounds, both as separate aerosols and combined. Other chemical components are likely to be present, possibly including phosphoric acid, elemental sulfur and aluminium chloride, but to date these have not been conclusively identified.

1.3 Chemistry of the Atmosphere of Venus

1.3.1 Introduction

Discussions of the atmospheric chemistry of Venus have made a strong distinction between the chemistry occurring above and below the cloud layers. As on Earth, the upper atmosphere is characterised by non-equilibrium chemistry due to photochemical processes. Spectroscopic measurements have provided considerable information about the chemical composition and distribution of species above the upper cloud layer.

In contrast, the chemistry of the atmosphere below the clouds is governed by thermochemical equilibrium, since the heavy, opaque cloud cover prevents any short-wavelength light from causing photochemistry in this region. High temperatures are predicted to cause extensive weathering of minerals at the planet's surface, acting as both a source and sink for atmospheric species. Although the region below the clouds contains 80% of the mass of Venus' atmosphere, detailed information about its chemical composition is unavailable. Due to the opacity of the clouds, spectroscopic measurements from above are unable to penetrate the lower atmosphere, meaning that

the only knowledge that we have about its chemical makeup comes from insertion probes and theoretical predictions.

Several authors have proposed kinetic models for the chemistry of the stratosphere[19,20,21,22], attempting to match the observed distribution of chemical species. These models deal exclusively with the region above the clouds, and have tended to regard the lower atmosphere as a black box that can be used as a source or sink of various species as required, due to the lack of hard data for the lower atmosphere. Discussions of the chemistry of the troposphere have included surface-gas equilibria[13] and cloud formation[9], but no comprehensive model of the lower atmosphere has been attempted.

1.3.2 Chemistry of the Upper Atmosphere

The standard model for the chemistry of the Venusian atmosphere is that of Yung and DeMore, first published in 1982[22]. 114 reactions of gas-phase hydrogen, carbon, nitrogen, oxygen, sulfur and chlorine species were considered in the reaction scheme. Key objectives of the model were to explain the high mixing ratio of CO_2 and low O_2 abundance observed in the atmosphere.

The first problem that must be addressed is that CO_2 is photochemically dissociated by solar UV radiation at wavelengths less than 2050Å according to (1.1):

$$CO_2 + h\nu \longrightarrow CO + O \qquad (1.1)$$

The O formed by this reaction is in the (^{3}P) ground state if the light is close to the dissociation threshold, or in an excited state (^{1}S) or (^{1}D) if the photons are of shorter wavelength. However, most of the excited O atoms are quenched to (^{3}P) by collision with CO_2. The three-body collision which would reverse the CO_2 dissociation, ie

$$CO + O(^3P) + M \longrightarrow CO_2 + M \qquad (1.2)$$

is spin forbidden. In a pure CO_2 atmosphere, the only fate for the O atoms is reaction with other O atoms.

$$O + O \longrightarrow O_2 \qquad (1.3)$$

leading to an overall reaction of

$$2CO_2 \longrightarrow 2CO + O_2 \qquad (I)$$

While ground state O_2 has not been detected in the Venusian atmosphere, airglow from the relaxation of excited oxygen $O_2(^1\Delta) \rightarrow O_2(^3\Sigma) + h\nu$ has been observed[23]. It is inferred from this that a significant proportion of the O atoms from CO_2 photolysis eventually produce O_2, despite the spectroscopic upper limit for the mixing ratio of O_2 being 3×10^{-7}.

Reaction scheme (I) predicts a ratio of $CO:O_2$ of 2:1, and a large amount of both CO and O_2 is expected to be present. The rate of CO_2 photolysis due to solar irradiation[24] is estimated to be 1.1×10^{13} molecules.cm^{-2}s^{-1}, which is fast enough that the entire amount of CO observed could be produced in as little as 4400 years. Furthermore, the ratio of $CO:O_2$ in the atmosphere is at least 170:1. It is apparent that there are significant reaction pathways for the re-oxidation of CO and the removal of O_2.

Catalytic cycles involving HO_x, Cl and SO_x species have been proposed to increase the rate of $CO + O_2$ recombination. Yung and DeMore[4] report that the bulk of CO_2 photolysis is reversed by two Cl –catalysed cycles, where Cl is present due to the photolysis of HCl:

$$HCl + h\nu \xrightarrow{\lambda < 2375\text{Å}} H + Cl \qquad (1.4)$$

$$Cl + CO + M \longrightarrow ClCO + M \qquad (1.5)$$
$$ClCO + O_2 + M \longrightarrow ClC(O)O_2 + M \qquad (1.6)$$
$$ClC(O)O_2 + O \longrightarrow CO_2 + O_2 + Cl \qquad (1.7)$$
$$\overline{CO + O \xrightarrow{HCl,\ h\nu} CO_2} \qquad (IIa)$$

$$Cl + CO + M \longrightarrow ClCO + M \qquad (1.5)$$
$$ClCO + O_2 + M \longrightarrow ClC(O)O_2 + M \qquad (1.6)$$
$$ClC(O)O_2 + Cl \longrightarrow CO_2 + ClO + Cl \qquad (1.8)$$
$$ClO + O \longrightarrow Cl + O_2 \qquad (1.9)$$
$$\overline{CO + O \xrightarrow{HCl,\ h\nu} CO_2} \qquad (IIb)$$

In addition, Cl and SO_2 reactions are coupled, resulting in the simultaneous oxidation of CO to CO_2 and SO_2 to H_2SO_4, according to the scheme:

$$Cl + CO + M \longrightarrow ClCO + M \quad (1.5)$$

$$ClCO + O_2 + M \longrightarrow ClC(O)O_2 + M \quad (1.6)$$

$$ClC(O)O_2 + Cl \longrightarrow CO_2 + ClO + Cl \quad (1.8)$$

$$SO_2 + h\nu \longrightarrow SO + O \quad (1.10)$$

$$SO_2 + O + M \longrightarrow SO_3 + M \quad (1.11)$$

$$SO_3 + H_2O + M \longrightarrow H_2SO_4 + M \quad (1.12)$$

$$ClO + SO \longrightarrow Cl + SO_2 \quad (1.13)$$

$$CO + SO_2 + O_2 + H_2O \xrightarrow{HCl,\ h\nu} CO_2 + H_2SO_4 \quad (III)$$

The mechanism described by Yung and DeMore required that CO_2, SO_2 and H_2O were somehow produced in the lower atmosphere, and that CO was destroyed. They noted that O_2 from (I) was removed by CO and SO_2 oxidation, but that their mechanism did not fully account for the low O_2 mixing ratio.

1.3.3 Chemistry of the Lower Atmosphere

As has been already mentioned, the troposphere of Venus is very hot and has high pressure. Photochemistry is unlikely due to UV absorption in the stratosphere, and absorption and scattering of longer wavelength light in the cloud layers. Thus, it is expected that the chemistry of the troposphere will be determined by thermochemical equilibria. While thermodynamic data exists for many possible reactions, the kinetics of these reactions are unknown. Studies have assumed that the troposphere is in an equilibrium state, especially at the surface. This seems reasonable due to the high temperature, and the sluggish fluid motion that results from the high pressure.

Several studies have been carried out that detail the possible equilibrium reactions occurring between minerals and atmospheric gases at Venus' surface[13,25,26]. An outline of the results is found in Prinn[27]. In short, CO is oxidised to CO_2 via surface mineral equilibria. The amount of O_2 gas predicted is very low, so the main sulfur-bearing gas is OCS, with lesser amounts of H_2S and SO_2. HF and HCl exist in

equilibrium with the surface; the high mixing ratio observed can be fully explained by the surface temperature, but there are too many imponderables for this to be regarded as a definitive theory.

Krasnopolsky and Pollack[9] have successfully modelled the lower cloud boundary using a dynamic and chemical model. Sulfuric acid droplets formed photochemically in the upper clouds are transported to the lower clouds by gravitational settling. At lower altitudes, the temperature increases significantly, and the following reaction scheme comes into effect. This scheme is responsible for converting OCS from the surface into SO_2, which is transported into the upper atmosphere.

$$H_2SO_4 \rightleftharpoons SO_3 + H_2O \quad (1.14)$$

$$SO_3 + CO \longrightarrow CO_2 + SO_2 \quad (1.15)$$

$$SO_3 + OCS \longrightarrow CO_2 + (SO)_2 \quad (1.16)$$

$$(SO)_2 + OCS \longrightarrow CO + S_2 + SO_2 \quad (1.17)$$

$$CO + SO_2 \longrightarrow CO_2 + SO \quad (1.18)$$

1.4 Heterogeneous Chemistry Occurring in Terrestrial Aerosols

1.4.1 Introduction

A topic that has not been considered in any detail is the role of heterogeneous chemistry occurring in the clouds of Venus. Over the last thirty years, the importance of heterogeneous chemistry in Earth's atmosphere has been realised and has stimulated much research, including the role of the polar stratospheric clouds in seasonal ozone depletion – the so-called "hole" in the ozone layer – and the oxidation of SO_x and NO_x in water clouds to form "acid rain". Yung and DeMore[4] have suggested that heterogeneous chemistry may be significant on Venus, and have recommended it as one of the areas requiring investigation.

Oxidation of SO_2 in aqueous aerosols has been studied in considerable detail in the HALIPP (Heterogeneous And Liquid Phase Processes) program[28], as part of the EUROTRAC program on the transport and chemical transformation of pollutants in the troposphere, with particular emphasis on acid rain. One of the results from HALIPP is that transition metal ions – such as Fe^{2+}/Fe^{3+} - play an important role in the sulfur redox chemistry of terrestrial aerosols. In light of the discovery of large amounts of iron in the Venus aerosol, similar processes might also occur there.

One key difference between aerosol reactions on Earth and on Venus is the medium. The reactions studied in HALIPP occur in dilute acid solution, while on Venus, the reaction medium is concentrated sulfuric acid. As a result, the results from HALIPP studies cannot simply be applied to Venus without a consideration of the role of the solvent, on both a chemical and physical level. An immediate observation is that sulfuric acid is considerably more viscous than water, which means that reactions that are mechanism-controlled in aqueous solution may instead be diffusion controlled in a higher viscosity environment[29]. However, it is appropriate to begin with a discussion of sulfur oxidation reactions that have been studied in dilute acid solution before attempting to extend the results to concentrated sulfuric acid solutions.

1.4.2 Oxidation of SO_2 in Dilute Acid Solution

The oxidation of SO_2 in aqueous solution has been extensively studied over many years. A full review is beyond the scope of this work. Important oxidising agents are H_2O_2, $^{\cdot}OH$ and O_3. Recently, the peroxysulfate anion, HSO_5^-, has been proposed as a reactive intermediate in the reaction, and its' ability to oxidise $SO_{2(aq)}$ has been considered[30,31,32]. It is also widely known that SO_2 in aqueous solution is photochemically oxidised by UV light in a radical chain reaction. In this case, oxysulfur radicals ($^{\cdot}SO_3^-$, $^{\cdot}SO_4^-$ and $^{\cdot}SO_5^-$) are identified as the chain carriers[33], rather than $^{\cdot}OH$. An extensive set of rate constants for the reactions of $^{\cdot}SO_x^-$ radicals has been measured and reported as part of HALIPP[28].

1.4.3 Thermal Reactions of Fe(II)/(III) with SO_2 and O_2 in Dilute Sulfuric Acid Solution

It has long been known that trace amounts of Fe^{3+} and other transition metals act as catalysts for the oxidation of SO_2 in aqueous solution, producing either SO_4^{2-} or $S_2O_6^{2-}$, depending on the reaction conditions. If the concentration of Fe(III) is increased, the reaction can be regarded as the reduction of Fe^{3+} by SO_2. An early study of the reaction kinetics[34] found that the reaction proceeded by the disproportionation of a $Fe(HSO_3)^{2+}$ complex to form $\cdot HSO_3$ radicals, followed by the reduction of Fe^{3+} by $\cdot HSO_3$.

$$Fe(HSO_3)^{2+} \longrightarrow Fe^{2+} + \cdot HSO_3 \quad (1.19)$$

$$Fe^{3+} + \cdot HSO_3 + H_2O \longrightarrow Fe^{2+} + SO_4^{2-} + 3H^+ \quad (1.20)$$

If oxygen was present, a catalytic cycle was established which resulted in the regeneration of Fe^{3+} and the oxidation of SO_2, according to the proposed mechanism:

$$\cdot HSO_3 + O_2 + H_2O \longrightarrow SO_4^{2-} + 2H^+ + HO_2 \quad (1.21)$$

$$HO_2 + Fe^{2+} + H_2O \longrightarrow Fe(OH)^{2+} + H_2O_2 \quad (1.22)$$

$$H_2O_2 + Fe^{2+} \longrightarrow Fe(OH)^{2+} + \cdot OH \quad (1.23)$$

$$\cdot HSO_3 + \cdot OH \longrightarrow 2H^+ + SO_4^{2-} \quad (1.24)$$

The oxidation of Fe(II) in dilute acidic aqueous solution by a stream of gas containing O_2 and SO_2 was studied in 1979 by researchers interested in the reaction for metallurgical application[35]. It was already known that the direct oxidation of Fe^{2+} to Fe^{3+} by oxygen is slow. They found that when SO_2 was added to the gas stream, the rate of the reaction was significantly increased. By varying the ratio of Fe^{2+}/Fe^{3+} in solution and SO_2/O_2 in the gas stream, they could perform oxidation of Fe(II), or reduction of Fe(III), or oxidation of SO_2. They proposed that reactions (1.19) – (1.24) were occurring, and added reaction (1.25) – the oxidation of Fe^{2+} with $\cdot OH$ – which competed with (1.24):

$$Fe^{2+} + \cdot OH + H^+ \longrightarrow Fe^{3+} + H_2O \quad (1.25)$$

A study of the reaction kinetics[36], again for metallurgical applications, found that the reaction was sensitive to the pH of the solution, with observed reaction rates decreasing dramatically below pH 0.5 and increasing appreciably above pH 2.5. The

rate of the reaction was found to be independent of the concentrations of Fe^{2+} and O_2, and directly proportional to the amount of sulfurous acid oxidised. It was proposed that Fe^{2+} was oxidised by an intermediate produced in the free-radical-chain oxidation of sulfurous acid by oxygen.

In 1988, at the start of the HALIPP project, the reaction mechanism for the transition-metal-ion catalysed oxidation of SO_2 was still speculative. It was unclear whether $^{\cdot}OH$ or $^{\cdot}SO_x^-$ was responsible for Fe^{2+} oxidation, due to the limited understanding of the behaviour of oxysulfur radicals in solution, and their oxidising ability relative to $^{\cdot}OH$. In HALIPP, these species and their reactions were the subject of experimental work by several groups.

All of the reaction mechanisms proposed for the Fe – SO_2 reaction involve the disproportionation of a Fe(III)-S(IV) complex to produce an oxy- or hydroxy-sulfur radical. The formation and decomposition of transient Fe(III)-S(IV) complexes was the subject of a more extensive investigation by Kraft and van Eldik[37,38]. They found that the chemistry of complex formation was complicated by the many possible acid-base equilibria in which $SO_{2(aq)}$ and $Fe(III)_{(aq)}$ were involved. The dependency on [total S(IV)] and pH indicated that the reactive complex was formed by substitution of HSO_3^- into $(H_2O)_5Fe(OH)^{2+}$.

$$(H_2O)_5Fe(OH)^{2+} + HSO_3^- \longrightarrow (H_2O)_4Fe(HSO_3)(OH)^+ + H_2O \quad (1.26)$$

If the concentration of HSO_3^- was sufficiently large, a second and third HSO_3^- was substituted into the complex. The pK_a of the complexes was undetermined, so it was unknown whether the S(IV) was present as SO_3^{2-} or HSO_3^-, although evidence suggested that the S(IV) species was bonded by Fe – S rather than Fe – O. The amount of complex formed was strongly affected by the pH, with a maximum at around pH = 3. This was attributed to the optimisation of $[HSO_3^-]$ and $[(H_2O)_5Fe(OH)^{2+}]$ in the solution; at lower pH, both species are protonated. The fully protonated Fe(III) complex, $Fe(H_2O)_6^{3+}$, is approximately 300 times less labile than $(H_2O)_5Fe(OH)^{2+}$, which effectively prevents it from forming any S(IV) complex.

The decomposition of the complex is considerably slower than its formation, being measured over a period of several seconds rather than milliseconds. The mono-, bis-

and tris-(sulfito)Fe(III) complexes each decomposed at different rates, with the tris-complex reacting most rapidly. The products of the decomposition were not monitored, but were known to include a Fe(II) complex, SO_4^{2-} and $S_2O_6^{2-}$. If dissolved oxygen was present, an alternative reaction could occur where O_2 was substituted into the Fe(III)-S(IV) complex, followed by oxidation of S(IV) to either $S_2O_6^{2-}$ or SO_4^{2-}, and reduction of O_2 to H_2O_2 instead of Fe(III) to Fe(II). This increased the amount of S(IV) being oxidised without the corresponding reduction of Fe(III).

Bal Reddy and van Eldik extended this study to the kinetics and mechanism of the sulfite-induced oxidation of Fe(II)[39]. They noted that there was always a trace of Fe(III) in aqueous Fe(II) solutions, presumably from oxidation by atmospheric oxygen. Their experiments showed that the Fe(II) oxidation was autocatalysed by Fe(III), by way of the decomposition of Fe(III)-S(IV) complexes as previously described. When the reaction was carried out with very low initial [Fe(III)], an induction period of several seconds was observed. The observed reaction rate was observed to be dependent on [Fe(III)], [S(IV)] and pH, but not on [Fe(II)] in agreement with earlier results. They also noted that if sulfite was present in excess, the initial autoxidation of Fe(II) was followed by Fe(III) reduction with S(IV) oxidation. Thus, the reaction was sensitive to the relative amounts of iron and sulfite to determine whether the overall reaction resulted in Fe(II) being oxidised or Fe(III) being reduced.

The mechanism reported by HALIPP for the reaction between Fe and S(IV) is essentially the same as that proposed by Bal Reddy and van Eldik in 1992. Fe(II) and Fe(III) each refer to a number of iron complexes in various hydration states. The rate-determining step is (1.30), which is actually a combination of several similar reactions as has already been discussed. Many of the reactions also occur in the photochemical oxidation of SO_2, and rate constants for many of the reaction steps have been published[28,40,41,42].

Initiation

$$Fe(II) + O_2 \longrightarrow Fe(III) + O_2^{\cdot-} \quad (1.27)$$

or

$$Fe(II) + HSO_3^- \longrightarrow FeHSO_3^+ \quad (1.28)$$

$$FeHSO_3^+ + O_2 \longrightarrow FeHSO_3^{2+} + O_2^{\cdot-} \quad (1.29)$$

Autocatalysis

$$Fe(OH)^{2+} + HSO_3^- \longrightarrow [Fe(OH)HSO_3]^+ \quad (1.26)$$

$$[Fe(OH)HSO_3]^+ \longrightarrow Fe^{2+} + {}^{\cdot}SO_3^- + H_2O \quad (1.30)$$

$$SO_3^{\cdot-} + O_2 \longrightarrow {}^{\cdot}SO_5^- \quad (1.31)$$

$${}^{\cdot}SO_5^- + Fe^{2+} + H_2O \longrightarrow Fe(OH)^{2+} + HSO_5^- \quad (1.32)$$

$$HSO_5^- + Fe^{2+} \longrightarrow Fe(OH)^{2+} + {}^{\cdot}SO_4^- \quad (1.33)$$

$${}^{\cdot}SO_5^- + HSO_3^- \longrightarrow HSO_5^- + {}^{\cdot}SO_3^- \quad (1.34)$$

$$\longrightarrow SO_4^{2-} + {}^{\cdot}SO_4^- + H^+ \quad (1.35)$$

$${}^{\cdot}SO_4^- + Fe^{2+} \longrightarrow Fe^{3+} + SO_4^{2-} \quad (1.36)$$

$${}^{\cdot}SO_4^- + HSO_3^- \longrightarrow SO_4^{2-} + {}^{\cdot}SO_3^- + H^+ \quad (1.37)$$

Termination

$$HSO_5^- + HSO_3^- + H^+ \longrightarrow 2SO_4^{2-} + 3H^+ \quad (1.38)$$

$${}^{\cdot}SO_3^- + {}^{\cdot}SO_3^- \longrightarrow S_2O_6^{2-} \quad (1.39)$$

$${}^{\cdot}SO_4^- + {}^{\cdot}SO_4^- \longrightarrow S_2O_8^{2-} \quad (1.40)$$

$${}^{\cdot}SO_5^- + {}^{\cdot}SO_5^- \longrightarrow S_2O_6^{2-} + 2O_2 \quad (1.41)$$

$${}^{\cdot}SO_5^- + {}^{\cdot}SO_5^- \longrightarrow S_2O_8^{2-} + O_2 \quad (1.42)$$

$${}^{\cdot}SO_5^- + {}^{\cdot}SO_3^- \longrightarrow S_2O_6^{2-} + O_2 \quad (1.43)$$

Bal Reddy and van Eldik also proposed the following reactions to account for $O_2^{\cdot-}$ generated in the initial oxidation of Fe^{2+}. A more complex series of reactions for $O_2^{\cdot-}$ is probable; however, as (1.27) and (1.29) are slow only a small amount of $O_2^{\cdot-}$ is formed and it is unimportant in the overall scheme.

$$O_2^{\cdot-} + H^+ \rightleftharpoons HO_2 \quad (1.44)$$

$$O_2^{\cdot-} + HO_2 \longrightarrow HO_2^- + O_2 \quad (1.45)$$

$$HO_2^- + H^+ \rightleftharpoons H_2O_2 \quad (1.46)$$

$$HSO_3^- + H_2O_2 \longrightarrow HSO_4^- + H_2O \quad (1.47)$$

1.4.4 Photochemical Reactions of Fe(II) and Fe(III)

1.4.4.1 Photolysis of Fe^{2+} in Aqueous Sulfuric Acid

The reaction mechanism described in Section 1.4.3 comprises the reactions that are responsible for the oxidation of Fe(II) and SO_2, and the reduction of Fe(III) in dilute acid solution. Since the reaction involves a number of radical species, it is not surprising that it is also photochemically active.

The ultraviolet absorption spectrum of Fe^{2+} in aqueous solution shows a continuous, featureless absorption. The molar extinction coefficient is reported as 14.8±0.15 $L.mol^{-1}cm^{-1}$ at 253.7nm, increasing rapidly at shorter wavelengths[43]. Quantum yields for the 253.7nm photooxidation of Fe^{2+} to Fe^{3+} in aqueous sulfuric acid, accompanied by the formation of H_2, were reported by Heidt et al in 1962[44]. A mechanistic study by Stein[43,45] suggested that the primary process was absorption of light by Fe^{2+} to produce an electronically excited state, which could transfer an electron to the surrounding water to form an H atom:

$$Fe^{2+}_{(aq)} + h\nu \longrightarrow [Fe^{2+}]^*_{(aq)} \longrightarrow Fe^{3+}_{(aq)} + OH^- + {}^{\cdot}H \qquad (1.48)$$

However, competition studies by Airey and Dainton[46] indicated that the primary process was instead the formation of a hydrated electron:

$$Fe^{2+} + h\nu \longrightarrow Fe^{3+} + e^-_{(aq)} \qquad (1.49)$$

It was proposed that the electron was transferred to a potential well created by nearby randomly oriented solvent molecules. Logan[47] observed an increase in the quantum yield at 228.8nm, which was attributed to the electron being transferred to a more distant trap – and thus less likely to recombine with the Fe^{3+}.

Papp et al[48], recognised that several absorbing species exist in a solution of Fe^{2+} in dilute sulfuric acid. In addition to $Fe^{2+}_{(aq)}$, there are $FeSO_{4(aq)}$ and $FeHSO_4^+{}_{(aq)}$ complexes to consider. By combining the solution equilibria data with measurements of the total quantum yield for the solution, Papp was able to obtain individual quantum yields for each component:

$$\Phi_i\ (Fe^{2+}{}_{(aq)}) = 0.15 - 0.16$$

$$\Phi_i\ (FeSO_{4(aq)}) = 0.30$$

$$\Phi_i\ (FeHSO_4{}^{+}{}_{(aq)}) = 0.67$$

The quantum yields for $Fe^{2+}{}_{(aq)}$ and $FeSO_{4(aq)}$ show a small dependence on $[H^+]$.

1.4.4.2 Photolysis of Fe^{3+} in Aqueous Sulfuric Acid

In all of the studies of Fe(II) photolysis, a substantial portion of light was absorbed by Fe(III). Although photolysis of Fe(III) in aqueous solution produces ·OH, the Fe(III) absorption was treated as an internal filter, reducing the amount of light available to be absorbed by Fe(II), rather than as part of the reaction. Logan assumes that the only contribution of ·OH is to re-oxidise Fe(II) from Fe(III) photolysis:

$$Fe^{3+}.H_2O + h\nu \longrightarrow Fe^{2+} + H^+ + \cdot OH \quad (1.50)$$

$$\cdot OH + Fe^{2+} \longrightarrow OH^- + Fe^{3+} \quad (1.51)$$

or

$$\cdot OH + H_2 \longrightarrow H_2O + \cdot H \quad (1.52)$$

$$\cdot H + Fe^{2+}.H_2O \longrightarrow H_2 + Fe^{3+} + OH^- \quad (1.53)$$

In systems containing a high concentration of Fe(III) relative to Fe(II), or other reactive species, the role of ·OH should not be dismissed so lightly. Several groups have studied the photolysis[49,50,51], and have identified $[Fe(OH)]^{2+}{}_{(aq)}$ as the active species:

$$Fe(OH)^{2+}{}_{(aq)} + h\nu \longrightarrow Fe^{2+}{}_{(aq)} + \cdot OH \quad (1.50a)$$

Quantum yields for ·OH formation reported by Benkelberg and Warneck[51] showed marked wavelength dependence, increasing from 0.074 at 370nm to 0.312 at 280nm, which was the lower limit of the wavelength range studied.

1.4.4.3 Photolysis of $[FeSO_4]^+$ and $[FeSO_3]^+$ in Aqueous Sulfuric Acid

Benkelberg and Warneck have also investigated the photolysis of iron(III) sulfato complexes to produce $\cdot SO_4^-$ radicals[51].

$$FeSO_4^+{}_{(aq)} + h\nu \longrightarrow Fe^{2+}{}_{(aq)} + \cdot SO_4^- \qquad (1.51)$$

The reported quantum yield was significantly smaller than that for $\cdot OH$ formation by (1.50a), which occurred in the same solution. At 350nm, $\Phi(\cdot SO_4) = 1.56\times10^{-3}$, increasing to 7.90×10^{-3} at 280nm. The photolysis of $[FeHSO_4]^{2+}$ has not been reported separately, although it may contribute to the reported quantum yield for (1.51).

Iron(III) sulfito complexes are already known to decompose thermally to produce $\cdot SO_3^-$ radicals[37]. Photolysis of the complex is expected to yield the same products[28].

$$FeSO_3^+{}_{(aq)} + h\nu \longrightarrow Fe^{2+}{}_{(aq)} + \cdot SO_3^- \qquad (1.52)$$

1.5 Conclusion: Possible Redox Chemistry in the Clouds of Venus

The best information currently available indicates that the clouds of Venus include highly concentrated sulfuric acid aerosols containing up to 1% Fe by mass, which corresponds to a concentration of $(3\text{-}3.3)\times10^{-4}$M, depending on the exact concentration of the acid. The oxidation state of the iron cannot be determined by the analytic methods used. A significant concentration of gas-phase SO_2 has been reported in the atmosphere at the same altitude as the clouds. Since SO_2 is highly soluble in both sulfuric acid and concentrated sulfuric acid solutions, it is expected that the aerosols will contain a small, but potentially significant concentration of S(IV). In addition, it is possible but unconfirmed that some oxygen gas is present in the lower cloud atmosphere.

It is highly probable that the clouds of Venus are a source of redox activity in the atmosphere of Venus, a possibility that has not yet been investigated experimentally or considered in computational models of the atmosphere. The next chapter of this thesis describes an experiment in which an aerosol of concentrated sulfuric acid is photolysed with UV light in the presence of CO, resulting in the formation of CO_2. The results of this experiment support the proposition that photochemical reactions in the cloud layer play an important role in maintaining the high proportion of CO_2 in the Venus atmosphere.

Chapter 2

Photochemical Oxidation of Carbon Monoxide in a Sulfuric Acid Aerosol

Chapter 2

Photochemical Oxidation of Carbon Monoxide in a Sulfuric Acid Aerosol

2.1 Introduction

Earlier work in this laboratory established that concentrated sulfuric acid aerosols provide a medium for the photochemical oxidation of CO to CO_2. In 1994, Mills et al reported a maximum quantum yield for the production of CO_2 of 0.04 at 193nm, based on experiments performed in 1993[1,2]. In 1994, further experiments were conducted which gave a lower estimate of the quantum yield of 0.012 ± 0.002. These experiments also observed the production of SO_2 with a reported maximum quantum yield of 0.038 ± 0.007[3]. The results for SO_2 were not very reproducible; indeed some of the experiments showed SO_2 being consumed by the reaction instead of being produced. The reason for this was unknown, as was the reason for the quite large variation in the quantum yield of CO_2 between experiments.

The first goal of the present work was to produce a reliable measurement of the quantum yields for production of CO_2 and SO_2, and to determine why previous experiments have yielded inconsistent results.

2.2 Experimental

The apparatus is directly descended from that used for the earlier measurements. A more comprehensive discussion of the design considerations is given by Mills[1]. The experiment is performed in a closed pyrex flow system, illustrated schematically in Fig. 2.1, in which the following operations take place.

(1) Aerosol Generation

(2) Characterisation of Aerosol by Light Scattering

(3) Laser Irradiation of Aerosol

(4) Aerosol Removal

(5) Detection of Products

2.2.1 *Aerosol Generation*

An aerosol is formed spontaneously when the vapour pressure of some species exceeds the saturation vapour pressure by a factor of 2-10 times, depending on the species involved[4]. This is an ideal process for forming sulfuric acid aerosols under laboratory conditions, as sulfuric acid has a very low vapour pressure at STP, and is readily generated in the gas phase by reaction between H_2O and SO_3.

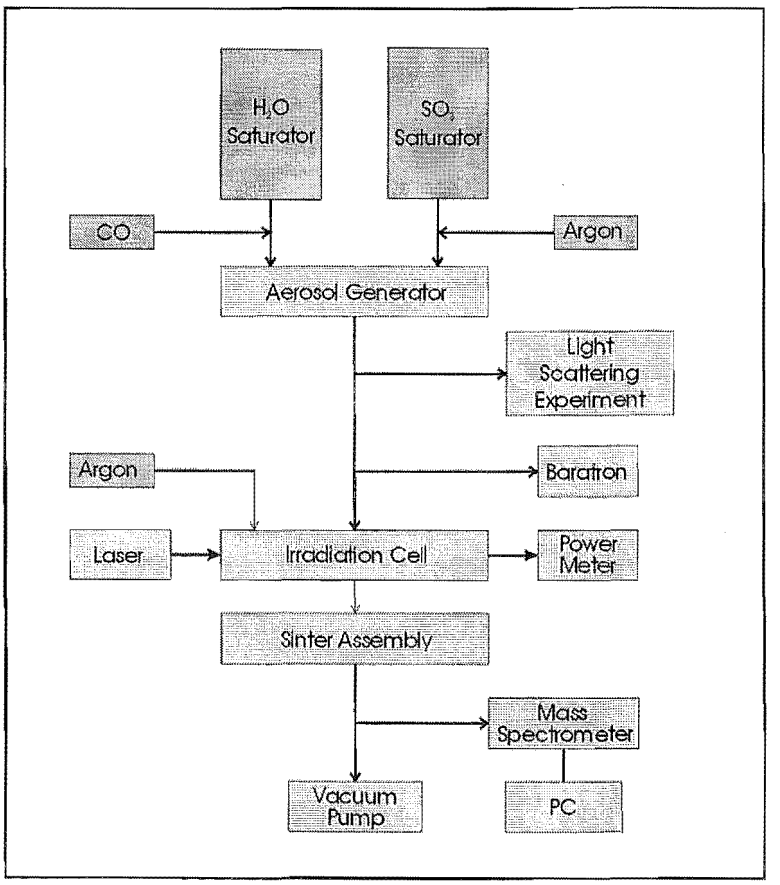

Figure 2.1 Block diagram of the aerosol photolysis system. Minor components, eg stopcocks, omitted.

In these experiments, a metered flow of $H_2O_{(g)}$ was mixed with a second metered flow of $SO_{3(g)}$ in a small (ca. 100mL) mixing vessel. The H_2O flow was obtained by flowing argon through a saturator (Fig 2.2) containing triply distilled water, which was immersed in a temperature-controlled waterbath. The saturator consisted of a vertical pyrex column with a sintered glass frit at the base, through which the carrier gas entered. Bulbs with sufficient volume to accommodate the liquid from the saturator were placed both upstream and downstream, as a precaution against the liquid flowing into other parts of the flow system. In addition, the downstream bulb had a coarse sinter at one end to remove any large droplets that were carried through from the saturator. The concentration of H_2O vapour in the flow was calculated from the temperature of the liquid in the saturator, the flow rate of argon and the total pressure.

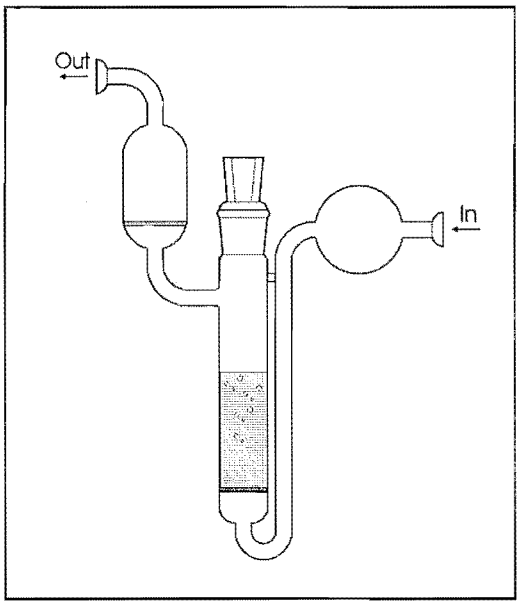

Figure 2.2 Saturator Design for H_2O and SO_3 flows.

A flow of SO_3 was generated by passing argon through a second saturator containing oleum, in a separate waterbath. The oleum was degassed by bubbling argon through it while under vacuum for two days prior to use, in order to remove any dissolved SO_2. The waterbath was normally held at a temperature of 25°C, although on some occasions it was raised to around 30°C to prevent crystals of $H_2SO_4.SO_3$ forming in the sintered glass frit at the bottom of the saturator. An additional flow of argon was added immediately downstream of the oleum saturator to dilute the concentration of SO_3 in the flow. The concentration of SO_3 was determined by measuring the absorption of monochromatic UV light from a small mercury lamp (253.7nm) and using the absorption coefficient at this wavelength reported by Fajans and Goodeve[5]. (Fig 2.3)

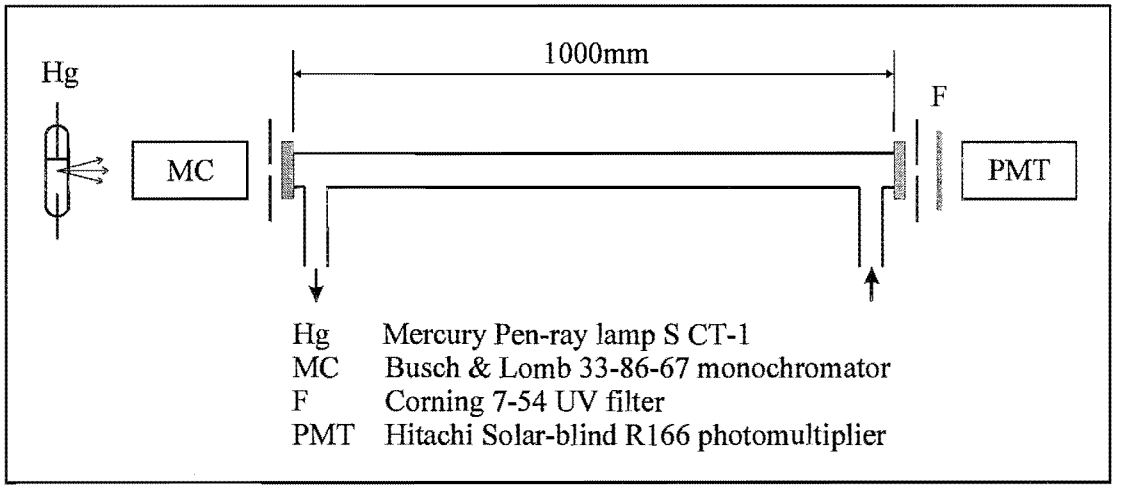

Figure 2.3 Diagram of apparatus for SO_3 determination

Carbon monoxide was introduced into the H_2O flow after it had passed through the saturator. In these experiments, a large flow of CO was used, so that it comprised between 75-85% of the final gas mix. The two flows – H_2O in Ar and CO, and SO_3 in Ar – were combined in a pyrex mixing cell using a shower-head design. (Fig 2.4) This design had been found by Mills to be the most effective for achieving rapid mixing of the two streams. H_2SO_4 was formed in the gas phase, by reaction between H_2O and

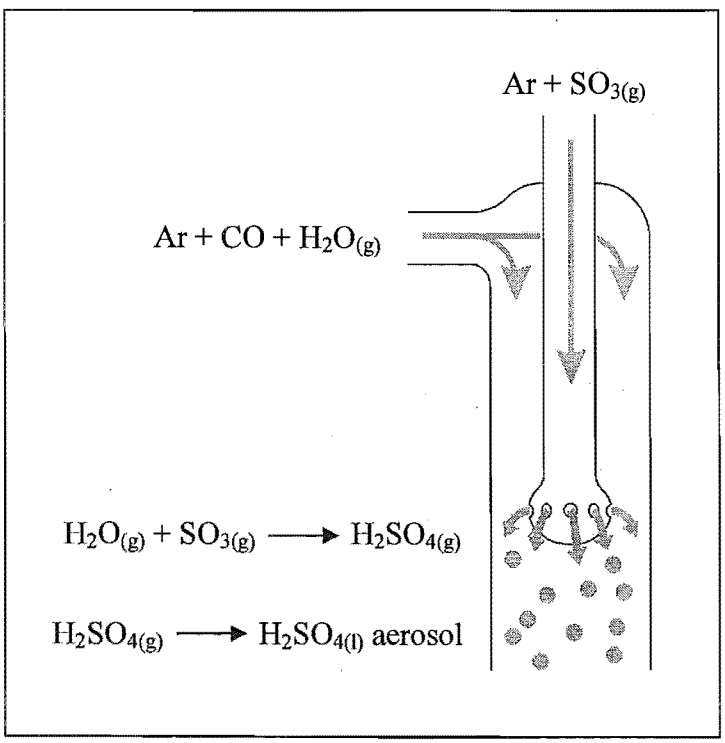

Figure 2.4 Shower-head mixer for generation of H_2SO_4 aerosol

SO_3, in amounts significantly greater than the saturation vapour pressure and H_2SO_4 rapidly condensed to form liquid droplets. The formation of the aerosol was visually observed in the cell.

2.2.2 Characterisation of Aerosol by Light Scattering

Aerosol from the shower-head generator was normally passed directly to the irradiation cell. It was however possible to divert the flow into a cylindrical cell in order to determine the size of the droplets by measuring the angular dependence of light scattering from the aerosol. Using this technique, Westergren[6] found that the mean diameter of the aerosol droplets from the shower-head generator was 0.8μm. It was noted that the aerosol flow was inhomogeneous, the walls of the cell became coated with sulfuric acid during measurements, and that the total number density of the aerosol was too high for accurate results. The variation introduced by these factors could not be corrected for, and thus the droplet size from the light scattering experiment must be regarded as a first approximation.

2.2.3 Laser Irradiation of Aerosol

The light source for the irradiation was a Lumonics EX-744 excimer laser, with argon fluoride as the emitter. This gave a pulsed, monochromatic output at 193.3nm, with an average emitted power of up to 8W at 35 pulses per second. The laser pulses were approximately 10ns in duration, and a typical firing rate was 30-35 pulses per second. In practice, it was difficult to maintain a high power output from the laser; this required a fresh fill of laser gas, which degraded quickly when high laser power was extracted. The typical power used in an experiment was 3W.

The irradiation cell was constructed from a 120mm length of rectangular cross-section pyrex tube. The windows at each end were Suprasil quartz, which has an acceptable transmission at 193nm. Mills' finding that the transmission of each window was 84.4

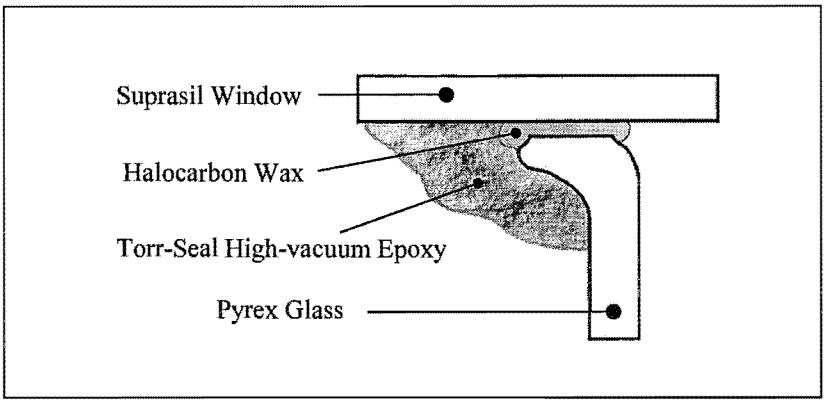

Figure 2.5 Diagram of window sealing technique, used whenever sulfuric acid was likely to contact the joint.

±0.2% was confirmed, and this value was used when calculating the amount of light absorbed during an experiment. The windows were attached to the tube with a halocarbon wax (Halocarbon Prod. Inc. Series 15.00), and supported with an external bead of high-vacuum epoxy resin (Dexter Corp. Epoxi-Patch, "Torr-Seal").(Fig 2.5)

Halocarbon wax was included as a barrier between the interior of the cell and the epoxy resin, as it was the only sealant we found that was not degraded by the concentrated acid. Despite this precaution, there were several occasions where leaks developed due to the epoxy being corroded by accumulated sulfuric acid.

Aerosol was introduced into the cell from a port at the lower rear, and was removed from the top front. Three small flows of argon were introduced at the front of the cell, between the window and the main flow outlet, in order to prevent aerosol from depositing on the front window and lowering the transmission (Fig 2.6). The total pressure in the cell was maintained between 200 and 600 torr. The system was kept underpressure in order to prevent the escape of carbon monoxide or sulfuric acid aerosol into the laboratory. Pressure in the cell was measured with an MKS baratron, protected from damage by the acidic aerosol with a sintered glass filter and a dry ice/ethanol trap.

The cell walls and windows became coated with a thin film of sulfuric acid over a period of 3-4 hours. They were cleaned after each experimental run by rinsing the

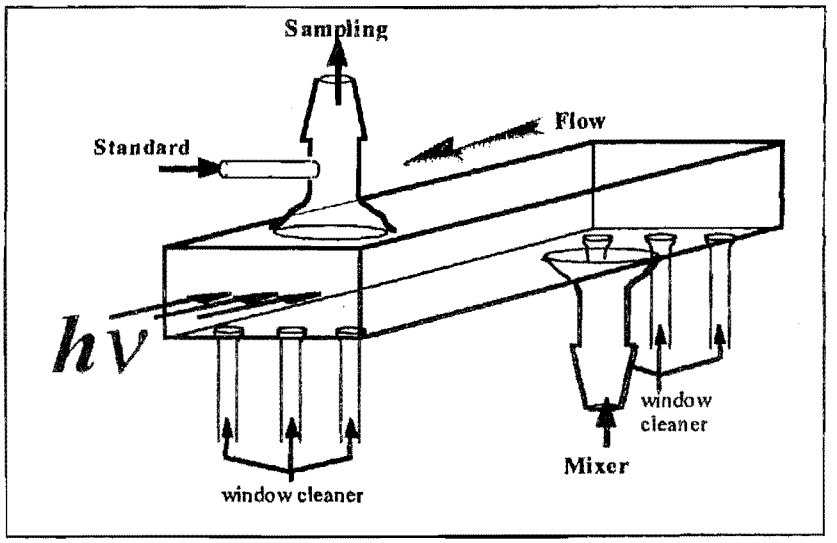

Figure 2.6 Laser Photolysis Cell.

cell thoroughly with distilled water and drying under vacuum. Acid which remained in the cell for prolonged periods of time became discoloured and damaged the seals which held the windows in place.

Laser power was measured using a Scitech model 864 power/energy meter, and a built-in photodiode power meter in the laser. The two measurements disagreed to the extent of between 10-20%. The photodiode reading was preferred because, unlike the Scitech meter, it was not subject to significant drift during use. However, the Scitech meter was used to determine the amount of light transmitted through the cell during an experiment, for which the variability was typically less than the uncertainty of the meter.

2.2.4 Aerosol Removal

A series of sintered glass discs fused inside a length of pyrex tubing was used to remove the aerosol without blocking the gas flow. Conventional aerosol filters were unsuitable because they were attacked by the acid. The sintered discs required an initial period of aerosol flow, with duration around 30 minutes, during which they became wet and developed a stable resistance to gas flow. After this, they remained

stable for 2-5 hours before becoming blocked with liquid acid or an unidentified crystalline material, at which point they were removed and cleaned. The sinters performed the dual functions of removing all visible aerosol from the gas flow and of acting as a flow restrictor, causing a pressure drop between the irradiation cell and the downstream sampling region where reaction products were detected.

2.2.5 Detection of Products

The gas flow was sampled via a 0.5mm capillary tube into a quadrupole mass spectrometer (Dataquad DAQ200). The mass spectrometer was connected to an IBM 386 computer using an RS232 interface. Software written by Professor Phillips using Microsoft QuickBasic (DATAQUAD.BAS) enabled multiple channel recording at specified time intervals of up to 30 seconds. Charge/mass ratios corresponding to the argon isotope with mass 38, carbon dioxide, sulfur dioxide and molecular oxygen were monitored.

Low pressure was maintained in the sampling region using a rotary vacuum pump, protected with a liquid nitrogen trap to prevent the sampling region being contaminated with pump oil vapour.

Earlier experiments had indicated that there was a background level of CO_2 in the mass spectrometer, and that there was a threshold for the detection of SO_2. To overcome these difficulties, small, metered flows of CO_2 and SO_2 were introduced, and changes in the amounts of these species were measured relative to this baseline. The flows were also used to standardise the system response to CO_2 and SO_2. The standard flows were initially introduced through the front window-cleaning vents of the irradiation cell so that the walls of the cell and the sinters would reach equilibrium with respect to CO_2 and SO_2 adsorption, and would not be a sink for the photolysis products. In later experiments, the standards were introduced into the system immediately after the irradiation cell, so that they would not be photolysed during their passage through the cell.

2.3 Results

Of 32 runs with this apparatus, only 15 runs yielded significant results. For all of the remainder, some experimental misfortune meant that no useful data could be gathered. Typical difficulties which resulted in no results being obtained included failure to generate an aerosol in the shower-head generator, leaks developing in the flow apparatus, excessive pressure rise due to blocked sinters, burnout of mass spectrometer filaments, and computer crashes.

Two sets of data were recorded during an experiment. The first set consists of information about the flow conditions and concentrations of the gases entering the system. For each run, the following data was recorded:

- Total pressure in the flow system (torr)
- Flow of Ar through the SO_3 saturator (standard cubic centimetres per minute, sccm)
- Flow of Ar through the H_2O saturator (sccm)
- Flow of Ar as diluent into the SO_3 line (sccm)
- Flow of CO introduced into the H_2O line (sccm)
- Flow of Ar introduced to irradiation cell as window cleaner (sccm)
- I_0 and I for the SO_3 determination
- Temperature in (i) ambient air (^oC)
  (ii) SO_3 waterbath (^oC)
  (iii) H_2O waterbath (^oC)

This information is used to calculate the relative concentrations of the species being introduced into the irradiation cell, including the average concentration of the sulfuric acid in the aerosol droplets.

The second set of data contains information relevant to the changes that occur in the system while it is irradiated. This consists of:

- Mass spectrometer traces for selected masses, with a typical interval of 21s between data points. The masses monitored were 32 (O_2), 38 (Ar isotope), 44 (CO_2) and 64 (SO_2).

- Times at which changes were made to the system, eg when flows were altered, cell was exposed to laser, laser power was altered or other significant events occurred.
- Laser power (W)
- Flows of CO_2 and SO_2 (sccm)

During an experimental run, the pressure in the flow tube increased, due to the buildup of sulfuric acid liquid in the sintered glass frits used to remove the aerosol. As liquid accumulated in the frits, their resistance to gas flow increased. Downstream from the filter, the pressure dropped due to the continual pumping from the rotary vacuum pump. This affected the mass spectrometer data, as the mass spectrometer was sampling from a region in which the pressure dropped as the experiment continued.

In order to determine whether there was a change in the amount of CO_2 or SO_2 due to the irradiation, the mass spectrometer data was normalised against the Ar trace at mass 38. The partial pressure of Ar in the system is only affected by the pumping efficiency, and hence it is ideal for use as an internal standard. Mass 38 is the third most abundant isotope of argon, and was selected because it was present in a similar abundance to CO_2 in the system. This normalisation means that the mass spectrometer data can be considered to be independent of the pressure in the system.

The raw data files generated by DATAQUAD.BAS were processed by QPLOT.BAS, also written in MS QuickBasic by Professor L.F. Phillips and modified by C.T. Mills and the present author. QPLOT removed any data points that were more than two standard deviations different from the surrounding points, and smoothed the trace by taking a weighted running average over ten points. The data files conditioned by QPLOT were compared with the original data to ensure that no qualitative changes had been made. The illustration on the following page (Fig. 2.7) shows the data conditioning sequence.

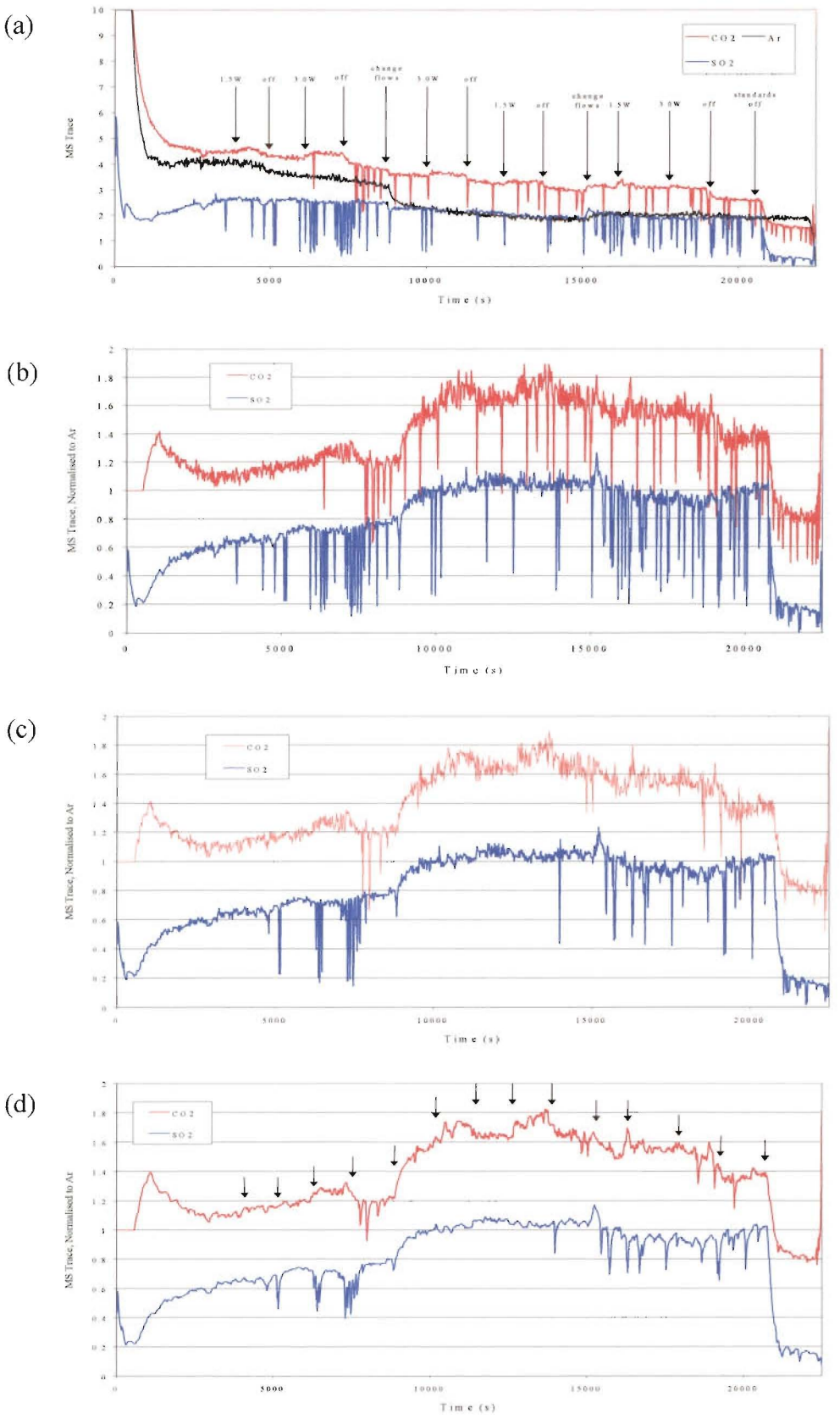

Figure 2.7 Data Conditioning Sequence. (a) Raw Mass Spec. Data (b) Traces Normalised to Ar (c) Spikes Removed (d) Running Average Smoothing

The mass spectrometer response to CO_2 and SO_2 was standardised by introducing metered flows of these two gases. The response was found to be linear in both cases (Fig 2.8), although there was a non-zero intercept for the SO_2 standardisation. It was found that the response varied slightly from one day to the next, presumably due to variations of the pressure in the sampling region, and thus in the sampling efficiency of the mass spectrometer. To allow for this, the standardisation was performed each day with at least three points on the calibration curve. The standardisation allowed the arbitrary units of the mass spectrometer trace to be converted into equivalent flow rates in standard cubic centimetres per minute through the flow system.

Data processed in this way shows that CO_2 is produced when the aerosol is photolysed. During a typical run, the laser is fired at several different output powers. The production of CO_2 is first order with respect to laser power over the range of 1 to 3W for any given run. The results show a wide scatter when compared between runs, indicating that factors other than the laser power are responsible for determining the yield. Earlier work by Mills indicates that the first order response breaks down at higher laser power, with a decrease in the apparent quantum yield. This was attributed to a saturation effect.

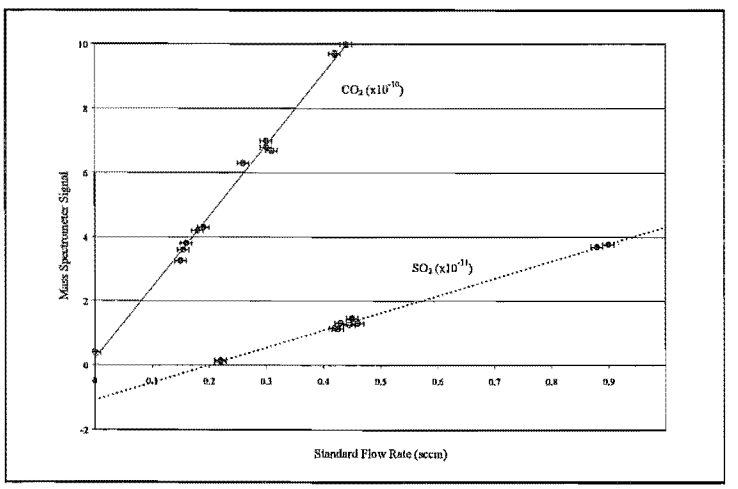

Figure 2.8 Standardisation of Mass Spectrometer Signal with metered flows of CO_2 and SO_2

SO_2 was either formed or destroyed during irradiation on any given run. Its destruction could be observed as a decrease in the mass spectrometer signal when a standard flow was running. It was not possible to determine beforehand whether SO_2 would be produced or destroyed during a run. However, it was noted that the response – either an increase or a decrease – was first order with respect to laser power. (Fig 2.9)

The quantum yield for a product, Φ, was defined as the number of molecules formed by the overall process per photon absorbed by the reactant. It was assumed that the laser light was fully absorbed in the irradiation cell. No transmitted light was observed at the far end of the cell; however no allowance was made for light scattered off the aerosol. In addition, while an allowance was made for transmission losses through the suprasil window, it was noticed that there was progressive misting of the windows during the course of a run. Both of these factors would lead to an overestimation of the amount of light absorbed, and hence to an underestimation of the quantum yield.

Quantum yields for each product were calculated based on the line of best fit between the yield of product and the laser power, rather than on single firings of the laser. The mean of ten determinations of the quantum yield for CO_2, incorporating 49 separate measurements, is 0.0107, with a standard deviation of 0.0053. Taking the uncertainty

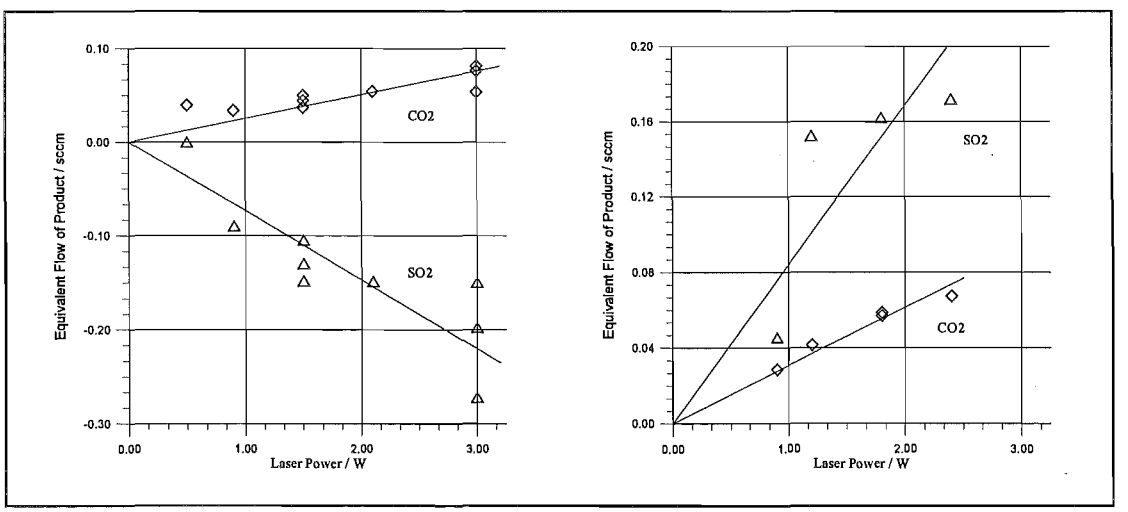

Figure 2.9 (a) Data from 29-11-94 showing CO_2 production, SO_2 destruction, (b) data from 2-8-94 showing CO_2 production, SO_2 production.

in the measurement to be plus or minus twice the standard error of the mean, the result can be expressed as $\Phi_{CO2} = 0.011 \pm 0.010$. For the reasons discussed above, this should be regarded as a lower limit for the actual quantum yield. The detection limit for changes in the flow of CO_2 was 0.016sccm, which is equivalent to $\Phi_{CO2} = 0.006$ at one watt of laser output power.

The quantum yield of SO_2 was determined for six different runs. Of these, three results showed an increase, and three a decrease in the amount of SO_2 present. In addition, there were four occasions where no change in the amount of SO_2 was detected. The detection limit was estimated to be 0.05sccm of SO_2, which corresponds to a quantum yield of 0.017 at one watt of laser output power. The measured quantum yields ranged from +0.08 to –0.07. Obviously, no meaning is attached to the average of the measurements.

2.4 Discussion

This initial attempt to find a definitive measurement of the quantum yield for the photo-oxidation of CO into CO_2 in a sulfuric acid aerosol resulted in more questions than answers. Firstly, it is observed that a reaction is occurring, but it is not clear what factors are responsible for determining its course. Of the final products of the reaction, one is consistently produced, while the other shows enormous variation.

Mills and Phillips proposed a reaction scheme based on their earlier work to account for the formation of CO_2 and SO_2. It was assumed that all reactions occurred within the sulfuric acid solution.

$$H_2SO_4 + h\nu_{(\lambda=193nm)} \longrightarrow \cdot OH + \cdot HSO_3 \quad (2.6)$$

$$CO + OH \longrightarrow CO_2 + \cdot H \quad (2.7)$$

$$\cdot H + \cdot HSO_3 \longrightarrow SO_2 + H_2O \quad (2.8)$$

$$H_2SO_4 + CO + h\nu_{(\lambda=193nm)} \longrightarrow SO_2 + CO_2 + H_2O \quad (IV)$$

This reaction scheme is now seen to be deficient in two respects. It makes no allowance for the destruction of SO_2, and it predicts that equivalent quantities of CO_2 and SO_2 will be formed by the reaction. Furthermore, the scheme does not account for the removal of SO_2 introduced after irradiation has taken place. This latter consideration requires that a variable amount of some long-lived reactive species is formed during the irradiation, which is capable of destroying SO_2.

One possible candidate for this long-lived reactive species is H_2O_2. This is formed during the radiolysis of water[7] by:

$$\cdot OH + \cdot OH \longrightarrow H_2O_2 \qquad (2.9)$$

which may be followed by

$$H_2O_2 + SO_2 \longrightarrow H_2SO_4 \qquad (2.10)$$

This reaction is plausible in irradiated H_2SO_4, if $\cdot OH$ is one of the primary reaction products. It does however require that OH radicals from two separate photolysis events come together in the solution, which would mean that the decrease in SO_2 should show a second order dependence on the laser power. Although this may be obscured by other reactions occurring in the system, we would expect to see at least a stronger dependence on laser power than for the production of CO_2. This does not match with our experimental observation, which shows the dependence of SO_2 destruction on laser power to be first order or less.

The primary process for the reaction scheme was initially assumed to be dissociation of H_2SO_4 resulting in the formation of OH and HSO_3 radicals. There is, however, no experimental evidence that this is the only, or even the most important process. Other products of the photodissociation could be:

$$H_2SO_4 + h\nu_{(\lambda=193nm)} \longrightarrow \cdot H + \cdot HSO_4 \qquad (2.11)$$

$$H_2SO_4 + h\nu_{(\lambda=193nm)} \longrightarrow \cdot O + \cdot H_2SO_3 \qquad (2.12)$$

In the case of process (2.11), the $\cdot HSO_4$ radical may have sufficient internal energy to dissociate into $\cdot OH$ and SO_3. If this occurs, the $\cdot OH$ will produce CO_2 by way of reaction (2.7). SO_2 can be formed by the photolysis of SO_3, provided that the concentration of the acid is in excess of 100 weight percent, ie that there is no free

water. Where water is present in the droplets, it will combine with the newly formed SO_3 to form H_2SO_4. SO_2 could be destroyed by ·OH via reactions (2.9) and (2.10).

If this mechanism were correct, we would expect that the yield of SO_2 would always be negative when the concentration of acid is less than 100wt%, and either positive or small negative when the concentration of acid was greater than 100wt%. The negative yields of SO_2 should show stronger dependence on the laser power than first order, as described earlier. Neither of these predictions are matched by the experimental observation, which leads us to reject this reaction mechanism, and reaction (2.11) as the primary photolysis process.

If (2.12) were the primary process, SO_2 would be formed by the dissociation of H_2SO_3:

$$H_2SO_3 \longrightarrow H_2O + SO_2 \qquad (2.13)$$

CO_2 could be formed by the direct combination of CO and O:

$$CO + {\cdot}O \longrightarrow CO_2 \qquad (2.14)$$

Alternatively, the O atom could react with surrounding H_2SO_4:

$$H_2SO_4 + {\cdot}O \longrightarrow {\cdot}HSO_4 + {\cdot}OH \qquad (2.15)$$

On the basis of the available thermochemical data[8,9], reaction (2.15) is approximately thermoneutral in the gas phase, and may be fast enough to be diffusion limited in the liquid phase. Following (2.15), the two radicals are trapped within a solvent cage, which allows time for them to recombine:

$${\cdot}HSO_4 + {\cdot}OH \longrightarrow H_2SO_5 \qquad (2.16)$$

The formation of H_2SO_5 by direct insertion of O into H_2SO_4 seems less plausible than the two-step combination of (2.15) and (2.16), which is facilitated by the two radicals being formed within the same solvent cage. H_2SO_5, also known as peroxymonosulfuric acid or Caro's acid, is a peroxide and is capable of oxidising SO_2. It is stable in acid solution for extended periods of time, and is sufficiently long-lived to be able to oxidise SO_2 which is added to the flow downstream from the irradiation cell. It would provide strong supporting evidence for the mechanism if H_2SO_5 could be detected in the irradiated acid, and this work is considered in Chapter 4.

In order to explain the variable yields of SO_2 – both positive and negative – we need to know more about the relative rates of reactions (2.14) and (2.15). The rate of (2.15) is expected to depend only on the amount of O present, and thus only on the laser power. Reaction (2.14) will be affected by the amount of O present, but also significantly by the concentration of CO dissolved in the sulfuric acid droplets. Likely factors which will determine the concentration of available CO are the mixing ratio of CO in the gas stream, the size of the droplets and the concentration of the sulfuric acid.

Previous work by Mills has shown that the yield of CO_2 increases and the yield of SO_2 decreases as the mixing ratio of CO in the gas stream is increased. In the current set of experiments, the mixing ratio of CO in the carrier gas was not varied over a sufficiently wide range to observe this effect, nor was the variation in [CO] large enough to account for the variation in quantum yield between experiments.

The concentration of sulfuric acid in the droplets was well defined, as the concentration of both H_2O and SO_3 in their respective flows before mixing was known. The gas phase combination reaction of $H_2O + SO_3 \rightarrow H_2SO_4$ was assumed to proceed rapidly until the SO_3 was fully consumed. H_2SO_4 formed by this reaction was present at concentrations much larger than the saturation vapour pressure, and so condensed to form liquid aerosol droplets. As concentrated sulfuric acid is highly hydrophilic[10], water vapour condensed onto the droplets, enlarging them and reducing the concentration of sulfuric acid in solution. The process was assumed to continue until the droplet reached equilibrium with the water vapour in the surrounding gas flow. The final acid concentration in the droplets was calculated iteratively by mass balance, using tabulated vapour pressure data for concentrated sulfuric acid solutions[11] and the concentrations of H_2O and SO_3 in the original flow. The composition of the aerosols was calculated by computer during each experimental run, and the results were used to determine whether more H_2O or SO_3 flow should be added. Thus, the concentration of acid in the aerosol could be determined and controlled during each run. Approximately half of the runs were performed with ~100% sulfuric acid aerosols, with the remainder being between 80-95wt%. No variation in the quantum yields of CO_2 or SO_2 was noted when the acid concentration was varied.

A significant unknown quantity in the experiment is the number density and size distribution of the aerosol generated. Westergren[6] has attempted to determine the size of this aerosol using optical scattering measurements, which resulted in an estimated diameter of 0.8μm. In this work, it was noted that the aerosol flow was inhomogeneous, and this limited the accuracy of the determination. Westergren's measurement of a 0.8μm diameter is inconsistent with a visual inspection of the aerosol[4]. To the naked eye, the aerosol is highly opaque, and individual droplets can be seen distinctly. These direct observations of the aerosol have been used to estimate the speed of aerosol passage through the flow tube and to observe flow patterns around the windows of the tube. This suggests that the aerosol used by Mills et al[1] was larger, and possibly considerably larger, than 0.8μm. In Mills' experiments, and in the present work, the aerosol had a different appearance from one run to the next, suggesting significant variations in the aerosol size.

In order to more fully characterise the reactive system, and determine a stable quantum yield for the reaction, it was desirable to generate sulfuric acid aerosols of consistent, known size and number density. This work is considered in the next chapter.

Chapter 3

Controlled Generation of Sulfuric Acid Aerosol

Chapter 3

Controlled Generation of Sulfuric Acid Aerosol

3.1 Introduction

As discussed in the previous chapter, the size of the droplets is expected to determine the extent of carbon monoxide oxidation when an aerosol of sulfuric acid containing dissolved CO is irradiated with ultraviolet light. It was considered necessary to generate a sulfuric acid aerosol with known particle size and number density that would be suitable for further irradiation experiments. This aerosol would be used in a similar experiment to that described in Chapter 2, with the goal of correlating aerosol particle size with the quantum yields of CO_2 and SO_2.

An extensive scientific and technological literature exists on the generation, measurement and physical properties of aerosols. In addition, there are many commercially available instruments that can be used for the generation and study of aerosols. These have been developed primarily for the use of researchers interested in the physical properties of aerosols for industrial, environmental and medical applications. However, many of the instruments can be used in an investigation of the chemical properties of an aerosol.

Two possible strategies exist for producing a suitable aerosol. One involves generating an aerosol containing a wide distribution of particle sizes, and then selecting and isolating a certain size range for the irradiation experiment. The second method requires generating aerosol particles of a well-defined size with minimal variation, and using this aerosol directly. The former method was attempted first, due to the availability of suitable equipment.

3.2 Uncontrolled Aerosol Generation Followed By Size Selection

3.2.1 Overview

In this method, an aerosol is generated which contained a wide range of particle sizes. Suitable techniques of formation are by condensation from a supersaturated gas (as in the experiment described in Chapter 2) or from a spray atomiser. The aerosol is passed through an electrostatic classifier, also called a differential mobility analyser, which selects particles within a certain size range and removes the remainder. The aerosol flow is then directed to either a particle counter, or the irradiation system.

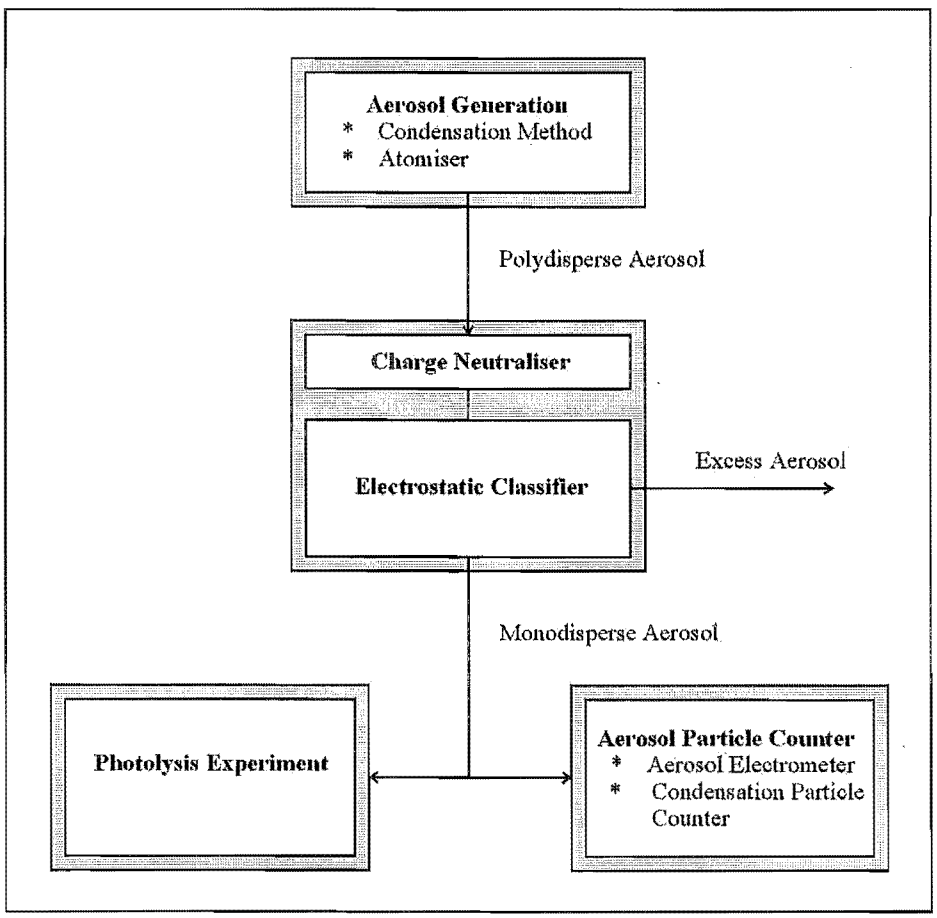

Figure 3.1 Schematic of Uncontrolled Aerosol Generation followed by Conditioning for Use in Irradiation Experiment

3.2.2 Aerosol Formation

3.2.2.1 Condensation Aerosols

An aerosol may be formed by spontaneous condensation when a supersaturation of vapour is present. While it is possible for homogeneous nucleation to occur, ie the aerosol forms from the pure material, it is more common in practice for the vapour to condense onto small existing particles known as condensation nuclei. This requires much lower saturation ratios of the aerosol-forming vapour, and hence is more likely to form under natural conditions.

The major objection to generating an aerosol in this manner is that it is not composed of a chemically pure substance. The aerosol droplets will always be contaminated by the material from the condensation nuclei. This is not a concern for studies of the physical properties of aerosols; for investigating chemical reactions within the droplet, the contamination presents an unnecessary complication. Unless the chemical composition of any condensation nuclei is known, it is better to avoid them altogether.

It is uncertain whether the aerosol generated for the earlier experiment was formed by heterogeneous or homogeneous nucleation. It was originally assumed that a homogeneous process was occurring, and that the aerosol was condensing onto clusters of sulfuric acid molecules which were sufficiently large to be stable against evaporation. A high vapour pressure of sulfuric acid – many times greater than the saturation vapour pressure – is required for these clusters to exist. A more likely situation is that small particles were already present in the gas flow, and that these served as nuclei for the sulfuric acid to condense onto and grow into an aerosol. The most likely source for these particles is from bubbling which occurs in the two saturators providing H_2O and SO_3. When a bubble bursts, many small droplets are formed. Liquid evaporates from these droplets until a tiny particle of involatile material remains. This is true even for distilled water, where the involatile compound is a carbonate formed from dissolved atmospheric carbon dioxide.

In either type of nucleation process, the resultant aerosol contains a range of droplet sizes that can be described by a log-normal distribution, ie the numbers of droplets of each size follows a normal distribution when plotted against the base 10 log of the droplet size. John[1] suggests that the size distribution of an aerosol formed by condensation is likely to have a geometric standard deviation of between 1.1 and 1.4. In practice, this means that the range of droplet diameters will cover between half and one order of magnitude.

While the nucleation process described here is an elegant method of aerosol generation, it suffers from some practical difficulties. The most severe of these is that the aerosol produced is found to be inconsistent, even under the same flow conditions. It is uncertain whether the total number of droplets present is varying, but the opacity of the aerosol is seen to change, indicating significant variation in the size distribution. Thus, even if an aerosol generated in this way is passed through a size-selection device, the variation in the number density of selected particles will make it improbable to obtain reproducible results in the photochemical experiment. For this reason, an alternative method of aerosol generation was sought.

3.2.2.2 *Atomiser Generated Aerosols*

One of the simplest ways of generating an aerosol is by atomising a solution with a stream of compressed air. The same principle is used as in a paint sprayer. A flow of high-pressure gas is passed through an orifice and expands past a liquid inlet. The low pressure at the liquid inlet draws a filament of liquid into the gas stream, where it breaks up into droplets as it enters the fast-moving flow. Larger droplets precipitate out of the flow due to gravity; smaller droplets remain in the airflow and make up the aerosol.

Several atomisers were constructed following the pattern shown in Fig 3.2. The capilliary for the compressed air inlet was made by drawing out a piece of thick-walled pyrex tubing until the bore collapsed, then grinding it back until a pinhole appeared. Thick-wall tube was used to allow the piece to withstand high pressures of

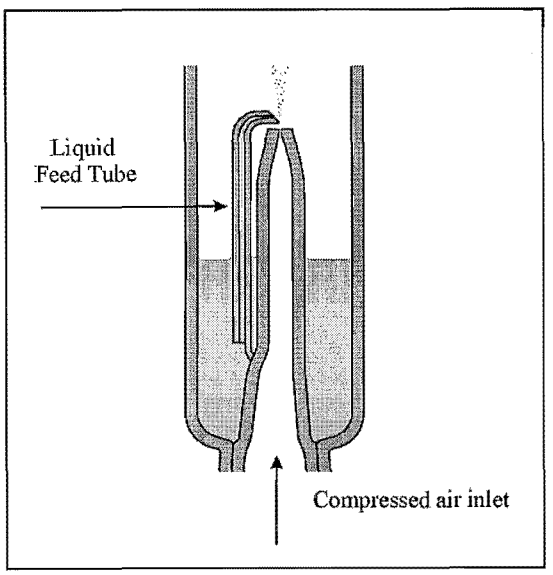

Figure 3.2 Detail of Atomiser Assembly

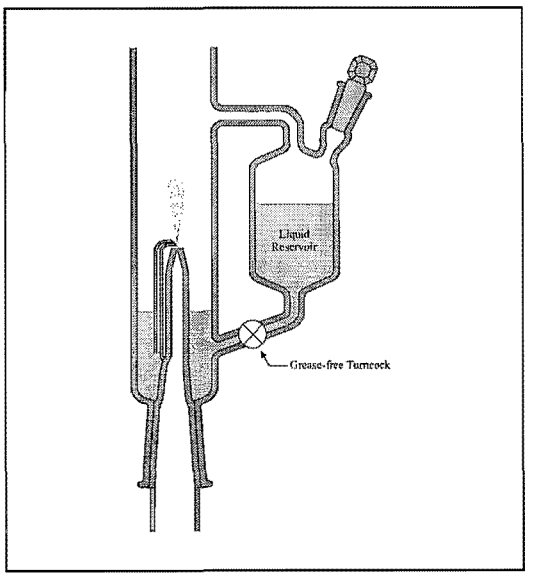

Figure 3.3 Liquid Supply to Atomiser

compressed gas without shattering. The liquid feed tube was made of a smaller piece of pyrex tubing, drawn out and ground in a similar fashion, but with the cut on the end being made at a nominally 45° angle. The positioning of the liquid feed tube was adjusted until the atomiser formed an aerosol. Aerosol formation was easily observed; the aerosol generated using these atomisers appeared as a thick mist, indicating that large numbers of droplets were being formed.

The solution to be atomised was contained in the 'cup' formed by the housing of the atomiser. Initial trials showed that the liquid was depleted rapidly, over a period of around ten minutes. In order to run the atomiser for longer periods of time, a reservoir of liquid was added, and the cup refilled while the atomiser was running by opening the turncock. Later, the reservoir was modified so that the atomiser could be refilled at pressures other than atmospheric. (Fig. 3.3)

The atomisers were tested using water as the aerosol material, rather than sulfuric acid, which could only be used in a contained system. This was done for convenience – a water aerosol could be safely released into the lab, whereas a concentrated sulfuric acid aerosol would pose a serious hazard. The size distribution of the water aerosol generated was measured using an electrostatic classifier to isolate particles of a given

size and a condensation particle counter to count the number density of the selected particles. Both of these pieces of equipment are discussed later in this chapter.

The size distribution of an aerosol from the atomiser was approximately normal, and not log-normal as expected. A normal distribution indicates that the aerosol droplets are being formed with a single size, being acted on by a random addition error, as opposed to a random multiplicative error which would lead to a log-normal distribution. This is compatible with the atomiser producing an essentially monodisperse aerosol, determined by the orifice diameters of the two jets, but being subject to distortions such as fluctuations in the delivery pressure of the compressed air, variations in the liquid level, mechanical vibration and imperfections in the jets.

The size distribution could be altered by changing the delivery pressure of the compressed air. The delivery pressure was varied between 0 and 29 psig, ie p.s.i. above atmospheric pressure. No aerosol was generated with delivery pressures less than 9 psig. At 9.5 psig, the total output of particles was small and the median

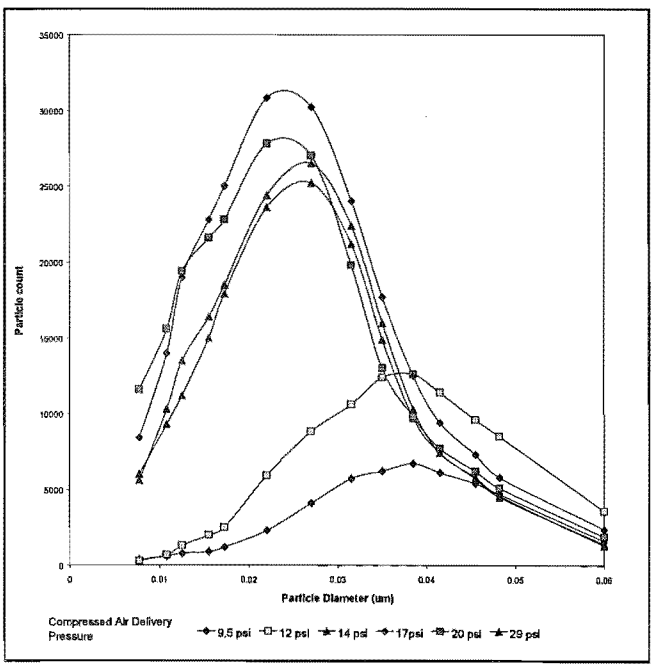

Figure 3.4 Size distribution of aerosol from atomiser, operating at various compressed air delivery pressures.

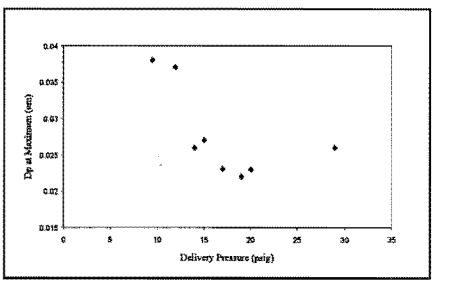

Figure 3.5 Size Distribution Maxima vs Delivery Pressure

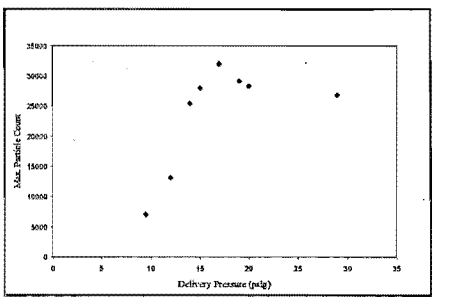

Figure 3.6 Maximum Particle Count vs Delivery Pressure

diameter was large. As the delivery pressure was increased, the total output rose and the median diameter decreased, as shown in Fig. 3.4, 3.5 and 3.6.

The particle sizes observed were very small compared with those typically obtained from commercial atomisers. John[1] suggests that droplets from an atomiser have a typical diameter of 1-6μm – which is two orders of magnitude larger than the aerosol observed here. After consideration, we realised that the particles that were being observed were the residue from the water droplets after all the water had evaporated. Because water has a relatively high vapour pressure at room temperature, and we were using dry nitrogen as the compressed gas, the water was simply evaporating and leaving behind a small core of non-volatile material. Hinds[2] calculates the time required for a 10μm diameter water droplet to fully evaporate into vapour-free air to be 0.08s; for a 1μm droplet, the time is 0.001s. This suggests that the particles we observed were the dried remains of the originally generated water aerosol.

Hinds' calculation of the water droplets' lifetime uses an equation derived by Davies[3].

$$\frac{dd_p}{dt} = \frac{4D_v M}{R\rho_p d_p}\left(\frac{p_\infty}{T_\infty} - \frac{p_d}{T_d}\right)\left[\frac{2\lambda + d_p}{d_p + 5.33\left(\lambda^2/d_p\right) + 3.42\lambda}\right] \qquad (3.1)$$

This can be used to calculate the lifetime of a droplet of any pure material, given its initial size and the ambient vapour pressure of the droplet material. In some situations, the droplet will reach a size where it is in equilibrium with its surroundings, and Davies' expression can be used to determine this size. The equation cannot be used to determine the equilibrium size of a droplet which is made up from more than one chemical component. In this case, the forces acting on molecules at the droplet surface are different to those in a pure liquid.

In order to confirm the suggestion that the observed particles were formed by the complete evaporation of water, an experiment was performed where the size distributions of three solutions were compared. The first solution was triply-distilled water, the second was 0.52g/L NaCl dissolved in water and the third was 4.72g/L NaCl solution. If complete evaporation were occurring, the particles from the second solution would be larger than those from the first, while the particles from the third solution should be $(4.72/0.52)^{1/3} = 2.1$ times larger than those of the second solution.

The size of the original droplets generated by the atomiser could then be calculated from the size of the fully dried particles.

The size distribution of the first solution was determined using 37 measurements, and was found to have a log-normal distribution with a mean diameter of 0.040μm and a geometric standard deviation(gsd) of 0.22. Since the size distribution was described extremely well by the log-normal distribution, fewer measurements were used for the second and third solutions. The second solution had a mean diameter of 0.030μm with gsd of 0.29, and the third solution had a mean diameter of 0.049μm and a gsd of 0.29. The size distributions are shown in Fig 3.7. It was concluded that the aerosol particles were not the product of complete water evaporation from the initially formed droplets as had been supposed. Instead, the final droplets were large enough that the presence of dissolved salt had little to no effect on the droplet size.

The effect of water vapour in the gas surrounding the aerosol particles was demonstrated by installing water vapour saturators as described in Chapter 2 in the gas supply lines used for the electrostatic classifier and the atomiser. No attempt was made to control the temperature of the water in the saturators; they were used at room temperature. Thus, all gas that came into contact with the aerosol was pre-saturated

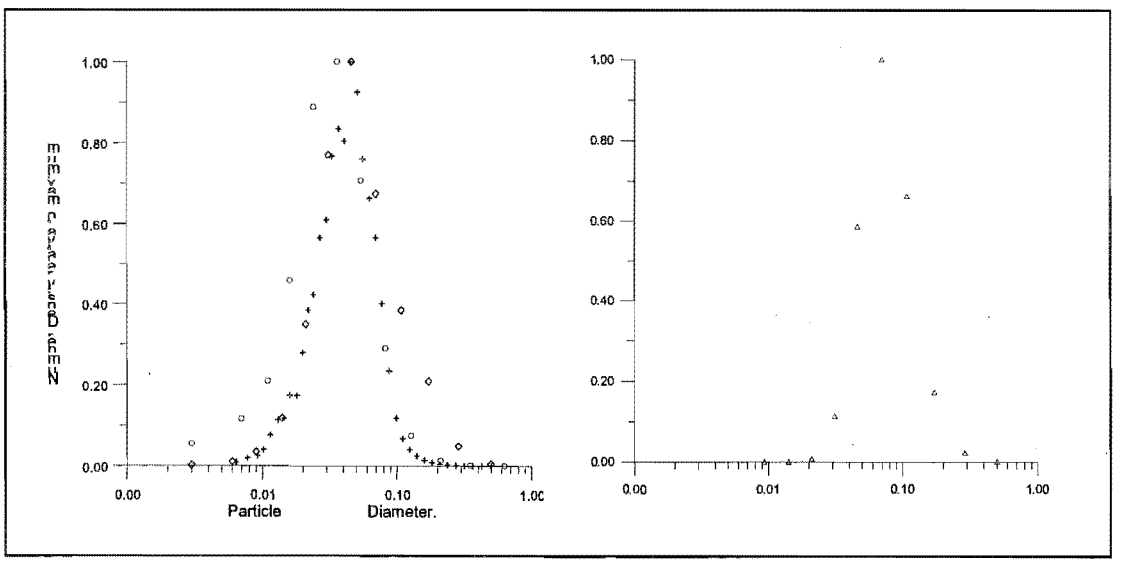

Figure 3.7 Size Distribution of aerosols from salt solution. (+) distilled water aerosol, (O) 0.52g/L NaCl solution, (◇) 4.72g/L NaCl solution, (△) distilled water with water-saturated gas flow

with water vapour. The aerosol was generated from triply distilled water. The size distribution was measured and is also shown in Fig 3.7. The mean diameter was 0.074 and the gsd was 0.19. This result indicates that some water remains in the aerosol after evaporation has occurred, in agreement with the dissolved-salt experiment.

These experiments demonstrate the importance of the liquid-vapour equilibrium in determining the size of an aerosol made up from a volatile liquid. The droplet size cannot be expected to remain constant when additional gas flows are introduced, since the partial pressure of vapour in the new flow does not match the equilibrium partial pressure around the aerosol droplets. This is significant when working with aerosols containing a volatile component, such as sulfuric acid solutions.

Using an atomiser to generate the aerosol represents a significant improvement over the earlier condensation method, in that the output is stable and consistent between runs. However, when the liquid being atomised is volatile, the final droplet size is governed by the liquid-vapour equilibrium in the flow rather than the atomiser itself.

It is not possible to significantly vary the primary particle size using a single atomiser; instead, several different atomisers with different diameter orifices are required. The atomisers are cheap and reasonably easy to construct, so this does not present any real objection. It is still difficult to do comparative experiments for different sized droplets, since the concentration of the aerosol cannot be held constant while the droplet size is varied.

3.2.3 Size Selection of Aerosol

Once a suitable polydisperse aerosol has been generated, a monodisperse aerosol fraction can be isolated by utilising some size-dependent property of the aerosol particles. We have investigated the use of an electrostatic classifier for producing a monodisperse sulfuric acid aerosol for use in photochemical experiments. An electrostatic classifier selects particles based on their electrical mobility – which in

turn is dependent on the size of the particles. The instrument that we used was a TSI 3071A Electrostatic Classifier, a commercially produced instrument for aerosol research. In conjunction with an aerosol particle detector, it can be used to either measure the size distribution of a polydisperse aerosol, to isolate a monodisperse fraction of an aerosol, or to determine the electrostatic charge distribution of a monodisperse aerosol. The EC is able to measure particles with a diameter from 0.01μm to about 1.0μm.

3.2.3.1 Operating Principles of the TSI 3071A Electrostatic Classifier

A brief explanation of the operation of an electrostatic classifier is necessary. Although the instrument that we were using was factory standard, it was being used with a significantly lower gas flow than it had been designed for, in order that the aerosol would be suitable for the photolysis experiment. Some changes to the normal operating procedure were needed as a result of this.

An aerosol to be characterised is first passed through an aerosol neutraliser, model TSI 3077.(Fig. 3.8) The neutraliser, also known as a bipolar diffusion charger, is used to establish a Boltzmann charge distribution on the aerosol particles. It is common for

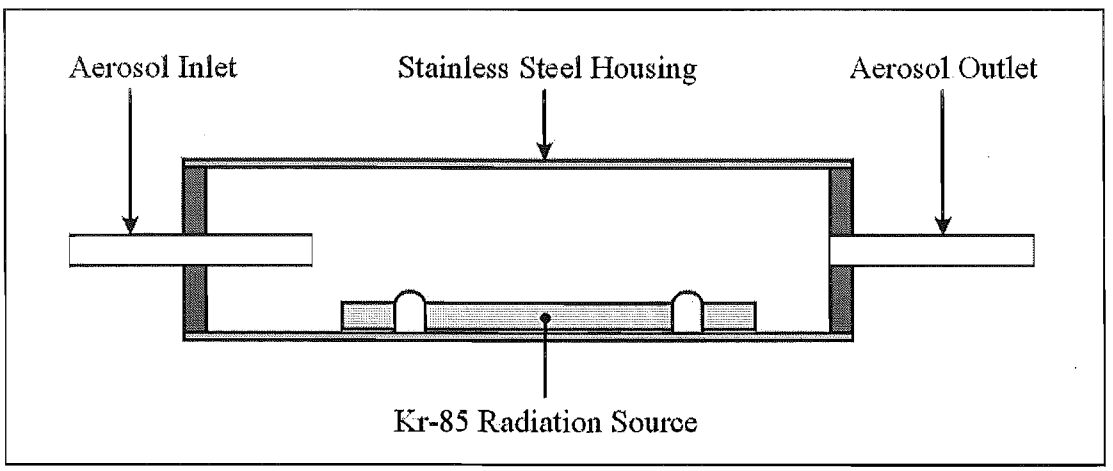

Figure 3.8 Construction of TSI3077 Aerosol Neutraliser

aerosol particles to carry a large electrostatic charge, especially when the aerosol was generated by a mechanical process. Because the operation of the classifier depends on the electrical charge on the aerosol particles, it is necessary to impose a known charge distribution on them.

The aerosol neutraliser consists of a 38cm long cylinder in which is housed a smaller thin-wall stainless steel tube containing a radioactive source – 2 millicuries of Kr-85 gas. Kr-85 emits β-radiation which ionises the gas molecules inside the cylinder. The bipolar ions thus produced undergo frequent collisions with aerosol particles, and the net effect is to neutralise most of the charge contained on the particles. The aerosol remains in the neutraliser for long enough to establish a Boltzmann charge distribution on the particles.

From the neutraliser, the sample flow containing the aerosol is passed into the differential mobility analyser (DMA). This consists of a vertically mounted flow tube, with an electrically isolated stainless steel centre rod mounted concentrically with the main tube.

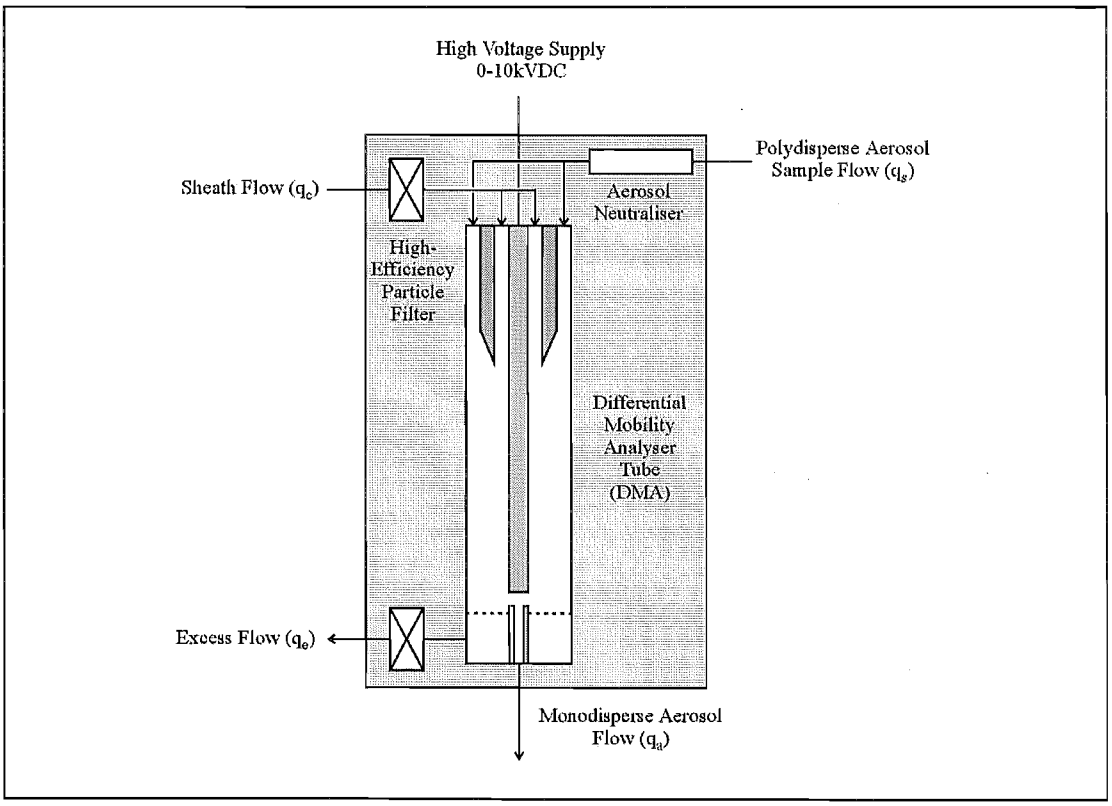

Figure 3.9 Schematic of TSI 3071A Electrostatic Classifier

The schematic in Fig 3.9 is useful in understanding how the EC functions. The EC has two input flows and two output flows. Firstly, there is a sheath flow (q_c) into the mobility analyser's main tube. This flow consists of a clean, non-reactive gas such as dry nitrogen, which is passed through a high-efficiency aerosol filter before entering the DMA tube. This sheath flow passes through the DMA and is removed at the bottom of the tube. The second input flow (q_s) contains the aerosol particles being studied. This flow is typically an order of magnitude lower than the sheath flow.

It is critical that these two flows through the DMA are laminar, ie the flow lines are smooth, orderly and do not cross one another. The sheath flow is on the inside of the tube, surrounding the high-voltage collector rod, and the sample flow is spread around the outside of the tube.

When a DC voltage is applied to the collector rod, any charged particles will be either attracted towards or repelled from the rod, depending on the relative polarities. In this instrument, the high-voltage source is negative, and can nominally deliver up to 10kV. The speed at which a charged particle moves towards the collector rod depends on both the charge and the size and shape of the particle, according to the electrical mobility equation

$$Z_p = \frac{eC_c \times 10^7}{3\pi\mu D_p} \tag{3.2}$$

where Z_p = Electrical mobility of particle (cm^2/volt/s)
$e = 1.6\times10^{-19}$ coulombs = elementary charge unit
C_c = Cunningham slip correction factor
μ = gas viscosity (poise)
D_p = Aerodynamic particle diameter (cm)

For liquid aerosols, which are spherical in shape, the aerodynamic particle diameter is the same as the actual particle diameter. For non-spherical aerosol particles, typically fumes or other agglomerates, the aerodynamic particle diameter refers to the spherical particle having equivalent aerodynamic properties. Since all of my work has been conducted with liquid aerosols, this complication can be ignored.

The slip correction factor is required to account for the aerodynamic drag on the particle due to the surrounding gas. The Cunningham slip correction factor, C_c, is used when the particle size approaches the mean free path of the gas molecules. In practice, it is determined empirically rather than theoretically[4].

$$C_c(D_p) = 1 + \frac{\lambda}{D_p}\left[2.514 + 0.800\exp\left(-0.55\frac{D_p}{\lambda}\right)\right] \tag{3.3}$$

At the same time that the particles are being drawn towards the collector rod, the aerosol is carried down the length of the DMA by the gas flow. At the lower end of the DMA, a small portion of gas is removed from the base of the collector rod via a sampling slit, and the remainder is removed as excess flow (q_e). By adjusting the voltage on the collector rod, it is possible to select the mobility (and thus the size) of the aerosol particles which will be attracted to the vicinity of the sampling slit, where they are swept out as monodisperse aerosol flow q_a. This flow, which contains an essentially monodisperse aerosol, can then be fed into an aerosol counting device, or into an experimental system.

One limitation of the EC as a source of aerosols for the photochemical experiment is that the number density of the size-selected aerosol is very low. The operation of the EC results in most of the original aerosol being removed. Firstly, the aerosol neutraliser establishes a Boltzmann charge distribution on the aerosol particles. However, the only particles selected in the EC are those which have a charge of +1 elementary charge unit – approximately 20 percent of the original aerosol. This proportion is further reduced by the size-selection which occurs in the DMA. For an initial aerosol which contains a broad spread of particle sizes, such as that from the shower-head aerosol generator, as little as 10-20% of the aerosol particles are of an appropriate size, depending on how narrow a size range is required. Overall, only 2-4% of the original aerosol remains in the EC's monodisperse outlet flow.

3.2.3.2 Calculating the Selected Particle Size

Provided that the flow inside the DMA tube is laminar, the electrical mobility of the selected particles can be calculated from the gas flows and collector rod voltage:

$$Z_p = \frac{\left[q_t - \frac{(q_s + q_a)}{2}\right] \ln\left(\frac{r_2}{r_1}\right)}{2\pi V L} \tag{3.4}$$

where q_t = total airflow through the DMA (cm^3/s)

q_s = sample airflow into DMA (cm^3/s)

q_a = monodisperse aerosol flow out of the DMA (cm^3/s)

r_2 = outer radius of the DMA tube = 1.958cm

r_1 = inner radius of DMA tube = radius of collector rod = 0.937cm

V = magnitude of the voltage on the collector rod (V)

L = length of the collector rod between the aerosol entrance and the sampling slit = 44.44cm

The particles extracted at the sampling slit are not perfectly monodisperse, but instead cover a range of electrical mobilities, and therefore particle sizes. The width of this range is determined by the sample flow through the classifier.

$$\Delta Z_p = \frac{(q_s + q_a)\ln\left(\frac{r_2}{r_1}\right)}{2\pi V L} \tag{3.5}$$

Equations (3.2) and (3.4) are not readily rearranged to give the particle size D_p in terms of the known flowrates and collector rod voltage, since the slip correction factor (equation 3.3) depends on the particle size. In order to quickly determine the particle size being selected under a given set of conditions, I have written a computer program in Microsoft Visual Basic. The program calculates Z_p from the flowrates and collector rod voltage, then uses an approximate value of the slip correction factor C_c to determine the particle size, D_p. This value of D_p is used to calculate a more accurate C_c, and the process was repeated iteratively 150 times. This is more than sufficient, given the inaccuracies in the measurements of the flow rate and the collector rod voltage, for determining the particle size.

3.2.4 Measuring the Concentration of Aerosols

There are a number of standard measures of aerosol concentration. For these experiments, aerosol concentration is expressed as number density, being the number of particles per unit volume of carrier gas. The instruments for measuring the concentration of aerosols described in this section are designed to count the number of particles in this way. I shall use the term "aerosol concentration" to refer to number density throughout this work. Another common measure of concentration is mass density, which refers to the total mass of particulates per volume of carrier gas. This is especially relevant to industrial applications where mass transport is the focus of attention, for instance the deposition of particles onto an air filter. Much of the data on Venus' clouds is also recorded as mass density. It is worth noting that the two measures do not necessarily match one another. For instance, the pre-cloud aerosol layer on Venus contains two sizes of aerosol particle – Mode 1 particles with a radius of 0.15μm and Mode 2 particles with radius 1.25μm. The number density of Mode 1 particles is $300cm^{-3}$, while that of Mode 2 particles is only $60cm^{-3}$. However, the mass density of the Mode 1 aerosol is 5×10^{-11} $g.cm^{-3}$ while that of Mode 2 is 3×10^{-10} $g.cm^{-3}$, meaning that the less numerous Mode 2 particles contain most of the aerosol mass. It should also be noted that the average density of the Mode 2 particles is approximately twenty times less than that of the Mode 1 particles. One possible explanation for this is that the chemical composition of the two types of particle is substantially different; another is that the Mode 2 particles are actually non-spherical in shape, and the observed "radius" is a misnomer.

3.2.4.1 TSI 3068 Aerosol Electrometer

One of the simplest instruments for measuring the concentration of aerosol particles coming out of an electrostatic classifier is an electrometer. The aerosol flow from the classifier is directed onto an electrically isolated filter. The build-up of electrostatic charge on the filter is monitored using a sensitive electrometer. Since the aerosol particles from the classifier each hold a single positive charge, the number of particles collected is directly proportional to the measured charge on the filter.

A small correction needs to be made to allow for multiply charged particles that have the same electrical mobility as the singly charged target particles. This effect is only a problem when the original aerosol sample contains a wide range of particle sizes.

The aerosol electrometer is used in conjunction with an EC in order to measure the size distribution of an aerosol. The voltage on the EC's collector rod is varied systematically, and at each voltage, the number of particles in the output flow is recorded. In this manner, the size distribution of an aerosol can be determined, assuming that the composition of the aerosol remains constant. The electrometer removes all aerosol from the gas flow, so it cannot be used continuously as part of an aerosol-generation system. Instead, the concentration of aerosols in a flow is measured by diverting the flow into the electrometer, making the measurement, and then returning the flow to the main system.

After attempting to measure the size distribution of an aerosol made up of concentrated sulfuric acid, it was discovered that the filter of the electrometer was badly corroded by the acid. Continuing to use sulfuric acid with this piece of equipment would have resulted in permanent damage. It was decided to avoid running sulfuric acid aerosols through the aerosol electrometer.

3.2.4.2 TSI 3022A Condensation Particle Counter

The condensation particle counter, abbreviated CPC, represents a significant improvement over the aerosol electrometer as an aerosol concentration measuring instrument. It is capable of measuring an aerosol directly, without first passing it through the EC. This means that it can be used to measure the total number density of aerosol present, regardless of the size or charge distribution of that aerosol, which the electrometer could not do. Alternatively, the CPC can be used in conjunction with the EC to measure the size distribution of an aerosol in the same way as the electrometer.

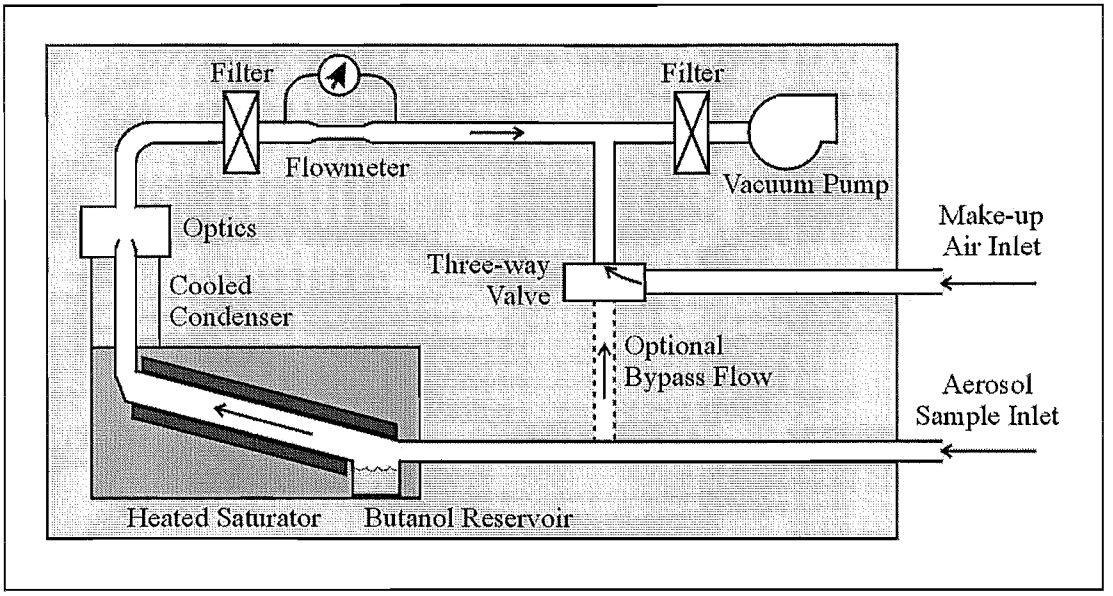

Figure 3.10 Schematic of TSI3022A Condensation Particle Counter

The CPC works as follows. (Fig.3.10) A metered flow of aerosol-bearing gas is drawn into the instrument at atmospheric pressure. There are two flow options – "low flow" draws 0.3 L/min into the CPC, while "high flow" draws 1.5 L/minute, of which 0.3 L/min flows through the sensor and the remaining 1.2 L/min goes through a bypass. The high flow rate is advantageous because it minimises particle losses due to diffusion to the walls of the system.

Aerosol entering the instrument is first saturated with n-butyl alcohol vapour in a heated saturator flowtube. The aerosol then enters a cold condenser tube, where the butanol vapour condenses onto all the aerosol particles present. This results in a rapid increase in diameter, from an initial size range of between 0.01-1μm to a final size of 10-12μm. The final particle size is almost completely independent of the starting size, because the volume of condensed butanol is far greater than that of the original particle.

The large, uniform droplets are then counted by measuring the amount of light from a laser diode which is scattered by the particles. For low concentrations of particles (less than 1000particles/cm^3), the light scattered from individual particles is detected. At higher concentrations, a correction is made for the "dead-time" when scattered light from two or more particles is detected at the same time. All optical

measurements are made automatically by the instrument, which gives a digital readout of the particle concentration in real-time. This output can also be recorded on a personal computer for later analysis. The CPC is capable of measuring a wide range of particle concentrations, from $0.007 - 9.99\times10^{6}$ particles/cm^{3}.

3.2.4.3 Limitations of the CPC

As with all the commercially produced equipment, there were some limitations of the CPC when applied to our experimental requirements. Firstly, the CPC relies on the aerosol being made up of particles that are not chemically reactive with butanol. This means that aerosols made up of concentrated sulfuric acid droplets were considered unsuitable for measuring using the CPC. Furthermore, the instrument is expensive and not readily stripped and cleaned like the EC could be. It was decided that the CPC should not be used with a sulfuric acid aerosol. Instead, it was used to measure size distributions and particle concentrations of water aerosols from the atomisers described in Section 3.2.2.2.

Secondly, the CPC is required to run at a pressure close to one atmosphere, and can not be dropped to a significantly lower pressure. When cleaning the other parts of the experimental equipment, it is common to rinse them with distilled water, then to evaporate the remaining water under vacuum. This procedure was clearly inappropriate for the CPC, as it contains a permanent reservoir of liquid butanol.

Finally, the flow rate into the CPC, which must be within quite narrow limits, does not match the flow through other instruments, such as the EC. The typical aerosol output flow from the EC is 4000sccm, while the required input flow for the CPC is 1500sccm. As a result, the excess flow from the EC must be vented. When working at any pressure other than atmospheric, it is difficult to establish a stable flow through the CPC. In effect, this limits the gases which can be used to those which are safe to vent into the fume cabinet at reasonably large flow rates. Highly toxic aerosols or gases must be avoided.

3.2.5 Sulfuric Acid Aerosol Measurements Using the Electrostatic Classifier

3.2.5.1 Condensation Generated Aerosols

Initial measurements of the size distribution of a sulfuric acid aerosol generated using the shower-head mixer described in Chapter 2 and the normal flow rates through the classifier failed to detect any aerosol particles. Equation (3.4) shows that the electrical mobility of selected particles is inversely proportional to the collector rod voltage, for a given sheath air flow. Since the maximum collector rod voltage is limited by the instrument to 10kV, this means in practice that there is a minimum detectable particle mobility for a given sheath flow. According to (3.2), particle mobility is inversely proportional to particle size, so the fact of a minimum detectable particle mobility corresponds to a maximum detectable particle size. In order to increase the maximum detectable size, it is necessary to decrease the sheath flow through the classifier. Combining equations (3.2), (3.3) and (3.4) shows that a sheath flow of 20 000 sccm, which is the recommended sheath flow for normal operation, results in a maximum particle size of 0.20μm. Reducing the sheath flow to about 2300sccm enables the classifier to detect particles of up to 1μm in diameter.

It was found that the calibration of the built-in thermal flowmeters was inaccurate at low flows. This problem was easily solved by re-calibrating the flowmeters against an Airco Model B-200-10000 mass flowmeter, which had, in turn, been calibrated using a glass bubblemeter. The bubblemeter consisted of a glass cylinder with a liquid reservoir at the base and appropriate fittings at each end. The cylinder was positioned vertically and a small amount of water and detergent solution was added to the reservoir. When a flow of gas was passed through the meter, bubbles were formed in the reservoir and these rose up the cylinder. A flow measurement was made by timing the passage of a single bubble between two marks on the cylinder separated by a known volume. The calibration was performed at 20°C and at ambient pressure.

The EC flowmeter output is a voltage dependent on the gas flow past the sensors. The output voltage is not directly proportional to the gas flow; in order to determine the flow, the output voltage is compared with a graph of the calibration curve. To speed up the process of determining the flowrates and particle size during operation, the calibration curves were approximated using fifth order polynomial equations, and these were incorporated into the computer program.

The valves used in the EC for regulating the flow of the sheath air, excess air and the monodisperse aerosol are designed for large flows and are not well suited for fine-control of small flows such as we have been using. However, we decided not to replace the valves, since their design allows an aerosol to pass through with a minimum of sharp changes in the flow direction which result in particle loss. The alternative was to use regulating valves which have a long needle stem – these allow easier fine-control of flows, but would force the aerosol through a long, narrow path where many of the particles would be lost by collision with the walls or valve stem.

A second complication lies in the operating pressure of the system. In the previous experiments, the total pressure in the flow system was kept below atmospheric pressure. This was done as a safeguard against carbon monoxide or sulfuric acid aerosol escaping into the laboratory in the event of a leak. It was quite common for the pressure to be as low as 300 torr, and it was never above 600 torr. When the classifier was operated at approximately 300 torr without any aerosol present, it was discovered that the high voltage on the collector rod reached a maximum of 346V, instead of the normal 10kV. It was discovered that the collector rod was arcing to earth inside the analyser tube, due to the low pressure. Increasing the pressure to greater than 440 torr eliminated this problem. This placed a lower limit on the system pressure for an experiment where the electrostatic classifier was in use.

The aerosol particles from the shower-head generator had previously been measured as having an average diameter of 0.8μm using a light scattering technique[5]. The sheath flow was set at 1137 sccm and the aerosol sample flow reduced to 220 sccm in order to detect these particles. With these flows, particles in the size range 0 - 2μm

could be detected, although the uncertainty in the size measurements due to the relative flows was up to 25% for the larger particles. Aerosol particles were detected using a TSI Aerosol Electrometer, which is described in Section 3.2.4.1. Figure 3.11 shows a typical measurement of the size distribution. The negative readings for particle sizes between 0.3 and 0.5μm are very unstable, which is reflected in the error bars, and are

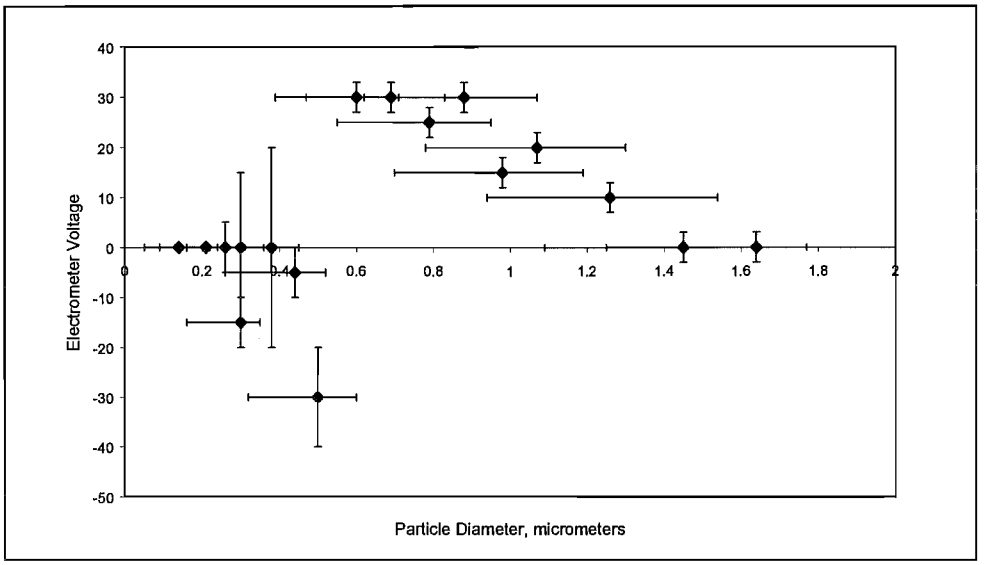

Figure 3.11 Size Distribution of Aerosol from Shower-head Generator

apparently an error in the electrometer. The measurements show a wide range of particle sizes being present in the aerosol, and are consistent with the earlier reported size of 0.8μm.

Each time the classifier was exposed to acid, it was stripped, washed with distilled water and inspected for corrosion. No visible damage was done to the classifier, provided that it was washed immediately after use. A discoloured acid deposit was present on the collector rod if it was left to stand for a few hours before washing, or if the run continued for several hours, but no permanent damage resulted. The electrometer was more vulnerable, as the filter which collected the aerosol was made of organic fibres, and was slowly consumed by the acid. The metal filter housing was also badly corroded. It is suspected that the instability of some of the measurements made by the electrometer were also due to the acid. As a result, attempts to measure the concentration of sulfuric acid aerosols were stopped.

3.2.5.2 Atomiser Generated Aerosol

A sulfuric acid aerosol was generated using the atomiser, with the aerosol being removed by filtration rather than being vented to the atmosphere. When concentrated acid solutions (80wt.%), such as those required for the laser irradiation experiment, were atomised, a higher delivery pressure of compressed air was required in order to generate the aerosol. This was attributed to the higher viscosity of the sulfuric acid, which made it more difficult to draw it up the liquid feed capillary tube. The sulfuric acid aerosol was observed to be long-lived relative to the water aerosols; no doubt due to the lower vapour pressure of sulfuric acid and hence slower evaporation. No measurements of the size distribution were attempted. This was because the concentrated sulfuric acid solutions were incompatible with the internal construction of the electrostatic classifier and the condensation particle counter.

More significantly, it was decided that attempting to measure the size of sulfuric acid aerosols using the EC was unlikely to generate meaningful results. This is because the size of sulfuric acid aerosols is readily affected by the partial pressure of water vapour in the surrounding gas flow. This effect was observed with water aerosols generated using the atomiser, as described in 3.2.2.2.

For a pure liquid, it is possible to calculate the required partial pressure to maintain mass equilibrium. It is known that the partial pressure of vapour required to maintain mass equilibrium (i.e. no condensation or evaporation) at a highly curved surface, eg an aerosol droplet, is larger than that required for a flat liquid surface. This is called the Kelvin effect. The required vapour pressure for mass equilibrium at a droplet with diameter d_p is given by

$$p = p_s e^{4\gamma M/\rho_p RTd_p} \tag{3.6}$$

where p_s = saturation partial pressure

γ = surface tension

M = molecular weight

ρ_p = liquid density

For a sulfuric acid solution, all of the relevant properties vary with the concentration of the solution. Since the concentration of the solution was, in turn, dependent on the condensation or evaporation of water from the droplets, it was decided that calculating the required water vapour pressure was not feasible. With aerosols made from sulfuric acid solution, the problem is further complicated by the strong interaction between the sulfuric acid and water. Phillips describes the formation of sulfuric acid hydrates at the surface of concentrated sulfuric acid solutions resulting in low concentrations of free water being found at the surface[6]. The effect that this would have on the kinetics of droplet condensation/evaporation is uncertain. However, it is clear that attempting to measure the size distribution of sulfuric acid aerosols using the EC is extremely problematic and the confidence in any such measurement should be low.

3.3 Controlled Aerosol Generation Requiring No Size Selection

3.3.1 Overview

The alternative strategy for producing a well-characterised aerosol suitable for photochemical studies is to use a technique that generates a monodisperse aerosol directly, without the need for size-selection in an electrostatic classifier. In this case, the aerosol can be fed directly into the irradiation cell. Such an aerosol can be made using another TSI instrument, a Vibrating Orifice Monodisperse Aerosol generator (VOMA).

As in the previous section, difficulties were encountered due to the corrosive nature of the sulfuric acid solutions we were attempting to form aerosols from. As a result, the VOMA was not used with sulfuric acid. However, at the time of the present work, I was intending to conduct experiments with aerosols other than sulfuric acid as part of this thesis, so the VOMA was tested and calibrated using the electrostatic classifier and condensation particle counter described earlier.

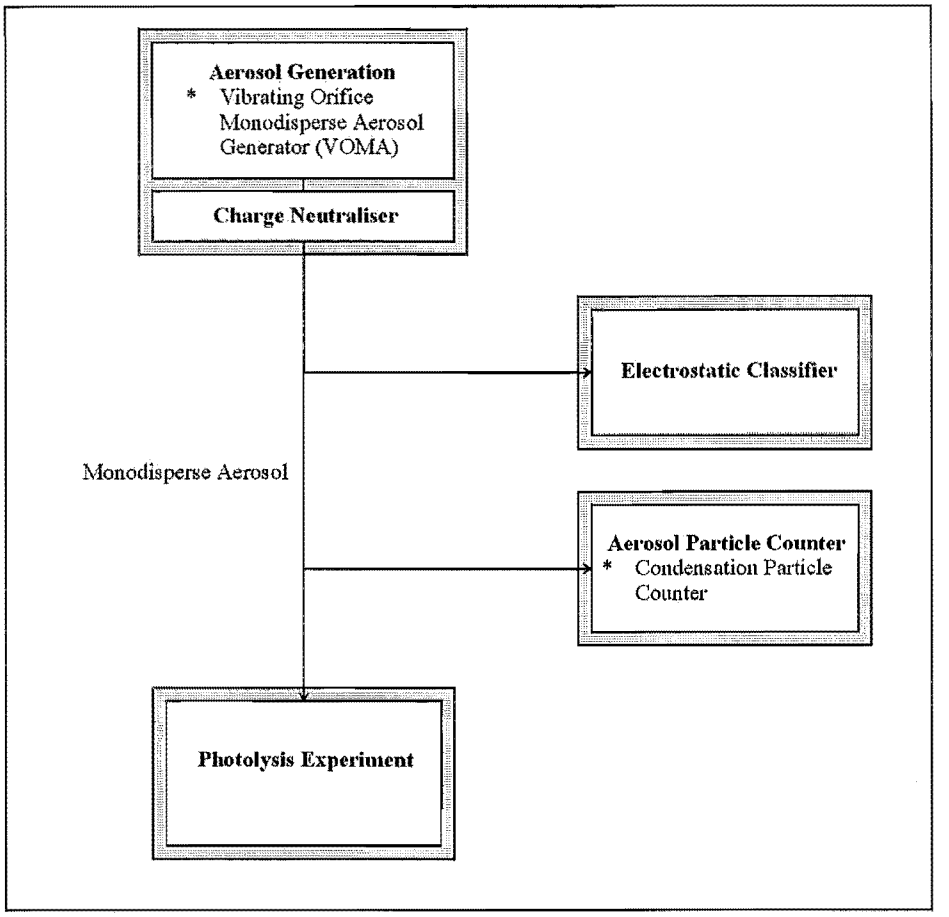

Figure 3.12 Schematic of Controlled Aerosol Generation ready for use in Irradiation Experiment

3.3.2 TSI3450 Vibrating Orifice Monodisperse Aerosol Generator (VOMA)

3.3.2.1 Operating Principles of the VOMA

The Vibrating Orifice Monodisperse Aerosol Generator, abbreviated as VOMA, is used to generate a continual flow of constant-sized liquid droplets from a prepared solution. Liquid is forced through an orifice to form a cylindrical liquid jet. Such a jet is unstable, and would normally break up into non-uniform droplets. In the VOMA, the orifice vibrates at a constant frequency while the jet is being formed. This results in a periodic mechanical disturbance in the jet, which in turn results in the jet breakup forming extremely uniform-sized droplets. Exactly one droplet is formed per cycle of oscillation, and thus the number of droplets and the volume of each can

be calculated from the oscillation frequency and the liquid flow rate through the orifice.

The droplet generator system consists of a syringe pump, an orifice assembly mounted on a piezoelectric ceramic and an electrical signal generator connected to the ceramic. (Fig.3.13) A gas flow system introduces a flow of dispersion air past the orifice in order to prevent the droplets from coagulating, ie two or more droplets sticking together to form a larger droplet. A larger flow of dilution air is added as a carrier gas for the aerosol droplets. The entire flow is passed through an aerosol neutraliser (see 3.2.3.1) to remove any electrical charge on the droplets which was generated during the breakup of the jet.

The syringe pump establishes a constant flowrate of liquid to the orifice assembly. The syringe is operated by a ram rod, driven at constant speed using a precision lead screw and a stepper motor. This ensures that the liquid flow is not affected by changes in the pressure of the liquid in the syringe.

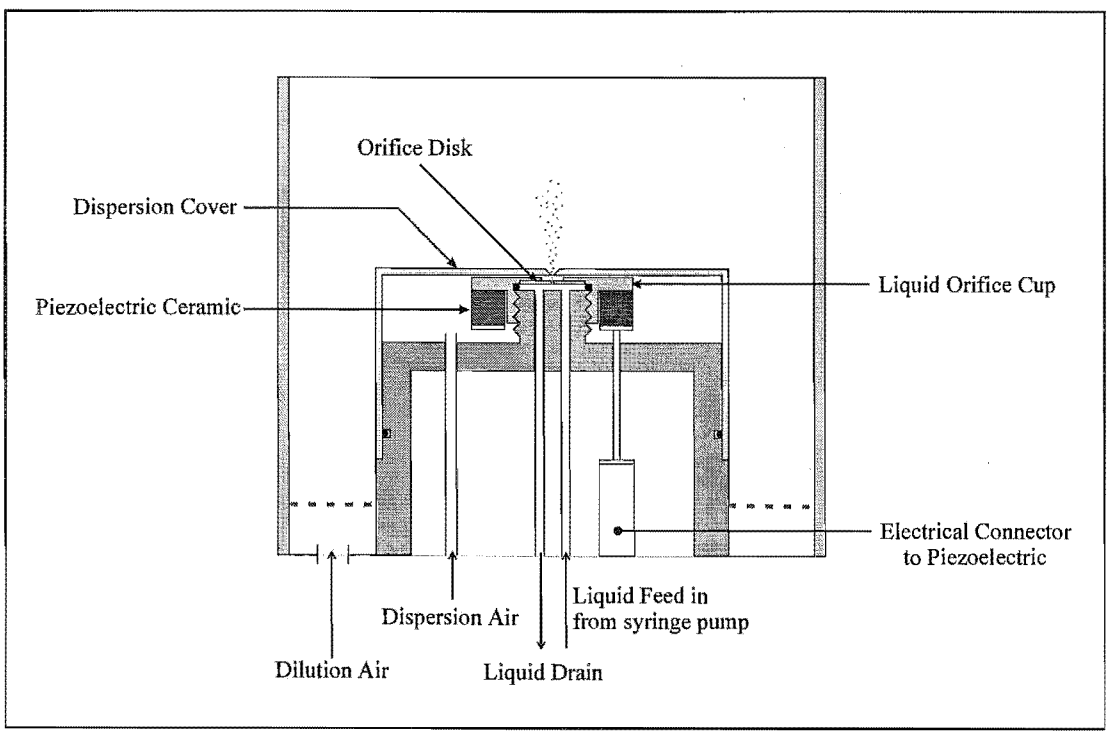

Figure 3.13 Detail of Vibrating Orifice Assembly on VOMA Aerosol Generator

The liquid orifice assembly consists of a cup, on which is mounted a stainless steel orifice disk containing a 10 or 20μm aperture. The cup is screwed onto a base plate, creating a small chamber to contain liquid. The liquid flow from the syringe is passed through a membrane filter to remove any solid impurities, and enters the chamber of the liquid orifice assembly through the base plate. The chamber is pressurised, and liquid is forced out through the aperture in the orifice disk, forming a jet. The system quickly reaches a steady state where the flowrate through the orifice is identical to the flowrate from the syringe pump. This is independent of the actual diameter of the orifice in the disk.

An annular piezoelectric ceramic is attached to the outside of the cup with epoxy adhesive. An electrical connector links the ceramic to an AC signal generator when the cup is mounted on the base plate. When an AC voltage is applied to a piezoelectric ceramic, the ceramic vibrates at the same frequency as the AC signal. The vibration in the ceramic is transmitted directly to the orifice disk. Since each complete oscillation produces one droplet, the diameter of the droplets (D_d) is calculated using:

$$D_d = \sqrt[3]{\left(\frac{6Q}{\pi f}\right)} \tag{3.7}$$

with Q being the liquid flow rate and f being the frequency of the signal from the AC generator.

The nominal frequency range used for a 20μm orifice is 40-80kHz, and for a 10μm orifice is 150-300kHz. Varying the vibration frequency within these ranges allows control over the exact number of droplets being produced, and hence over the size of the droplets. If too great a vibration frequency is applied, the jet becomes unstable and does not break up uniformly. The upper limit of the vibration frequency is different for each orifice and must be determined experimentally.

The diameter of the initial droplets formed by the VOMA using a 20μm orifice ranges from 38-48μm, and for a 10μm orifice from 21-26μm. In most cases, these initial droplets are larger than the required aerosol size. To overcome this, the liquid being aerosolized is actually a solution of the desired aerosol material in a pure, highly

volatile solvent. After the initial droplet is formed the volatile solvent evaporates away, leaving a residual particle of the desired size and composition. The diameter of the final droplet, D_p, is related to the initial droplet D_d by

$$D_p = D_d (C + I)^{1/3} \quad (3.8)$$

where C is the volumetric concentration of dissolved aerosol material in the solvent, and I is the volumetric concentration of non-volatile impurity in the solvent.

Liquid aerosols are commonly made from low vapour pressure oils such as olive oil or di (2-ethyl-hexyl) phthalate (commonly referred to as DOP), dissolved in isopropyl alcohol. Isopropyl alcohol is used because it has low viscosity, requires no special handling precautions and evaporates readily in the drying column. Solid aerosols, eg NaCl, are made using a 50-50 mix of pure water and isopropyl alcohol as the solvent. The water is added to slow the drying time of the droplet, which makes the final particle more uniform in shape and density.

3.3.2.2 Calibration of the VOMA: Aerosol Concentration

As the VOMA was a new piece of equipment in this laboratory, it was necessary to check its operation and calibration. This was done by generating a test aerosol from a solution of di nonyl phthalate (DNP) dissolved in Analar grade isopropyl alcohol. Di octyl phthalate, and to a lesser extent di nonyl phthalate, are standard materials for liquid test aerosols. Both of these have low vapour pressure ($<10^{-7}$ mmHg at 20°C) and therefore they produce aerosols which are size-stable for several hundred seconds. DNP was used in preference to the more common DOP because DOP is a known carcinogen. The health effects of DNP are unknown, although it is probably also carcinogenic, and it was handled accordingly.

The total number of particles being produced by the VOMA at different operating frequencies was measured using the condensation particle counter described in 3.2.4.2. The aerosol was generated from a solution of 1 part DNP to 2000 parts isopropyl alcohol, using a 10μm orifice in the VOMA. A 2.0LPM flow of dry

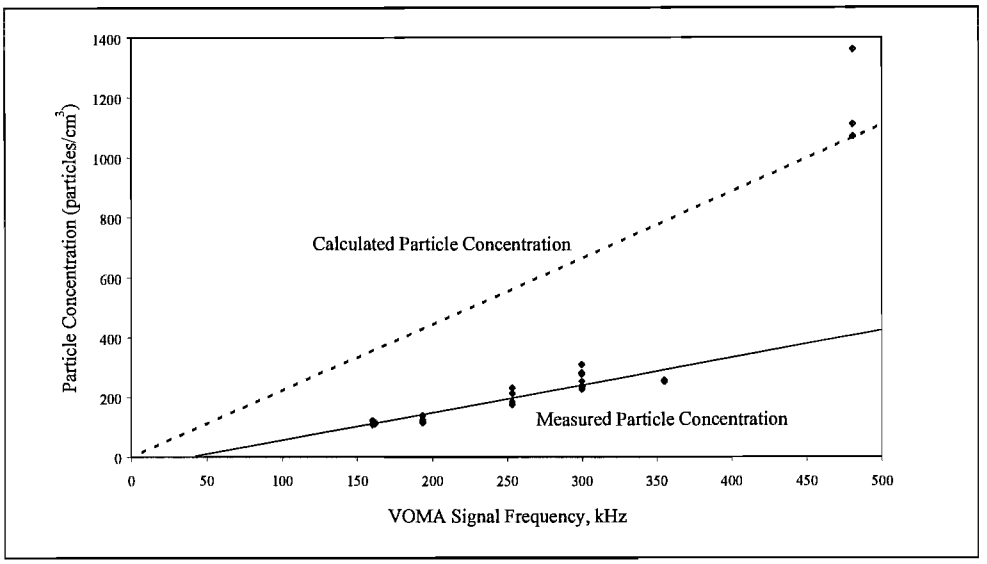

Figure 3.14 Particle Output From VOMA at various operating frequencies.

nitrogen was used to disperse the droplets as they were generated, and a 25.0 litre-per-minute flow of dry nitrogen was introduced to dilute the aerosol and prevent coagulation. The results are shown in Figure 3.14. The particle concentration measured with the CPC was approximately 35% of the theoretical concentration calculated from the VOMA's operating frequency. The signal from the AC supply was checked and was found to be correct. This suggests that the "missing" particles were being removed from the airstream somewhere between generation in the VOMA and detection in the CPC, either by coagulation or by collision with the walls of the carrier tube. The unusually large concentration of particles detected when the VOMA was operated at 480kHz indicate that the frequency had exceeded it's upper limit for the orifice, and that the jet was breaking up in an irregular pattern, producing an excessive number of under-size droplets.

To determine the effect of the gas flowrate, the VOMA was run at a constant vibration frequency of 300kHz while the flow of dilution air was varied. The same orifice and solution were used as in the previous test. The results in Fig. 3.15 and 3.16 show that the least losses occur when the dilution air flow is between 25-40 Lpm. At lower flows, particles are lost due to coagulation and to gravitational settling, while at

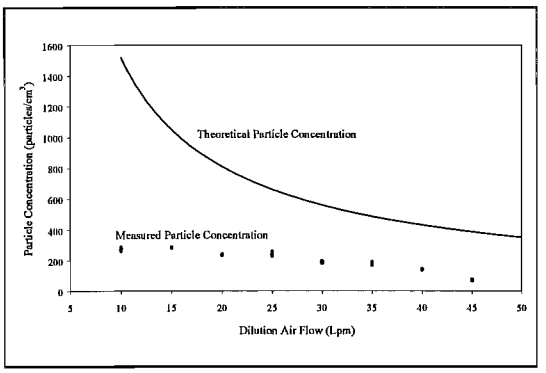

Figure 3.15 Effect of Dilution Air Flow on Measured Particle Concentration

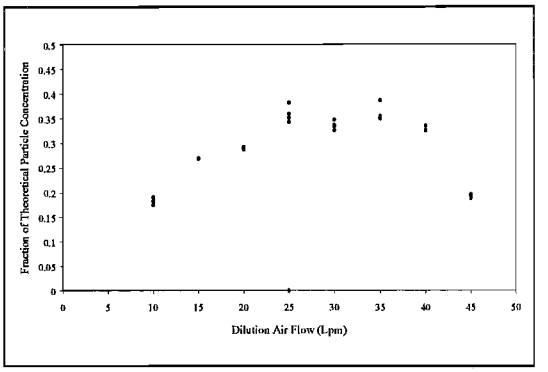

Figure 3.16 Proportion of Theoretical Concentration being detected at various Dilution Air flowrates

higher flows the fast-moving particles are removed by impaction against the walls whenever the flow direction changes, ie at a curve or bend in the flow tube.

One complication that appeared at this point is that the output flow from the VOMA is significantly greater than the required input flow for the CPC. In order to measure the aerosol concentration, a sample was withdrawn from the VOMA output flow and the remainder was vented into a fume hood. Care was required to ensure that the sample being removed was representative of the aerosol flow. One of the requirements for this is that the velocity of the gas entering the sampling tube must be identical to the free stream velocity approaching the sampling inlet. This is known as isokinetic sampling[7]. (Fig. 3.17a) If the velocity of the sample gas is greater than the free stream, then additional gas streamlines will be drawn into the sampling tube. The heavier aerosol particles are not able to change their direction so rapidly, and as a

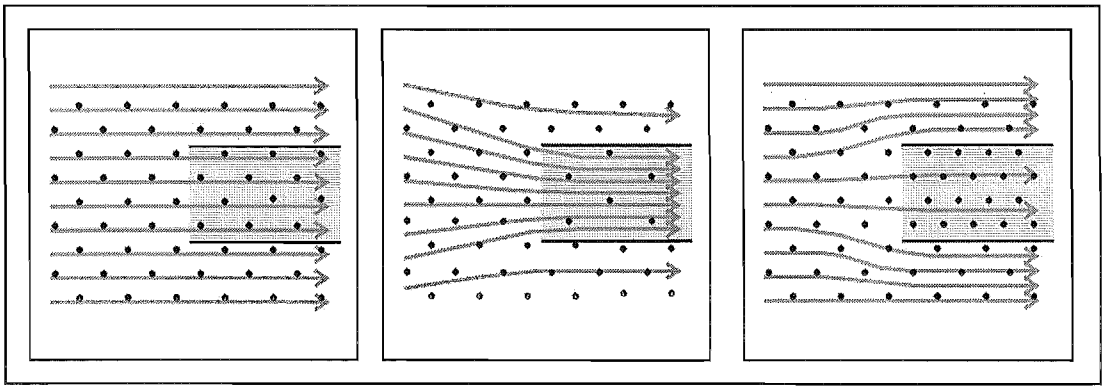

Figure 3.17 Effect of Sampling Velocity. (a) Isokinetic Sampling: sample velocity = flow velocity (b) sample velocity > flow velocity (c) sample velocity < flow velocity

result are not drawn into the sampling tube, leading to the sample containing a lower concentration of aerosol than the bulk flow. (Fig. 3.17b) On the other hand, if the sample velocity is less than the free flow, flow streamlines are deflected away from the sample inlet. The aerosol particles are not so readily deflected, and enter the sampling tube, resulting in a sample with greater concentration of aerosol than the bulk. (Fig. 3.17c)

The CPC has an inlet flow rate of 5.0cm^3/s, and the internal diameter of the inlet tube is 5.50mm. This corresponds to an inlet flow velocity of 21.0cm/s. In order to meet the requirement of isokinetic sampling while varying the aerosol flow rate, a special sampling tube was constructed. This consisted of a shallow-angled cone, mounted concentrically to the CPC's sampling tube as shown in Fig 3.18. The flow from the VOMA entered the cone at the large end, where the flow velocity was least. As the flow moved towards the narrow end of the cone, the velocity increased. The sampling inlet tube was moved to the position in the cone where the flow velocity was 21.0cm/s, in order to match the velocity of the sample being drawn into the inlet tube. When the flow rate from the VOMA was large, the sample was withdrawn from the wide end of the cone, and when the flow rate was low the sample was removed from the narrow end. This ensured that the aerosol sampled by the CPC was representative of the bulk output from the VOMA generator.

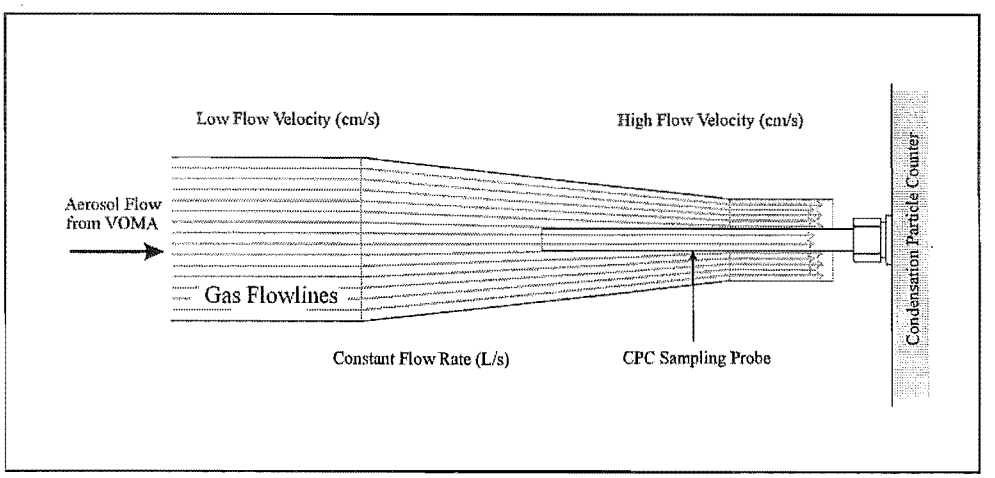

Figure 3.18 Isokinetic sampling of aerosol from VOMA generator

3.3.2.3 Calibration of the VOMA: Aerosol Particle Size

The second stage in the calibration of the VOMA was to measure the size distribution of the aerosol after it had fully dried. The electrostatic classifier would provide an independent measurement of the particle size which could be compared with the size calculated from the VOMA liquid flow rate, vibration frequency and solution concentration. In addition, the size distribution gave an indication of the amount of coagulation that was occurring, since a coagulated droplet would have a volume which was a multiple of the single-droplet volume.

Once again, the particles being measured were outside of the size range which could be measured by the EC using standard flows. This was because there is a lower limit on the size of the particles which can be generated by the VOMA. As previously described, the desired particle size is obtained from the VOMA by using a solution of some non-volatile aerosol material dissolved in a volatile solvent, in this case DNP dissolved in isopropyl alcohol. As the concentration of DNP in the solution is reduced, the final aerosol diameter also decreases. In theory, the particle diameter should drop to zero when there is no added DNP. In practice, the isopropyl alcohol contains a small amount of non-volatile dissolved impurity, and this means that there is a minimum-sized particle which is left after all the isopropyl alcohol has evaporated. The users manual for the VOMA suggests that the impurity level is typically 40ppm for reagent grade isopropyl alcohol. When operating the VOMA at 300kHz and using a 10μm orifice, this corresponds to a minimum particle diameter of 0.84μm. AnalaR grade isopropyl alcohol has an impurity of 10ppm non-volatiles, which makes the minimum diameter 0.53μm.

Four DNP solutions were prepared, with volumetric concentrations of 50μL/L, 139μL/L, 500μL/L and 2315μL/L, which corresponded to final particle diameters of 0.96, 1.30, 1.96 and 3.27μm respectively, after the solvent impurity was taken into account. The solutions were prepared in 100mL volumetric flasks using a microsyringe to add the DNP. The size distribution for aerosols prepared from the 500 μL/L solution is shown in Fig.3.19.

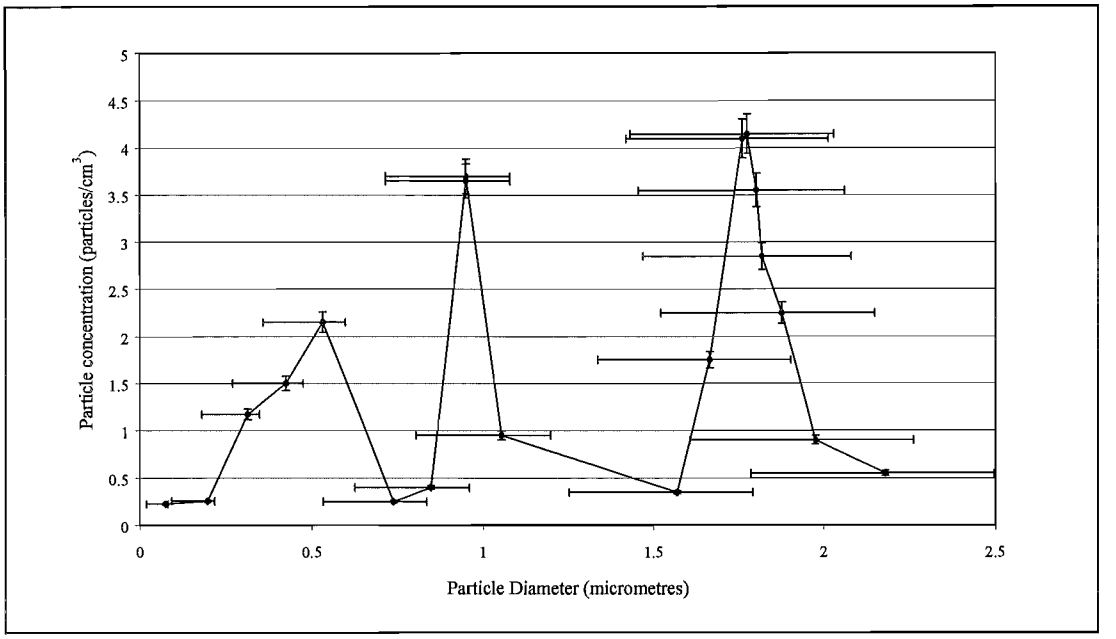

Figure 3.19 Size Distribution of particles from VOMA generator, Nominal droplet diameter = 1.96 microns

This size distribution, if taken at face value, suggests that extensive coagulation of the aerosol droplets is occurring, giving rise to multiple size maxima. However, the apparatus is expected to generate droplets with a diameter of 1.96μm. If the size maximum at 1.77μm is taken to be a single uncoagulated droplet, coagulated particles should have sizes corresponding to multiples of the single-droplet volume, i.e. 1.77μm, 2.23μm, 2.55μm, 2.81μm... Thus, the observed size distribution does not indicate that coagulation is occurring.

Instead, the multiple peaks that are observed are due to the detection of multiply-charged particles in the electrostatic classifier. The aerosol produced by the VOMA carries a large static charge, which is generated during the breakup of the jet. This charge is removed by passing the aerosol flow through a large neutraliser column, similar to the one described in 3.2.3.1, and is replaced by a bipolar charge distribution as a result of collisions with ionised gas in the neutraliser. The charge distribution is determined by Boltzmann's law. The ratio of particles carrying 1, 2, 3...n_p elementary charge units to uncharged particles is given by

$$\frac{N_{n_p}}{N_0} = \exp\left(\frac{-n_p^2}{2\sigma^2}\right) \tag{3.9}$$

$$\text{where} \quad \sigma = \left(\frac{rkT}{\varepsilon e^2}\right)^{1/2} \tag{3.10}$$

Here, r is the particle radius, k is Boltzmann's constant, T is the absolute temperature, ε is the dielectric constant of the aerosol material and e is the elementary charge unit. The fraction of particles, f_n, carrying n_p elementary charge units is given by

$$f_n = \frac{\exp\left(-n_p^2/2\sigma^2\right)}{\sum_{n=-\infty}^{\infty}\exp\left(-n_p^2/2\sigma^2\right)} \tag{3.11}$$

The charge distribution is size-dependent. For small particles (<0.1μm diameter) nearly all of the particles carry 0 or 1 unit of charge, and there is no interference in the EC operation due to multiply charged particles. However, for larger particles the fraction of particles carrying multiple charges becomes significant. For a 1μm droplet, 69% of the particles carry a charge of greater than ±1 unit. When the EC is being used to measure the size distribution of these large particles, multiple peaks are observed for each particle size due to this multiple charging effect.

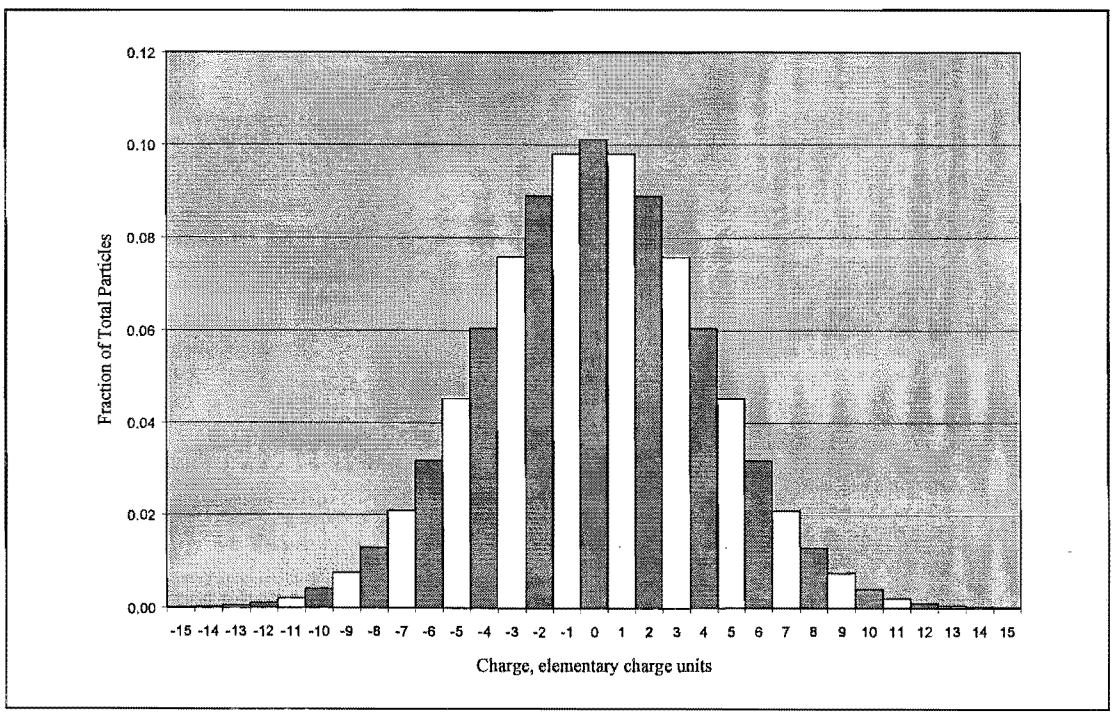

Figure 3.20 Bipolar Charge Distribution for 1.77μm aerosol droplets

A computer program was written to calculate the charge distribution for a given particle size, using equation 3.11. Charges of up to ±60 units were considered. The charge distribution for 1.77μm aerosol droplets is shown in Fig 3.20.

The EC isolates particles on the basis of their electrical mobility, Z_p, as given by Equation 3.4. The electrical mobility of particles is dependent on both their size and the charge they carry. The Z_p of the variously charged 1.77μm particles is shown in Table 3.21.

Charge, elementary charge units	Z_p, $cm^2.volt^{-1}.s^{-1}$
0	0
+/- 1	$+/- 5.72 \times 10^{-6}$
+/- 2	$+/- 1.14 \times 10^{-5}$
+/- 3	$+/- 1.72 \times 10^{-5}$
+/- 4	$+/- 2.29 \times 10^{-5}$
+/- 5	$+/- 2.86 \times 10^{-5}$
+/- 6	$+/- 3.43 \times 10^{-5}$
+/- 7	$+/- 4.01 \times 10^{-5}$
+/- 8	$+/- 4.58 \times 10^{-5}$
+/- 9	$+/- 5.15 \times 10^{-5}$
+/- 10	$+/- 5.72 \times 10^{-5}$
+/- 11	$+/- 6.29 \times 10^{-5}$
+/- 12	$+/- 6.87 \times 10^{-5}$

Table 3.21 Electrical Mobility of 1.77μm droplets carrying charge of up to ±12 elementary charge units

The size distribution data from Fig. 3.19 is replotted as Z_p vs Particle Count in Fig. 3.22. Also shown is the spectrum predicted from a monodisperse 1.77μm aerosol, using the charge distribution shown in Fig. 3.20 and calculated Z_p from Table 3.21. A close match is observed for the first two peaks. For Z_p larger than 1.6×10^5 $cm^2.volt^{-1}.s^{-1}$, there is insufficient data to comment on the fit, but the first two peaks demonstrate that the observed distribution is due to multiply-charged particles with a single size maximum centred around 1.77μm diameter.

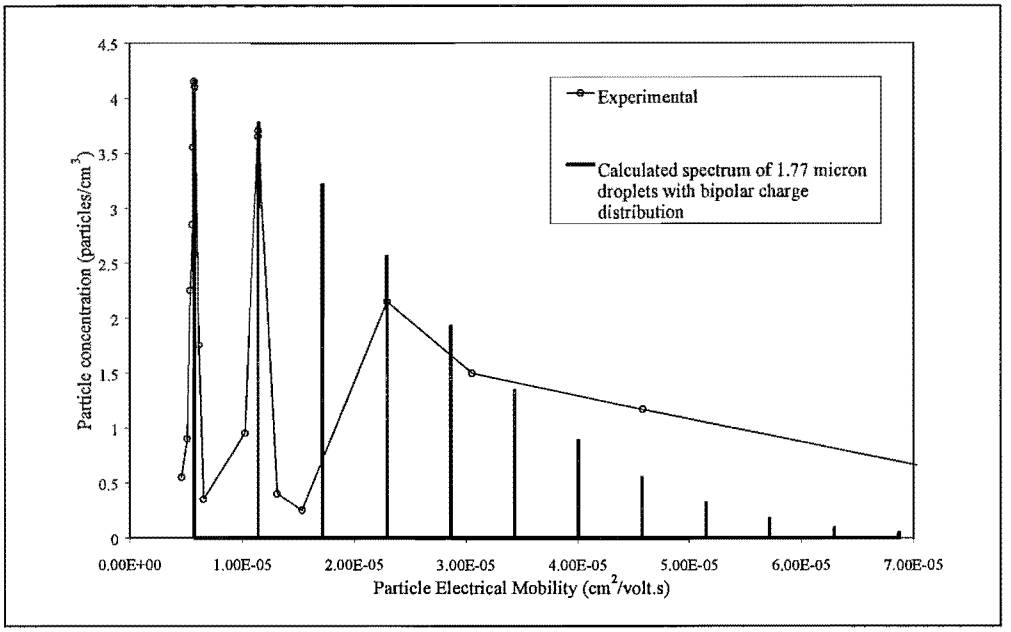

Figure 3.22 Electrical Mobility Distribution of aerosol from VOMA, compared with calculated mobility distribution for multiply-charged 1.77μm droplets

The size distribution measurement was repeated using much smaller steps between the measurements. To simplify this, the EC and CPC were interfaced with an IBM 486 personal computer which was used to systematically vary the voltage on the EC collector rod and to record the measured particle concentration from the CPC. In the measurement shown in Fig. 3.23, the aerosol was being generated from a solution of 50μL/L DNP in isopropyl alcohol, which was calculated to produce particles with a 0.96μm diameter. The diameter of the observed particles was 1.06μm; the discrepancy is due to uncertainties in the volume of DNP added to the solution and in the concentration of non-volatile impurities.

Repeating the EC measurement shows that the first three peaks, ie those due to aerosols with charges of +1, +2, and +3, are reproducible, but the concentrations of particles with electrical mobilities larger than $3.5\times10^{-5}cm^2.volt^{-1}.s^{-1}$ show a large variation. The maximum particle diameter is reproducible to within ±0.03μm. The size distribution is approximately normal, with a mean of 1.03μm and standard deviation of 0.05μm. The TSI operating manual suggests that aerosols with standard deviations of less than 1% may be generated using the VOMA; however these aerosols are much larger and as a result their diameter is less affected by variations

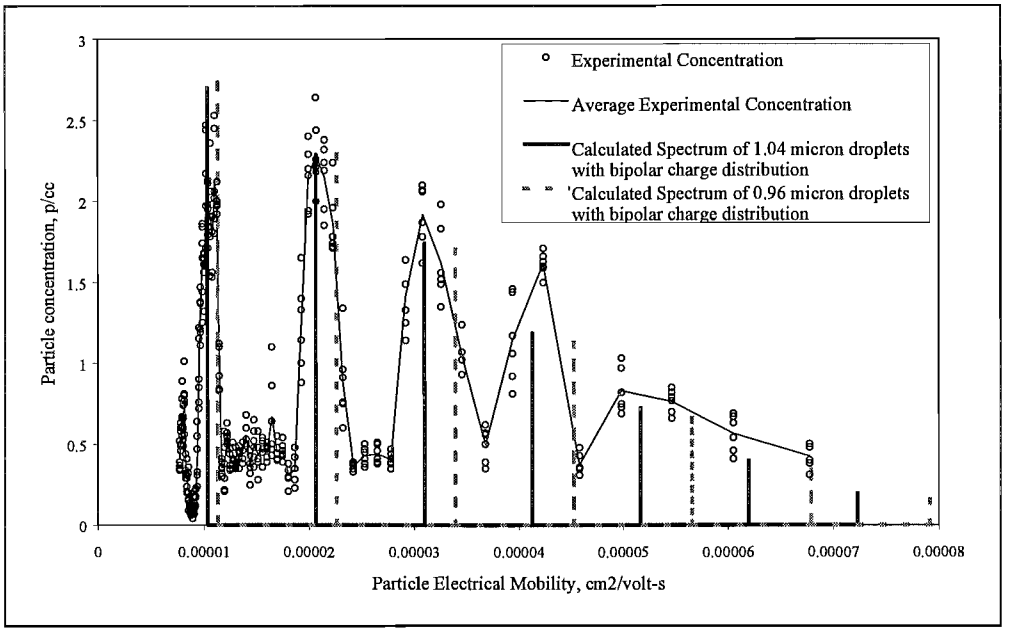

Figure 3.23 Electrical Mobility Distribution for VOMA aerosol generated with 50μL/L DNP in isopropyl alcohol. Calculated diameter = 0.96μm; Observed diameter = 1.04μm.

in the droplet volume. The aerosols that I have produced are at the lower limit of the size range that can be generated using the VOMA, where the errors in particle size are greatest.

Further DNP solutions were made up, with concentrations of up to 2315μL/L (calculated droplet size = 3.27μm). Measurements of the size distributions of aerosols from these solutions show that there is no systematic discrepancy between the calculated size and the actual measured size. The greatest uncertainty in the particle size appears to come from the concentration of the DNP solution.

3.3.2.4 *Usefulness of the VOMA for Aerosol Photolysis Experiments*

Once the correct operation of the VOMA had been established and I was familiar with its use and limitations, it was possible to assess the usefulness of the VOMA for

generating aerosols to be irradiated. Two areas needed to be considered – the physical properties of the generated aerosol and the chemical properties of the system.

The VOMA produces an aerosol with a reasonably narrow size distribution – the standard deviation for the diameter of 1μm particles from the VOMA was 5% of the diameter, compared with around 30% for the atomiser aerosols and 50% for the condensation aerosol. This means that the VOMA can be used as an aerosol source without the need for size-selection using the EC, provided that the solvent is fully evaporated.

The maximum concentration of aerosol from the VOMA is 280 particles/cm^3, which is obtained using a dilution air flow of 15 litres per minute. This maximum is obtained by balancing the initial particle concentration generated by the VOMA (which is highest when the gas flow is low) against the particle losses resulting from low flow rates. The aerosol flow from the VOMA is much larger than required for the photolysis experiment. It is not possible to reduce this flow; instead, a sample must be removed using a flow splitter and the rest of the aerosol from the VOMA is discarded. This is an inelegant, but effective method of achieving the desired flowrate.

In comparison, the maximum concentration of size selected aerosol from the atomiser, ie after it had been passed through the EC, was over 30 000 particles/cm^3. If the VOMA aerosol were to be used in a photolysis experiment, the pathlength of the irradiation cell would need to be very long in order to compensate for the low number density of the droplets, and hence the low absorption of light in the droplets. Alternatively, the flow velocity through the cell could be kept low in order to allow more photolysis events in a single droplet during its time in the cell, or the droplets could be composed of some strongly absorbing substance.

All three of these solutions introduce new difficulties. In the first case, the total volume of the cell becomes large, which makes it difficult to detect reaction products due to their low concentrations. Alternatively, if the flow velocity is slowed, the loss of particles due to gravitational settling becomes prohibitively large. The settling

velocity can be calculated using Stokes' Law which relates the force on a small particle to its velocity. Thus, the amount of settling which may occur in an irradiation cell can be calculated for any given flow rate. This establishes the minimum flow which may be used. An additional drawback of low flow rates is that detection of the reaction products using the mass spectrometer becomes very slow, increasing the time required for an experiment.

The final suggestion, that the droplets be composed of a strongly absorbing substance, removes the need for high particle concentrations. In this case, the VOMA becomes ideal for generating the required aerosol. The obvious drawback is that not all substances that we would like to perform irradiation experiments on are strong absorbers – sulfuric acid, for instance, is not.

The chemical properties of the required aerosol also need to be considered. In the sulfuric acid system under investigation, it is desirable to keep the system chemically simple – i.e. not to introduce additional species which may absorb light or become involved in the reaction – as the reaction mechanism is not yet well known. The presence of evaporated solvent in the aerosol flow coming from the VOMA may cause undesirable complications.

Most applications of a VOMA are to studies of the physical properties of an aerosol, and in these cases the presence of solvent vapour is not significant. For photochemical experiments, the choice of solvent is important, because it may become involved in chemical or photochemical reactions. In order to avoid a chemically complicated aerosol system, the solvent should be a species already present in the system, or one which is known to be unreactive under the experimental conditions. For these reasons, purified water may be more appropriate than isopropyl alcohol as a solvent, if it is already present in the aerosol system, as was the case with sulfuric acid aerosols. Care is needed when determining the size of these aerosols, since not all of the water may evaporate, and the final droplets may include some water in equilibrium with the surrounding vapour. This is especially so for aerosols which have a high affinity for water, such as concentrated sulfuric acid or the NaCl aerosols generated in 3.2.2.2. In these cases, the size distribution of the aerosols needs to be measured using the EC, and cannot be assumed from the operating parameters of the

VOMA. This is significant, because it means that the VOMA can not be used to generate a sulfuric acid or salt aerosol of known size and concentration without the use of the EC.

An additional source of chemical complication lies in the aerosol droplets containing a large fraction of impurity from the solvent used. In the original solvent, the non-volatile impurity may be 10 ppm, as for AnalaR isopropyl alcohol, but in the final aerosol droplet this impurity is concentrated due to evaporation of the solvent. In the 1.0μm droplets described in the previous section, the fraction of impurity is 17%. Obviously, an impurity this large may have a significant effect on the course of a reaction.

Finally, the desired aerosol material must be compatible with the components of the VOMA. These include plastic and rubber in the syringe, a fibrous filter in the liquid feed line, teflon tubing and stainless steel in the liquid chamber and orifice disc assembly. Concentrated sulfuric acid is obviously incompatible with this, but dilute solutions are more acceptable. A solution of 100μL/L sulfuric acid in water has a molar concentration of 1.9×10^{-6}M and is compatible with the materials inside the VOMA generator. The only risk lies in the large volume of liquid which accumulates on the top of the dispersion cover and in the drying column due to settling of aerosols. The concentration of acid in this solution is unknown since it is made up of liquid from partially-evaporated droplets, and may be high. To prevent damage from this, the VOMA needs to be carefully washed following operation.

3.4 Conclusion

Two strategies for generating a sulfuric acid aerosol for photolysis experiments have been investigated. It has been shown that an aerosol can readily be formed from a prepared solution, using either an atomiser or a vibrating orifice monodisperse aerosol generator.

An atomiser can produce an aerosol with a broad size distribution and high concentration of particles, in excess of 40,000 particles/cm^3. Aerosol from the VOMA has a narrow size distribution, but much smaller particle concentration of 280 particles/cm^3. Either generator is potentially useful.

In both cases, the major difficulty lies in determining the exact size and concentration of sulfuric acid within the droplets. This cannot be measured using an electrostatic classifier as had been intended. This is because the droplet size and composition is determined by an equilibrium with water vapour in the surrounding gas flow, which is upset when the EC is used to measure the particle size. Thus, the measurement instrument itself results in a change in droplet size.

In short, the formation of a stable, well-characterised aerosol of concentrated sulfuric acid solution is a non-trivial problem, as is systematically varying the particle size without affecting the composition. Due to this, it was decided to abandon the attempt to probe the photo-oxidation reaction of CO in a sulfuric acid aerosol, as described in Chapter 2, by varying the physical properties of the aerosol.

Instead, the behaviour of irradiated sulfuric acid systems in the bulk liquid was considered. Once this is properly understood, the results can be applied to sulfuric acid aerosols to determine the reactions that they are likely to occur within them. This work is the topic of subsequent chapters.

At the time when the work described in this chapter was completed, it was thought that determining the reactions occurring in irradiated sulfuric acid would be a straightforward process, and that other photochemical systems involving aerosols – preferably less corrosive ones – could be investigated using the instruments and techniques described in this chapter. Due to the time spent investigating the liquid sulfuric acid system, this was not possible. However, another student in this department, Chris Knox, took up this work in 1998 as the subject of a Doctorate under the title "Photochemistry of Liquid Aerosols".

Chapter 4

Studies of the Photochemistry of Bulk Sulfuric Acid and Sulfuric Acid Solutions

Chapter 4

Studies of the Photochemistry of Bulk Sulfuric Acid and Sulfuric Acid Solutions

4.1 Introduction

In the light of our failure to generate a stable, well-characterised sulfuric acid aerosol, our attention shifted to the photochemical properties of bulk solutions of concentrated sulfuric acid. The experiments described in Chapter 2 show that an aerosol consisting of 80-100wt.% sulfuric acid droplets is able to oxidise CO when irradiated with 193nm ultraviolet light. The proposed mechanism for the reaction involves the production of peroxymonosulfuric acid from the photolysis products of sulfuric acid. In the work described in this chapter, the effect of ultraviolet light on concentrated solutions of sulfuric acid was investigated experimentally.

4.1.1 Concentration Units for Sulfuric Acid Solutions

When working with concentrated sulfuric acid solutions, there are several commonly used units for reporting concentration, specifically moles per litre ($mol.L^{-1}$), weight percentage of acid (wt.%) and mole fraction. These units are not trivially related, since the density of sulfuric acid solutions at 25°C varies non-linearly from 0.9971 $g.cm^{-3}$ to 1.8269 $g.cm^{-3}$ as the composition changes from pure H_2O to pure H_2SO_4.

High-quality measurements of the density of sulfuric acid solutions were made during the late nineteenth and early twentieth centuries, and are tabulated in *International Critical Tables*. Using the data for solutions at 25°C, conversion tables for the different concentration units were prepared. (Fig. 4.1) Also included is the volume percentage of water that must be used to prepare a sulfuric acid solution of the given concentration.

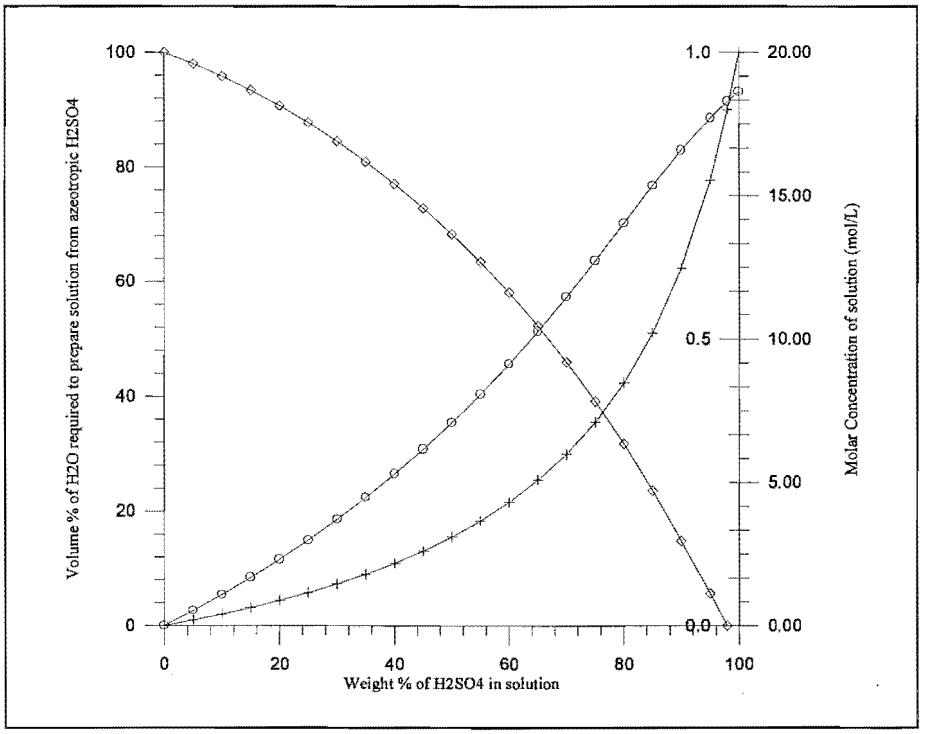

Figure 4.1 Conversion between concentration units for sulfuric acid – water solutions, taking weight% (H_2SO_4) as the base unit, for solutions at 25°C.

- o Molar Concentration of H_2SO_4 ($Mol.L^{-1}$)
- \+ Mole Fraction of H_2SO_4
- ◇ Volume % of H_2O required to prepare solution from azeotropic H_2SO_4

4.1.2 UV-VIS Absorption Spectrum of Sulfuric Acid

The UV absorption spectrum of sulfuric acid solutions was first reported by Morgan and Crist[1] for 0.05M and 5M solutions. The spectra contained a single absorbance feature at short wavelength: a sharp rise that began at 201nm for 0.05M solution and at 221nm for 5M solution. No absorbance was noted at longer wavelengths. The spectra obtained from Morgan and Crist's data are plotted in Fig 4.2.

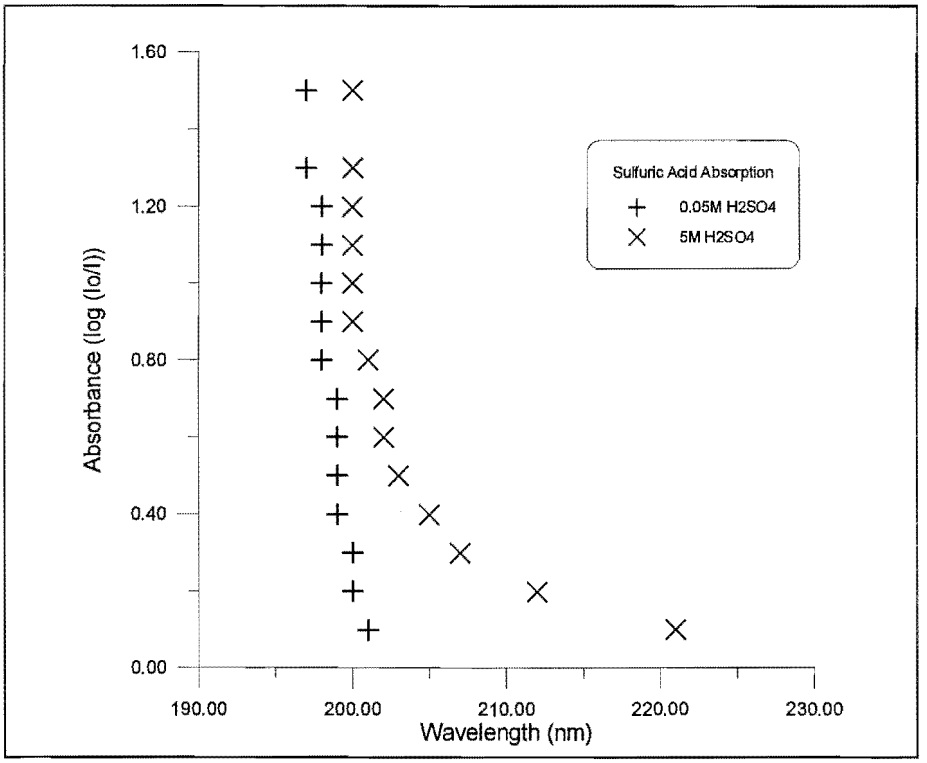

Figure 4.2 Absorption spectrum of sulfuric acid solutions reported by Morgan and Crist[1].

We have attempted to measure the UV absorption spectrum of concentrated sulfuric acid solutions using a standard split-beam laboratory spectrophotometer (GBC920 UV-VIS) with an operating range of 190-850nm. Spectra were measured in 1cm pathlength quartz cuvettes, which had a transmission of 85.0% at 200nm. Before the sample spectrum was measured, the baseline absorbance spectrum of the empty cell was recorded, and this baseline measurement was subtracted point-wise from the sample spectrum as it was recorded.

It was observed that the absorption spectra of sulfuric acid solutions are highly variable at wavelengths shorter than 340nm. This was clearly related to impurities in the solution, rather than absorbance by sulfuric acid itself. Figure 4.3 shows the spectra of three 80wt% sulfuric acid solutions. The first was prepared from triply distilled water and CP grade sulfuric acid. The second solution was prepared from triply distilled water and AnalaR grade sulfuric acid, and the third spectrum is of the same acid solution after being left to stand for several weeks. The peak at 260nm is attributed to dissolved SO_2.

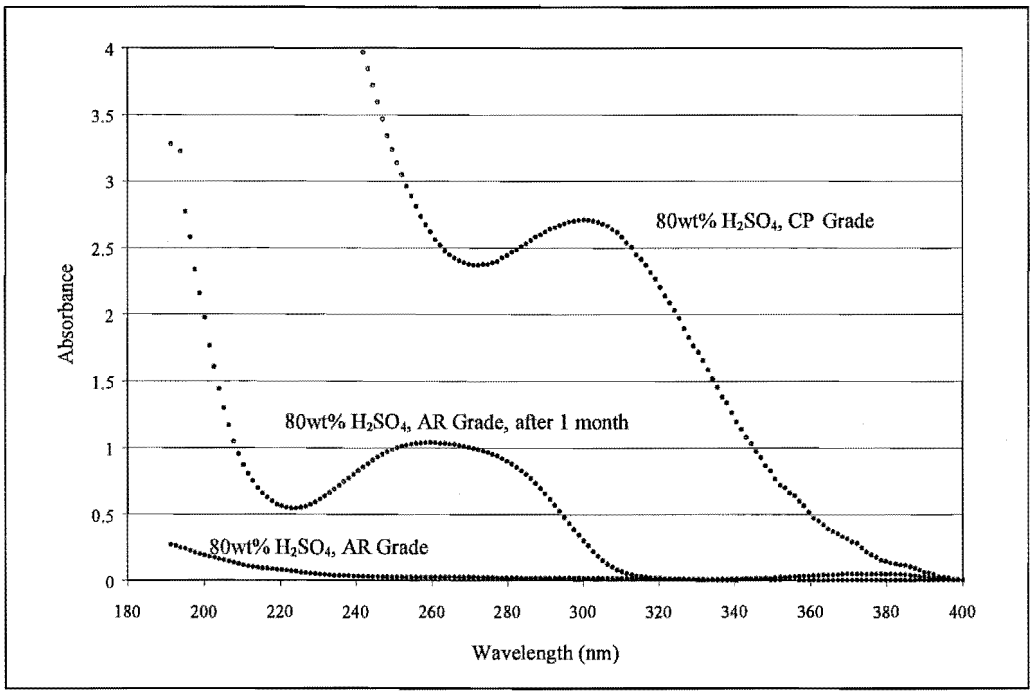

Figure 4.3 Absorption Spectra of three sulfuric acid solutions, showing spurious absorbances due to dissolved impurities.

Samples of sulfuric acid solution were freed from dissolved SO_2 and other gases by pumping on them with a rotary vacuum pump at a pressure of 1×10^{-2} torr for several days. The sample was protected against contamination by back-diffusion of pump oil with a liquid nitrogen cold trap. Using samples of AnalaR grade 98wt.% sulfuric acid that had been degassed using this method, the maximum value for the molar absorption coefficient of liquid H_2SO_4 at 200nm was found to be (0.0033 ± 0.0002)L.mol^{-1}cm^{-1}, and at 190nm $\varepsilon < (0.0044\pm0.0003)$ L.mol^{-1}cm^{-1}. These measurements indicate that absorption by sulfuric acid is very weak in the range accessible with the spectrophotometer used.

Recently, the gas phase absorption cross-section of H_2SO_4 was measured by Burkholder, et al[2], who were investigating the extent of sulfuric acid photochemistry in Earth's stratosphere. They reported an upper limit for the absorption cross-section of $<1\times10^{-21}$cm^{2}molecule^{-1} over the wavelength range 195-330nm. This corresponds to a molar absorption coefficient limit of < 0.6L.mol^{-1}cm^{-1}, which does not conflict with our measurement for liquid sulfuric acid.

Ab initio calculations of the energy required for the transitions from the ground state to either the first or second excited electronic state of gas-phase sulfuric acid have recently been completed by Professor Laurie Butler of the University of Chicago. This work was done at our suggestion, in order to help determine the primary photochemical process in irradiated sulfuric acid. The results of these calculations are discussed in Section 4.4.

4.2 Investigation of Insoluble Products formed during the UV Irradiation of Concentrated Sulfuric Acid Solutions

During the experiments described in Chapter 2, it was noted that the sintered glass disks used for removing aerosol droplets from the gas flow sometimes became blocked after the aerosol was irradiated. The flow through the sinters was stable until irradiation began, at which time the blockage occurred and the pressure in the system started increasing rapidly. In addition, a discolouration – either black, brown, yellow, or blue-green – was observed on the sinters when they were removed for cleaning. It was proposed that a solid product was formed in the aerosol droplets during irradiation, which was responsible for both the blockages and discolouration.

When a closed quartz cell containing concentrated sulfuric acid was irradiated with 193nm light from the ArF excimer laser, liquid became visibly darkened. Close examination showed that a suspension of black particles was formed. The suspension was observed only in the section of the cell that had been exposed to the laser light, which was taken to be proof of its photochemical origin. Because of the high viscosity of the sulfuric acid, the suspension remained localised and did not diffuse into the non-irradiated part of the cell.

The most obvious suggestion for the identity of the suspension was elemental carbon, produced by either photolysis or acid digestion of organic contaminants in the sample. An alternative possibility – supported by the varied discolourations observed on the

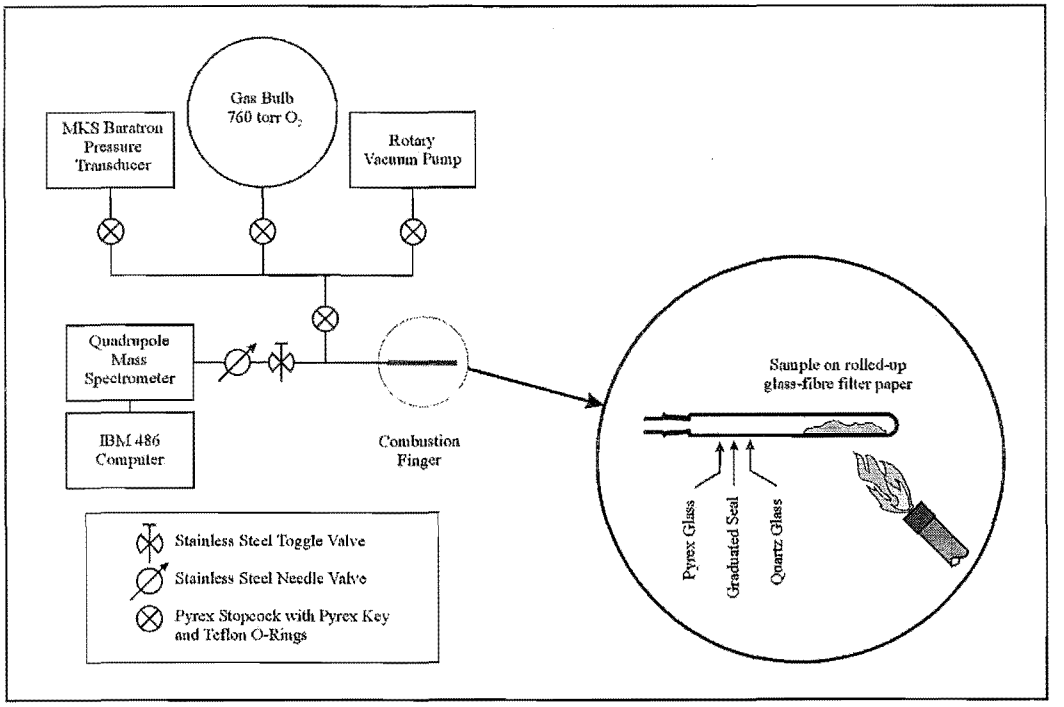

Figure 4.4 Experimental apparatus for determining elemental composition of black suspension.

sinters – was that it was a S_x species produced by the reduction of H_2SO_4 during irradiation

Both carbon and sulfur will burn when heated in the presence of excess oxygen to form their respective dioxide. To determine whether the suspended particles contained either C or S, a sample was collected on a glass-fibre filter and heated in an oxygen atmosphere until it ignited. The gaseous products were sampled with a quadrupole mass spectrometer to determine whether CO_2 or SO_2 had been produced (Fig. 4.4). Results are given in Table 4.5.

	ΔM18/M32 (Water)	ΔM44/M32 (CO_2)	ΔM64/M32 (SO_2)
Empty Cell	$+ (6\pm1) \times 10^{-3}$	$- (4\pm1) \times 10^{-3}$	$+ (1\pm1) \times 10^{-5}$
Filter Only	$+ (2\pm1) \times 10^{-2}$	$+ (3\pm1) \times 10^{-2}$	$+ (1\pm1) \times 10^{-5}$
Filter washed with non-irradiated 15M sulfuric acid	$+ (2\pm1) \times 10^{-2}$	$+ (6\pm1) \times 10^{-2}$	$+ (2\pm1) \times 10^{-3}$
Filter containing black suspension	$+ (4\pm1) \times 10^{-2}$	$+ (8\pm1) \times 10^{-2}$	$+ (5\pm1) \times 10^{-4}$
Filtered sample of dilute sulfuric acid containing sulfur suspension	not available	$+ (9\pm1) \times 10^{-2}$	$+ (2.2\pm0.2) \times 10^{-1}$

Table 4.5 Mass Spectrometer Results for Suspension-burning experiment

The results from this experiment were unable to determine whether the suspension consisted of C or S, as the background level of both elements in the combustion finger was too high. Carbon was introduced into the finger from the "glass-fibre" filter, and sulfur was introduced when washing the filter with sulfuric acid. The amount of product present on the filter was too small to give a result for either C or S that could be distinguished from this background.

This series of experiments was abandoned after the excimer laser that was used to irradiate the sulfuric acid solutions broke down and was unavailable for several months. Attempts to generate the suspension by irradiation with a longer-wavelength light source were unsuccessful. We believe that the black suspension is most likely due to organic contamination of the sample, and that it is not a genuine photochemical product of H_2SO_4.

4.3 Investigation of Soluble Products formed during the UV Irradiation of Concentrated Sulfuric Acid Solutions

4.3.1 Introduction

Following the abortive attempt to identify the solid product, our attention now turned to soluble photolysis products of sulfuric acid. In Chapter 2, it was noted that a long-lived reactive species was produced during the irradiation, which was responsible for removing SO_2 introduced into the system downstream from the irradiation cell. It was proposed that peroxymonosulfuric acid, H_2SO_5, was formed during the irradiation according to Equations 2.12, 2.15 and 2.16.

$$H_2SO_4 + h\nu_{(\lambda=193nm)} \longrightarrow O^{\cdot} + H_2SO_3 \qquad (2.12)$$

$$H_2SO_4 + O^{\cdot} \longrightarrow HSO_4^{\cdot} + {}^{\cdot}OH \qquad (2.15)$$

$$HSO_4^{\cdot} + {}^{\cdot}OH \longrightarrow H_2SO_5 \qquad (2.16)$$

The reaction mechanism described in Chapter 2 would be supported if peroxymonosulfuric acid could be detected in an irradiated sulfuric acid solution.

Several experiments were performed in an attempt to detect H_2SO_5 as a reaction product. Since the proposed mechanism does not involve reactions with dissolved gases, the reaction should occur equally well in a sample of irradiated bulk liquid sulfuric acid as in an aerosol.

Monger and Redlich have reported that H_2SO_5 is formed in a reversible reaction between H_2O_2 and H_2SO_4 in concentrated sulfuric acid solutions[3], according to Equation 4.1:

$$H_2O_2 + H_2SO_4 \rightleftharpoons H_2O + H_2SO_5 \qquad (4.1)$$

The reported equilibrium constant, $K_{4.1}$ for the reaction varies markedly with the total concentration of sulfuric acid in the solution, ranging from 0.13 in 5M acid solution to 3.4 in 15M acid solution. The variation was explained by proposing that the reactive acid species was undissociated sulfuric acid, H_2SO_4, and that dissociated species, ie HSO_4^- and SO_4^{2-} did not contribute to the reaction. In highly concentrated acid solutions, the proportion of undissociated acid is greater than in dilute solutions, accounting for the apparent increase in $K_{4.1}$.

The rate of the reaction was also reported to increase with acid concentration. In solutions that initially contained H_2O_2 in 5M acid, the time required for 50% conversion to H_2SO_5 at 25°C was in the order of a few days. In 12M acid solution, however, the time required for 50% conversion is only 3 minutes. No data is available for more concentrated solutions, but it is reasonable to assume that the rate is similarly fast. Monger and Redlich did not discuss the reaction mechanism.

One immediate consequence of the reaction is that if H_2SO_5 is formed in irradiated concentrated sulfuric acid, then H_2O_2 is also likely to be present. Any analytical method for determining the amount of H_2SO_5 present in a concentrated sulfuric acid solution must be able to distinguish it from H_2O_2.

4.3.2 Analytical Techniques for the Determination of Low Concentrations of H_2SO_5

Three analytical methods were considered for determining whether H_2SO_5 was being formed when sulfuric acid was irradiated. The first two of these were direct spectroscopic methods, in turn looking at the UV-VIS and infrared spectra of the irradiated solutions. The third method involves measuring the oxidising capacity of the solution by spectrophotometric titration.

4.3.2.1 UV-VIS and Infrared Absorption Spectra

The UV-VIS absorbance spectrum of H_2SO_5 is similar to that of other peroxides – a broad, featureless absorption in the far UV[4] – and contains contributions from H_2SO_5, HSO_5^- and SO_5^{2-}. The absorbance begins at about 270nm and continues to below 190nm. The molar extinction coefficient of H_2SO_5 in concentrated sulfuric acid solution is about 180 $L.mol^{-1}.cm^{-1}$ at 200nm. It is not possible to distinguish the spectra of H_2SO_5 in concentrated sulfuric acid from that of H_2O_2, which makes UV-VIS spectroscopy a poor technique for quantifying the amount of either species that may be present. However, a measurement of the UV-VIS spectrum of an irradiated sulfuric acid solution can be used to indicate the upper limit of the concentration of H_2SO_5 present.

The second spectroscopic method that was considered was infrared spectroscopy. The infrared spectra of liquid sulfuric acid[5] and peroxymonosulfuric acid[6] have been reported, and contain distinctive features that can be used to differentiate them. Because sulfuric acid is highly corrosive, the KBr plates that are normally used to support a sample cannot be used. Instead, we attempted to design an apparatus that would allow the spectrum to be measured without requiring infrared-transparent disks or windows (Fig. 4.6). This was unsuccessful, due to difficulty in constructing a cell that did not interfere with the beam-path.

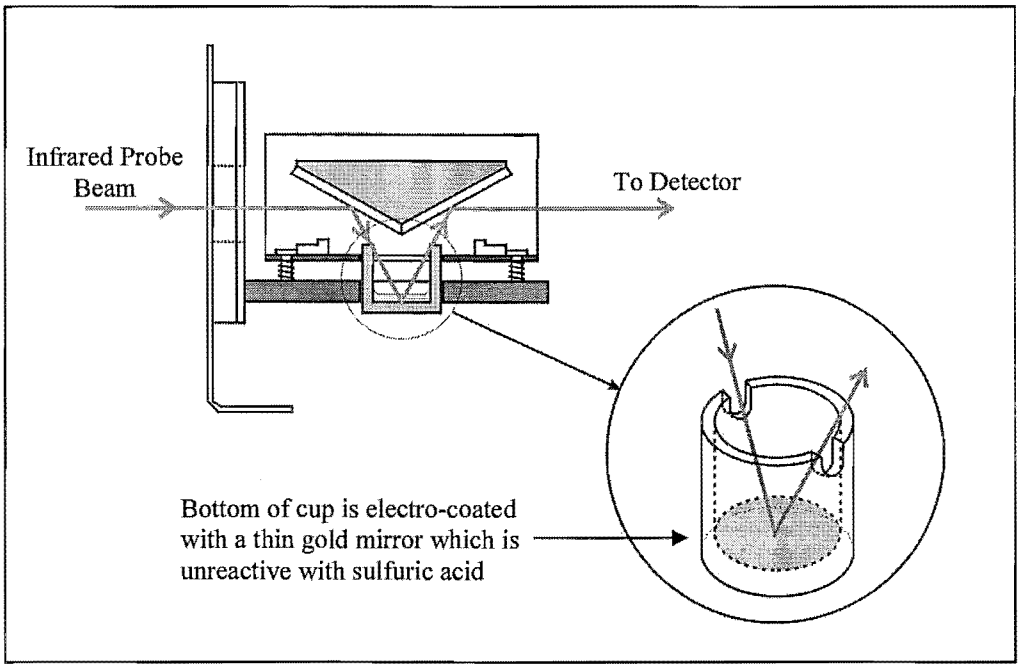

Figure 4.6 Device for measuring the infrared absorption spectrum of sulfuric acid solutions in an open cell (unsuccessful)

4.3.2.2 *Phototitrimetric Method based on Redox Properties*

Attempts to measure the infrared spectrum of concentrated sulfuric acid solutions were abandoned in favour of a third technique for determining the amount of H_2SO_5 present. This was to measure the oxidising ability of the solution by spectrophotometric titration with Fe(II), using a similar procedure to that described by Mariano[7] for the quantitative determination of small concentrations of H_2SO_5 in sulfuric acid solutions, in the presence of hydrogen peroxide and/or peroxydisulfate ion ($S_2O_8^{2-}$).

The total concentration of oxidising species present, i.e. ($[H_2O_2]$ + $[H_2SO_5]$ + $[H_2S_2O_8]$), was determined by titration with Fe(II) solution. All of these species react rapidly with Fe(II) to form Fe(III). The amount of Fe(III) produced was determined by measuring the absorbance of the solution at 304nm. At this wavelength, Fe(II) has a negligible absorbance whereas Fe(III) absorbs strongly.

To distinguish H_2SO_5 from H_2O_2, the reducing ability of the solution was also determined by titration with cerium(IV) sulfate. In dilute sulfuric acid solutions, both H_2O_2 and H_2SO_5 reduce Ce(IV), and while H_2O_2 produces a stoichiometric amount of Ce(III) according to 4.2, the reaction with H_2SO_5 is complex and non-stoichiometric.

$$2Ce^{4+} + H_2O_2 \longrightarrow 2Ce^{3+} + 2H^+ + O_2 \qquad (4.2)$$

Mariano found that when the reaction was carried out in more concentrated sulfuric acid solutions (5M), there was a significant difference in the rates of reaction of Ce(IV) with H_2O_2 and H_2SO_5, such that the reaction with H_2O_2 went to completion in a few seconds, but the reaction with H_2SO_5 could be ignored. The change in Ce(IV) concentration was again determined by spectrophotometry, as Ce(IV) has a strong absorption band centred on about 320nm, where Ce(III) does not absorb.

If $S_2O_8^{2-}$ was present in the solution, its concentration could be determined by first adding As_2O_3 to reduce any H_2SO_5 present without affecting H_2O_2 or $S_2O_8^{2-}$, then adding Ce(IV) to oxidise H_2O_2. Dissolved O_2 is removed by purging the solution with nitrogen, and finally the solution is titrated with Fe(II). Any Fe(III) produced is attributed to reaction with excess Ce(IV) – a known quantity – and to $S_2O_8^{2-}$. Although Mariano has demonstrated that this method can be used to determine the amount of $S_2O_8^{2-}$ present, the number of steps required increases the experimental uncertainty considerably. We decided to omit this measurement, assuming that the amount of persulfate present would be negligible.

Mariano has reported that the analysis is best performed in a solution of 5M H_2SO_4. At this acid concentration, there is a balance between the speed of the reactions taking place, and the interference in the analysis by acid catalysis and decomposition of the peroxyacids. Since all of the sulfuric acid solutions that we wanted to analyse were more concentrated than 5M, the samples were diluted before the analysis was performed. The dilution was carried out in an iced water bath to minimise heating of the solution. To minimise the conversion of H_2SO_5 to H_2O_2 as described in 4.3.3.2, the dilution was carried out as soon as possible after the sample had been irradiated.

We have determined the molar extinction coefficient of Ce(IV) in 5M acid to be ε=5503 $M^{-1}cm^{-1}$ at 320nm, using absorption measurements for 11 different solution concentrations. Our value was significantly lower than Mariano's reported value of 6800 $M^{-1}cm^{-1}$. Similarly, we measured the extinction coefficient of Fe(III) in 5M acid to be ε=4524 $M^{-1}cm^{-1}$ at 304nm; Mariano's value was 2874 $M^{-1}cm^{-1}$. The absorption spectrum of Fe(III) in sulfuric acid solutions is considered in greater detail in Chapter 5, where it is noted that the absorption coefficient of Fe(III) varies considerably depending on the concentration of sulfuric acid in the solution. The results in Chapter 5.4.1 indicate that Fe(III) has ε_{304nm} = 2874 $M^{-1}cm^{-1}$ in approximately 1.1M sulfuric acid solution. Thus, the disagreement between the molar extinction values reported by Mariano and the present work are attributed to a mis-reporting of the acid concentration in Mariano's work.

The analytical procedure used for quantitatively determining the amount of H_2O_2 and H_2SO_5 in irradiated 98wt% sulfuric acid is outlined below. All solutions were prepared from triply-distilled water and AnalaR grade 98wt% sulfuric acid. Reagents were AnalaR grade, from BDH Laboratories, and used without further purification.

1. Take a 2mL aliquot of irradiated acid and place in a small beaker. Slowly add 10mL of 2.248M H_2SO_4 solution, while cooling in an ice water bath. The resulting solution contains approximately 12mL of 5M H_2SO_4.
2. Take a 5mL aliquot of the diluted acid, and add 1mL of 2.25×10^{-3}M $Ce(SO_4)_2$ in 5M H_2SO_4 solution. Mix well.
3. Measure the absorbance of the acid+Ce solution at 320nm for 2 minutes and determine the average absorbance over this time.
4. Prepare a fresh solution of approximately 0.02M Fe(II) from 0.8g Mohr salt (that is, $(NH_3)_2SO_4.FeSO_4.6H_2O$) in 100mL of 5M H_2SO_4. Because Fe(II) solutions are slowly oxidised by atmospheric oxygen, a fresh solution was prepared at least every other day.
5. Take another 5mL aliquot of the diluted acid, and add 1mL of 0.02M Fe(II) in 5M H_2SO_4 solution. Mix well.

6. Measure the absorbance of the acid+Fe solution at 304nm for 2 minutes and determine the average absorbance over this time.
7. Repeat the analysis twice, using fresh, non-irradiated AnalaR grade sulfuric acid (98wt%). The variation between the two results for these sample blanks is used to estimate the uncertainty in the measurement for the actual irradiated sample.

The total concentration of peroxides in the solution was determined using the difference between the average amount of Fe(III) produced in the blank solution and in the sample solution. The stoichiometry of the reaction is the same for both H_2O_2 and H_2SO_5:

$$\text{R-OOH} + 2Fe^{2+} + 2H^{+} \longrightarrow H_2O + \text{R-OH} + 2Fe^{3+} \qquad (4.3)$$

Thus, the total peroxide concentration in the diluted sample is half the increase in [Fe(III)], and the peroxide concentration in the original acid sample is $\frac{18}{5} \times \Delta[\text{Fe(III)}]$.

The concentration of H_2O_2 was found by comparing the final Ce(IV) concentrations in Step 3 for the sample solution and the blanks. The difference between the measurements was attributed to reaction with H_2O_2, with a 2:1 stoichiometry as shown in Reaction 4.2. Thus, the concentration of H_2O_2 in the original sample is $\frac{18}{5} \times \Delta[\text{Ce(IV)}]$, and the concentration of H_2SO_5 is the difference between [total peroxides] and $[H_2O_2]$.

The experimental accuracy of this method was limited by the measurement of small aliquots of the titrant solution, ie Ce(IV) or Fe(II). The problem was most severe for Ce(IV) solution, where a small error in the volume was translated directly into an error in the measured absorbance. The 1mL aliquots were measured using a gold line pipette, with a measurement error of ±0.7%. For the 2.25×10^{-3}M Ce(IV) solutions that were used for the analysis, this corresponds to a ±0.015 error in the measured absorbance. The observed discrepancy between absorbance measurements for the two blanks was normally less than 0.01 absorbance units. Thus, the uncertainty in $[H_2O_2]$ was found to be $\pm1\times10^{-5}$M. In most cases, the uncertainty in the total peroxide

concentration due to measurement errors was much smaller, at ±1% of the measurement.

To test the analytical method, sulfuric acid solutions containing between 5×10^{-6}M and 1×10^{-3}M of HSO_5^- and H_2O_2 were prepared from Oxone®, a peroxymonosulfate compound produced by Aldrich Chemical Company[(i)] and hydrogen peroxide solution. When the solutions were analysed using the method described, it was found that the total peroxide concentration could be determined with an accuracy of ±5% in this range. The concentration of H_2O_2 was often found to be larger than expected (up to 25% greater), presumably due to hydrolysis of H_2SO_5 that occurred while the concentrated sulfuric acid solution was being diluted to 5M. This effect was minimised by performing the dilution slowly and avoiding excessive heating.

In summary, the phototitrimetric method was capable of determining the concentrations of H_2O_2 and H_2SO_5 in concentrated sulfuric acid in the range 1×10^{-5}M to 1×10^{-3}M, with an uncertainty of $\pm1\times10^{-5}$M or ±5%, whichever is greater.

4.3.3 1849Å Irradiation of 80wt.% and 98wt.% Sulfuric Acid Solutions Using Immersible Mercury Lamps

The preferred light source for UV irradiation, an ArF excimer laser emitting at 1933Å that was used in the experiments described in Chapter 2, was not operational for an extended period of time, and thus an alternative light source was required. The first option that was considered was the use of mercury lamps. 80wt.% and 98wt.% sulfuric acid solutions were irradiated with a high-powered (~500W) mercury lamp with output at 2537Å, but no reaction was observed. This was expected, since the UV-VIS absorption spectrum of sulfuric acid shows no absorbance at this wavelength.

[(i)] Aldrich does not state the composition of Oxone®; however, several groups have reported its composition to be ($2KHSO_5.KHSO4.K2SO4$).

Alternative types of mercury lamp can be used as sources of ultraviolet light at wavelengths other than 2537Å. Mercury has atomic emission lines at 5791Å, 5770Å, 5460Å, 4359Å, 4048Å, 3652Å, 3132Å, 2537Å and 1849Å. Low pressure lamps, containing a minimal amount of mercury vapour in a few torr of an inert gas, are used to generate an ultraviolet emission, mostly consisting of 1849Å and 2537Å light. Medium and high-pressure mercury lamps have a stronger intensity at the longer wavelengths, and the emission lines are considerably broadened.

The mercury emission line at 1849Å is often overlooked as a light source for solution photochemistry, since there are some practical difficulties involved with its use. 1849Å light is readily absorbed by oxygen, as well as pyrex glass and some grades of quartz. In addition, the light is normally fully absorbed by a few centimetres of water. In order to overcome these limitations, immersible low-pressure mercury lamps have been developed, which are operated while the lamp is submerged in the solution being irradiated. The pressure and operating voltage are chosen so that the temperature of the lamp does not exceed 100°C, which makes the lamps suitable for use in aqueous solutions. By immersing the lamp directly into the target solution, absorption of the 1849Å light by atmospheric oxygen and cell windows is avoided.

Immersible mercury lamps ought to be well-suited for the irradiation of concentrated sulfuric acid solutions. In our experiments, the sulfuric acid itself was expected to absorb the 1849Å light, so there was no problem due to unwanted solvent absorption. An additional advantage lay in not needing to incorporate windows into the irradiation cell design, since sulfuric acid is incompatible with many window materials, and quartz glass is difficult to work with.

Three immersible low-pressure mercury lamps from Jelight Co. were obtained for the irradiation of sulfuric acid solutions. The lamp cavity was U-shaped, and was incorporated into a single finger, 155mm long and with a circular cross-section of 9mm diameter. The lamp electrodes and electrical connections were contained in a sealed aluminium tube at the base of the lamp, which was powered by a 3000V DC supply. The apparatus designed for irradiating sulfuric acid solutions with these lamps is shown in Fig. 4.7.

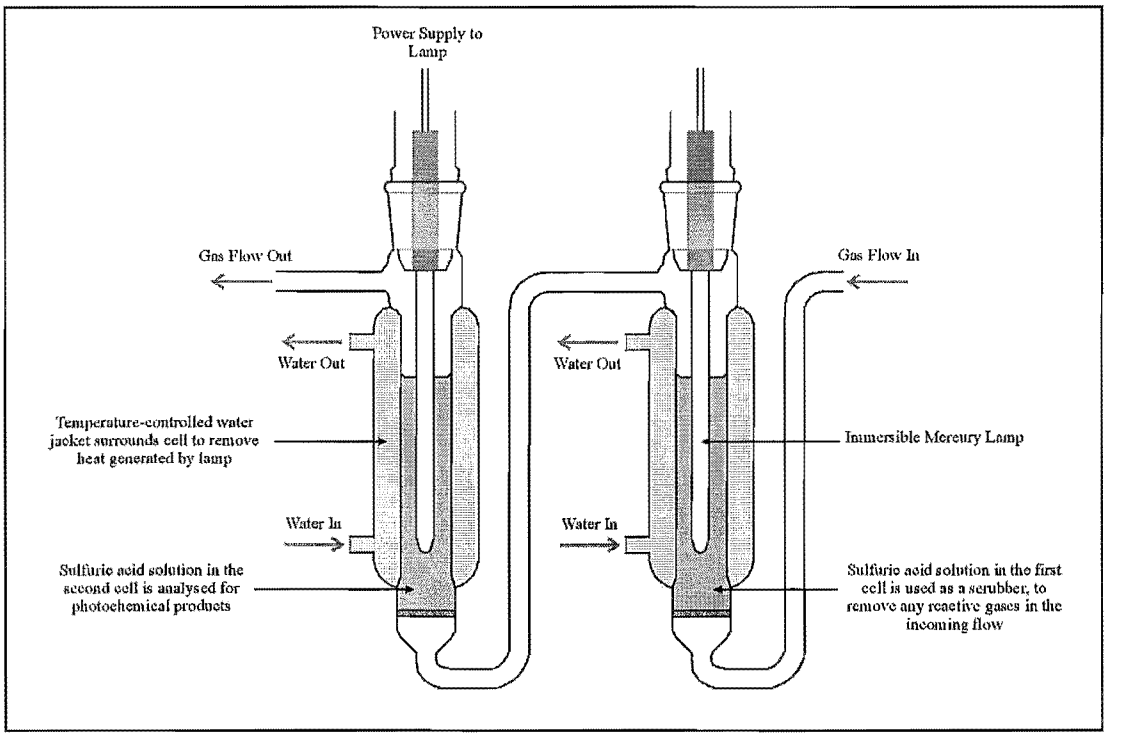

Figure 4.7 Cell for irradiating concentrated sulfuric acid solution with immersible mercury lamp.

Two irradiation cells were placed in series, with a continual flow of gas being passed through the solutions to ensure that they were well mixed. The cells were surrounded with a temperature-controlled water jacket in order to dissipate heat generated by the mercury lamps. The first cell was intended to act as a "scrubber", removing any contaminants in the gas flow that were either soluble or photochemically active in sulfuric acid. Either an inert gas such as argon or dinitrogen, or a potentially reactive gas such as carbon monoxide or dioxygen, could be used. The composition of the gas flow was monitored using a quadrupole mass spectrometer to determine whether any gaseous products, specifically sulfur or carbon dioxide, were formed during irradiation. No statistically significant changes in the mass spectrum were observed during irradiation.

The primary method that was used to determine whether a reaction had taken place during irradiation was by comparing the UV-VIS absorption spectra of the sulfuric acid solution before and after irradiation. A number of absorbance peaks were found in irradiated solutions of both 80wt% and 98wt% sulfuric acid, at wavelengths between 200-400nm. None of the absorption spectra were reproducible, and it was

found that the changes in absorption were greatest in the up-stream cell. Thus, it was determined that the absorption peaks were caused by contaminants introduced into the acid from the gas stream. This was confirmed when it was found that acid solutions also developed an absorption spectrum when gas was bubbled through them without any irradiation. Various measures were taken to eliminate this source of contamination. The gas stream was passed through a dry ice/ethanol cold trap to remove any condensable vapours. This reduced the size of the absorbance peaks in the spectra of the down-stream sample, but did not entirely remove them.

Several series of irradiations failed to show any evidence of a reproducible chemical change due to the photochemical reaction of sulfuric acid, and we began to suspect that the lamps were not as effective a source of 1849Å light as we had been led to believe. The intensity of the lamp output was measured using a MacPherson monochromator and 955QB photomultiplier, while excluding oxygen. It was discovered that the intensity of the 1849Å line was very weak – less than 0.1% of the 2537Å line. We concluded that the emission from the lamp was insufficient to cause detectable photochemistry in sulfuric acid samples. A more intense light source was required in order to study the photochemistry of sulfuric acid solutions.

4.3.4 1783Å Irradiation of 98wt.% Sulfuric Acid Solutions with an Iodine Resonance Lamp

4.3.4.1 Introduction

Since the early part of the century, it has been common practice among photochemists and physicists to utilise the phenomenon of resonance radiation of excited atoms for the construction of ultra-violet lamps. The target atoms are excited by some means, e.g. electrical arc or microwave discharge, into an elevated electronic state. From this state, the atoms emit light in order to return to the ground electronic state.

Since other atoms of the same type can readily absorb the light emitted by this process, it is necessary to run the lamp at relatively low pressure. For many lamps, including those exciting the noble gases Ar, Kr and Xe, it is found that introducing He into the lamp increases the output intensity of the lamp. These lamps can be considered to contain active atoms of excited emitting gas, in a sea of inert He atoms. The He buffer gas reduces the effect of atoms being lost by sticking to the walls of the lamp.

The wavelength of the emitted resonance radiation depends, of course, on the type of atoms used in the lamp. In 1971, Brewer and Tellinghuisen[8] reported the use of resonance radiation of iodine atoms, excited by a microwave discharge, as a means of studying the kinetics of I atom recombination in I_2 vapour. They described the construction of an iodine lamp, containing I_2 vapour (the pressure of which was regulated by a cold finger immersed in ethanol-dry ice, and containing an excess of purified I_2 crystals) and about 1 torr of spectroscopic grade argon. This lamp was operated by discharging a 100 W microwave generator into the main lamp tube. Once operating temperature was reached, the molecular I_2 dissociated into I atoms. Iodine has a major resonance line at 1783Å, due to the ($6s\ ^2P_{3/2} \leftarrow 5p^5\ ^2P_{3/2}$) transition. A spin-forbidden transition at 1830Å ($6s\ ^4P_{5/2} \leftarrow 5p^5\ ^2P_{3/2}$) has an intensity about 15-20 times weaker than the 1783Å resonance. These resonance lines (actually multiplets, since they contain hyperfine splitting) can be used as a light source in the iodine lamp.

4.3.4.2 Experimental

Following the method of Brewer and Tellinghuisen, we constructed an iodine lamp as a source of vacuum UV light for irradiating sulfuric acid solutions. The lamp design is shown in Fig. 4.8. Iodine vapour was introduced into the lamp by gently warming a few iodine crystals in a side-arm. Before use, the crystals were cooled with liquid nitrogen and degassed to remove adsorbed oxygen and other atmospheric gases. Helium was added as a buffer gas, until the pressure in the lamp was about 0.25 torr. A Raytheon 3184 Microwave Power Generator, capable of delivering up to 800W of microwaves, was used to excite the iodine atoms and stimulate light emission. In

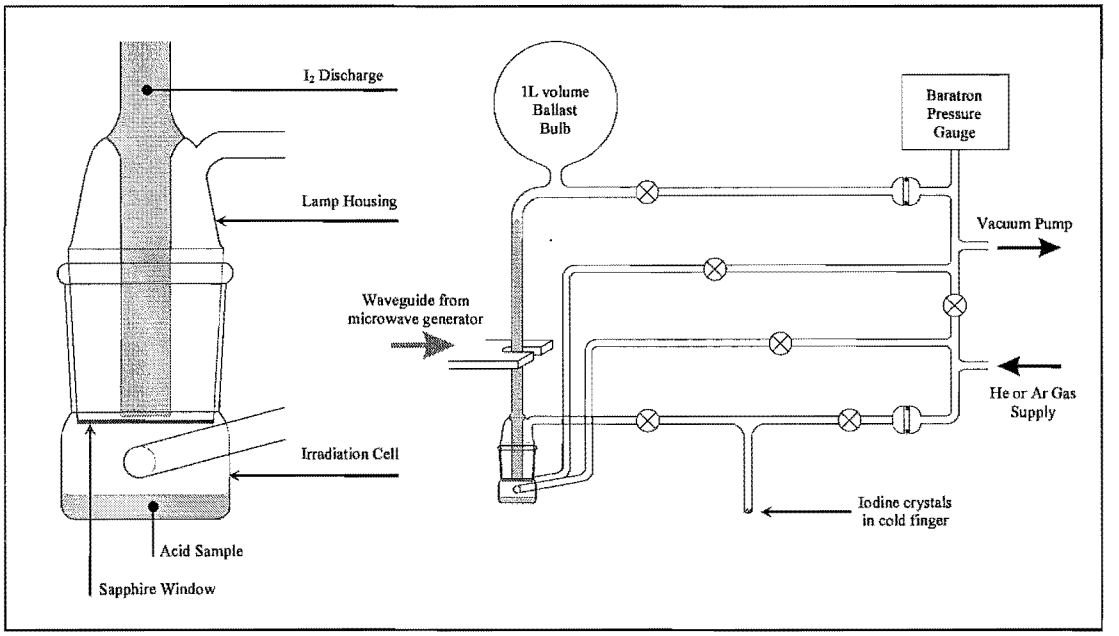

Figure 4.8 Design of iodine vapour resonance lamp and irradiation cell

practice, the microwave generator was operated at the lowest possible power that would sustain a discharge in the lamp. If the power was increased too much, the lamp discharge would jump into the glassware surrounding the lamp cavity, resulting in serious overheating (Fig. 4.9). When functioning properly, the lamp output appeared pink, with a blue tinge visible around the edges of the discharge.

Throughout the experiments using the iodine lamp, we experienced difficulties in regulating the temperature of the lamp and the irradiated solution. Immersing the lamp housing and irradiation cell in a temperature-controlled waterbath was counterproductive, since the water absorbed the microwave energy and effectively killed the discharge. The lamp could not be run for any length of time without cooling, as was demonstrated in an accident where the lamp was heated by the discharge so much that the graded

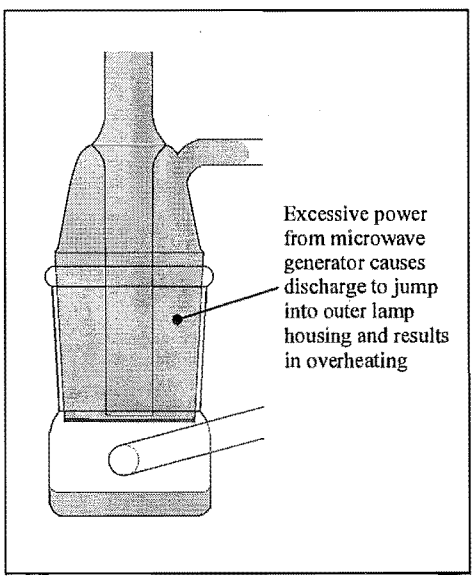

Figure 4.9 Discharge escape into lamp housing

quartz-pyrex seal melted and the lamp imploded!

The best solution we found to the overheating problem was to cool the cell containing acid by immersing it in an ice slurry bath, and to air-cool the discharge tube of the lamp with a small fan. With this set-up, we were able to conduct irradiation experiments without too much difficulty, although the lamp could not be run for prolonged periods of time without overheating. It was vital that this did not occur, firstly because of the possible damage to the apparatus itself, but also because the proposed reaction product, peroxymonosulfuric acid, is thermally unstable and will decompose with temperatures in excess of 40°C.

4.3.4.3 Results

A series of experiments were carried out where 2.5mL samples of AnalaR grade 98wt% sulfuric acid were irradiated with the iodine resonance lamp for up to 4 hours. A 50sccm flow of argon was passed over the acid sample during irradiation, and the total pressure in the cell was approximately 10 torr. The cell was immersed in an ice-water bath during irradiation, in order to maintain a constant, known temperature despite significant heating from the lamp. After irradiation, the concentrations of H_2O_2 and H_2SO_5 were determined using the spectrophotometric titration method described in (4.3.2.2). The results are plotted in Fig. 4.10 and 4.11 as concentration of product vs. irradiation time, although there is no observed correlation. In Fig. 4.12, the concentration of H_2O_2 is shown to increase proportionately to the total concentration of peroxides present. From this, it was inferred that both H_2O_2 and H_2SO_5 in the solution had a common origin – although it was unclear whether H_2O_2 was formed during the irradiation, or whether it was formed by thermal hydrolysis of H_2SO_5 when the irradiated 98wt.% (18.3mol.L^{-1}) acid sample was diluted to 5M.

The average concentration of H_2SO_5 formed during an irradiation experiment was 2×10^{-5}M ± 2×10^{-5}M (2 standard deviations), and the average concentration of H_2O_2 was 1×10^{-5}M ±2×10^{-5}M. The large variation in these results makes it difficult to draw any conclusions about the reactions that are responsible for the formation of the

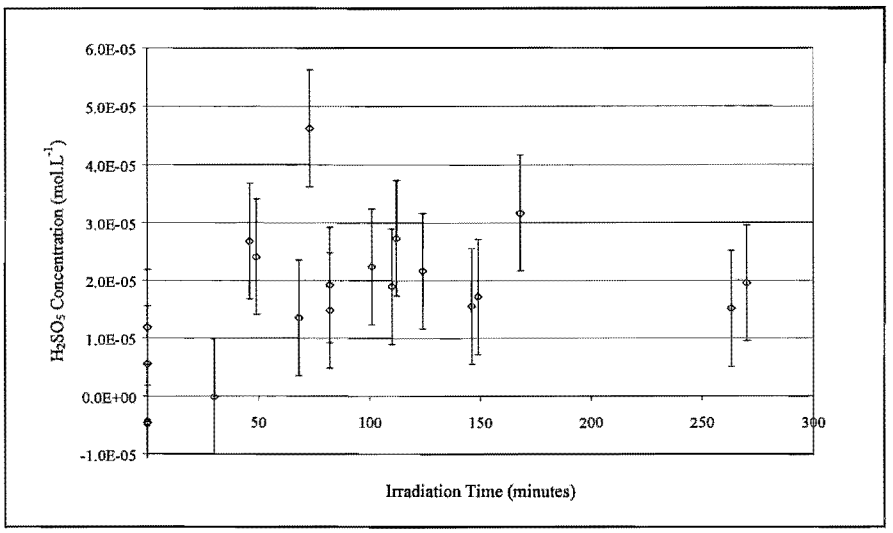

Figure 4.10 Concentration of H_2SO_5 formed during irradiation of 98wt% sulfuric

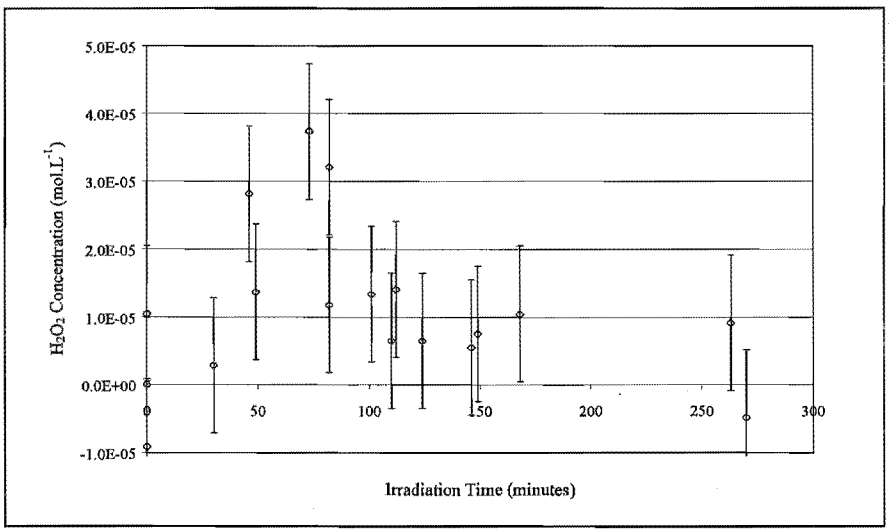

Figure 4.11 Concentration of H_2O_2 formed during irradiation of 98wt% sulfuric acid

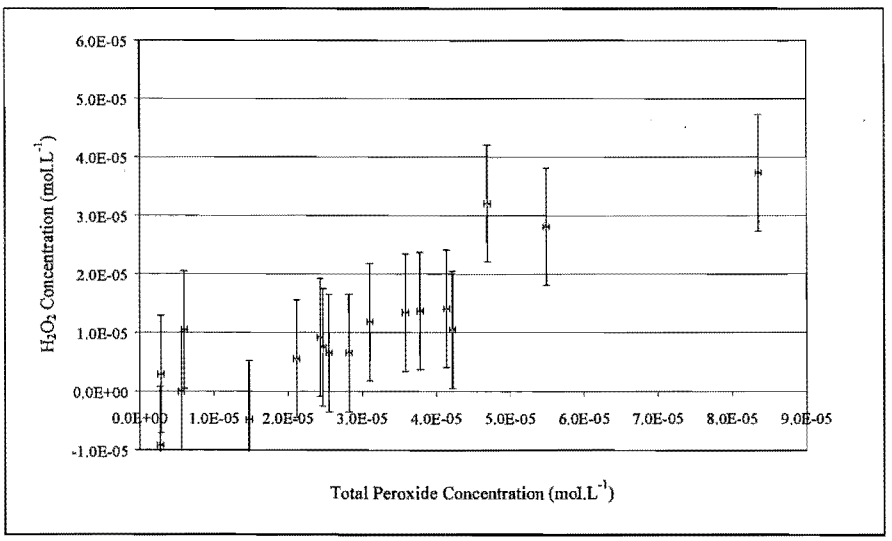

Figure 4.12 Correlation between $[H_2O_2]$ and total peroxide concentration

peroxide compounds. However, the results are a clear indication that long-lived, reactive, oxidising species are formed when concentrated sulfuric acid is irradiated with 178.3nm UV light.

The greatest limiting factor in this experiment was the iodine lamp light-source. The lamp overheated readily, resulting in the acid solution being heated (which would certainly decompose any H_2SO_5 present.) The lamp discharge was also prone to jumping out of the lamp area into the rest of the glassware, which required the microwave power supply to be shut off and restarted. Thus, the use of "irradiation time" as an indication of the extent of irradiation is tenuous. Furthermore, the output intensity of the iodine lamp output was unknown, and the only indication was an estimate of 1×10^{14} photons/s, based on Professor Phillips' previous experience with similar lamps. The geometry of the lamp made it difficult to measure the output intensity directly. If the results of the irradiation had been more successful, a chemical actinometer such as potassium ferrioxalate would have been used to quantify the resonance lamp intensity.

4.3.5 1933Å Irradiation of 98wt.% Sulfuric Acid Solutions with an ArF Excimer Laser

4.3.5.1 Introduction

The Lumonics EX-744 excimer laser that had been used as a source of 193nm light in earlier irradiation experiments was unavailable for use for a long period of time, after developing a fault in the high-voltage supply that could not be repaired in New Zealand. As soon as the laser was repaired, an apparatus was assembled for the irradiation of concentrated sulfuric acid solutions (Fig. 4.14).

The ArF laser has significant advantages over the I_2 resonance lamp used for the previous irradiation experiments, in that the power output can be easily and reproducibly controlled, the light intensity is much greater, and the solution is

unlikely to overheat. In addition, using the laser allows the results of the irradiation to be compared directly with the sulfuric acid aerosol irradiations described in Chapter 2.

4.3.5.2 Experimental

The acid sample to be irradiated was contained in a cup-shaped cell with a quartz window cemented to the top using Torr-seal high-vacuum epoxy and halocarbon wax, according to the method described in Chapter 2. 193nm light from the laser was directed downwards into the cell by a mirror with a UV-reflective coating. The cell was filled and emptied with a pipette through a Schott GL14 screw thread fitting on the side of the cup, which was blanked off during the photolysis.

The cell was connected into a gas flow system by Kontes o-ring joints on each side. These allowed the cell to be easily removed for washing. One side of the cell led to a

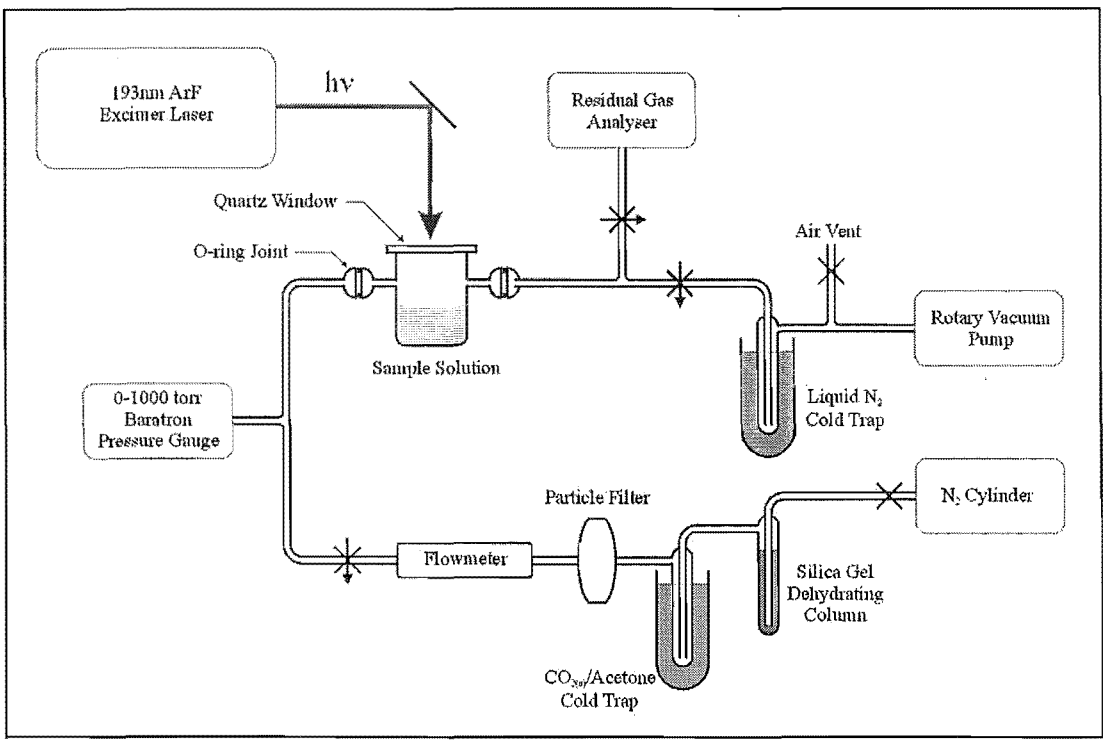

Figure 4.14 Experimental Apparatus for 193.3nm irradiation of H_2SO_4

gas supply, and the other to a mass spectrometer sampling port and a rotary vacuum pump. The gas used was oxygen-free nitrogen from BOC Gases, which was passed through a silica gel column, a dry ice/acetone cold trap and a particle filter before it reached the cell. This procedure removed particulates, water and any other condensable gases from the nitrogen supply. Downstream from the cell, the gas flow could be sampled with a MKS Quadrupole Residual Gas Analyser (mass spectrometer), to determine whether there were any reaction products that did not remain dissolved in the sulfuric acid. A throttling valve leading to the vacuum pump was used to regulate the system pressure.

Acid solution was introduced into the cell through the screw thread fitting using a pipette, taking care not to leave any acid on the fitting. The screw thread fitting was capped with a plastic blanking plug and a viton o-ring to seal the cell. The cell was placed under vacuum, and it was flushed with nitrogen to remove any atmospheric air. Photolysis runs were conducted under a flow of 50sccm of nitrogen, at a pressure of 3-5 torr.

4.3.5.3 Results

Samples of 98wt.% sulfuric acid were irradiated for up to 100 minutes, at a laser power of 6W. This corresponds to approximately 3.5×10^{22} irradiating photons, 10^4 times more than in the longest iodine lamp irradiations. After irradiation, samples were analysed for H_2O_2 and H_2SO_5 using the spectrophotometric titration method.

Results showed that the combined amount of H_2O_2 and H_2SO_5 formed during irradiation was $(3 \pm 10)\times10^{-6}$mol.L^{-1}. This is less than the effective lower detection limit of 1×10^{-5}M. It was concluded that if either peroxide was formed during the irradiation, the concentration was too low to be detected using the spectrophotometric titration method.

4.4 Ab Initio Calculations for Electronically Excited Sulfuric Acid

Since a photochemical reaction was observed at 178.3nm but not at 193.3nm, we considered it possible that sulfuric acid did not, in fact, absorb 193.3nm light as had previously been assumed. Experimental measurements of the far-UV absorbance spectrum of sulfuric acid showed that the short-wavelength absorbance began at progressively shorter wavelengths as the acid was purified (Section 4.1), but failed to determine the ultimate short-wavelength cut-off for chemically pure H_2SO_4.

The problem was discussed with Professor Laurie Butler of the University of Chicago, and as a result, her group undertook a theoretical study of spin-allowed electronic excitation of monomeric gas-phase sulfuric acid[9]. Ab initio calculations were run using Gaussian 94 software with a 6-31 G* basis set of atomic orbitals, and included configurational interactions for single electron excitations (CIS). The results of the calculations are summarised in Table 4.15. Typical errors for CIS calculations are ±1-2eV, and occasionally as much as ±3eV, which has been used as the maximum uncertainty for the current results.

Transitions to each of the first four excited electronic states have been qualitatively described as non-bonding → σ* (antibonding). The first excited state has the antibonding character localised on O – H (Fig. 4.16) while the second excited state has antibonding localised on both the O – H and S – O portions (Fig. 4.17).

Excited State	Transition Energy (eV)	Equivalent Photon Wavelength (nm)	Transition character
1	11.1775 ±3	110.92 (87.5-151.6)	non-bonding → σ* (O-H)
2	11.2592 ±3	110.12 (87.0-150.1)	non-bonding → σ* (O-H, S-O)
3	11.5916 ±3	106.96 (85.0-144.3)	non-bonding → σ* (O-H, S-O)
4	11.7782 ±3	105.27 (83.9-141.2)	non-bonding → σ* (O-H)

Figure 4.15 Excited state ab initio calculation results for H_2SO_4

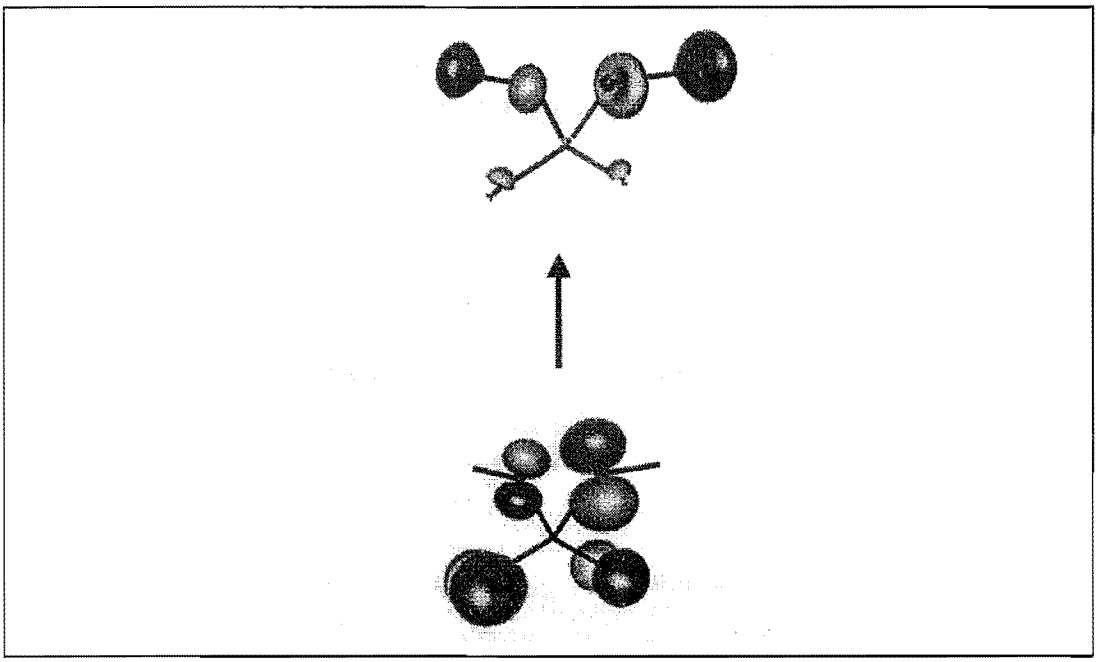

Figure 4.16 Visualisation of the strongest one-electron excitation contributing to the first excited state of H_2SO_4

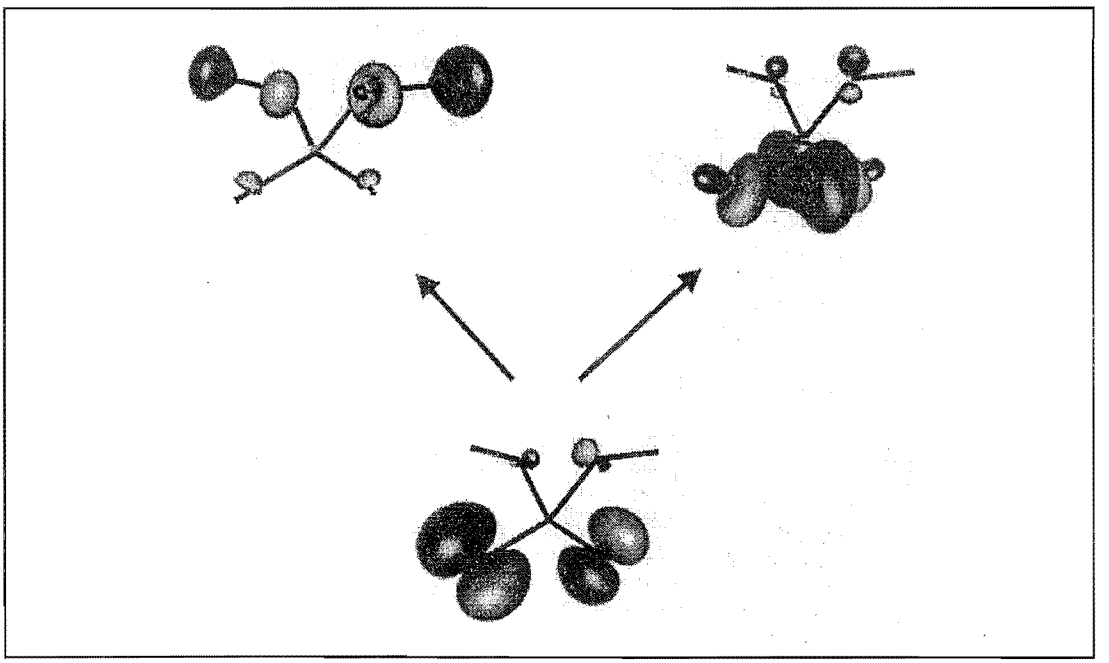

Figure 4.17 Visualisation of the two strongest one-electron excitations contributing to the second excited state of H_2SO_4

It is immediately apparent from these results that single-photon absorption via a spin-allowed transition cannot result in photochemistry in sulfuric acid vapour irradiated at either 178.3nm or 193.3nm. Spin-forbidden transitions, from the singlet ground state to a triplet excited state are observed in some systems, for instance gas-phase SO_2, but

require that the triplet state energy is close enough to the lowest singlet state to allow the two to mix. The calculated energy of the lowest singlet state in sulfuric acid is too high for a spin-mixed state to be accessible at 178.3 or 193.3nm.

The results from calculations on gas-phase sulfuric acid cannot be trivially or indiscriminately applied to the liquid phase. Like water, sulfuric acid liquid has extensive intermolecular interactions due to hydrogen bonding, and therefore condensed-phase calculations are required to fully predict the UV absorption of the liquid. However, it seems highly improbable that the absorption would be red-shifted enough for photochemistry to occur at either 178.3 or 193.3nm.

4.5 Discussion of the Photochemistry of Liquid Sulfuric Acid

Although ab initio calculations have indicated that sulfuric acid liquid is unlikely to absorb light at either 178.3 or 193.3nm, photochemical reactions have been observed when concentrated sulfuric acid is irradiated at both wavelengths. The final section of this chapter attempts to rationalise these conflicting observations.

4.5.1 Photochemistry Occurring during 1783Å Irradiation

In this case, the most likely source of the photochemical activity is trace impurities in the liquid sulfuric acid. AnalaR grade sulfuric acid was used, without further purification, in the series of experiments reported in Section 4.3. The manufacturers reported impurity levels in this grade of acid are given in Table 4.18.

Many of these species are likely to form complexes with H_2SO_4 that absorb at 178.3nm. For instance, Fe(III) dissolved in 98wt% sulfuric acid absorbs strongly at all wavelengths less than 400nm. Trace amounts of Fe, or other transition metals, are

NH_3	<3ppm	Fe	<0.5ppm	Residue after Ignition	<0.002%
As	<0.05ppm	NO_3^-	<0.3ppm	Substances reducing $KMnO_4(SO_2)$	<1ppm
Cl	<0.2ppm	Se	<5ppm		
Pb	<1ppm				

Table 4.18 Manufacturers Maximum Impurity Levels in AnalaR grade H_2SO_4

likely to be involved in initiating photochemical reactions when the solution is irradiated with 178.3nm light. A detailed investigation of the photochemistry of iron salts in concentrated sulfuric acid is described in Chapters 5 and 6.

4.5.2 Photochemistry Occurring in Sulfuric Acid Aerosols during 1933Å Irradiation

Absorption by trace contaminants cannot be used to explain away the photochemical reactions that were observed in the experiments described in Chapter 2. In these experiments, sulfuric acid aerosols were generated by the condensation of gas-phase H_2SO_4, which had been formed by the gas-phase reaction between H_2O and SO_3. This method did not allow any contamination by transition metals or other species likely to be photochemically active at 193.3nm.

Instead, it is proposed that the reactions observed in sulfuric acid aerosols are due to multiphoton absorption processes occurring within the droplets. Two-photon absorption is always a possibility during laser irradiation, even with an unfocussed beam, due to 'hot spots'. When the irradiated system contains aerosols, multi-photon absorption events are even more likely, due to the existence of morphology-dependent resonance modes (MDRs) in small droplets[10].

It has been found that when aerosols of a certain size and refractive index are irradiated, they are capable of absorbing laser light, even at wavelengths that are not absorbed by the bulk material. The effect is significant in that aerosols of "virtually all substances are susceptible to breakdown when illuminated by a sufficiently intense

laser beam"[11]. The key observation is that the breakdown is dependent on the laser's intensity, rather than the wavelength of the photons. Chang et. al. have described the processes leading to laser-induced breakdown in large (radius ca. 30μm – which is large by aerosol standards), transparent water droplets irradiated with visible light[12] - ie. at wavelengths where there is no optical absorption in the bulk medium.

The MDRs observed in aerosol droplets correspond to the solutions to the characteristic equations of the electromagnetic fields in the presence of a sphere. They can be visualised by imagining an incident light ray undergoing multiple internal reflections inside a spherical droplet. At a resonance, the ray makes an integral number of reflections and returns to its starting position in phase. The result is that the droplet is capable of internally focussing an incident beam, so that there are areas within the droplet that have an exceptionally high optical field intensity (Fig. 19). If the incident beam is intense enough, the droplet will absorb so much light that it becomes superheated and explodes, forming a plasma.

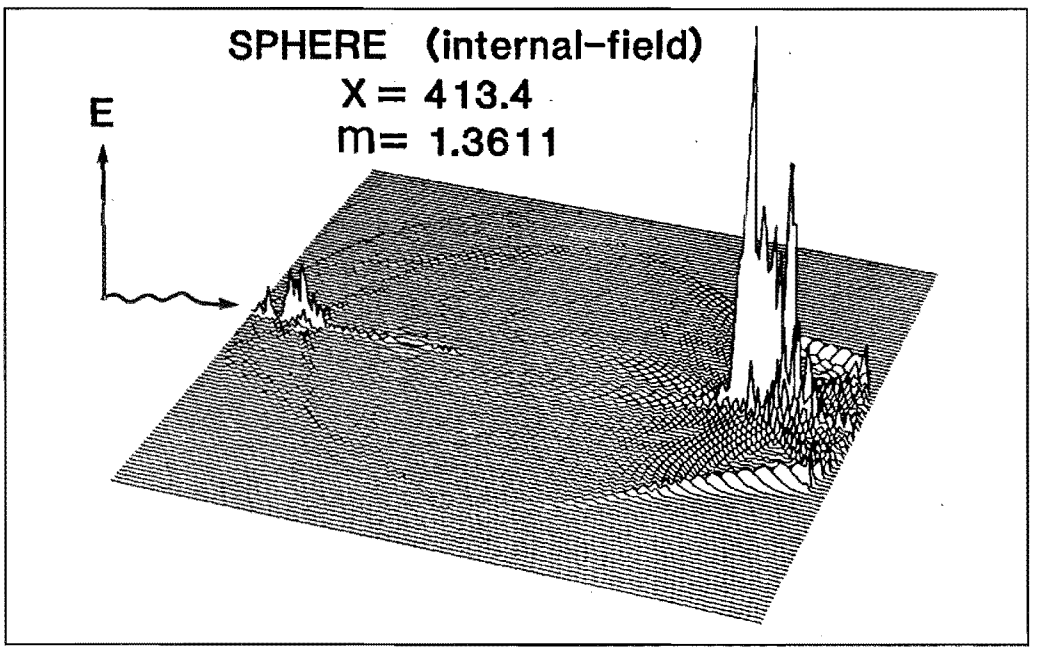

Figure 4.19 Internal intensity distribution in equatorial plane for light absorption by a spherical particle. The sphere is centred at the centre of the plot. The size and refractive index of the sphere do not lie on a resonance[10]. A similar distribution of internal intensity within irradiated sulfuric acid droplets is thought to be responsible for multi-photon absorption.

We believe that the same processes observed by Chang, et al in large water droplets are responsible for multiple-photon absorption in sulfuric acid aerosols, resulting in the photochemical reactions described in Chapter 2. The droplet properties required for internal focussing are less stringent than in Chang's work, since we only need sufficient light intensity to cause two-photon absorption, rather than to generate a plasma by dielectric breakdown. A similar process is likely to be responsible for the photoluminescence of laser-irradiated sulfuric acid aerosols reported by Lee et al.[13]

The decomposition products of excited H_2SO_4 following multiple photon absorption remain unknown. The first four excited states calculated by Butler et al. contain anti-bonding components that are localised on both O-H and S-O bonds, which makes either of (2.11) or (2.12) possible. However, there is likely to be sufficient energy available in the excited system for higher excited states to be accessed, and thus it is best to avoid speculation about the decomposition products.

$$H_2SO_4 + h\nu_{(\lambda=193nm)} \longrightarrow \cdot H + \cdot HSO_4 \qquad (2.11)$$

$$H_2SO_4 + h\nu_{(\lambda=193nm)} \longrightarrow \cdot O + \cdot H_2SO_3 \qquad (2.12)$$

Although this reaction is interesting, it is unable to cause photochemical reactions in the clouds of Venus, as the intensity of solar irradiation is insufficient to allow multi-photon absorption, even when the internal focussing effect is considered. In the next two chapters, a photochemical system that is more likely to be relevant to Venus is investigated – single photon absorption by iron salts dissolved in concentrated sulfuric acid.

Chapter 5

Photochemical Interconversion of Fe(II) and Fe(III) in Concentrated Sulfuric Acid

Chapter 5

Photochemical Interconversion of Fe(II) and Fe(III) in Concentrated Sulfuric Acid

5.1 Introduction

In the previous chapter, it was shown that the photochemical oxidation of CO in concentrated sulfuric acid aerosols described in Chapter 2 was best explained by multi-photon absorption processes occurring within the aerosol droplets. This was due to the partial focussing of the light within aerosol droplets, resulting in high local light intensities. While this is an interesting phenomenon, it is one, which is unlikely to occur in the Venusian clouds.

There may, however, be other photochemical reactions occurring within the Venusian cloud layers that contribute to the oxidation of CO. There is direct physical evidence for the presence of iron in the cloud layers, provided by XFS experiments aboard Veneras 12 and 14 and Vega 2. Many research groups have demonstrated the role that transition metals play in the redox chemistry and photochemistry of terrestrial aerosols. With this in mind, we thought to investigate the photochemical reactions of iron salts in concentrated sulfuric acid.

5.2 Preliminary Studies

5.2.1 Experimental

The experiment was performed using the cell and flow system described in Chapter 4.3.5.2, which had been designed for the irradiation of 98wt% sulfuric acid solutions with UV laser light (Fig. 5.1). The same procedure was used as before, except that Fe(II) salt was added to the acid samples before irradiation.

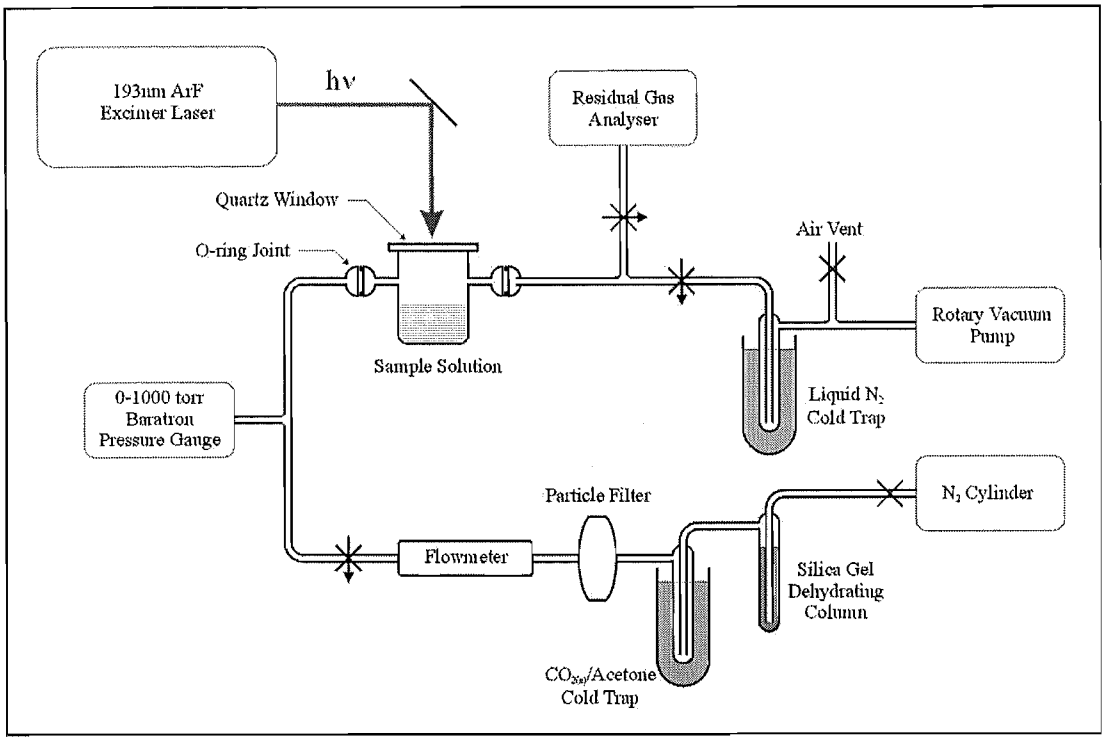

Figure 5.1 Experimental Apparatus for Fe(II)/H_2SO_4 Photolysis

Solutions of Fe(II) dissolved in sulfuric acid for photolysis were prepared from Analar grade ammonium ferrous sulfate and sulfuric acid. The concentration of the solutions ranged from (1.9- 12.6)×10^{-4}M. A fresh solution was prepared for each photolysis experiment, to minimise the concentration of Fe(III) formed due to the oxidation of the Fe(II) solution by atmospheric air.

In the experiments described in 4.3.5.2, the acid solution was irradiated once and then the whole sample was removed for analysis. In the current series of experiments, a single sample of Fe(II) solution was irradiated repeatedly, with a 2mL sample removed after each successive period of irradiation for analysis. When a sample was to be removed, the vacuum was shut off and the pressure allowed to increase to approximately 800 torr. The nitrogen flow was then shut off and the blanking plug unscrewed. Since there was a positive pressure inside the cell when the plug was removed, the amount of atmospheric air drawn into the cell was kept to a minimum. After the sample was removed using a 2mL pipette, the cell was resealed and flushed with nitrogen. In this manner, the solution in the cell could be photolysed and sampled repeatedly.

5.2.2 Detection of Reaction Products

Reaction products were detected by measuring the ultraviolet absorption spectrum of a sample of the irradiated acid. Spectra in the wavelength range 190-400nm were recorded using a GBC920 UV-VIS spectrophotometer. Before irradiation, the absorption spectrum of the solution contained at least two absorbing species. One of these had an absorbance centred on 315nm, and the other absorbance was centred on 260nm. In addition there was a small absorbance below 200nm, although it was often uncertain whether this was genuine or an instrumental artefact. The relative intensity of the 260nm and 315nm absorbances varied between solutions; this was the primary reason for assigning them to different species. In later experiments, sulfuric acid was thoroughly degassed before being used as a solvent (Section 5.3.5). Measurements of the UV spectrum of Fe(II) in thoroughly degassed sulfuric acid showed no sign of either the 260nm or the 315nm absorbance peak.

After irradiation, the absorbance spectrum of the irradiated solution contained three overlapping absorption peaks (Fig. 5.2a). The largest peak was centred on 264nm, with shoulders observed at 228nm and 300nm. The peak centred on 300nm obscured the absorbance at 315nm. This observation was complicated by the fact that the size of the 264nm peak varied widely between successive irradiation experiments. On some occasions, the 264nm peak was dominant (Fig.5.2b) and on others it was not detected at all (Fig 5.2c).

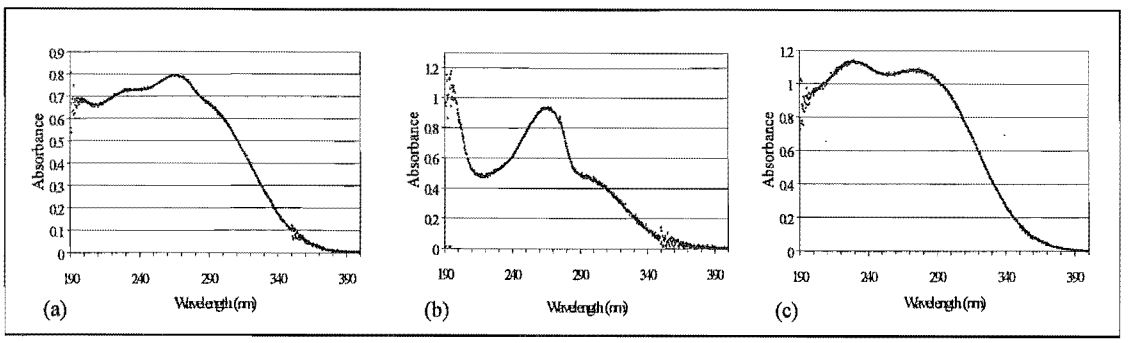

Figure 5.2 UV Absorption Spectra of Photolysis Products

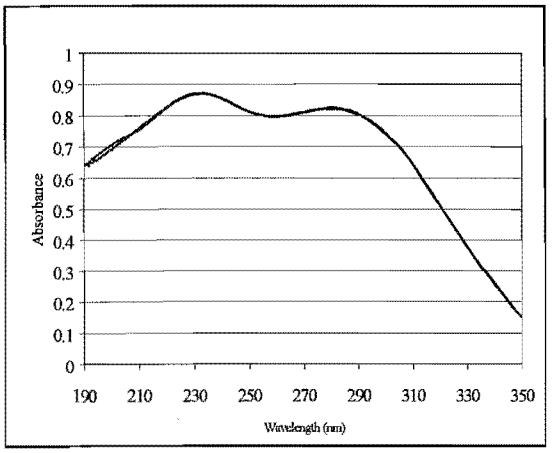

Figure 5.3 UV Spectrum of Fe(III) in H_2SO_4

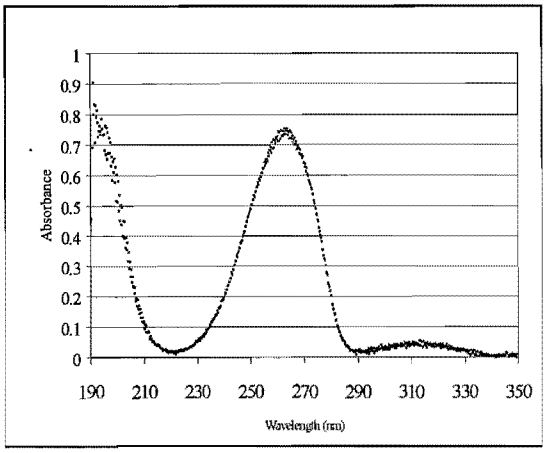

Figure 5.4 UV Spectrum of Unidentified Product

The peaks at 228nm and 300nm were identified as both belonging to Fe(III). The absorption spectrum of a solution of ammonium ferric sulfate dissolved in 98% sulfuric acid is shown in Fig.5.3. The absorption maxima occur at 230nm and 278nm[(i)]. When the Fe(III) absorption spectrum is scaled and subtracted from the spectrum of irradiated $Fe(II)_{(acid)}$ solution, the spectrum of the second photolysis product can be isolated (Fig. 5.4). This contains two absorption peaks, one centred on 264nm and the other below 200nm. In addition, the 315nm peak is once again observed. Comparison with spectra of the acid solution before photolysis indicates that the same species is present, at a lower concentration, in the solution before photolysis occurs.

5.2.3 Concentration of products after photolysis

The buildup of reaction products in the irradiated solution was studied by irradiating a sample of acid for a fixed period of time, withdrawing a sample for analysis, then repeating the photolysis. This cycle was repeated until all of the acid had been sampled. Up to six 2mL samples of photolysed acid could be taken, as well as a

---

[(i)] A systematic study of the absorption spectrum of Fe(III) in sulfuric acid solutions is found in Section 5.4.1.

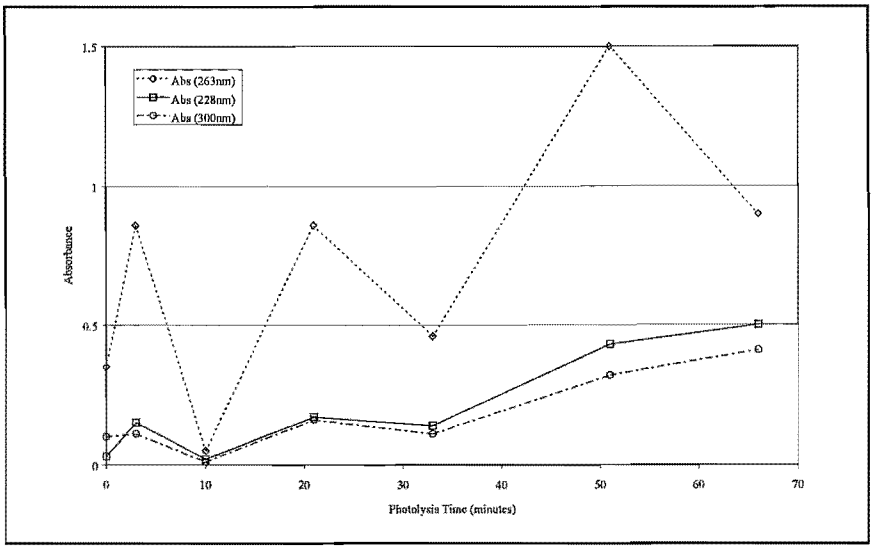

Figure 5.5 UV Photolysis of 2.0×10^{-4}M Fe(II) in H_2SO_4, Laser Power = 5.7W

sample before the photolysis began. The cell contained approximately 18mL of acid; however, the final 6mL could not easily be removed from the cell due to the angle of the port on the side of the cell. Fig. 5.5 shows the result of photolysing a solution of 2.0×10^{-4}M Fe(II) in sulfuric acid for two minute intervals at constant laser power, with samples withdrawn for analysis between each period of irradiation. While the absorbances at 228 and 300nm (mostly due to Fe(III)) showed a reasonably steady increase, the absorbance at 264nm varied widely.

It was discovered that the absorption at 264nm began to fade after irradiation stopped. Once this was recognised, the photolysis and sampling procedure was slightly modified. The laser was fired for two minutes and a sample withdrawn. The UV absorbance spectrum was measured as before, but with the spectrum measurement starting exactly 180s after the laser stopped firing. This period – 180s – was the shortest time in which a sample could be withdrawn from the cell and transferred into a UV cuvette. A second absorbance spectrum was measured after 390s. When the spectra were measured in this way, the 264nm peak was found to increase as a function of irradiation time also. Fig 5.6 shows the result of the photolysis of a 1.9×10^{-4}M Fe(II) solution over a period of 12 minutes, with nominally 1W of laser power.

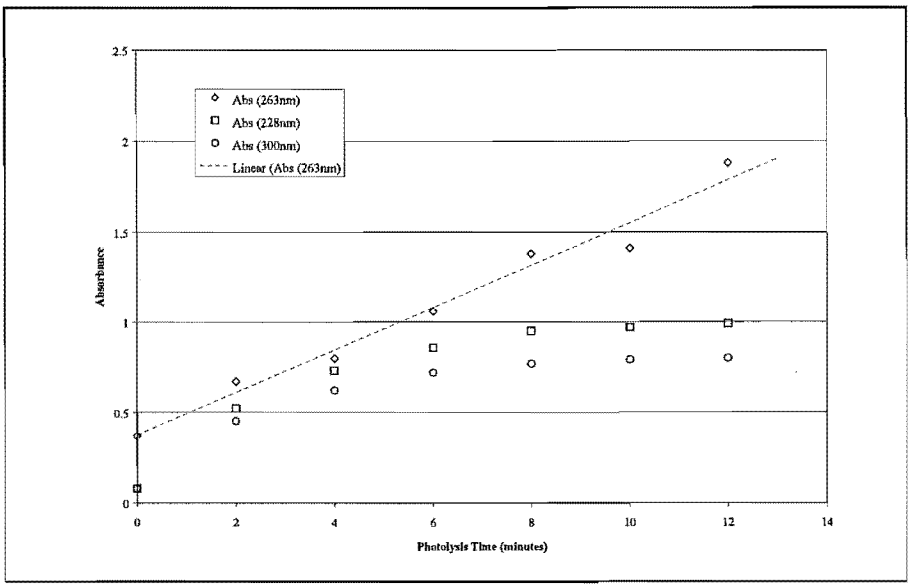

Figure 5.6 UV Photolysis of 1.9×10^{-4}M Fe(II) in H_2SO_4, Laser power = 1W

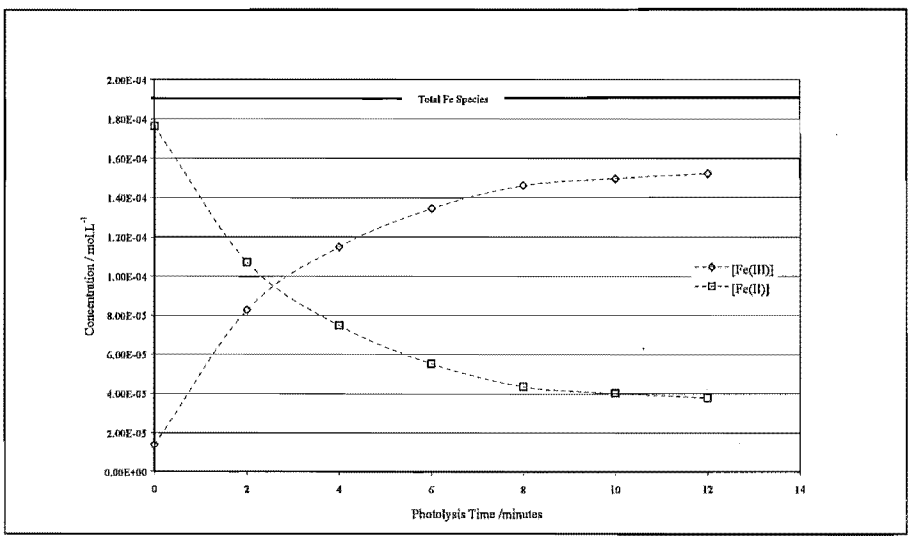

Figure 5.7 Concentration of Fe(II) and Fe(III) after successive periods of photolysis. Total Fe concentration = 1.9×10^{-4}M

Once the molar absorption coefficient of Fe(III) was determined, the results could be used to consider [Fe(II)] and [Fe(III)] as a function of photolysis time. Measurements showed $\varepsilon_{228} = 6500 mol.L^{-1}s^{-1}$ and $\varepsilon_{300} = 5260 mol.L^{-1}s^{-1}$.[(i)] If it is assumed that the absorbances at 228nm and 300nm are solely due to Fe(III), then the concentrations of Fe(II) and Fe(III) can be calculated as a function of photolysis time (Fig 5.9). It

[(i)] These extinction coefficients are taken from data collected and discussed in Section 5.3.1.

appears that the reaction did not result in full conversion of Fe(II) to Fe(III). For the photolysis shown in Fig. 5.7, the final ratio of Fe(III):Fe(II) was approximately 4:1.

5.2.4 Characteristics of the unidentified product

The species absorbing at <200nm and at 264nm, which I shall refer to as Product B, could not be conclusively identified. Solutions of various possible absorbers were prepared, and their UV-VIS absorption spectra measured. Fig. 5.8 shows the spectra for SO_2, H_2O_2, and $K_2S_2O_8$. None of these spectra match that of Product B. The nearest match is SO_2 – however, the SO_2 peak is centred on 280nm and the relative strengths of the <200nm and 280nm absorbances do not match Product B. The spectra of oxysulfur radicals $SO_3^{\cdot-}$, $SO_4^{\cdot-}$ and $SO_5^{\cdot-}$ have recently been reported[1] and are reproduced in Fig.5.9. Of these spectra, only $SO_5^{\cdot-}$ provides a possible match to the 264nm absorbance. These spectra are for oxysulfur radical ions in aqueous solution rather than acid. Obviously, there are acid-base equilibria between each of these anion radicals and their protonated counterparts, which are almost fully shifted towards the protonated forms in concentrated sulfuric acid. Polevoi[2] has reported that the positions of the absorbance maxima for the protonated species are slightly red-shifted, occurring at 275nm, 460nm, and 245nm for $HSO_3^{\cdot}$, $HSO_4^{\cdot}$ and $HSO_5^{\cdot}$ respectively.

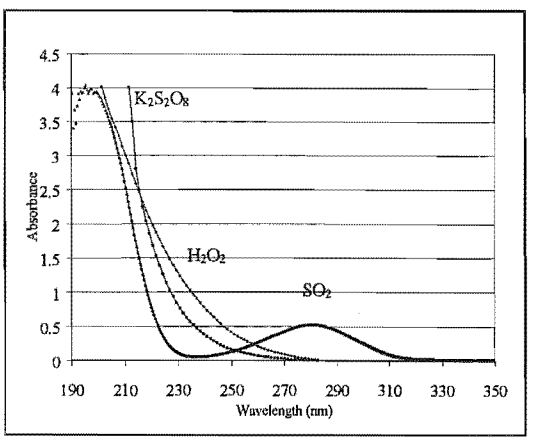

Figure 5.8 UV absorption spectra of SO_2, H_2O_2 and $K_2S_2O_8$ in 98% H_2SO_4

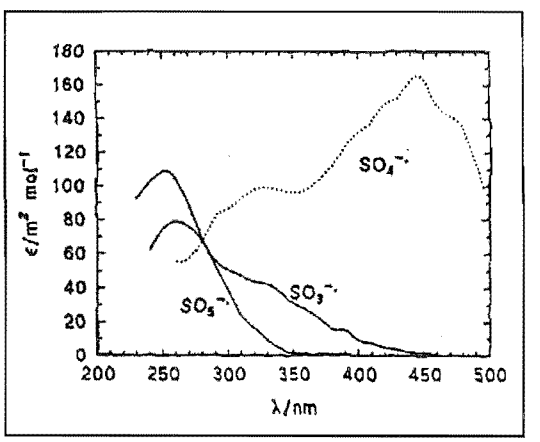

Figure 5.9 UV absorption spectra of $SO_3^{\cdot-}$, $SO_4^{\cdot-}$ and $SO_5^{\cdot-}$ in aqueous solution

The absorption spectrum due to Product B was observed to decrease after the photolysis ended. The first UV spectrum of the products was measured 180 seconds after photolysis. When the measurement was repeated 330 seconds later, the concentration of Product B had decreased by up to 25%. If the photolysed solution was left to stand overnight, its absorption spectrum was indistinguishable from the Fe(III) absorption spectrum.

The disappearance of the absorbance at 264nm allows for two possibilities. Either Product B is undergoing a chemical reaction, or else it is being removed by a physical process. If B were in equilibrium with a gaseous equivalent – for instance, if it were dissolved SO_2 – then the concentration would drop away once the sample was exposed to the atmosphere. In addition, it might be possible to detect the product using a mass spectrometer by sampling the gas above the solution during photolysis.

The photolysis experiment was performed while a small flow of oxygen-free nitrogen (normally 5sccm) was passed over the acid solution. A sample of this flow was diverted to an MKS quadrupole mass spectrometer. The mass spectrograph of the gas flow indicated that there were no major changes in the gas composition during photolysis. Particular attention was paid to charge/mass ratio 64, which is indicative of SO_2, but there was no observed increase. From the UV spectra and the failure to detect any SO_2 gas, it was concluded that Product B could not be SO_2.

As previously noted, Product B was observed during some photolysis experiments but not others. The appearance depended on two factors. The first, which has already been discussed, was that the concentration drops after the photolysis stops. Obviously, if there is a delay between the photolysis and measuring the UV spectrum of the sample, then B will not be detected. The second factor was the extent of degassing that the sample had undergone before irradiation. All of the acid samples were photolysed under a dry nitrogen atmosphere at a pressure of approximately 5 torr. However, some of the samples were photolysed almost immediately, while others were degassed by passing a flow of 50sccm of oxygen-free nitrogen through the cell at a pressure of 5 torr for up to thirty minutes before photolysis. When extensive degassing under N_2 had occurred, the 264nm peak did not occur. However,

when an acid sample was used immediately, the 264nm peak appeared strongly. This observation did not hold in every case.

5.2.5 Halt to Preliminary Studies

The experiments described in this section were stopped to allow necessary renovations to be made in the laboratory. During this period, all of the experimental apparatus was removed. As a result, the gas handling system had to be rebuilt before any further photolysis experiments could be carried out. This provided the opportunity to design a new experiment that would enable us to detect reaction products *in situ* and to monitor the progress of the reaction in greater detail.

5.3 Experimental Study of the Photochemical Interconversion of Fe(II) and Fe(III) in Concentrated Sulfuric Acid

5.3.1 Overview

A new experimental system was constructed to further explore the reaction. At the core of the system was a rectangular-faced cell, constructed of quartz, which allowed a liquid sample to be photolysed with laser light while the absorbance of the sample was simultaneously monitored using a probe beam at 90° to the laser beam. The apparatus included gas-handling facilities so that the sample could be degassed and photolysed in the presence of different gases. The apparatus is discussed here with reference to the irradiating light source, the product detection by absorbance measurement and the quartz cell and associated flow system.

5.3.2 Light Source for Photolysis

As in the previous experiments, a Lumonics EX-744 excimer laser was used as the light source for the photochemical reaction. In this case, the excimer complex was KrF, which emits light with a wavelength of 248nm. Earlier experiments had used 193nm light from the ArF excimer. The initial reason for the change in light source was that the laser had been converted to KrF operation for another experiment, and there was no evident advantage to switching back to ArF. Rather, KrF is preferable because it is more comparable with the light sources used in the HALIPP studies[3].

It was noted that the laser performance with KrF was much improved over ArF. When an excimer laser is operated, the gas fill degrades over a period of time until the power from the laser becomes insignificant. At this point, the old gas must be removed and replaced. With ArF as the laser excimer, a gas fill would typically last for 24 hours from the time of filling before it became unusable. Often, the power

output from the laser would drop significantly during the course of an experiment. This made it more difficult to obtain quantitative results for the experiment. In contrast, gas fills of KrF would routinely last for 10 days of operation. During this time, degradation of the gas would occur, but the drop in laser output power was slow enough to be ignored during an experiment. A further advantage was that using KrF resulted in less overall usage of fluorine gas, which can be difficult to source in New Zealand. Finally, the maximum laser power obtainable using KrF was 6W, compared with only 4W for the ArF excimer.

An excimer laser produces pulses of light, rather than a continuous output. When operated with KrF, the model we have been using is nominally capable of producing up to 50 pulses per second, with the energy per pulse ranging from 50-400mJ depending on the high voltage applied and the firing repetition rate. However, the gas lifetime is significantly shortened when too large a high voltage is used, so in practice a lower output energy is used. The output pulse energy and total laser power are monitored by an internal power meter and are displayed on the laser's remote control unit. The firing rate and high voltage can be varied during operation using the control unit, making it simple to achieve the desired output power.

In this experiment, the firing rate was set to 20 pulses per second and the high voltage adjusted to give an output energy of 100mJ per pulse. This resulted in a total irradiation power of 2.0W. To alter the irradiation power, the high voltage was adjusted while maintaining the same firing rate. The photon output from the laser was calculated to be 1.25×10^{18} photons.s^{-1}.W^{-1}.

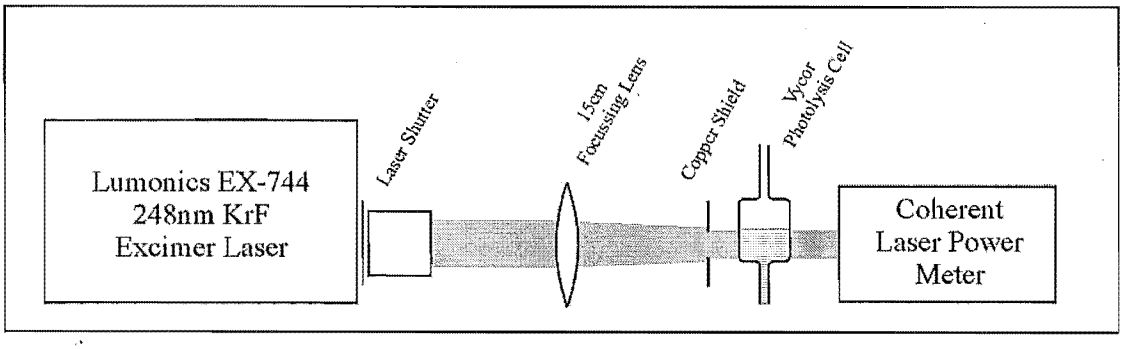

Figure 5.10 Laser Photolysis of Acid Solution

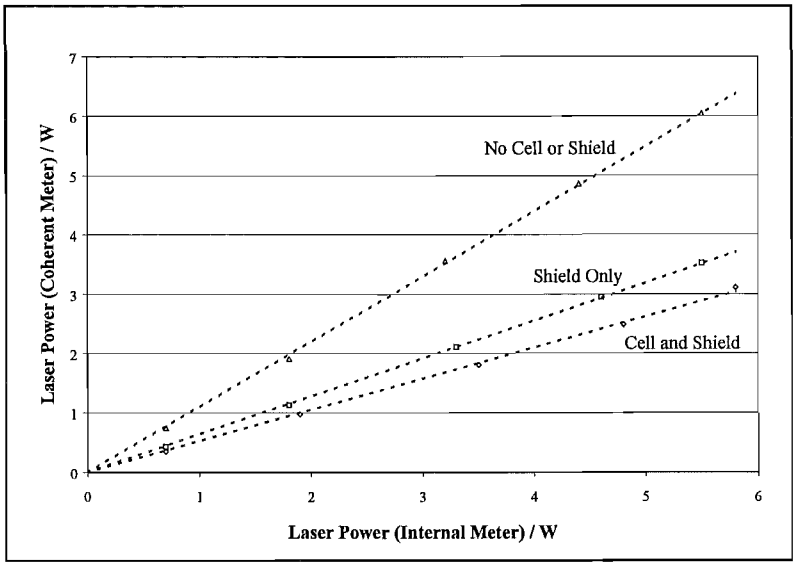

Figure 5.11 Correlation between laser power from internal meter and true laser power

The beam from the laser was focussed with a 15cm focussing lens placed approximately 20cm from the front window of the cell (Fig.5.10). The beam was not fully focussed, in order to reduce the likelihood of multi-photon processes occurring in the photolysed solution. The beam passed through an 18mm×10mm rectangular cutout in a screen of copper foil before reaching the cell. This screen was included in order to restrict the laser light to the portion of the cell required, limiting the effects of scattered laser light on the absorbance measurements for detecting reaction products. As the rectangular beam emitted by the laser is larger than this window, not all of the light emitted by the laser is incident on the cell. The amount of transmitted light was measured using a Coherent 100E laser power meter with the shield both in position and removed. The transmitted light intensity was found to be directly proportional to the laser output (Fig 5.11). It was found that the copper shield blocked 42% of the emitted light, and the cell removed a further 10%. All laser power measurements were adjusted to allow for this. In addition, the amount of transmitted light when the cell was empty was measured each time that experiments were performed.

Each time that the system was altered, the amount of laser light incident on the cell altered as well. The first major alteration occurred when the system for detecting the reaction products had to be replaced. After this, the transmitted light intensity was

found to be 31% of the reading from the laser's internal meter. Because of the practical difficulty of repositioning large pieces of equipment, this reduction in transmitted light was considered acceptable. The second discrepancy occurred following the laser breakdown in October 1999. After the laser was repaired, the transmitted power was found to be only 12% of the internal meter reading. This appears to have been due to the laser's internal power meter becoming miscalibrated during repairs, as it began to display abnormally high maximum power readings. The relationship between the internal power meter reading and the actual measured laser power remained linear.

The method for determining the amount of light absorbed by the solution during photolysis is described in Section 5.4.2.

An alternative light source for photolysis carried out at this wavelength is the 254nm line from a mercury lamp. This has the advantage of being cheap to operate and readily available. However, it was decided that since the intensity of the output from a mercury lamp was very low, and frequently unstable, it would make the measurement of reaction rates too difficult. In comparison, the output from the excimer laser is controlled by a microprocessor chip, and continually monitored by an internal power meter. This allows the output intensity to be selected and maintained to within ±3%. With the laser, it is possible to achieve acceptably reproducible measurements of the reaction rate, due to the consistent irradiation intensity. Thus, the laser was preferred over a mercury lamp as the light source for the photolysis.

5.3.3 Detection of Reaction Products

One of the main aims of this experiment was to monitor the changes in concentration of Fe(III) during laser photolysis. This was determined by measuring the absorbance of the sample *in situ* using a hydrogen lamp and photomultiplier mounted on an axis perpendicular to the laser beam, as shown in Fig. 5.12. A number of different instruments were used, due to either equipment failure (in the case of the light source) or the equipment being required for other experiments.

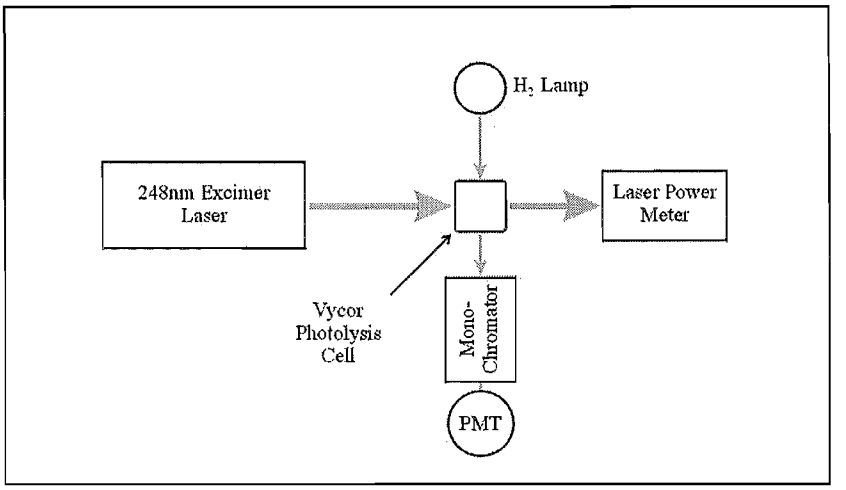

Figure 5.12 Simultaneous Photolysis and Monitoring in Quartz Cell

5.3.3.1 *Light Source, Monochromator and Photomultiplier*

Initially, an optical frame made by Applied PhotoPhysics was used. Components such as a broad-spectrum tungsten lamp, monochromator and photomultiplier were installed in factory-made housings and mounted on runners, which ensured that the system remained optically aligned. The F/3.4 grating monochromator had an operating range of 250 – 1000nm and was calibrated against the lines from a low pressure mercury lamp. The monochromatic light passed by the monochromator was detected and amplified with a 1P28 photomultiplier.

The Applied Photophysics equipment was required for another experiment, and was replaced with an independently mounted deuterium lamp, monochromator and photomultiplier housing. The alignment of the new system was a little more difficult, and it was easily misaligned, but there were no substantial changes required. The light source was initially an old deuterium lamp; when this became too unstable to use, it was replaced with the deuterium lamp from an unused VARIAN Techtron 635D UV-VIS spectrophotometer.

The new monochromator was a Spex Micromate grating monochromator with 1mm wide slits at the entrance and exit; the wavelength scale was again calibrated against a

low pressure mercury lamp. Light selected by the monochromator was detected with an EMI 9789QA photomultiplier tube (PMT) mounted at the exit port of the monochromator. The high voltage supply to the PMT was set so that the output current was approximately 1×10^{-6}A. Output current was measured using a Keithley 417 high-speed picoammeter, which provided a 0-3V DC output signal for a recording device.

5.3.3.2 Beam Conditioning and Alignment

The monochromator was used to select light at either 280nm – a known absorption maximum for Fe(III) – or at 248nm, which was very close to the KrF emission from the laser. 248nm was a preferable wavelength to monitor because Fe(III) absorbs strongly there, while SO_2 does not. In addition, measuring the sample's transmission at 248nm meant that a single set of measurements could provide information about the Fe(III) concentration and about the amount of laser light being absorbed by the sample during the photolysis. The monochromator was screened from the laser to prevent any stray light affecting the measurements. To test whether light from the laser was contributing the reading, the cell was filled with a non-absorbing solution of pure sulfuric acid and the laser fired. Under these conditions, there was no difference in the amount of 248nm light detected by the photomultiplier when the laser was operating.

Light from the deuterium lamp was focussed with a 15cm focussing lens placed between the lamp and the cell to maximise the intensity of the probe beam passing through the sample. A copper foil shield with a cutaway window was placed directly in front of the cell to limit the portion of the cell being probed and to prevent stray light from the deuterium lamp reaching the detector. An adjustable iris was placed between the cell and the monochromator, again to restrict the size of the beam.

Early results showed that the observed changes in transmission were dependent on the position in the cell that the probe beam passed through. In particular, the change in transmission began as soon as the laser started firing when the probe beam passed through the front of the cell, while there was a delay of 5-10 seconds before any

change was observed if the probe beam was positioned at the back of the cell. As a result of this, the positions of the iris and the focussing lens were swapped, so that the probe beam first passed through the iris, then the cell, and finally the lens before entering the detector. This arrangement limited the size of the probe beam entering the cell to a diameter of 2-3mm. The system was aligned so that the beam passed through the front portion of the cell, parallel to but without impinging on the front window. While this did not address the problem of inhomogeneity in the cell, it meant that the measurements were made on the portion of the sample undergoing the greatest photochemical change.

Attempts were made to provide a method of mixing the solution in the cell during photolysis, and thus homogenising the sample, but these were unsuccessful. It was not possible to mix the solution with a magnetic stirring flea because there was no clear space beneath the cell. Bubbling a small flow of inert gas through the solution provided good mixing, but could not be done during an experiment because it interfered with the transmission measurements.

5.3.3.3 Data Recording and Analysis

The current generated by the photomultiplier was recorded as a function of time for kinetic analysis. Initially, the results were recorded on a chart recorder driven by the DC output from the Keithley picoammeter. After each experiment, the measurements would be manually transferred to a personal computer for analysis using a spreadsheet program – in this case Microsoft Excel. As this was an extremely time-consuming procedure, a more efficient method of data recording was sought. An Advantech PCL-818L Analog-to-Digital card was installed in the computer, and the DC output from the picoammeter was recorded directly to computer as unformatted text, using software provided by Advantech and modified for our use by Professor Leon Phillips. This method was significantly faster than before, and allowed for more data points to be recorded, so the A-D card was used to record data from most of the experimental runs reported here.

5.3.4 Reaction Cell and Flow System

The solution to be photolysed was contained in a quartz reaction cell connected to a gas handling manifold as shown in Fig 5.13. This enclosed system allowed the reaction to be performed either under an inert atmosphere such as argon or nitrogen, or in contact with potentially reactive gases such as oxygen.

All gases used in the experiment were research grade and were supplied by BOC Gases. Before use, they were first passed through a saturator containing azeotropic sulfuric acid, to remove water and any other acid-soluble components. Gas flow was measured using an Airco flowmeter and the pressure in the system monitored with a MKS 0-1000torr baratron pressure transducer. The system was evacuated using a rotary vacuum pump protected with a liquid nitrogen cold trap.

The reaction cell was made of vycor silica glass from Corning, which has good UV transmission properties. The cell's internal dimensions were 21×21×28mm and it was constructed from rectangular pieces of 1mm thick vycor sheet. No adhesive was used

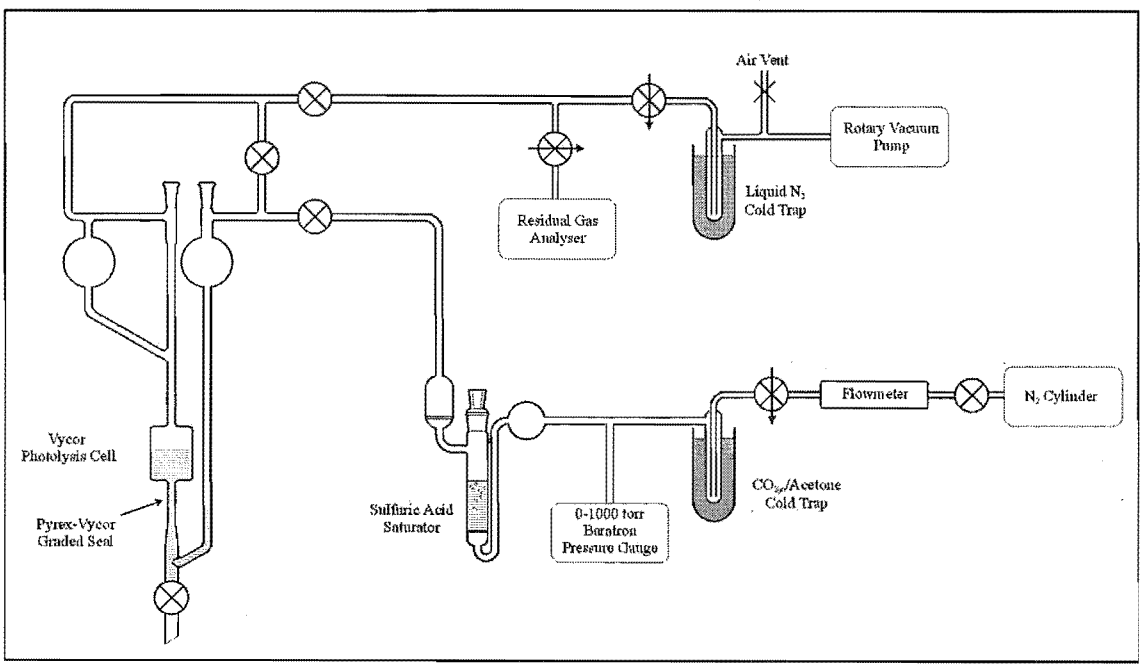

Figure 5.13 Liquid and gas handling system for photolysis experiment

The reaction cell was made of Vycor silica glass, which has good UV transmission properties. The cell's internal dimensions were 21×21×28mm and it was constructed from rectangular pieces of 1mm thick vycor sheet. No adhesive was used in the cell's construction; instead the vycor was fused together. The result of this was that no part of the cell was vulnerable to reaction with concentrated sulfuric acid; however there was a slight optical distortion near the edges of the cell which increased the amount of light scattering which occurred in the cell.

The cell was modified from an existing vessel, which meant that its dimensions were predetermined and could not be chosen to match the laser and hydrogen lamp beams. Consequently, the dimensions of the cell were larger than they needed to be, and there was considerable dead volume. This was overcome, in part, by not completely filling the cell with solution. Instead, it was filled to a depth of 13mm, which was marked on the outside of the cell to ensure consistency between experimental runs.

The reaction cell was connected to the rest of the flow system by two 4mm ID glass tubes mounted at the top and bottom of the cell. At the end of the lower tube was a turncock for draining the contents of the cell. Gas could be bubbled through the sample by means of a small nozzle projecting into the bottom tube, as shown in the diagram. This facility had been included in the cell design in order to provide mixing in the cell during irradiation, and also to allow a sample to be deoxygenated under a continual flow of nitrogen or argon. In practice it was found that the passage of bubbles through the cell during irradiation caused a violent instability in the intensity measurements of the probe beam, and it was not possible to simultaneously pass gas through the sample and monitor the build-up of reaction products. It was also unnecessary to deoxygenate sample solutions once they were in the cell, as the solutions were deoxygenated in bulk in a separate vessel, and they were introduced into the cell without exposure to air.

The total volume of the cell and glassware that was filled with sample solution during an experimental run was 9.5±0.3mL, of which the cell itself made up 5.7±0.2mL. Because of the high viscosity of the sulfuric acid, it was assumed that no mixing took place between solution the cell and in the bottom glass tubing.

The top tube connected the cell to the gas manifold and was topped with a B10 ground glass socket, through which sample solutions were introduced into the cell. No grease or wax was used on the joint in order to prevent contamination of the acid solutions. Initially the solutions were prepared in a volumetric flask, exposed to air while being loaded into the cell, and then degassed in situ. Due to the length of time required to displace oxygen from the sulfuric acid, this was a slow and inefficient procedure. In later experiments, solution was prepared and deoxygenated in bulk, and was introduced into the cell without exposure to atmospheric oxygen, as described in the next section.

5.3.5 Chemicals and Preparation of Solutions for Photolysis

Solutions for photolysis were prepared by dissolving small quantities of inorganic salts in deoxygenated azeotropic sulfuric acid, which is approximately 98wt.% H_2SO_4; the remaining 2 percent is predominantly water. Analar grade H_2SO_4 from either Fisons or BDH Laboratory Supplies was used as the solvent for all solutions. Before use, dissolved oxygen was removed from the acid by bubbling research grade argon through the acid while under vacuum for between 2-6 hours. A glass vessel was constructed for the purpose of deoxygenating samples of up to 250mL of acid, as shown in Fig 5.14. Typically, 250mL of acid would be deoxygenated, then transferred into volumetric flasks for storage. A little air was reintroduced

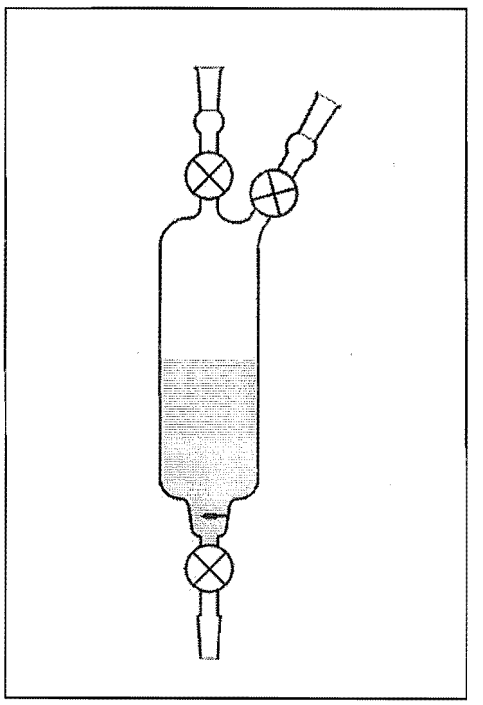

Figure 5.14 Degassing vessel.

during the transfer, but the effect of this was considered negligible due to the small surface area of acid that was exposed to air and the short period of time for which the acid was left in storage.

Fe(II) solutions were prepared from Analar grade ammonium ferrous sulfate ($(NH_4)_2SO_4.FeSO_4.6H_2O$), also known as Mohr salt, from BDH Laboratory Supplies. This was used in preference to ferrous sulfate, following the practice of Logan[4], as ferrous sulfate solutions contain an observable amount of Fe(III) after standing for a few hours, which was undesirable. The concentration of the solutions was determined by UV-VIS spectrophotometry. Since Fe(II) has no strong absorbances in the wavelength range 200-800nm, the sample was fully oxidised using Oxone®, a monoperoxysulfate compound produced by Aldrich Chemical Company[(i)], and the absorbance of the resulting Fe(III) was determined. This spectrophotometric method was used to determine concentrations because of relatively large uncertainties in weighing the small samples required.

Fe(III) solutions for the early experiments were prepared from reagent grade ferric sulfate from Hopkin & Williams, as no Analar grade ferric sulfate was available. This was found to be only sparingly soluble in concentrated sulfuric acid. Instead, solutions for the photochemical experiments, as well as those used to determine the extinction coefficient of Fe(III) in a 98% sulfuric acid solvent, were prepared from Analar grade ammonium ferrous sulfate which was fully oxidised using Oxone. Oxone was added sparingly to a solution of ferrous ammonium sulfate until the UV-VIS spectrum of a sample showed no further increase in the characteristic Fe(III) peaks and there was a slight rise in the absorbance at 200nm due to peroxymonosulfate from the Oxone[(ii)]. After the solution was left to stand, the peroxymonosulfate peak disappeared. At this point, the solution was assumed to contain Fe(III) with only trace amounts of Fe(II) and HSO_5^- present. The actual

---

[(i)] Aldrich does not state the composition of Oxone®; however, several groups have reported its composition to be ($2KHSO_5.KHSO_4.K_2SO_4$).

[(ii)] The experimentally determined absorption spectrum of Oxone, attributed to HSO_5^-, can be found in Section 5.4.1.

concentration of Fe(III) was determined by measuring the absorbance at 248nm, using the molar extinction coefficient determined in 5.4.1.

Solutions containing S(IV) were prepared from GP reagent grade sodium sulfite, again from BDH, as there was no Analar grade sodium sulfite available. The UV-VIS spectrum of the sodium sulfite solutions was identical to that obtained when SO_2 gas was bubbled through 98% sulfuric acid. Consequently, the same S(IV) species was assumed to be present in both solutions. Preparing the solutions from weighed samples of $NaSO_3$ was more convenient than bubbling sulfur dioxide gas through an acid solution – the concentration of S(IV) in the sample solution could be easily reproduced, and there was no risk of releasing noxious sulfur dioxide gas into the laboratory. The exact concentration of S(IV) in the solutions was determined by spectrophotometric measurement (Section 5.4.1).

All solutions were prepared using deoxygenated sulfuric acid in 100mL volumetric flasks. The SO_2 and Fe(II) solutions had a limited lifespan and any unused solution was discarded after one week, or if any Fe(III) was shown to be present by the UV-VIS spectrum. Samples for photolysis were made up immediately before use by mixing appropriate volumes of Fe(II) solution, Fe(III) solution, S(IV) solution and deoxygenated sulfuric acid, in the same vessel as was used for deoxygenation. Vacuum was applied and argon was bubbled through the solution for five minutes to purge atmospheric oxygen from the solution and vessel. Next, the vessel was filled with approximately 1000torr of argon and sealed. Finally it was fitted to the ground glass socket on the top of the reaction cell. Solution was transferred into the cell by partially evacuating the cell, then slowly opening the stopcock at the bottom of the storage vessel.

5.3.6 *Photolysis Experiments*

Photolysis experiments were conducted on 98wt% sulfuric acid solutions containing Fe(II), Fe(II) + SO_2, Fe(II) + CO, Fe(III), and Fe(II) + Fe(III) at various concentrations, to determine the effect that these species had on the photolysis rate.

The effect on the rate of varying the irradiating laser power was also determined for Fe(II) and Fe(III) solutions.

Although all of the solutions were prepared using degassed sulfuric acid, measurements made with a dissolved oxygen probe indicate that the solutions contained a residual concentration of dissolved oxygen of $6\text{-}9\times10^{-5}$M. (Section 5.4.11) Experiments were performed where additional oxygen was added to the solution by bubbling O_2 gas through the degassed acid, before any other chemicals were added. The effect of this on the reaction rate varied widely – from making no measurable difference, to increasing the initial rate tenfold. No reproducible effect was observed, and consequently the experimental results for the effect of oxygen on the reaction rate are not discussed in this chapter. Instead, the role of oxygen in the reaction was probed by measuring the concentration of dissolved oxygen before and after photolysis. Unfortunately, the instrument used for this measurement was not available until after the reaction rate experiments were completed, so it was not possible to perform both experiments simultaneously.

5.3.7 Dissolved Oxygen Measurements

Other than the concentration of Fe species, one of the parameters that we were particularly interested in was the concentration of dissolved oxygen in the photolysed acid solution, as this would be important in any mechanism that was proposed for the reaction. Studies of photochemical oxidation reactions in terrestrial aerosols, most notably the photochemical oxidation of SO_2 to H_2SO_4 in water aerosols, have shown dissolved O_2 to be a vital part of the reaction cycle. On Venus, the atmosphere is reported to contain a very small proportion of O_2. Therefore, the role of dissolved oxygen is important when assessing the contribution of this reaction to the atmospheric chemistry of Venus.

5.3.7.1 Principles of Operation of a Dissolved Oxygen Electrochemical Probe

A dissolved oxygen probe was available for the later stages of this experiment. This is an electrochemical probe that is specifically designed for measuring the concentration of dissolved oxygen in a solution. The probe was a DO-166-MT micro probe made by Lazar Research Laboratories. Unlike many commercially available dissolved oxygen probes, the DO-166 does not require the sample solution to be in direct contact with the electrodes. This meant that it could potentially be used in concentrated sulfuric acid solutions.

The DO probe consists of a galvanic oxygen electrode assembly covered with a semi-permeable fluorocarbon polymer membrane (Fig 5.15). This membrane permits the passage of dioxygen, but not other dissolved species or suspended particles that might interfere with the measurement. The electrodes are surrounded by a proprietary solution, provided by the instrument's manufacturer, which serves to maintain a constant ionic strength. Thus, the probe can be used to measure the amount of dissolved oxygen in sample solutions where the ionic strength is unknown or variable.

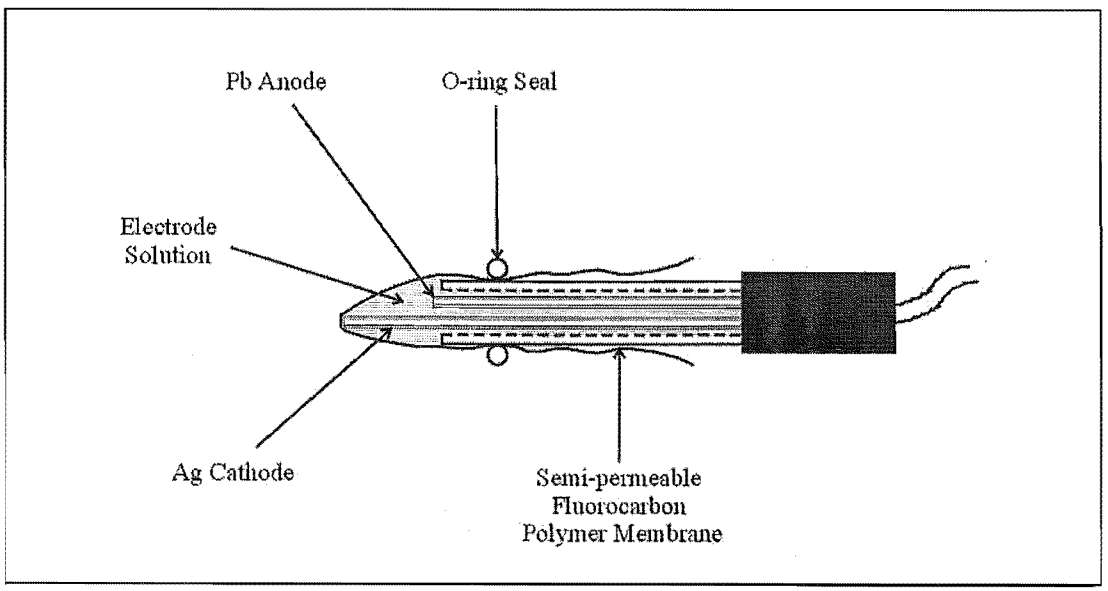

Figure 5.15 DO-166 MT Dissolved Oxygen Probe

When the DO probe is immersed in a sample solution, oxygen from the sample diffuses through the fluorocarbon membrane and into the electrode compartment. This contains two electrodes – a lead anode and a silver cathode, where dioxygen is reduced to hydroxide ions. The current generated by this reaction is amplified and converted into a 0-2V output signal which can be monitored using either a voltmeter or a chart recorder. The output was directly proportional to the concentration of dioxygen present in solution.

The meter was calibrated at two points – zero oxygen, and oxygen-saturated distilled water. An aqueous solution containing zero oxygen was prepared by adding 16g/L of sodium bisulfite to distilled water. Bisulfite reacts rapidly with any dissolved oxygen according to (5.1), leaving an effective concentration of $[O_2] = 0$:

$$HSO_3^- + O_2 \longrightarrow HSO_4^- + H_2O \qquad (5.1)$$

The second calibration point was determined using tables of dissolved oxygen concentration in air-saturated distilled water as a function of temperature and atmospheric pressure, supplied by the manufacturer of the probe. It was noted that the calibration was temperature dependent, as the temperature influenced the rate of electrochemical reaction at the electrodes, as well as the amount of oxygen dissolved in the saturated sample. All measurements were taken at ambient room temperature, which was maintained at 22°C by air conditioning. The temperature was measured when the calibration was performed, and it was assumed that no temperature changes occurred during measurement, although the temperature did vary by up to ±2°C from one day to the next.

The zero-oxygen calibration was checked weekly, and was found to be stable. The second calibration needed to be performed daily. The electrolyte solution was drained and the electrodes cleaned at the end of each day's operation, which affected the calibration.

5.3.7.2 Use of the DO Probe in Concentrated H_2SO_4

The DO probe was designed for use in aqueous solutions; however, we required a measurement of the concentration of dissolved oxygen in azeotropic sulfuric acid. Most electrochemical probes could not be used in this liquid, due to reaction between the acid and metal electrodes. However, the design of the Lazar DO probe meant that no acid would come into direct contact with the electrodes, and thus there was a possibility that the instrument could be used.

In previous experiments, we had satisfied ourselves that teflon – another fluorocarbon polymer – was unreactive in concentrated sulfuric acid. The fluorocarbon polymer membrane that encloses the electrode compartment was tested by immersion in 98% sulfuric acid for 24 hours, with no visible damage or discolouration of either the membrane or the acid. As the membrane covered the lower 3cm of the probe, it was possible to immerse the probe in a sample of acid without harm.

The second danger was that the semi-permeable membrane – which was intended to allow O_2 to pass through but to exclude other dissolved species that may affect the electrode reaction – would allow H_2SO_4 to enter the electrode compartment. On the basis of the relative sizes of the species, it was thought that H_2SO_4 would be unlikely to pass through the membrane. As no excessive corrosion was noted on the electrodes or the plastic electrode housing, it was assumed that sulfuric acid was not entering the electrode compartment.

The calibration of the DO meter was found to remain accurate when the DO probe was transferred from aqueous solutions to sulfuric acid, and then returned to aqueous solution. This indicated that there was no immediate problem with making measurements in sulfuric acid. One difficulty that did occur when alternating between samples was that it was difficult to completely dry the outside of the membrane, and so there was an increase of temperature as the acid and water mixed. This led to a small, random error in the measurements.

It was found that the measurements were incorrect when the same electrode solution was used for more than one day, whereas the manufacturer had suggested that the solution should only need to be changed after 2-3 weeks. In addition, there was a noticeable loss of liquid from the electrode compartment. We believe that water from the solution surrounding the electrodes was being drawn away through the membrane by the hydroscopic sulfuric acid, altering the ionic strength of the electrode solution and causing an error in the readings. At the end of each day's operation, the membrane was removed and the electrodes were thoroughly washed with distilled water. The membrane was replaced, the compartment refilled with electrolyte solution and the probe recalibrated before use the following day.

The greatest obstacle to using the DO meter in concentrated sulfuric acid was that the response time was much slower than for measuring aqueous solutions. The manufacturer's specifications claim that the response time at 25°C is 12s for 90% of the reading. We found that, in aqueous solution, the signal from the probe did not stabilise until 30s had passed. In sulfuric acid, at least 120s – and often longer – was needed before the signal became steady. For typical measurements, the probe was left for 30 minutes before the reading was made. On many occasions, the probe reading had not stabilised, even after this prolonged period. In this case, the measurement was treated with caution. The slow responses were possibly due to the high viscosity of sulfuric acid, leading to slow diffusion of oxygen into the electrode compartment from the sample. In order to observe the changes in the probe signal, the output voltage from the amplifier was used to drive a chart recorder. This visual record of the probe signal enabled us to determine when the probe signal had stabilised.

Finally, there remained some uncertainty as to the quantitative validity of the numerical measurements from the DO probe when used in sulfuric acid instead of water. Regardless of whether the numerical values for the amount of dissolved oxygen are correct, the probe results are still useful for determining relative changes in the amount of oxygen present as a result of photolysis.

5.3.7.3 Measurements of Dissolved Oxygen in Photolysed Solutions

It was initially intended that measurements of the dissolved oxygen concentration could be made *in situ* while a sample of sulfuric acid containing dissolved salts was irradiated, to give continuous data on the fate of oxygen during the reaction. However, this was not possible, due to the slow response time of the DO probe. Instead, measurements of the amount of dissolved oxygen before and after photolysis were compared.

Measurements were made with approximately 10ml of acid solution in a small beaker. The DO probe was inserted and clamped in position so that the end of the probe was immersed in acid and about 1mm from the bottom of the beaker. The beaker was covered with a piece of plastic film, and briefly flushed with nitrogen to reduce the effect of atmospheric oxygen being dissolved during the measurement. Contents of the beaker were swirled around periodically to prevent a false reading due to oxygen depletion near the electrode.

After the dissolved oxygen was measured, the sample was transferred to the photolysis cell, placed under an argon atmosphere, and photolysed at 248nm for between 20 and 110 minutes. The Fe(III) concentration was monitored during the photolysis using the equipment previously described. After this, the sample was drained into another small beaker and the amount of dissolved oxygen was again measured.

Not all of the acid sample was affected by the photolysis because the full volume of acid was not in the beam path of the laser. The total volume of acid used to fill the reaction cell was 9.5mL, but only 5.7mL of this was actually irradiated. Thus, the change in dissolved oxygen in the irradiated portion of the solution (DO_i) could be related to the measured change in the whole sample (DO_s) by:

$$DO_i = (9.5/5.7)DO_s$$

It was assumed that oxygen was only removed from the portion of the sample that was directly irradiated, and that there was no mixing of the sample during irradiation.

5.4 Experimental Results

5.4.1 Molar Absorption Coefficients for Fe(II), Fe(III) and SO_2 in H_2SO_4

The first experimental task was to measure molar absorption coefficients for Fe(II), Fe(III) and SO2 in concentrated sulfuric acid. The UV absorption spectra for these species are, of course, widely reported for aqueous solutions, but we are unaware of spectra for them in concentrated sulfuric acid. Molar absorption coefficients for these species were used experimentally to determine their concentration in acid solutions for photolysis.

For most chemical species, the amount of incident light absorbed is related to the concentration of the absorbing species by the Beer-Lambert Law:

$$\log_{10}\left(\frac{I_0}{I}\right) = \varepsilon c l \tag{5.2}$$

where I_0 is the initial intensity of the light, I is the final intensity of the light, l (cm) is the pathlength of light through the sample, c ($mol.L^{-1}$) is the concentration of the absorbing species and ε ($L.mol^{-1}cm^{-1}$) is the molar absorption coefficient, which depends on the species and the wavelength of the incident light.

The UV absorption spectrum of Fe(III) dissolved in azeotropic sulfuric acid is shown in Fig. 5.16. Molar extinction coefficients were obtained from measurements on 13 independent solutions of Fe(III) ranging from $(1.4 - 4.6)\times10^{-4}$M. 5×10^{-4}M was the highest concentration that could be measured; beyond this, the absorbance was outside the working range of the spectrophotometer. A plot showing the determination of the molar extinction coefficient at 248nm is shown in Fig. 5.17. All spectra were recorded in a 1cm quartz cell with a GBC UV/VIS 920 UV-Visible spectrophotometer.

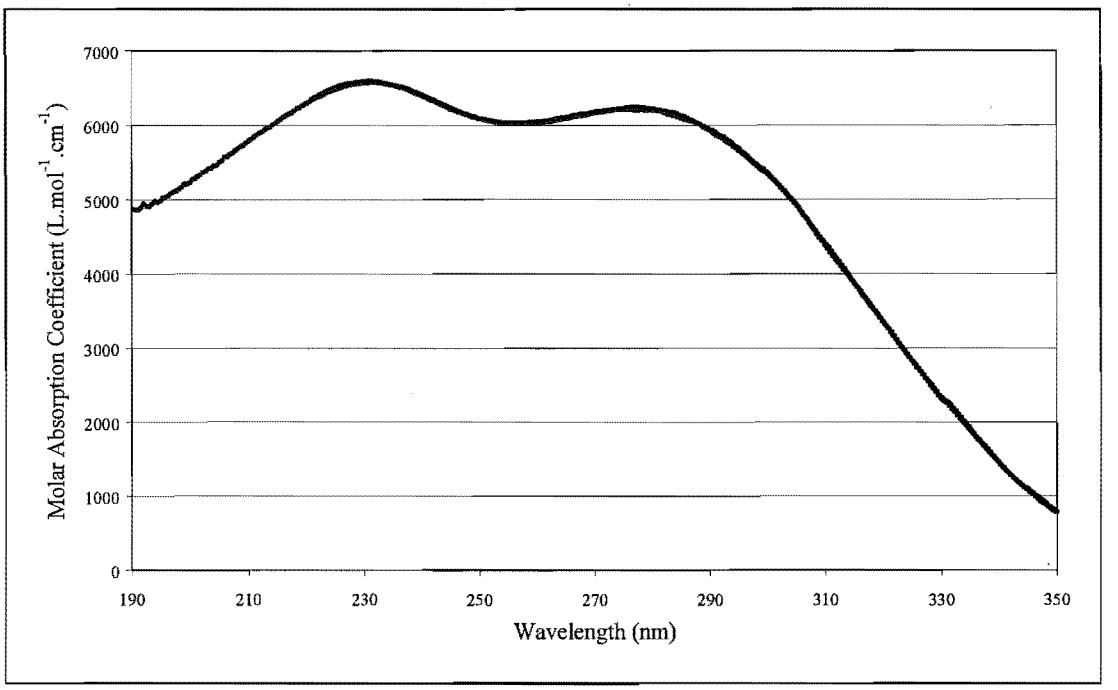

Figure 5.16 UV absorption Spectrum of Fe(III) in 98wt% H_2SO_4

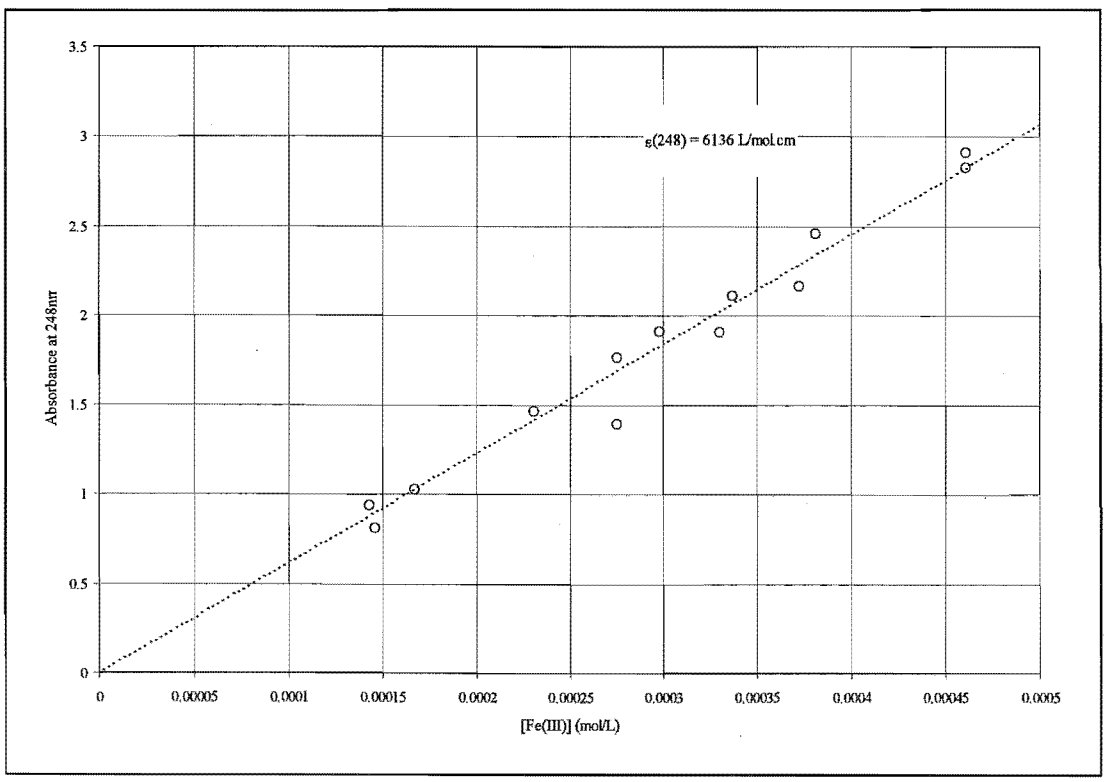

Figure 5.17 Determination of ε_{248nm} for Fe(III) in 98wt% H_2SO_4

Ferric sulfate is only sparingly soluble in concentrated sulfuric acid, so the standard solutions were prepared from Analar grade ammonium ferrous sulfate, which was fully oxidised by adding crystals of the peroxymonosulfate compound Oxone. Fe(II) was rapidly oxidised by HSO_5^-, and it was assumed that the reaction went to completion. The absorption spectrum of HSO_5^- dissolved in H_2SO_4 is shown in Fig. 5.18. As with other peroxy- compounds, the main feature is a strong absorbance at short wavelengths. The absorbance is slightly weaker than that of HSO_5^- in aqueous solution.[5] Oxone was added to the ammonium ferrous sulfate solutions until this peroxide absorbance was observed in the UV-VIS spectrum; at this point, all of the Fe(II) had been oxidised to Fe(III).

UV absorption spectra were measured for Fe(II) and SO_2, essentially following the same procedure as for Fe(III) solutions. The absorption spectrum of Fe(II) in sulfuric acid is very weak, and in practice is totally obscured by absorption due to a trace of Fe(III) in the solutions. The SO_2 spectrum contains absorption maxima at 200nm and 280nm, overlapping the Fe(III) absorption. In the absence of Fe(III), the concentration of SO_2 solutions was determined by measuring the absorbance at 280nm, using $\varepsilon_{280} = 191 L.mol^{-1}cm^{-1}$.

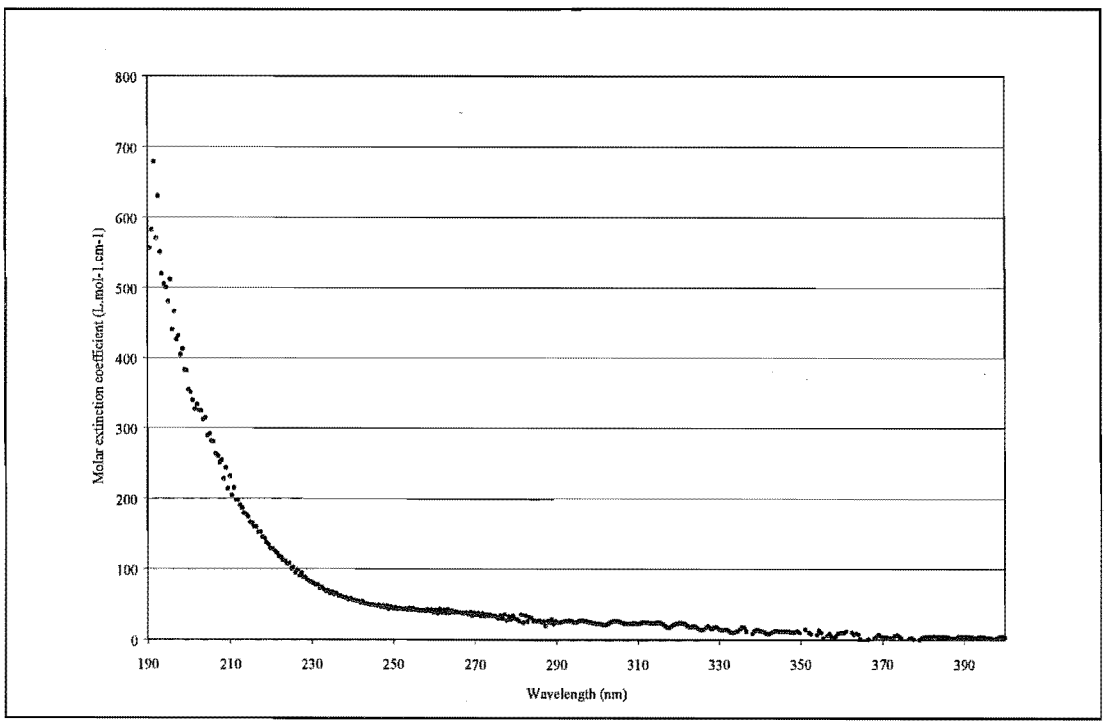

Figure 5.18 UV absorption spectrum of HSO_5^- in 98wt% H_2SO_4

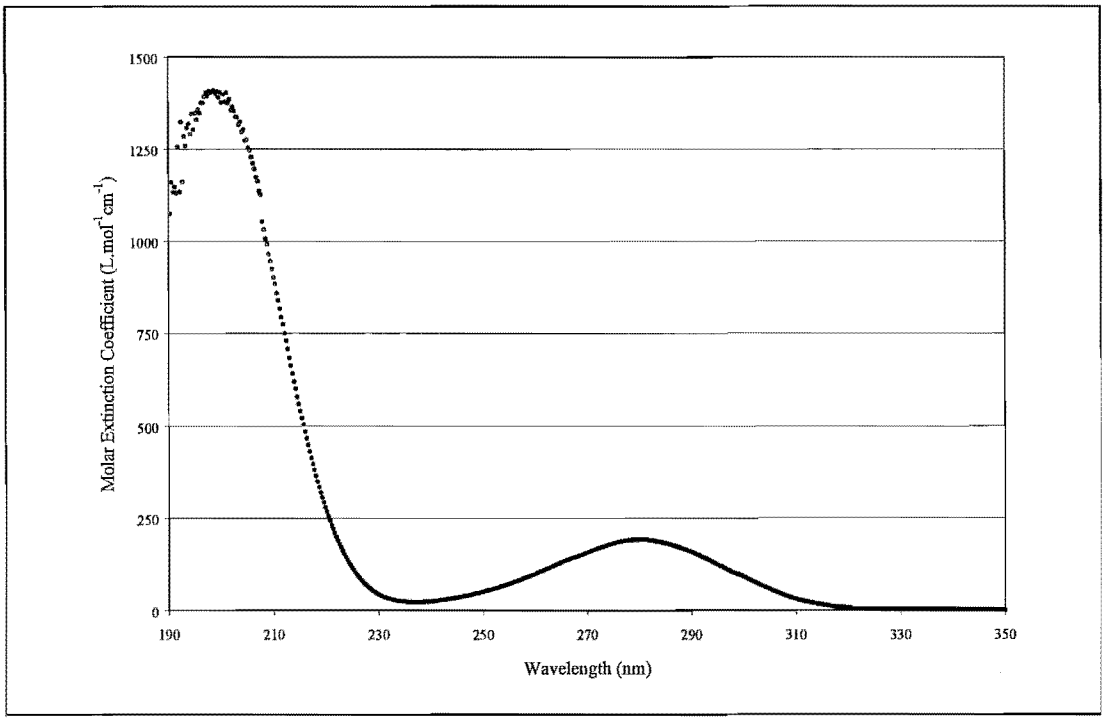

Figure 5.19 UV absorption spectrum of SO_2 in 98wt% H_2SO_4

In addition to spectra of Fe(III) dissolved in azeotropic sulfuric acid, the absorption spectra of Fe(III) in sulfuric acid – water solutions ranging from 20-98 wt.% have been measured. At each acid concentration, the absorption spectrum of six different Fe(III) solutions was measured and extinction coefficients were determined. A selection of this data is presented graphically in Fig. 5.20, showing the increase in absorption in more concentrated acid solutions. Fig. 5.21 shows the extinction coefficients at the absorption maxima as a function of acid concentration, and Fig. 5.22 shows the change in absorption maxima wavelength.

The maximum for both absorbance peaks occurs at around 85wt% of sulfuric acid, which corresponds to a mole fraction of 0.5. As the maximum concentration of HSO_4^- also occurs near this composition, the result suggests that the absorbing species involves HSO_4^- as well as Fe(III). The identity of the absorbing species is discussed more fully in Chapter 6.2.2.

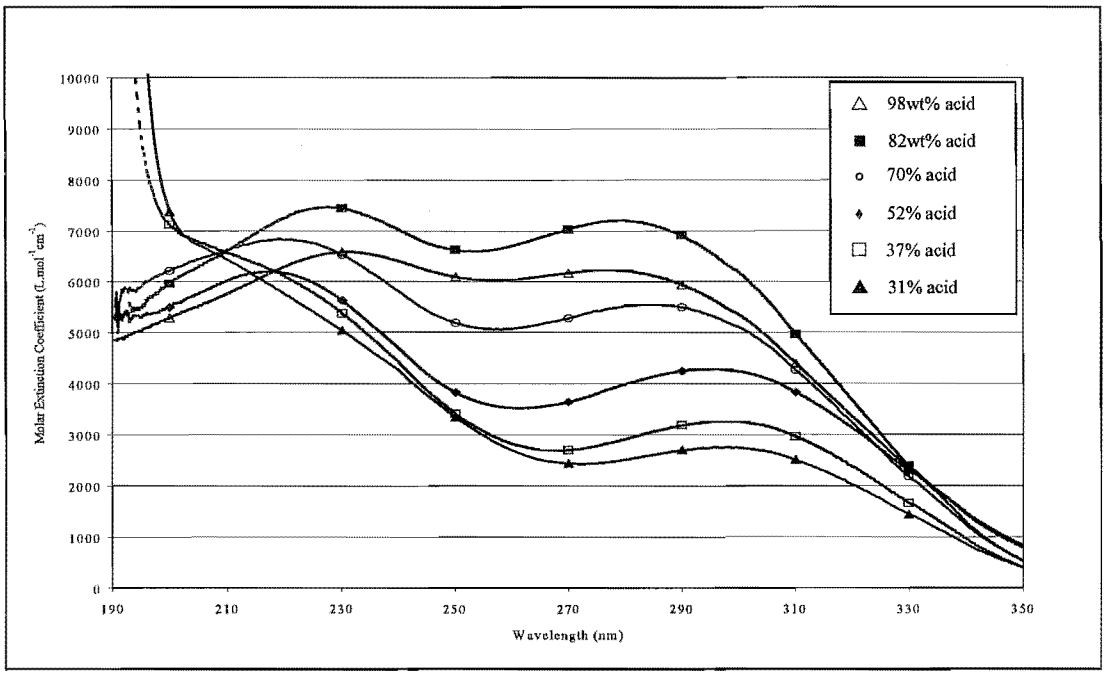

Figure 5.20 UV absorption spectrum for Fe(III) in various concentrations of H_2SO_4

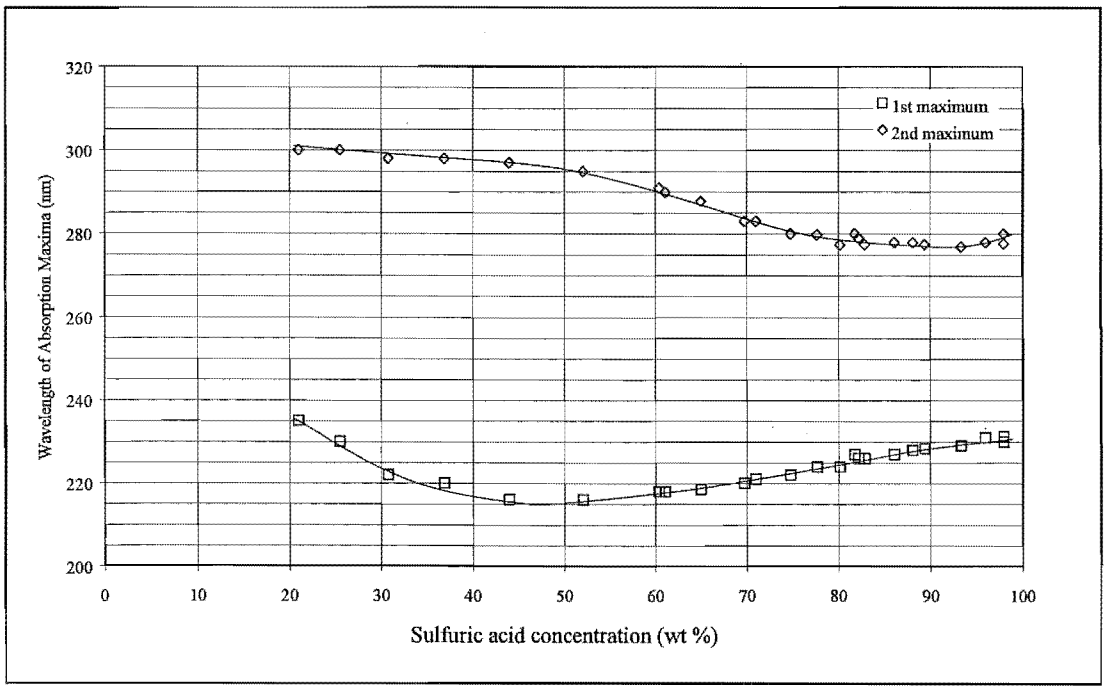

Figure 5.21 Absorption Maxima for Fe(III) in Sulfuric Acid solutions, as a function of acid concentration

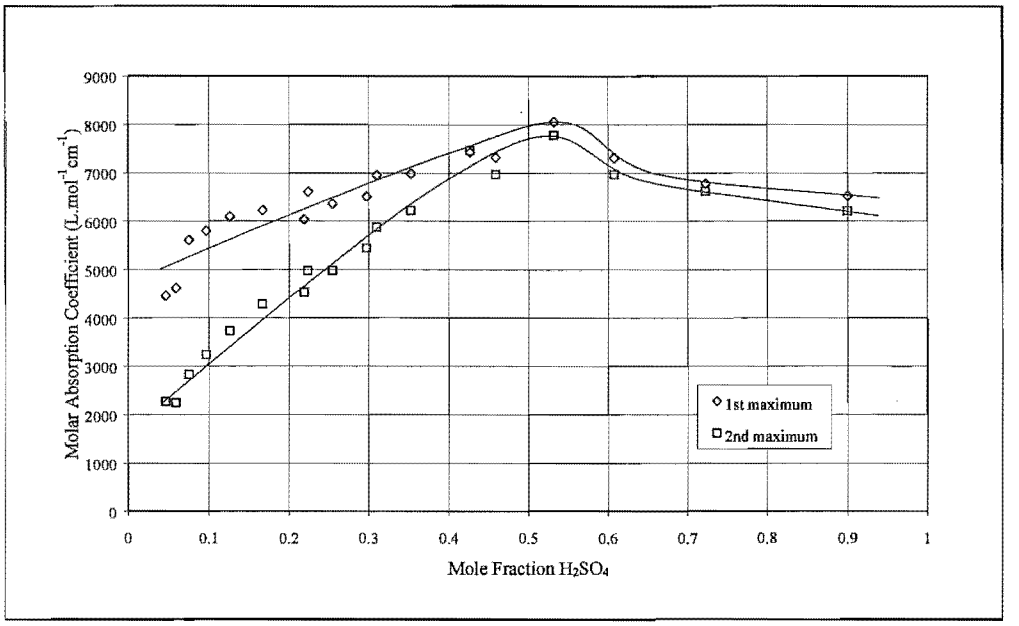

Figure 5.22 Extinction Coefficients at the absorption maxima for Fe(III) in sulfuric acid solutions, as a function of acid concentration

5.4.2 Calculating the concentration of Fe(III) in photolysed solutions

The output current from the photomultiplier was detected using a picoammeter and converted to an analog voltage signal. The output signal from the picoammeter was adjusted so that when there was no transmitted light the signal was 0V, and full transmission was between 2 and 2.5V. Data was recorded directly onto computer via an analog – digital interface as a series of voltages (representing the transmission intensities) at fixed time intervals (Fig 5.23). For each experiment, the initial intensity was recorded with the cell fully empty (I_{cell}), then with the acid solution (I_{acid}). The laser power and the starting and finishing times of the photolysis were manually recorded, along with the temperature, pressure of Ar in the cell and any changes in the reaction conditions during the photolysis.

To determine the concentration of Fe(III) present, the transmission intensities were used to calculate the absorbance of the sample, ie. $\log_{10}(I_0/I)$. Before this could be done, I_0 had to be determined. The initial transmitted light intensity with acid in the

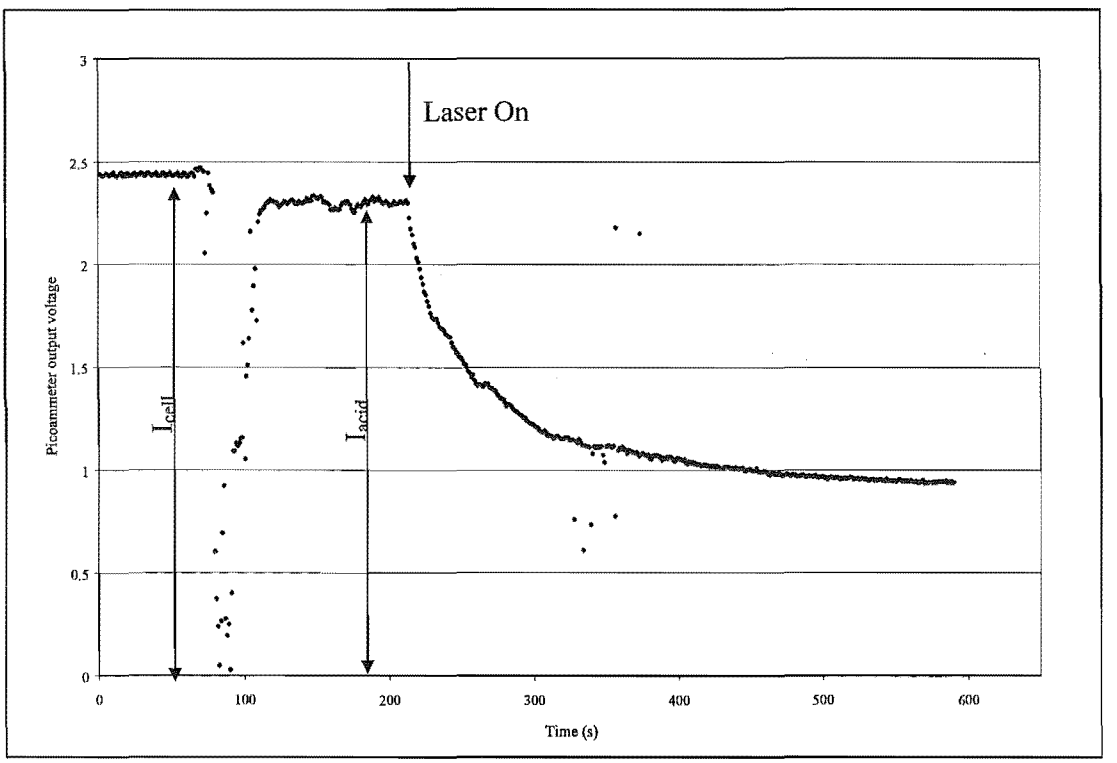

Fig 5.23 Raw Transmission Data

cell (I_{acid}) is typically only 75-85% of the empty cell transmission (I_{cell}). Comparison with absorbance measurements made in the GBC UV-VIS spectrometer show that the solution is not absorbing this light. Instead, the drop has been attributed to scattering from the cell, as the method of construction means that the front and back windows are not perfectly smooth or parallel. The exact amount of scattering depends on the cell contents. The transmission is highest when the cell is empty, less when the cell is filled with water, and is lowest when the cell contains sulfuric acid. The presence of dissolved Fe(II) in the acid has no observed effect on transmission. I_0 was initially taken to be the same as I_{acid}, ie. the transmission of the cell containing acid solution, before photolysis.

For some solutions, the initial solution had a non-zero absorbance due to the presence of Fe(III). In this case, I_0 had to be determined differently. The absorbance of the solution at 248nm was measured in a 1cm cuvette in the GBC spectrometer. The absorbance of the solution in the photolysis cell was 2.1 times greater, due to the longer pathlength. This value was then used to calculate I_0 from the measured intensity of light initially transmitted through the solution (I_{acid}), according to:

$$I_0 = I_{acid} \times 10^{(2.1 \times A_{spectrometer})} \tag{5.3}$$

I_0 values calculated in this way normally fell between I_{acid} and I_{cell}. In a few cases, the initial absorbance was large enough that the calculated I_0 was greater than I_{cell}, which was clearly an error. In this event, I_{cell} was used as the I_0 value; however, this situation was uncommon and was not a significant problem.

The raw data contained a significant number of aberrant points, which appeared as individual points with unusually low absorbance values, apparently as a result of electrical pickup. There appeared to be no physical basis for these points being legitimate, so they were removed from the data. The criterion for removing a data point was that if the change in absorbance from one point to the next was greater than 0.02, it was discarded. This value was chosen arbitrarily, after visual inspection of the data.

The concentration of Fe(III) as a function of time was finally determined by applying the Beer-Lambert law to the calculated absorbances, using the molar absorption coefficient $\varepsilon_{248nm} = 6136 L.mol^{-1}cm^{-1}$ (Section 5.4.1), and a pathlength of $l = 2.1cm$.

5.4.3 Calculating the amount of laser light absorbed

As discussed in Section 5.3.2, not all of the light emitted from the laser was incident on the cell, due to the geometry of the system. The total laser power output, as indicated by the internal power meter, was multiplied by an appropriate factor to determine the amount of light that was incident on the cell ($P_{incident}$). Much of this laser light passed through the sample without being absorbed. During photolysis, the transmitted light from the laser ($P_{transmitted}$) was detected using a Coherent laser power meter tuned to 248nm, and the results were recorded manually at 30s intervals.

Since the Fe(III) detection also involved measuring transmitted light at 248nm, we expected to find a close correlation between the laser power meter results and data from the H_2 lamp transmission. Fig. 5.24 shows the match between the two. Since the two sets of data are clearly measuring the same transmission, I decided to use the data from the photomultiplier to calculate the amount of laser light absorbed by the solution. The data recorded from the Coherent meter was taken at 30 second intervals, with a maximum precision of 0.01W, whereas the photomultiplier data was recorded at 3 second intervals with an equivalent precision of 0.002W.

The first measurement of the transmitted laser power was taken after the sample solution had been photolysed for five seconds, to allow for the slow response of the Coherent meter. This measurement was used to scale the photomultiplier data, and the amount of laser power absorbed was calculated using 5.4.

$$P_{absorbed} = P_{incident} - P_{transmitted} = P_{incident} - \left(\frac{P_{transmitted,5s}}{I_{trans,5s}} \times (I_{trans}) \right) \qquad (5.4)$$

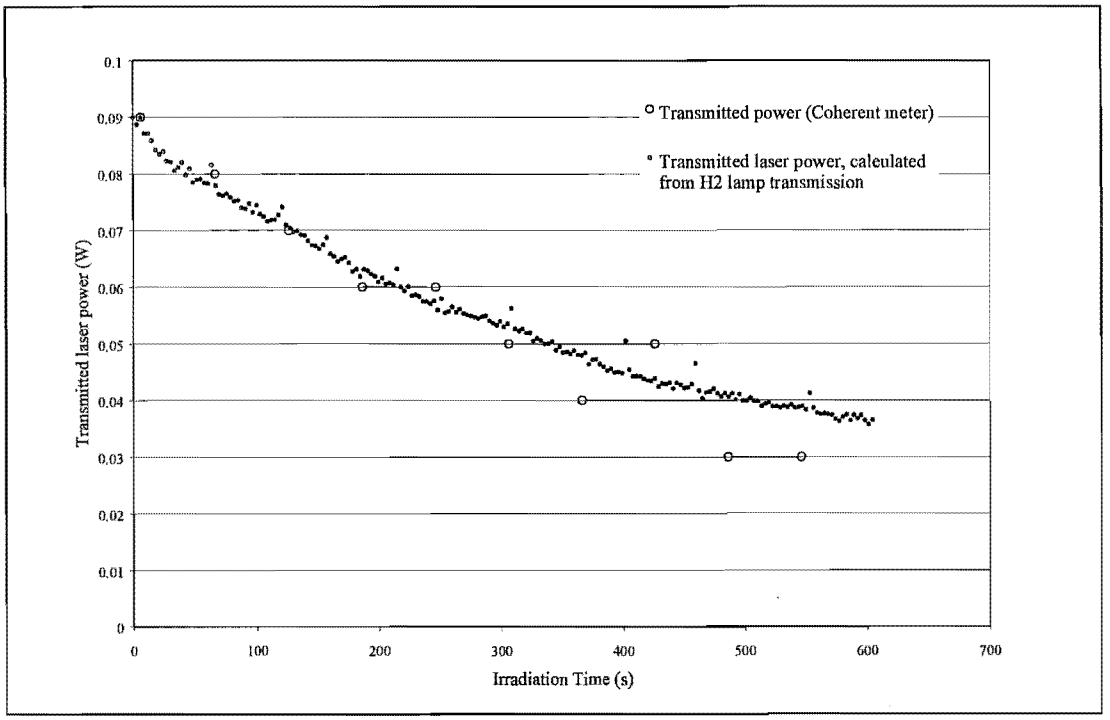

Figure 5.24 Transmitted light intensity at 248nm

The total amount of laser light absorbed during a time interval equals the absorbed power, multiplied by the length of the time interval. Equation (5.4) was used to determine the absorbed power at 3 second intervals, and the total amount of laser light absorbed was calculated as a function of time for each photolysis run by taking the sum of the power absorbed in each time interval. Using this data, the progress of the reaction could be followed by plotting either [Fe(III)] vs time or [Fe(III)] vs number of photons absorbed.

A serious problem was uncovered when transmission measurements from the two sources were compared. If the photomultiplier measurements are believed, the initial absorption in the cell is approximately zero. As photolysis occurs, the transmitted light begins to decrease slowly but steadily, as shown in Fig.5.24. However, if the Coherent power meter readings are correct, the transmitted light intensity drops suddenly and immediately when photolysis begins, before following the steady decrease shown in 5.24. Since this is highly implausible except as an artefact of the power meter, the only possible conclusion is that our estimated initial light intensity ($P_{incident}$) is still too high. For the experiment shown in Fig.5.24, the laser power

transmitted through the empty cell was 0.18W. By extrapolating the transmitted power measurements in 5.24 back to t = 0, this figure should be revised to 0.09W.

The interpretation of Fig.5.24 is now that the initial reaction proceeds due to the absorption of a very small amount of light, the amount of which is substantially less than the error in the measurement. As the photolysis progresses, more light is absorbed due to the production of Fe(III). However, the rate of Fe(III) production decreases significantly over the same period. For this reason, it would be misleading to attempt to represent the formation of Fe(III) simply in terms of a quantum yield dependent on the amount of light absorbed. Instead, the reaction will be characterised by the initial rate of Fe(III) formation throughout this chapter.

5.4.4 Results of Fe(II) Photolysis (I) – General Observations

Results from 370 separate photolysis runs were processed using Microsoft Excel. Plots of [Fe(III)] vs time for the 248nm photolysis of 2.22×10^{-4}M Fe(II) dissolved in 98wt% H_2SO_4 are shown in Fig.5.25. The concentration of Fe(III) is approximately zero until the start of photolysis, when it begins to rise rapidly. The rate of Fe(III) formation decreases over time, often tending towards zero over a sufficiently long period. As Fig. 5.25 shows, the apparent rate of Fe(III) formation did not always drop to zero, and sometimes showed a marked discontinuity. After photolysis, the solution contained both Fe(II) and Fe(III), although there was no consistency in the %conversion.

The first experimental goal was to achieve reproducible results. Fig 5.25 shows the results of four consecutive photolysis experiments, performed using samples taken from the same bulk solution and photolysed with the same laser power. The early progress of the reaction was similar in each case, but as the photolysis time increased, the Fe(III) measurements diverged significantly. As there was no difference in the

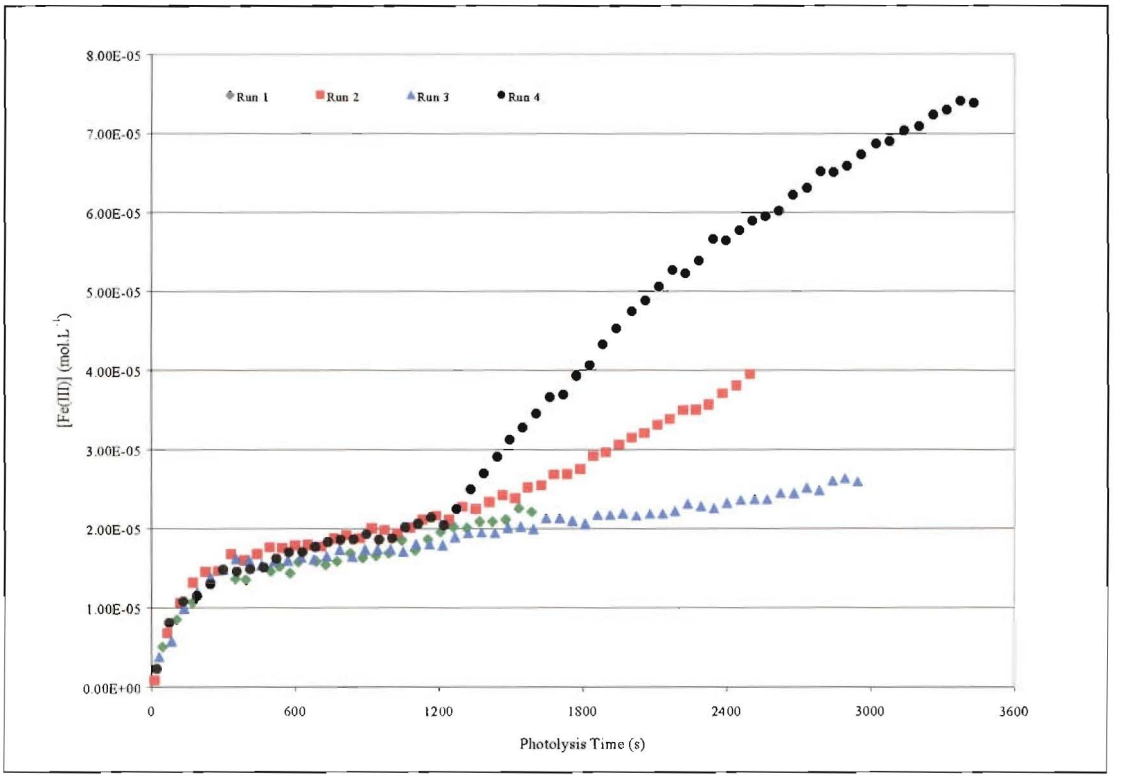

Figure 5.25 Photolysis of 2.22×10^{-4}M Fe(II) in 98wt% sulfuric acid, Laser power = 0.6W

chemical composition of the samples, it was unlikely that the divergence was due to chemical reaction.

Two possible explanations for this were proposed on physical, rather than chemical grounds. The first possible influence is that of diffusion of solution within the cell. As noted in Section 5.3.3.2, the transmission of the solution was different when measured at the front of the cell or at the back, implying that the concentration of products was not uniform throughout the cell. Moreover, there were some areas of

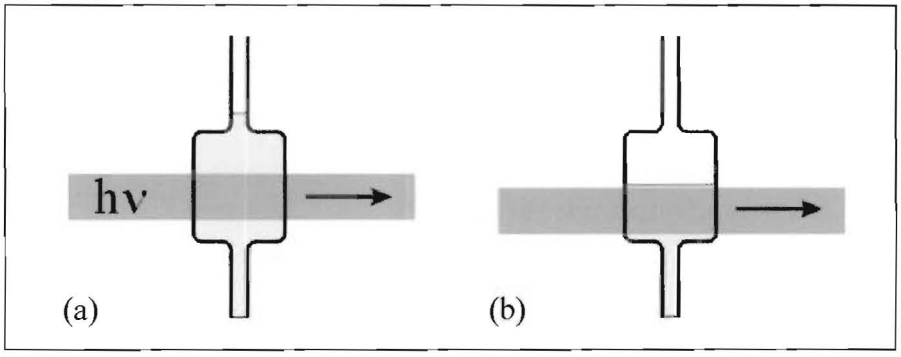

Figure 5.26 Minimising the volume of non-irradiated solution

the cell that received no laser light, due to the differing shapes of the laser beam and the photolysis cell (Fig 5.26a). In an attempt to minimise the volume of non-irradiated solution, the experiment was performed with the photolysis cell only half filled, to match the shape of the laser beam (Fig 5.26b). The liquid level in the cell was kept sufficiently high that the gas-liquid interface was not irradiated, because we did not want to have to consider the possible contribution of surface reactions to our observations.

Since concentrated sulfuric acid is highly viscous, diffusion is much slower than in aqueous solutions. The Stokes-Einstein relation states that the diffusion coefficient D in a liquid is inversely proportional to the viscosity. The viscosity of water[6] at 25°C is 8.9×10^{-4} kg/m.s, while the viscosity of 98wt% sulfuric acid[7] at 25°C is 2.3×10^{-2} kg/m.s. Thus, diffusion coefficients for species travelling in H_2SO_4 are smaller than those for water by a factor of $(8.9\times10^{-4}/2.3\times10^{-2}) = 4\times10^{-2}$. Since diffusion coefficients for ionic species in water are typically $1\text{-}2\times10^{-5}cm^2s^{-1}$, we estimate that diffusion coefficients in sulfuric acid will be approximately $4\text{-}8\times10^{-7}cm^2s^{-1}$.

In the photolysis cell, the distance between the edge of the laser beam path and the area monitored by the probe beam is 3.5mm. In order for species from outside the irradiated acid volume to affect the probe beam measurements, they would first have to travel across this distance. Using Fick's Second Law of Diffusion, the RMS distance travelled by diffusing particles in time t is given by

$$\bar{x} = \sqrt{2Dt} \tag{5.5}$$

If the diffusion coefficient is taken to be $1\times10^{-6}cm^2s^{-1}$, the time required for species to travel a distance of 3.5mm by diffusion in sulfuric acid is 6×10^4s = 17 hours. Thus, the effect of diffusion on the [Fe(III)] measurements can be disregarded.

The second factor that may contribute to the observed variation in transmission is changes in the density of the acid due to heating. Some of the light absorbed by the system during photolysis is converted to heat – after irradiation, the outside of the cell is noticeably warmer than the surrounding glassware. Striations are observed in the acid solution, marking the boundaries between acid at different temperatures and

densities. Because of the viscosity of the solution, these striations are long-lived. Scattering and divergence through these will affect the transmission of light through the solution. Since the striation pattern was different each time that an experiment is performed, this was the likely cause of many of our inconsistent results. In addition, heating effects could have led to convection currents, so that mixing was by eddy diffusion rather than simple diffusion.

Because the results of long irradiations were inconsistent, we decided that there was no value in continuing the photolysis for longer than 10 minutes per sample. This meant that the photolysis reaction was not taken to completion and the final proportion of Fe(II):Fe(III) could not be determined. The plots of [Fe(III)] vs time over the first 10 minutes of photolysis showed reasonable consistency (Fig. 5.27), although there were occasionally unexpected "bumps" in the progress of the reaction.

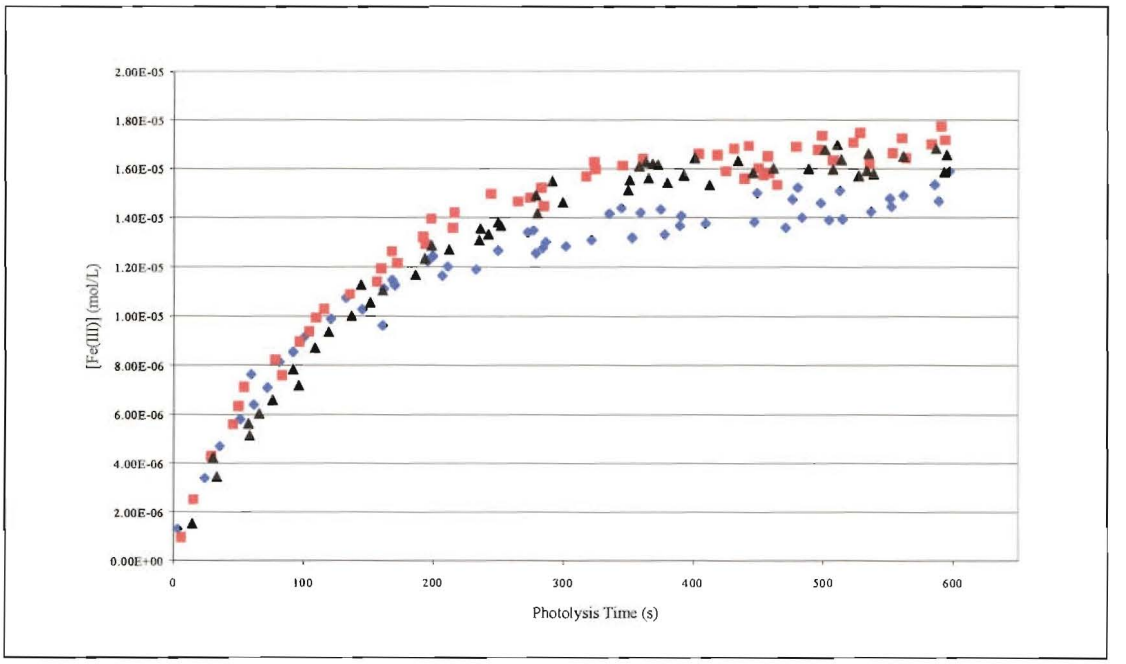

Figure 5.27 248nm photolysis of Fe(II) in acid solution, showing consistency of results from three consecutive runs. Initial [Fe(II)] = 2.22×10^{-4}M, laser power = 0.6W

The shape of the curve could not be described by a simple mathematical function, indicating that the reaction kinetics were complex. In order to compare results for solutions with different concentrations of Fe(II), the initial rate of the reaction was estimated by taking a linear least-squares fit of the data over the first 200s of photolysis. Beyond this time, the curvature became great enough that a linear fit was insufficient to represent the data.

In many of the photolysis runs, there was a discontinuity in the reaction rate after approximately 30s. The reaction proceeded rapidly during this initial period, then slowed to a more typical rate. For these runs, a least-squares fit was taken for the first 30s of data, and a second least-squares fit was taken for the data from 30-200s of photolysis. Fig.5.28 shows the two measurements of the reaction's initial rate.

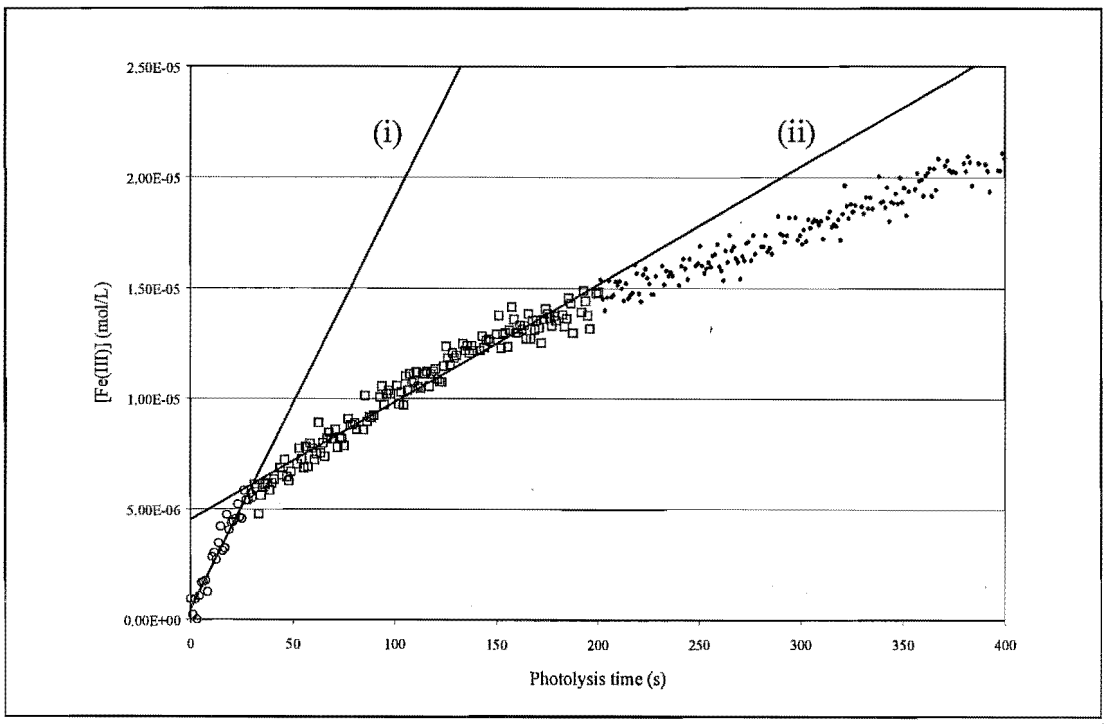

Figure 5.28 Initial rates of reaction are estimated by linear fits of (i) First 30s data (ii) Data from 30-200s

5.4.5 Results of Fe(II) Photolysis (II) - Dependence of Initial Rate on Laser Power

Several series of experiments were performed where samples containing the same initial concentration of Fe(II) were photolysed with different laser power. The initial rate of reaction was determined for each experiment, and the results were plotted as Initial Rate vs Laser Power.

Fig. 5.29 shows the results for a series of photolysis experiments performed with constant $[Fe(II)]_i = 1.10\times10^{-3}$M. A roughly linear dependence was found when the initial rates of these reactions were plotted against incident laser power. The scatter of the results for the first-200-seconds initial rate was much less than for the first-30-seconds initial rate.

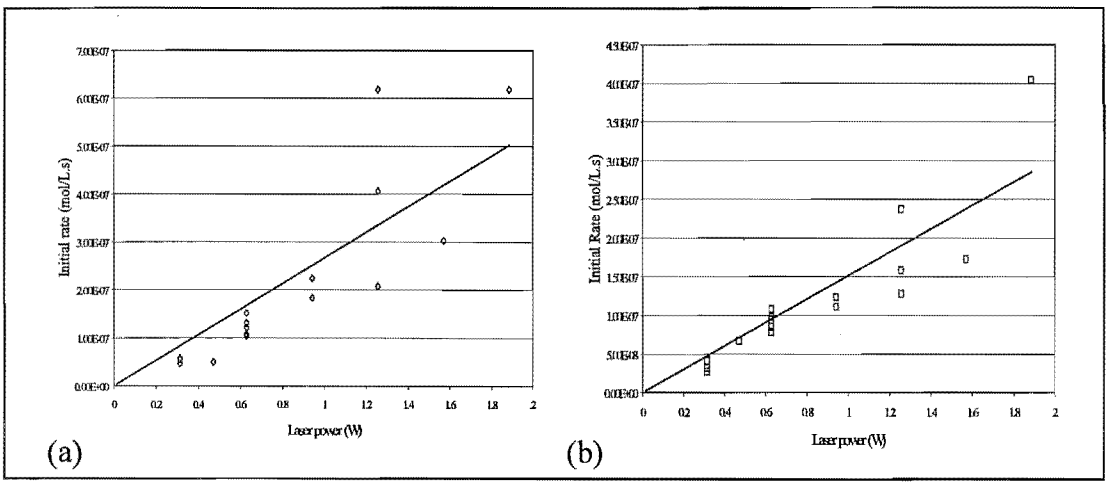

Figure 5.29 Dependence of Initial reaction Rates on Laser Power.
(a) First 30s Rate (b) 30-200s Rate

These comparisons do not take into account the amount of laser light actually absorbed during the photolysis, and thus do not represent a quantum yield for the reaction. What they show is that when the intensity of light incident on the cell is increased, the rate of reaction increases roughly linearly with intensity. Thus, it is concluded that the primary process involves the absorption of a single quantum of light.

5.4.6 Results of Fe(II) Photolysis (III) - Dependence of Initial Rate on [Fe(II)] and [SO_2]

It was expected that the rate of the photolysis reaction would depend on the concentration of Fe(II). In addition, studies on photochemical oxidation in aqueous acid aerosols have often involved S(IV) species. As SO_2 is highly soluble in sulfuric acid, it is likely to be present in sulfuric acid aerosols in the Venusian clouds.

A series of experiments were performed where the initial concentrations of Fe(II) and SO_2 were systematically varied, while all other reaction conditions – temperature, pressure, laser power, irradiation time – were kept constant. This allowed the effect of varying $[Fe(II)]_{(i)}$ and $[SO_2]_{(i)}$ to be determined. Experiments were performed for all possible combinations of the following concentrations:

$[Fe(II)]$: 4.78×10^{-5}M, 9.55×10^{-5}M, 1.97×10^{-4}M

$[SO_2]$: 0M, 1.56×10^{-5}M, 3.13×10^{-5}M, 6.25×10^{-5}M

For each combination of $[Fe(II)]_{(i)}$ and $[SO_2]_{(i)}$, 40mL of solution was prepared and degassed, as described in 5.3.5. The photolysis was repeated three times, using an approximately 9.5mL sample from the bulk solution for each run. If the data from the set of three experiments did not show acceptable agreement, the experiment was repeated with a fresh solution. A UV spectrum of the solution was measured before photolysis, and for each sample after photolysis, to determine whether there were any reaction products other than Fe(III) being formed. In each case, Fe(III) was the only species observed to form during the reaction. The unidentified Product B detected previously (Section 5.2) was not observed during this series of experiments, nor was it observed in any other experiments using acid that had been degassed in the new degassing vessel.

Graphs of [Fe(III)] vs time are shown on the following pages. Each plot displays the result of varying $[Fe(II)]_{(i)}$ while keeping $[SO_2]_{(i)}$ constant. The plots show the superposition of all three data series for each concentration of $[Fe(II)]_{(i)}$. The effect of increasing $[Fe(II)]_{(i)}$ on the total concentration of Fe(III) produced is immediately

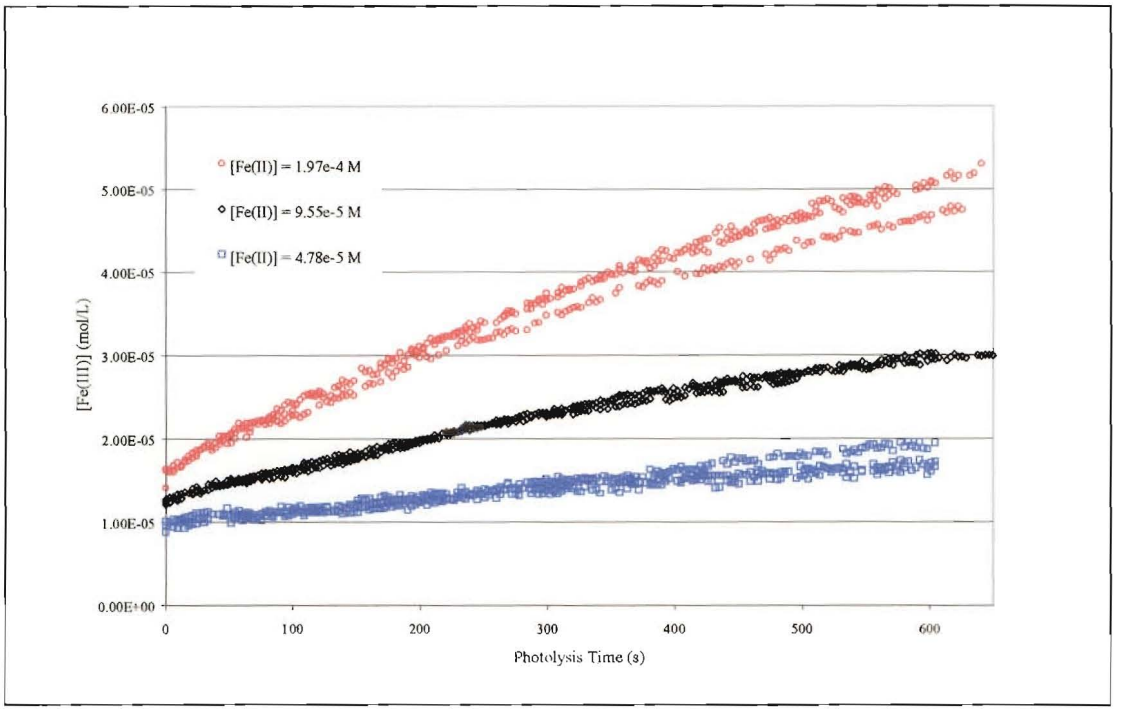

Figure 5.30 Various $[Fe(II)]_{(i)}$, $[SO_2]_{(i)}$ = 0M

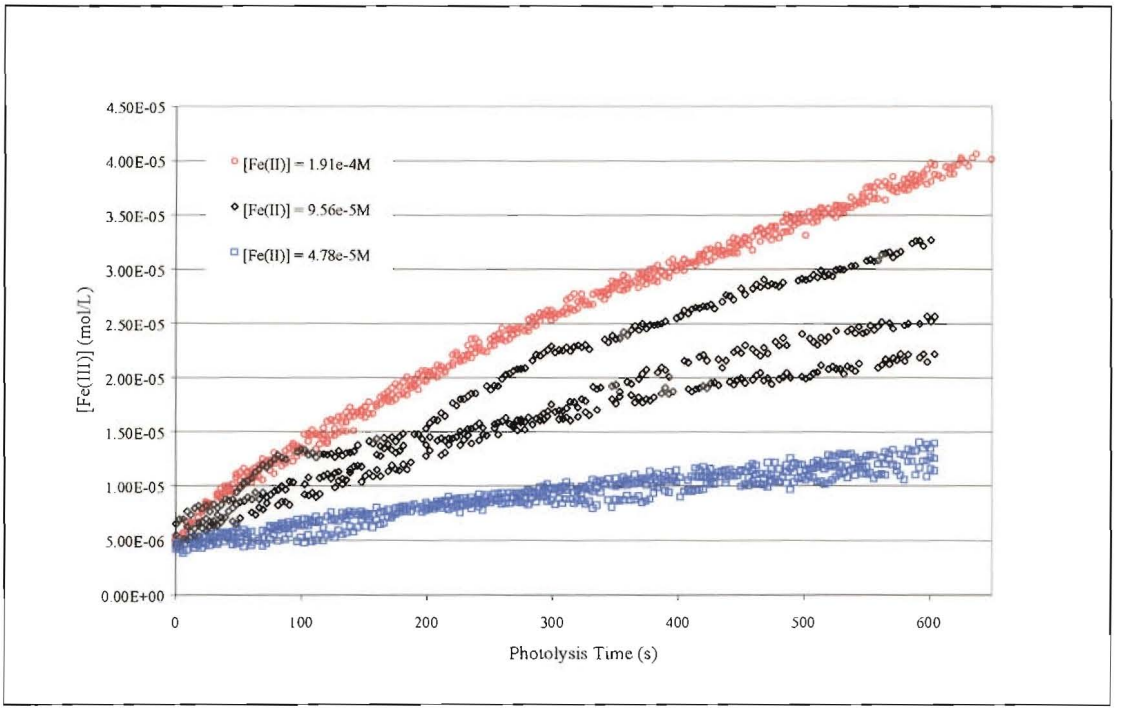

Figure 5.31 Various $[Fe(II)]_{(i)}$, $[SO_2]_{(i)} = 1.56 \times 10^{-5}$M

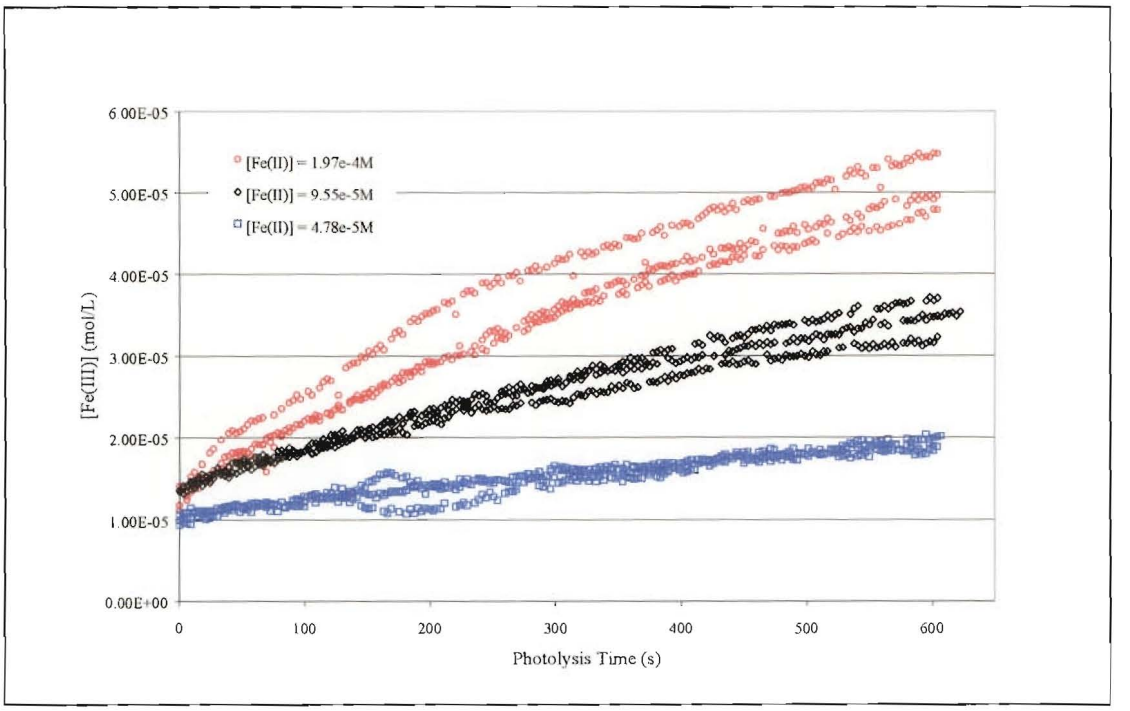

Figure 5.32 Various $[Fe(II)]_{(i)}$, $[SO_2]_{(i)} = 3.13x10^{-5}M$

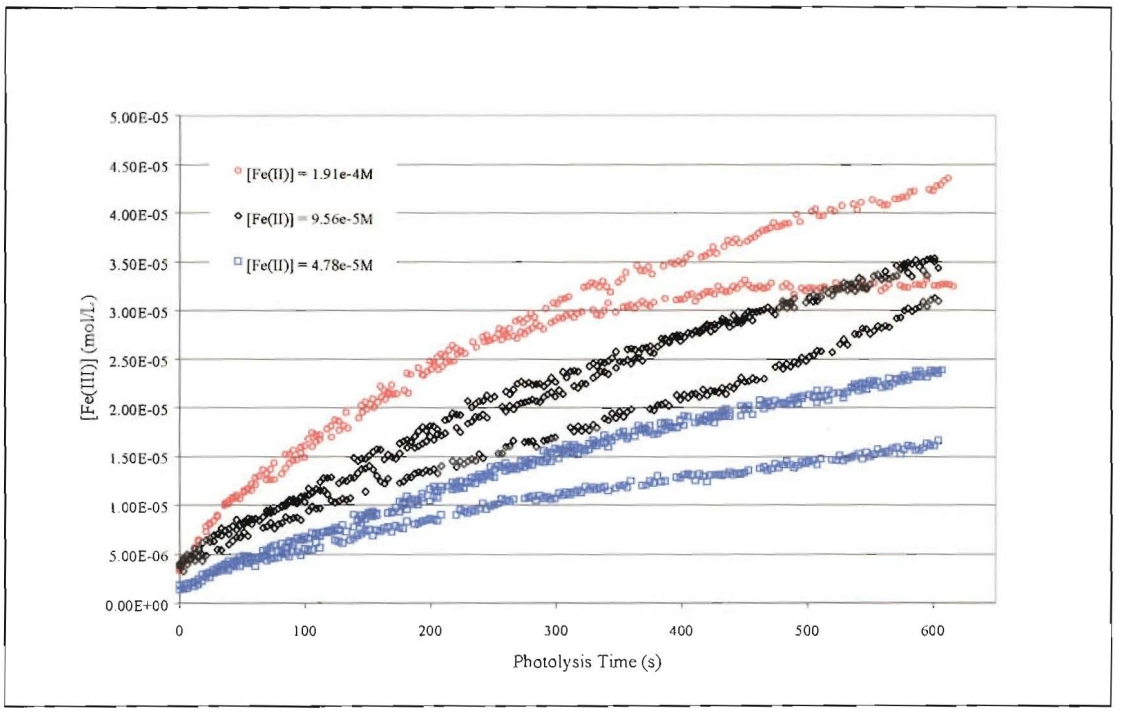

Figure 5.33 Various $[Fe(II)]_{(i)}$, $[SO_2]_{(i)} = 6.25x10^{-5}M$

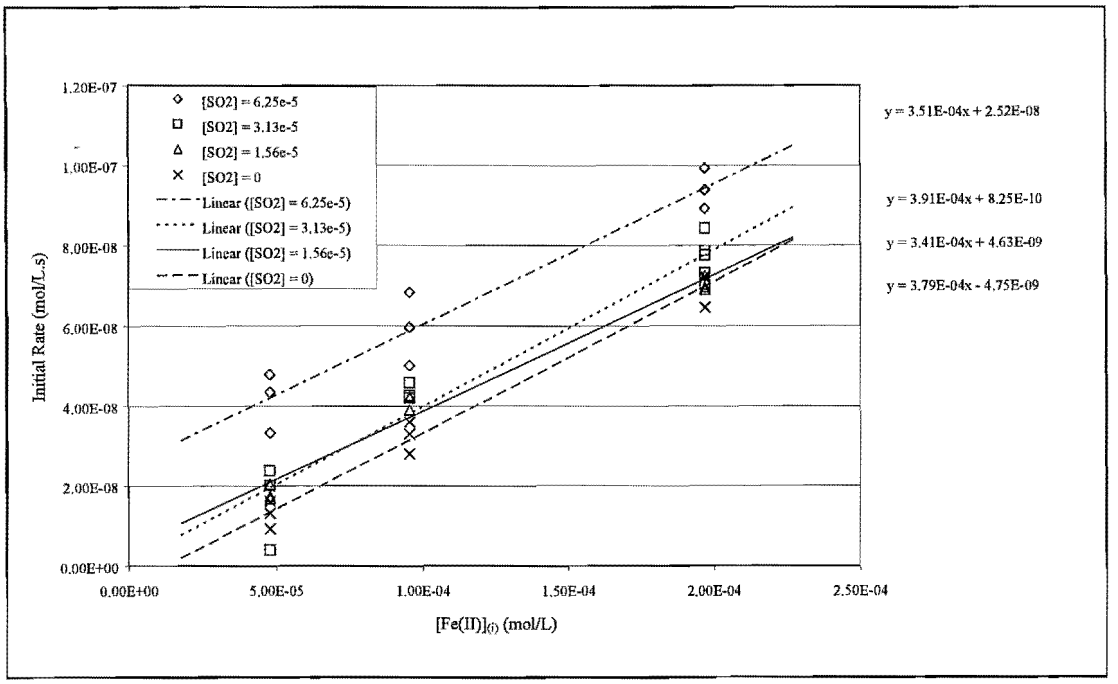

Figure 5.34 Initial Rate (30-200s) of Fe(III) formation as a function of $[Fe(II)]_{(i)}$ at constant $[SO_2]_{(i)}$

apparent. Note that the initial absorption by Fe(III) in solutions containing SO_2 was greater than zero, probably due to the formation of Fe(III) via non-photochemical oxidation of Fe(II) by H_2SO_4.

The initial rate was determined for each photolysis run using the data from 30-200s. Initial rate is plotted as a function of $[Fe(II)]_{(i)}$ for each concentration of $SO_{2(i)}$ in Fig.5.34. In each case, the relationship could be described by a linear fit, although the scatter of initial rate measurements for each combination of $[Fe(II)]_{(i)}$ and $[SO_2]_{(i)}$ is large enough that a non-linear fit is possible. The dependence of initial rate on $[Fe(II)]_{(i)}$ appears to be independent of the SO_2 concentration. The average of the gradients for the four linear fits shown in Fig. 5.34 is $3.7\times10^{-4}s^{-1}$.

Although the observed relationship between initial rate and $\{Fe(II)]_{(i)}$ was linear, it was not directly proportional. This was evidenced by the non-zero intercept, especially for the series performed at high $[SO_2]$, and must be accounted for in any mechanism proposed for the photolysis.

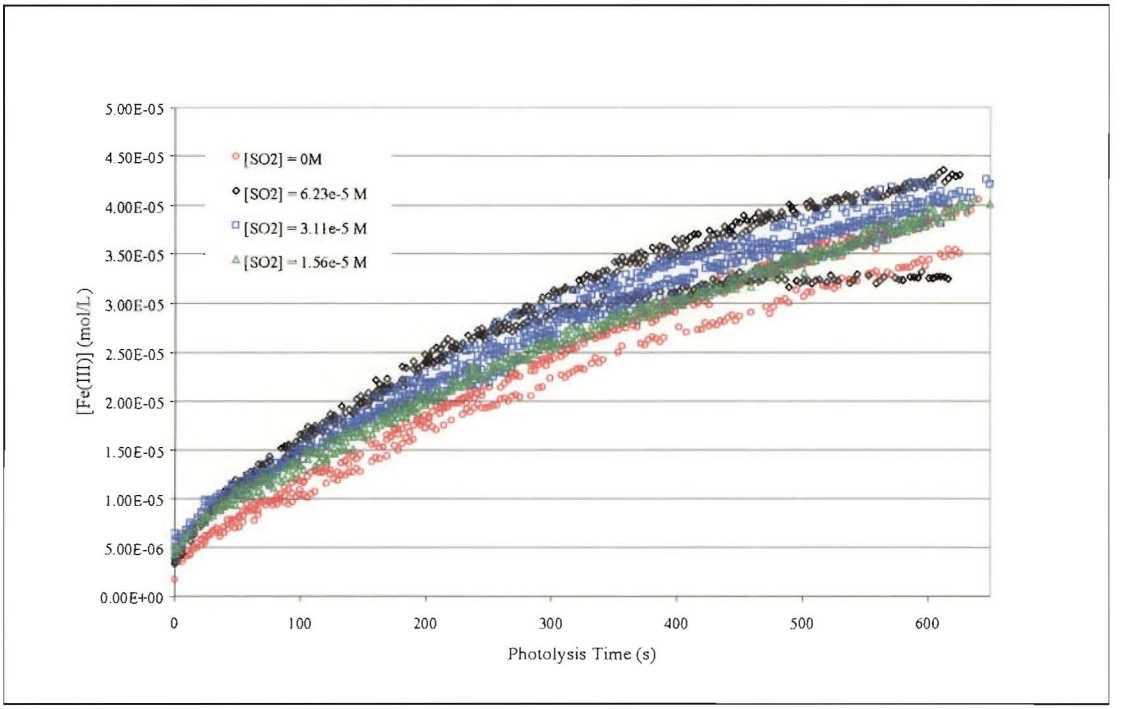

Figure 5.35 Progress of photolysis reaction with various $[SO_2]_{(i)}$, $[Fe(II)]_{(i)} = 1.97x10^{-4}M$

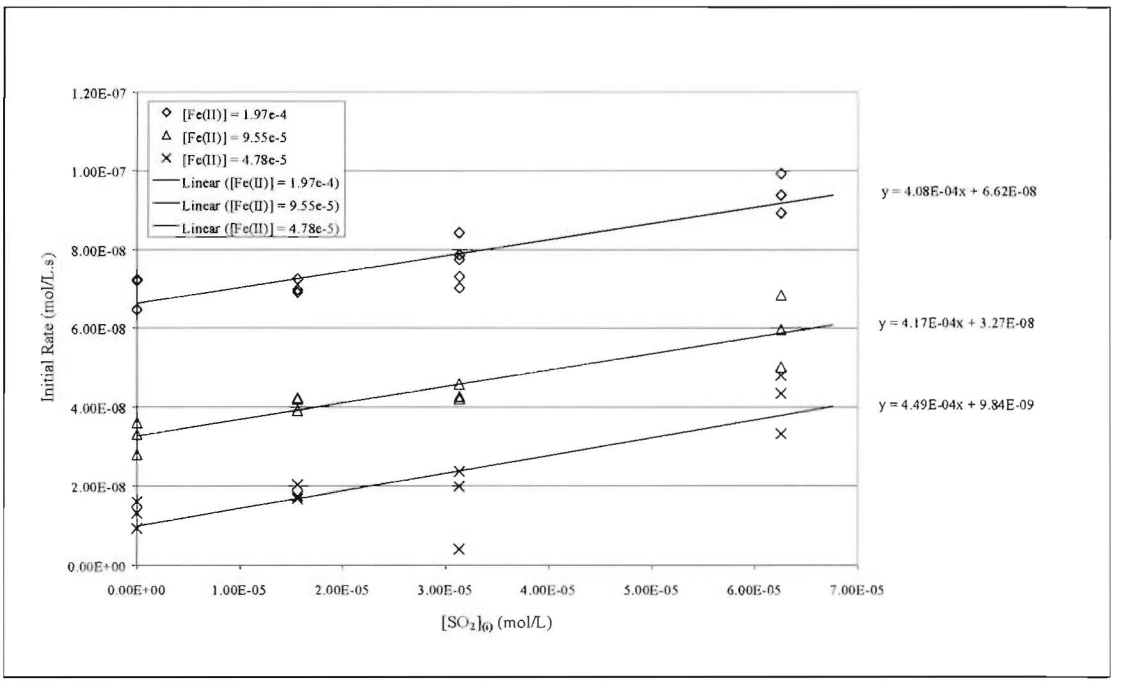

Figure 5.36 Initial Rate (30-200s) of Fe(III) formation as a function of $[SO_2]_{(i)}$ at constant $[Fe(II)]_{(i)}$

The effect of further increasing $[Fe(II)]_{(i)}$ could not be determined due to the difficulty of measuring larger concentrations of [Fe(III)] spectrophotometrically. Runs with $[Fe(II)]_{(i)}$ less than 5×10^{-5}M were attempted, but the results were not meaningful due to the inconsistency of the initial rate measurements.

The same set of results can be used to examine the dependence of initial rate on $[SO_2]_{(i)}$. When $[Fe(II)]_{(i)}$ was varied, it was seen that increasing the amount of Fe(II) resulted in an increase in both the rate and the concentration of Fe(III) produced. This was not immediately obvious when $[SO_2]$ was varied, as the final concentration of Fe(III) was not affected significantly (Fig. 5.35). Consideration of the initial rates, however, showed that the initial reaction proceeded faster with increased $[SO_2]$. (Fig. 5.36)

5.4.7 *Results of Fe(II) Photolysis (IV) - Dependence of Initial Rate on [CO]*

One of the objectives of these experiments is to investigate the role that photochemical aerosol reactions may play in the atmospheric chemistry of Venus. In Chapter 2, the photo-oxidation of carbon monoxide was observed in sulfuric acid aerosols. Now, as part of our experiments on the photo-oxidation of Fe(II), we consider the effect of the photolysis when dissolved carbon monoxide is present in the acid solution.

Carbon monoxide is generated when a formate salt is added to concentrated sulfuric acid. Formate is dehydrated by the acid, producing CO according to Equation 5.6:

$$HCOO^- + H_2SO_4 \longrightarrow CO + HSO_4^-.H_2O \qquad (5.6)$$

A solution of carbon monoxide in sulfuric acid was prepared by adding a weighed amount of ammonium formate to degassed sulfuric acid. Bubbles were observed as the formate salt dissolved, and it was assumed that some carbon monoxide remained dissolved in the acid. The actual concentration of CO in solution was unknown and no attempt was made to determine it.

Sample solutions for photolysis were prepared by mixing measured volumes of the carbon monoxide solution and solutions of Fe(II) in sulfuric acid. The formation of [Fe(III)] is shown as a function of photolysis time in Fig.5.37 and the initial rate as a function of [$HCOO^-$] is shown in Fig.5.38. The solutions contained a small initial amount of Fe(III) – up to 5% of the total iron present – due to the partial oxidation of Fe(II) in the bulk solution used to prepare sample solutions. The initial concentration of Fe(III) observed is not related to the presence of carbon monoxide in the solutions. Results from this series of photolysis experiments show that within the accuracy of the data, there was no systematic effect on the rate of Fe(III) formation due to the presence of CO in the solution.

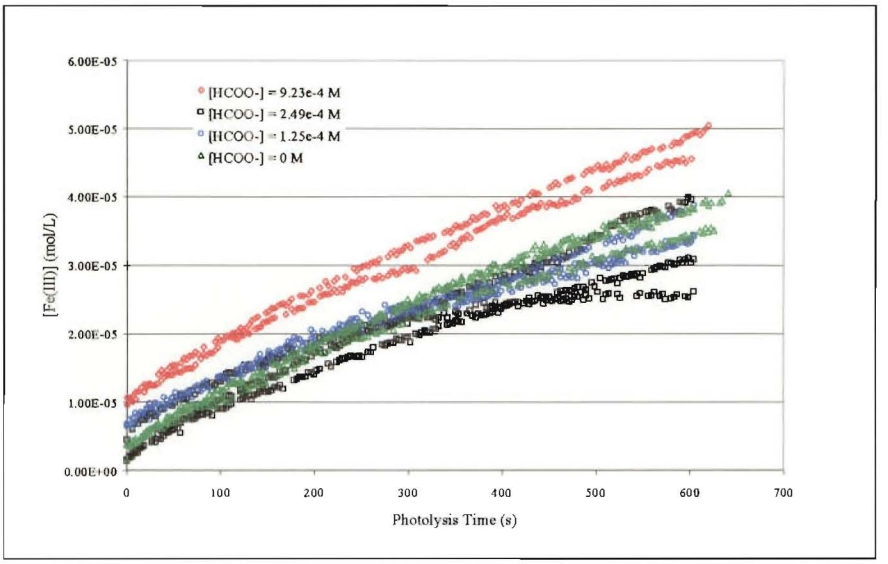

Figure 5.37 Progress of photolysis reaction with various $[HCOO^-]_{(i)}$, $[Fe(II)]_{(i)} = 1.97 \times 10^{-4}$M

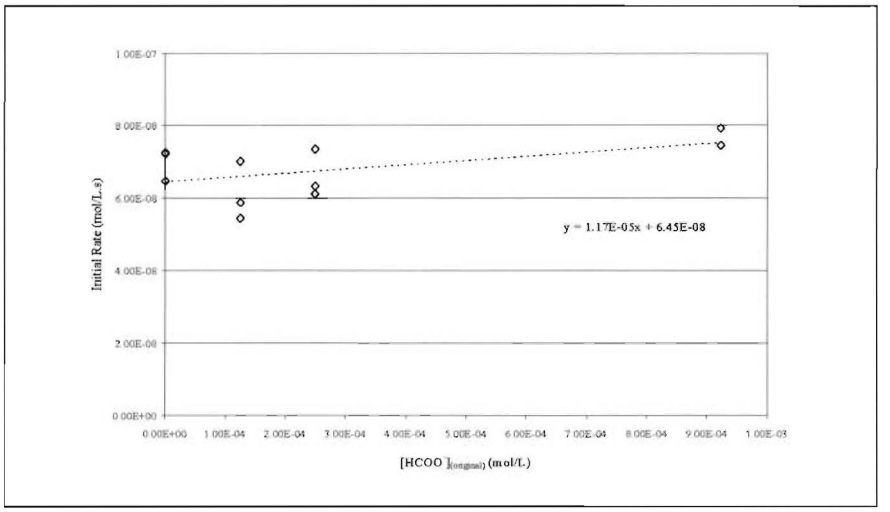

Figure 5.38 Initial Rate (30-200s) of Fe(III) formation as a function of $[HCOO^-]_{(original)}$ at constant $[Fe(II)]_{(i)}$

5.4.8 Results of Fe(III) Photolysis

In earlier experiments, it was observed that the photooxidation of Fe(II) in sulfuric acid did not result in full conversion to Fe(III). One possible explanation is that Fe(III) is also photo-reactive in sulfuric acid. To test this, solutions of Fe(III) dissolved in sulfuric acid were photolysed using the same method as in the Fe(II) experiments.

As with the Fe(II) experiments, the progress of the reaction was monitored by measuring the absorbance of the solution at 248nm during photolysis. The measurement was more difficult than for Fe(II) because the solutions already absorbed strongly at the beginning of the reaction. This required I_0 to be calculated from the measured transmission through the cell and an independent measurement of the absorbance of the solution (Section 5.4.2). Since I_0 was calculated by taking the exponential of the initial absorbance – already a large value – the value of I_0 was significantly affected by a small error in A. On some occasions, this resulted in estimates of I_0 that were greater than the light intensity transmitted through the empty cell by up to a factor of two. This introduced a minimal error when the solution absorbance was large, but the uncertainty in the measurement increased as the measured absorbance decreased.

Photolysed solutions of ferric sulfate dissolved in sulfuric acid showed a decrease in absorbance, which was attributed to Fe(III) being reduced to Fe(II). Initial experiments suggested that the reaction was much slower than the Fe(II) oxidation. Solutions irradiated with 0.6W of 248nm light for one hour showed a 10% drop in [Fe(III)] (Fig. 5.39).

Separate measurements of the absorption of the solution using the UV-VIS spectrometer indicated that the loss of Fe(III) was genuine, and not an experimental artefact produced by drift in the deuterium lamp output over the long monitoring time. However, the spectrometer measurements also revealed that the concentration of Fe(III) in the bulk solution increased slowly over a period of a few days. The reason

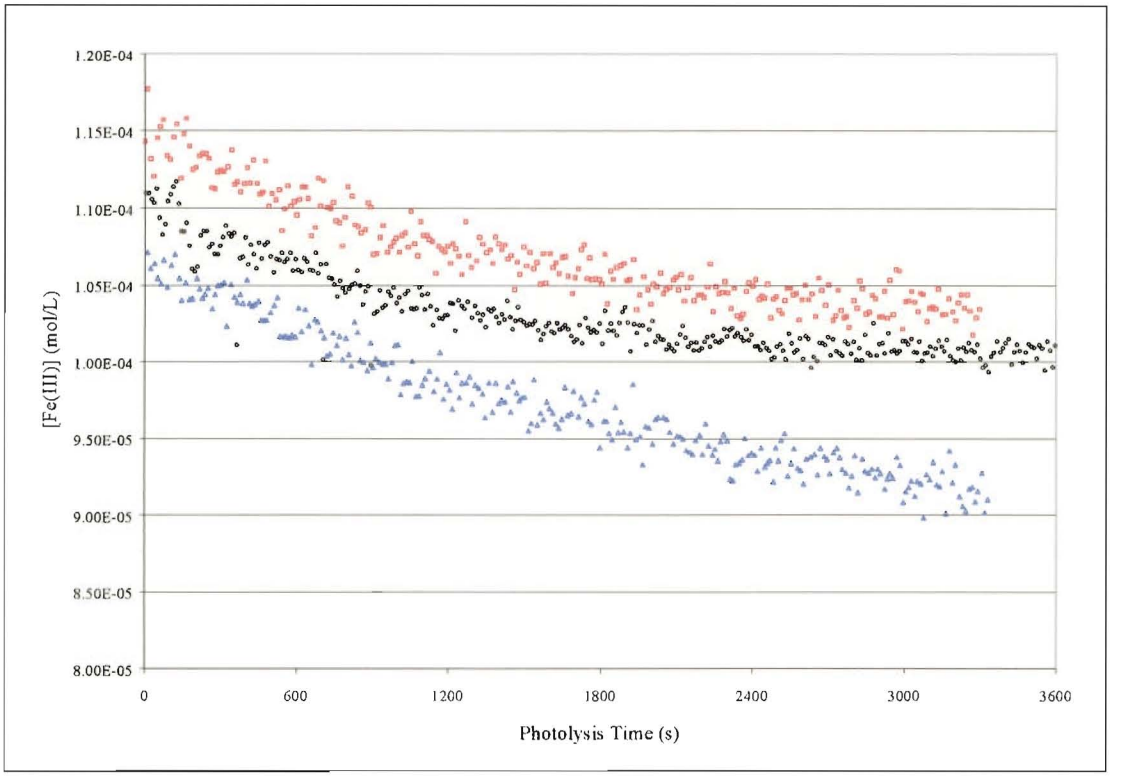

Figure 5.39 248nm laser photolysis of $Fe_2(SO_4)_3$ in 98wt% sulfuric acid. $[Fe(III)]_{(i)} = 1.1\times10^{-4}$M, laser power = 0.6W

for this was unclear, but it was thought to be due to slow rate of solvation of ferric sulfate in sulfuric acid. The observed experimental results were due to the combined effect of [Fe(III)] being decreased by photolysis and simultaneously increasing due to changes in Fe(III) speciation during the photolysis.

New experiments were performed on solutions prepared from ammonium ferrous sulfate, which was readily soluble in sulfuric acid, and oxidised to Fe(III) using Oxone. The solutions contained between $(0.4\text{-}3)\times10^{-4}$M of Fe(III), and a small amount of Fe(II), estimated to be less than 5×10^{-6}M. The presence of Fe(II) was preferable to adding an excess of Oxone, which would result in the solution containing HSO_5^-. The concentration of Fe(III) in the solution was determined by UV spectroscopy, and the total concentration of Fe was determined by fully oxidising the solution with excess Oxone and remeasuring the UV spectrum.

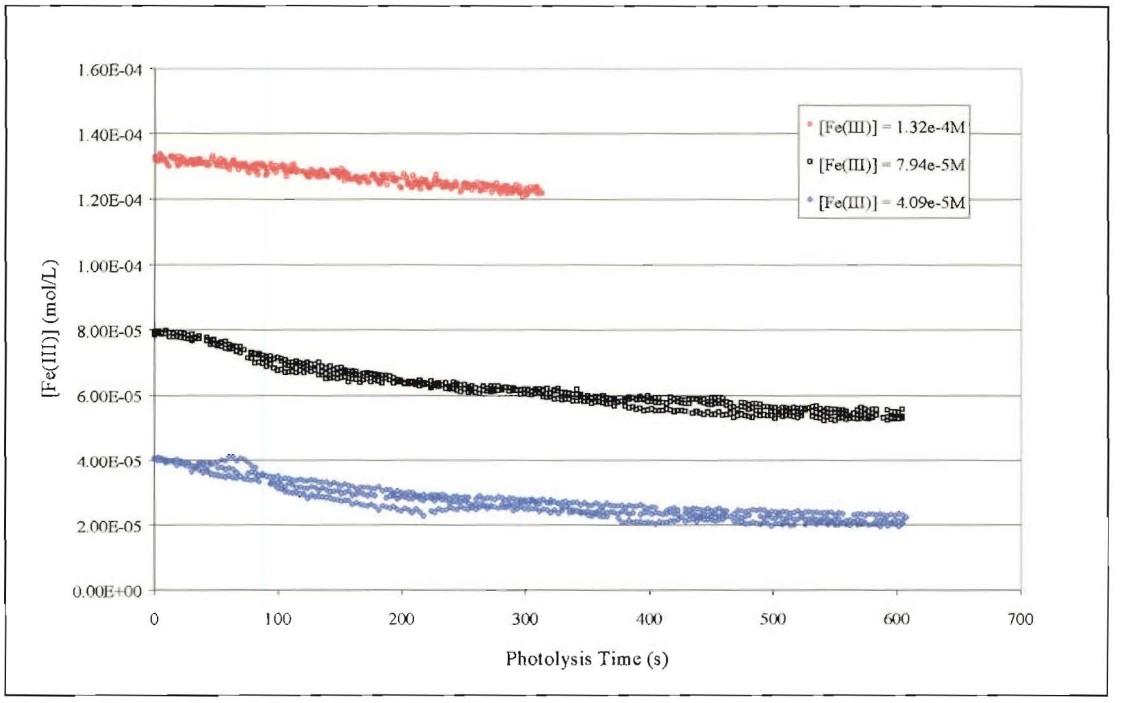

Figure 5.40 248nm laser photolysis of Fe(III) in 98% sulfuric acid. Laser power = 0.18W

Fe(III) solutions for photolysis were prepared by diluting samples from the bulk solution with degassed sulfuric acid. Results for concentrations of Fe(III) greater than 1×10^{-4}M were too noisy to be analysed, due to the low transmission of light by the sample. Plots of [Fe(III)] as a function of photolysis time are shown in Fig. 5.40, and show a rate of reaction comparable with the oxidation of Fe(II) solutions

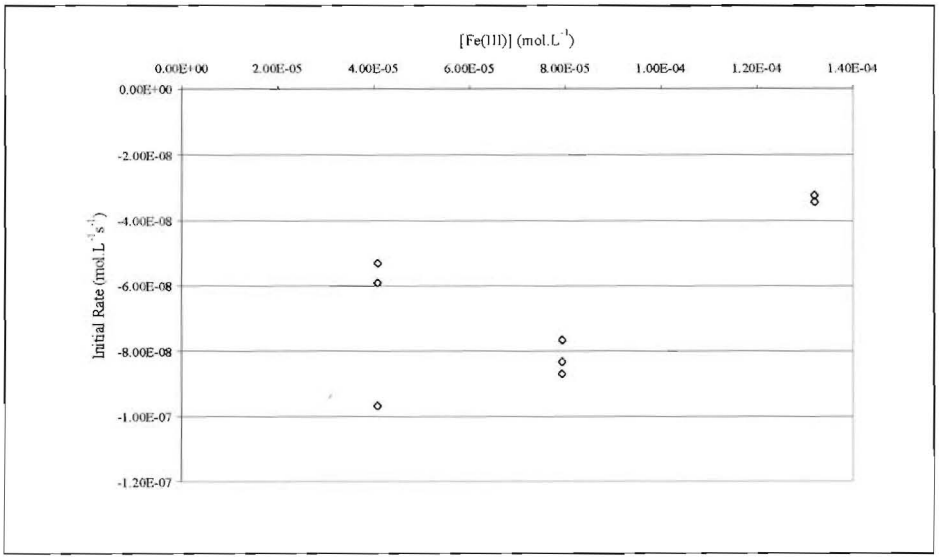

Figure 5.41 Initial Rate (30-200s) as a function of $[Fe(III)]_{(i)}$

of the same concentration. The initial rate (30-200 seconds) is minus (3-9)$\times 10^{-8}$ mol.$L^{-1}s^{-1}$, compared with minus1×10^{-8} mol.$L^{-1}s^{-1}$ for the $Fe_2(SO_4)_3$ solutions.

Using the new Fe(III) solutions, the dependence of the initial rate on [Fe(III)] was examined (Fig. 5.41). The result which shows an initial rate of minus 9.7×10^{-8} mol.$L^{-1}s^{-1}$ for $[Fe(III)]_{(i)} = 4.1\times 10^{-5}$M is probably incorrect, as the data trace contained several uncharacteristic bumps in the period 30-200s. The samples for $[Fe(III)]_{(i)} = 1.3\times 10^{-4}$M were taken from a different bulk solution of Fe(III) than the other $[Fe(III)]_{(i)}$ concentrations, and this may be the reason for the lower initial rates observed. The results in Fig. 5.41 indicate that the rate of Fe(III) reduction is not determined by the Fe(III) concentration, and that some other factor which was not experimentally controlled was instead responsible.

5.4.9 *Results of Fe(III) Photolysis (II) - Dependence on Laser Power*

Photolysis of Fe(III) solutions at different laser power failed to show any difference in the reaction rate due to the light intensity (Fig.5.42). Since the error on the initial rate measurements for Fe(III) solutions was larger than for Fe(II) solutions, it is possible

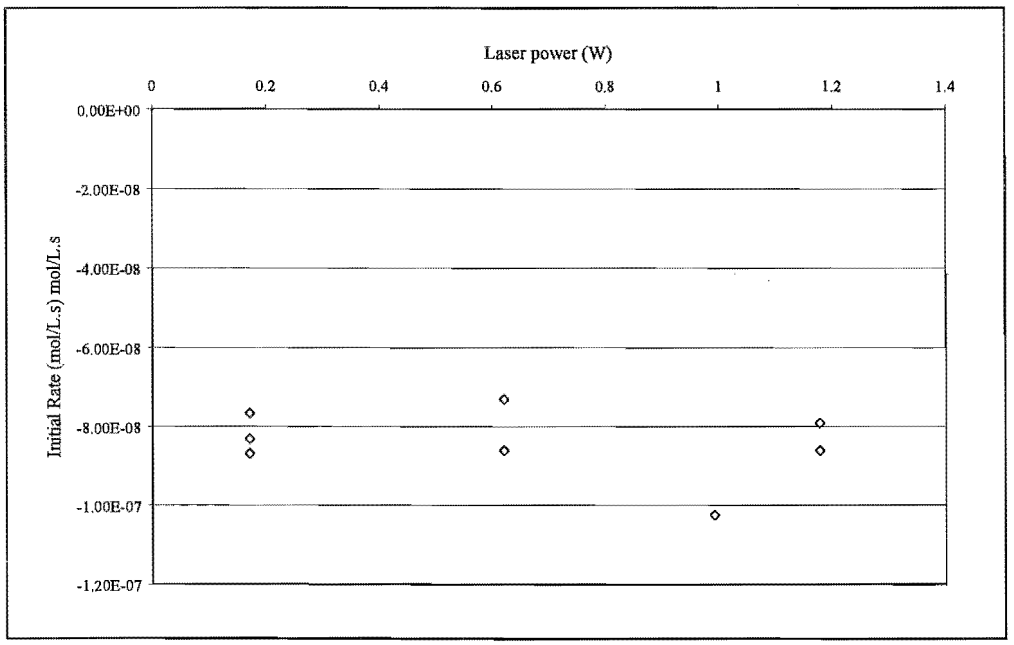

Figure 5.42 Dependence of initial reaction rate on laser power. $[Fe(III)]_{(i)} = 7.6\times 10^{-5}$M

that a power-dependency exists that was not observed experimentally. However, the most likely explanation for the lack of any power dependency is that the reaction is photochemically activated, but that the concentrations of species involved in the rate-determining step are not governed by the photochemical process.

5.4.10 Photolysis of Sulfuric Acid Solutions containing both Fe(II) and Fe(III)

Once it was established that photolysis would cause both the oxidation of Fe(II) and the reduction of Fe(III) in sulfuric acid solution, solutions containing a mixture of both species were prepared and photolysed. The original intention was to perform a series of experiments where the concentration of one species was held constant while the other concentration was varied, as had been done for Fe(II) and SO_2. Samples for photolysis were prepared from bulk solutions of Fe(II) and Fe(III) in degassed sulfuric acid. However, it was found that a significant amount of Fe(II) was immediately oxidised when the two solutions were mixed, before photolysis. This made it impossible to prepare solutions with systematically varying initial concentrations of Fe(II) and Fe(III).

Instead, sample solutions were prepared and the initial concentration of Fe(II) and Fe(III) were determined experimentally by measuring the absorbance of the solution at 248nm. $[Fe(III)]_{(i)}$ was calculated from the initial absorbance, while [Fe(total)] was found by fully oxidising the sample with Oxone. $[Fe(II)]_{(i)}$ was determined by taking the difference between the two measurements.

Experimental results for [Fe(III)] as a function of time are difficult to compare, since the initial concentration is different for each solution. Instead, the results are presented as the proportion of Fe(III)/total Fe as a function of time in Fig. 5.43.

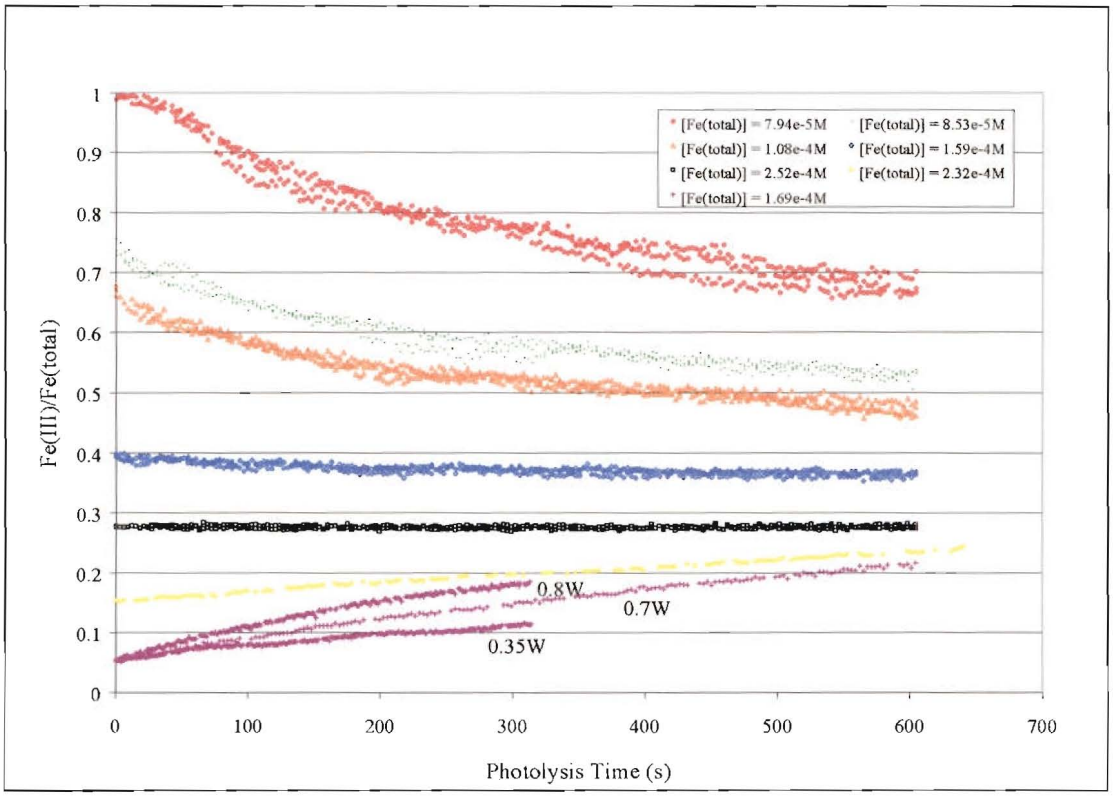

Figure 5.43 Photolysis of mixed Fe(II)/(III) solutions in 98wt% sulfuric acid

The total concentration of Fe in the samples for these experiments was not constant; it ranged from 8×10^{-5}M - 2.5×10^{-4}M for different runs. The proportion of Fe(III) in the photolysed solutions appears to tend towards a value between 0.3-0.35. This is our best estimate of the equilibrium composition of Fe species for the reaction. Too few experiments were performed to determine whether this composition is dependent on the intensity of the incident UV light, or whether increased intensity merely hastened the attainment of the equilibrium, as indicated in the lower three runs in Fig. 5.43. Similarly, it is unclear whether the total Fe concentration has an effect on the equilibrium composition.

5.4.11 Measurements of Dissolved Oxygen Concentration During Photolysis Experiments (I) – Effect of Varying Acid Concentration

A scan of a typical chart recorder trace of the dissolved oxygen measurement is shown in Fig. 5.44. The time scale used was 10 minutes per division, and the vertical scale is 2ppm of O_2 per major division. In this measurement, as in others, the greatest uncertainty in the measurement is due to the slow equilibration of the electrode. In light of this, the results are only regarded as a qualitative indicator of the amount of dissolved oxygen in the samples.

Measurements on the concentration of dissolved oxygen (DO) in sulfuric acid showed that some oxygen remained in solution despite considerable efforts to remove it. Sulfuric acid taken directly from the bottle contained between 6-7ppm of DO, ie. $[O_2] = (1.9\text{-}2.2)\times10^{-4}$M. Acid that had been purged by passing nitrogen or argon through it in the degassing vessel for 4 hours contained a residual DO concentration ranging between 2-3ppm, or $[O_2] = (6\text{-}9)\times10^{-5}$M. This is unfortunate, because it puts the oxygen concentration in the same range as Fe(II)/(III) and SO_2 in the earlier

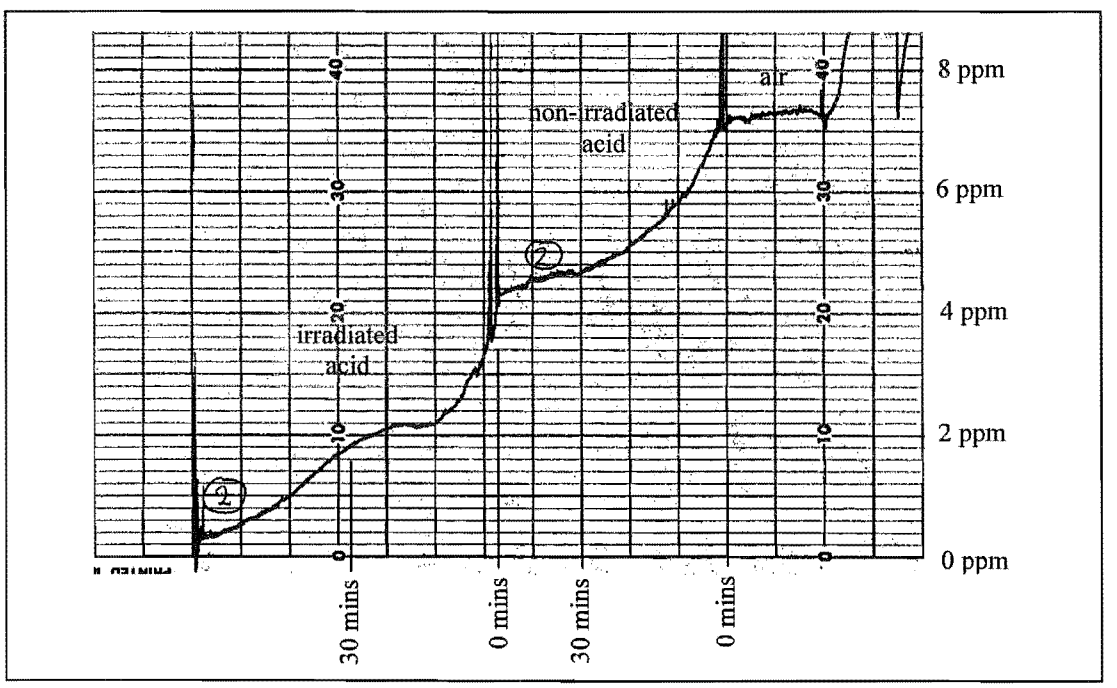

Figure 5.44 Typical record of signal from the DO electrode when measuring the concentration of dissolved oxygen in 98wt% sulfuric acid

experiments. Variations in the concentration of DO may account for the different rates of reaction that were observed when Fe(II) solutions were photolysed in separate series of experiments. This is speculative, however, since the dissolved oxygen meter was not available until long after the Fe(II) experiments were begun.

The concentration of dissolved oxygen in solution was measured before and after photolysis in order to determine how much was removed by the reaction. Two series of experiments were conducted. The first looked at changes in [DO] in photolysed aqueous solutions containing Fe(II), SO_2 and concentrations of H_2SO_4 ranging from 3.9M to 18.2M. The objective of these experiments was to determine how the concentration of sulfuric acid affected the photochemical removal of O_2 from solution. Sample solutions were prepared immediately before each experiment from freshly weighed ammonium ferrous sulfate, degassed distilled water, sulfuric acid, and $SO_{2(aq)}$ solution. The solutions were cooled in an ice-bath while H_2SO_4 was slowly added in order to prevent excessive thermal reaction before photolysis. Measurements were performed on solutions with acid concentrations of 3.9M (31.5wt%), 9.3M (60.8wt%), 12.4M (73.7wt%) and 18.2M (98wt%). All solutions contained initial concentrations of 1×10^{-3}M of Fe(II) and 1×10^{-1}M of S(IV). The solutions were photolysed with 0.3W of 248nm light from the KrF laser for 25minutes, with measurements of dissolved oxygen concentration made before and after photolysis.

The effects of photolysis on [DO] in solutions with different acid concentrations are reported in Table 5.45. Reported values of [DO] are averages of measurements between 3-13 experiments, and are representative of those observed. In many cases, the value of [DO] was difficult to determine, since the probe signal did not stabilise, and instead showed a continual decrease. The solution with 9.3M H_2SO_4 was described as having "no change" in dissolved oxygen, despite an apparent decrease. Based on the shape of the trace, the drop in [DO] was attributed to a continued decline in the electrode signal, rather than a genuine change in the amount of DO in the solution following irradiation. For the 12.4M acid solution, the decrease in [DO] appears to be genuine, but cannot be quantified due to the low initial concentration of

Acid Concentration	Initial DO concentration	Final DO concentration	Change in [DO] due to irradiation
3.9M	7.8 ± 1.0	2.6 ± 1.0	-5 ppm
9.3M	2.2 ± 1.0	0 ± 1.5	no change
12.4M	1.0 ± 1.0	0 ± 2	probable decrease
18.2M	6.5 ± 1.0	2.6 ± 2.0	-4 ppm

Table 5.45 Concentration of dissolved oxygen in various concentrations of H_2SO_4 solution containing Fe(II), SO_2, following irradiation with 248nm light.

O_2. There was no observed correlation between the change in [DO] and the length or intensity of irradiation.

The reason for the failure of the electrode to reach a steady voltage is thought to be related to the temperature of the solution. Sample solutions were prepared by mixing sulfuric acid with aqueous solutions. The heat generated by the mixing meant that the final temperature of the solutions was greater than room temperature. In order to minimise this, the mixing was carried out while the solutions were cooled in an ice-bath. Consequently, it is highly unlikely that the solutions were at thermal equilibrium with their surroundings when [DO] measurements were attempted. The calibration data supplied by Lazar indicate that the electrode reading was affected by about 10% for each 5°C change in temperature, so even a small temperature difference would affect [DO] measurements.

One solution to this problem would have been to allow the samples to fully cool before making any [DO] measurements; however, it is known that Fe(II) undergoes a non-photochemical reaction with atmospheric oxygen in acidic aqueous solutions containing SO_2.[8] Because of this reaction, we tried to minimise the time between preparing the solution and measuring the [DO] concentration.

It is significant that almost all of the dissolved oxygen was removed from the 9.3M and 12.4M sulfuric acid solutions, but that the 18.2M solution retained a high concentration of DO. Apparently the extent of the non-photochemical reaction of O_2 with Fe(II) and SO_2 is increased in moderately concentrated acid solutions, but limited

in very concentrated acid solution. This could be due to either speciation or kinetic restrictions.

Since the concentration of Fe(III) was not monitored during the photolysis of Fe(II) in 3.9M, 9.3M or 12.4M acid solutions, there is no context for the observed changes in [DO] in these solutions, and the measurements are not especially meaningful. The main purpose of these experiments was to satisfy ourselves that the DO Probe would function correctly in 18.2M (98wt.%). It appeared that the probe was working correctly, subject to the limitations discussed here and in Sections (5.3.7.2) and (5.3.7.3).

5.4.12 *Measurements of Dissolved Oxygen Concentration During Photolysis Experiments(II) – Effect of [Fe(II)] and [SO_2]*

The second series of experiments measured the concentration of dissolved oxygen in photolysed solutions of 98wt% sulfuric acid, containing Fe(II) and SO_2. These were conducted to complement the results of Section 5.4.6, where the concentration of Fe(III) in such solutions was monitored during photolysis. Solutions were prepared by dissolving solid ammonium ferrous sulfate and anhydrous sodium sulfite in Analar grade sulfuric acid. The acid was used straight from the bottle – without degassing – in order to increase the initial concentration of dissolved oxygen, and therefore improve the likelihood of detecting a decrease due to the photolysis. Sodium sulfite dissolved readily in the acid, but ammonium ferrous sulfate was slow to dissolve, and this limited the upper concentration of Fe(II) in the solutions. Experiments measured the [DO] before and after photolysis in solutions containing [Fe(II)] = 1×10^{-3}M and (i) [SO_2] = 0M, (ii) [SO_2] = 6×10^{-2}M and (iii) [SO_2] = 1×10^{-1}M, and also on solutions with [Fe(II)] = 5×10^{-4}M and [SO_2] = 1×10^{-1}M. These concentrations were higher than those used in Section 5.4.6 in order to increase the rate of the reaction and thus increase the likelihood of O_2 removal.

Solutions were photolysed with 0.25W of 248nm light for varying time periods, with [DO] measurements before and after photolysis. Results from the experiments are presented in Fig. 5.46 as the observed change in dissolved oxygen concentration as a function of photolysis time. It was found that the electrode signal stabilised more rapidly for [DO] measurements of non-photolysed solutions than on irradiated solutions. This is thought to be because the solution was at room temperature before the photolysis, and therefore the [DO] measurement was made at constant temperature. Measurements on irradiated solutions took longer to stabilise because the solutions had converted some of the absorbed light to heat, and therefore the [DO] measurement was affected by the solution cooling down after irradiation.

The results show a large scatter, and thus cannot provide detailed information on the fate of dissolved oxygen in irradiated solutions. Perhaps the most surprising observation was that many of the solutions retained a measurable concentration of dissolved oxygen, even after prolonged irradiation. This result was unexpected, and is thought to be an error due to the high uncertainty in the results. Since the amount of oxygen removed from solution does not appear to increase when the solution is irradiated for a longer time, we believe that the correct result is that all dissolved oxygen was removed from the portion of the acid sample that was irradiated. Some

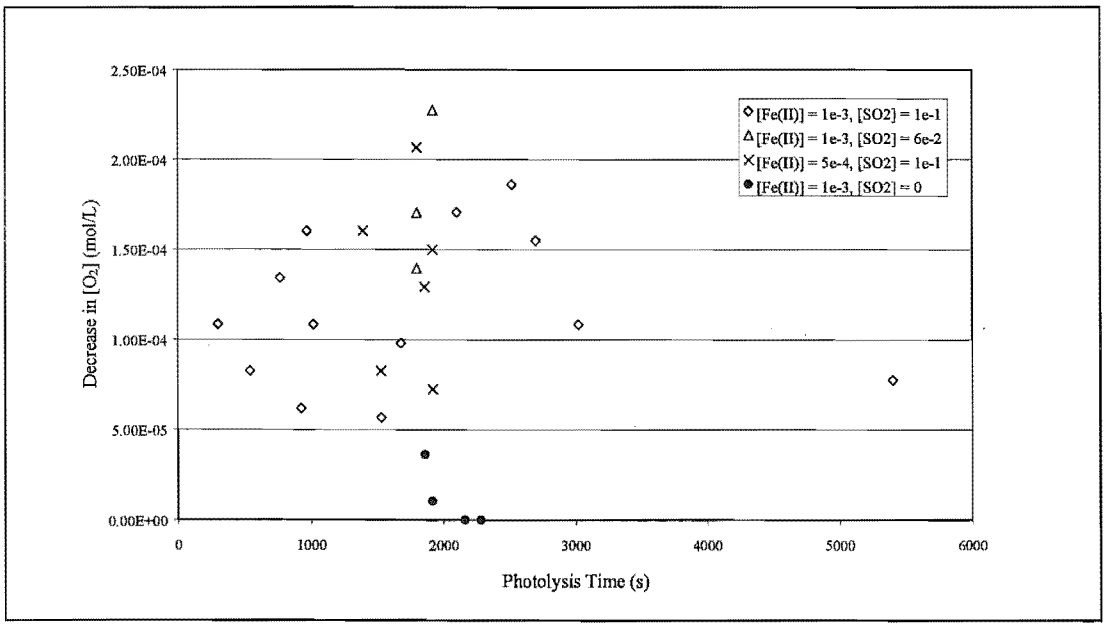

Figure 5.46 Effect of 248nm photolysis on dissolved oxygen concentration in sulfuric acid solutions containing Fe(II) and SO_2

residual oxygen was observed because the full volume of the acid was not in the path of the laser beam, and thus the photochemical reaction did not occur uniformly throughout the sample. From Fig. 5.46, it appears that oxygen was fully removed after less than 1000s irradiation. In comparison, it was found that the concentration of Fe(III) continued to increase after being irradiated for more than 4000s.

There was little or no change observed in the concentration of O_2 when SO_2 was not added to the solution, suggesting that the reaction responsible for removing O_2 also involved SO_2.

The measurement of dissolved oxygen concentration in concentrated sulfuric acid solutions has not provided data suitable for kinetic analysis, due to the variability of the results and the uncertainty introduced by slow electrode responses. However, the qualitative information gained from these experiments has significance for any reaction mechanism that is proposed. In particular, the mechanism must account for the removal of at least some of the dissolved oxygen during photolysis, and the necessity of having SO_2 present for the removal of any oxygen. In addition, the reaction must explain the continued oxidation of Fe(II) even after there is no further change in the oxygen concentration.

5.5 Conclusion

The photochemical interconversion of Fe(II) and Fe(III) has been observed experimentally, and the study of this reaction has provided results that are useful for determining a plausible mechanism for the reaction. The reaction mechanism and possible significance for the cloud chemistry of Venus are discussed in the final chapter of this thesis.

Chapter 6

Reaction Mechanism for the Photochemical Interconversion of Fe(II) and Fe(III) in Concentrated Sulfuric Acid Solution

Chapter 6

Reaction Mechanism for the Photochemical Interconversion of Fe(II) and Fe(III) in Concentrated Sulfuric Acid Solution

6.1 Overview of Experimental Results

In the previous chapter, the results from a number of irradiation experiments were described. The objective of this final chapter is to suggest a series of reactions that provide a plausible explanation of the experimental observations, and to discuss the implications of the results for the cloud chemistry of Venus. First, however, the results from Chapter 5 are briefly summarised, as a successful mechanism must be able to account for these observations.

(1) Fe(II) in concentrated sulfuric acid (98wt%) is oxidised to Fe(III) when irradiated at 193nm and 248nm. The reaction rate is directly proportional to [Fe(II)].

(2) Fe(III) in concentrated sulfuric acid is reduced to Fe(II) under the same conditions. The reaction is much slower than the oxidation of Fe(II).

(3) When a solution is irradiated, the two photochemical reactions compete, resulting in an equilibrium composition in which both Fe(II) and Fe(III) are present.

(4) Adding SO_2 increases the initial rate of Fe(II) oxidation, although it does not appear to affect the overall extent of the reaction. The increase in reaction rate is linearly related to the SO_2 concentration.

(5) Oxygen is consumed during the photochemical oxidation of Fe(II). The experimental results are unclear, but it is believed that dissolve O_2 is fully removed from the irradiated solution.

6.2 Primary photochemical processes

In all of the experiments, there are three groups of species that may be responsible for initiating the reaction by photochemical decomposition. These are Fe(II) complexes, Fe(III) complexes, and SO_2 complexes, and are each considered in turn.

6.2.1 Photolysis of Fe(II) Species

In aqueous solution, Fe(II) absorbs strongly at all wavelengths shorter than 290nm. In solutions of Fe^{2+} in dilute sulfuric acid, photolysis results in the formation of Fe^{3+} and a hydrated electron (Section 1.4.4.1):

$$Fe^{2+}_{(aq)} + h\nu \longrightarrow Fe^{3+}_{(aq)} + e^-_{(aq)} \qquad (1.49)$$

However, all attempts to determine the ultraviolet absorption spectrum of Fe(II) in concentrated sulfuric acid solution have been unsuccessful. Fe(II) does not absorb strongly in the wavelength range of 200-800nm, and any weak absorbance that may occur is masked by the presence of a trace amount of Fe(III) (Section 5.4.1). Our measurements give an upper limit for the molar extinction coefficient of Fe(II) in concentrated sulfuric acid of 4 $L.mol^{-1}cm^{-1}$ at 248nm. However, there is some evidence for a stronger absorption at shorter wavelengths, making it possible that an analagous process to (1.49) could occur at 248nm.

The reactions of solvated electrons in azeotropic sulfuric acid have been studied using the pulse radiolysis method[1] by Polevoi et al. When sulfuric acid is subjected to short bursts of ionising radiation, processes (6.1a) and (6.1b) occur.

$$H_2SO_4 \longrightarrow H_2SO_4^+ + e^- \qquad (6.1a)$$

$$\longrightarrow H_2SO_4^* \qquad (6.1b)$$

Polevoi et al demonstrated that no product formation could be attributed to reactions of $H_2SO_4^*$. Instead, they observed the formation of HSO_4 from $H_2SO_4^+$:

$$H_2SO_4^+ + H_2SO_4 \longrightarrow H_3SO_4^+ + HSO_4 \qquad (6.2)$$

and formation of HSO_3 from e^- by one or more of the following processes:

$$e^- + H_2SO_4 \longrightarrow H_2SO_4^- \xrightarrow{H_3O^+} 2H_2O + HSO_3^\cdot \quad (6.3)$$

$$e^- + H_2SO_4 \longrightarrow H_2O + SO_3^{-\cdot} \quad (6.4a)$$

$$\longrightarrow OH^- + HSO_3^\cdot \quad (6.4b)$$

These reactions were regarded as equivalent, because OH^- and $SO_3^{-\cdot}$ undergo rapid protonation in sulfuric acid. Significantly, the formation of $H^\cdot$, which is the normal fate of solvated electrons in water, was not observed. If the solution was saturated with O_2, then no $HSO_3^\cdot$ was observed and $HSO_5^\cdot$ was formed instead by the rapid reaction of $HSO_3^\cdot$ with O_2:

$$HSO_3^\cdot + O_2 \longrightarrow HSO_5^\cdot \quad (6.5)$$

Thus, combining reactions (1.49) (in sulfuric acid rather than water) with (6.3),(6.4a) and (6.4b), we propose that the photolysis of Fe^{2+} in concentrated sulfuric acid results in reaction (6.6):

$$Fe^{2+} + H_2SO_4 + H^+ + h\nu \longrightarrow Fe^{3+} + HSO_3^\cdot + H_2O \quad (6.6)$$

In practice, the extent of this reaction will be limited by the low absorption of Fe^{2+} relative to the photolysis product Fe^{3+}.

6.2.2 *Photolysis of Fe(III) species*

Fe^{3+} absorbs strongly at 248nm in concentrated sulfuric acid solution, with a measured molar extinction coefficient of 6136 $L.mol^{-1}cm^{-1}$, which is much larger than any other species present during our irradiation experiments. Fe^{3+} was present in all of the solutions that were irradiated, including those solutions that were prepared without intentionally adding Fe^{3+}. In these solutions, Fe^{3+} was formed by way of the following equilibrium:

$$2Fe^{2+} + H_2SO_4 + 2H^+ \rightleftharpoons 2Fe^{3+} + SO_2 + 2H_2O \quad (6.7)$$

A close inspection of the absorption spectra of standard Fe(II) solutions in concentrated sulfuric acid showed that between 0.5 to 2% of the Fe(II) initially added had been converted to Fe(III). There was also an absorbance shoulder at 280nm due to SO_2 in the solutions. The concentration of SO_2 was approximately ten times larger

than that of Fe(III), indicating that it was not produced by reaction (6.7). Since the H_2SO_4 used to prepare the standard solutions had not been degassed, it is most likely that there was SO_2 initially present in the acid.

The equilibrium constant of (6.7) is given by:

$$K_{6.7} = \frac{a(Fe^{3+})^2 a(SO_2) a(H_2O)^2}{a(Fe^{2+})^2 a(H^+)^2 a(H_2SO_4)}$$

In concentrated sulfuric acid solution, the activities of H_2O, H_2SO_4 and H^+ will remain approximately constant, regardless of the position of the equilibrium. Thus, the formula for the equilibrium constant can be re-written as:

$$K_{6.7} = K' \frac{a\left(Fe^{3+}\right)^2 a\left(SO_2\right)}{a\left(Fe^{2+}\right)^2}$$

The concentrations of Fe(III) and SO_2 in each of the Fe(II) standard solutions were determined from the solutions' UV absorption spectra, which contained quantifiable contributions due to Fe(III) and SO_2. The concentration of Fe(II) was calculated from the initial amount of Fe(II) salt added and the Fe(III) concentration. Using these values, the product of $[Fe^{3+}]^2.[SO_2] / [Fe^{2+}]^2$ was calculated for each solution. This was found to vary over one order of magnitude, indicating that the reaction had not reached equilibrium when the spectra measurements were recorded. It was noted that the intensity of the Fe(III) absorption continued to increase for more than a week, even in deoxygenated solutions. Thus, kinetic considerations prevent (6.7) from reaching equilibrium within the timeframe of our experiments. Furthermore, the reaction is assumed to be too slow to have any effect on the solution composition during irradiation. It does, however, produce enough Fe^{3+} to initiate photochemistry in all of our irradiated solutions.

The UV absorption spectra of Fe(III) in sulfuric acid solution was reported in Section 5.4.1. The molar extinction coefficient is dependent on the acid concentration, and reaches a maximum when Fe(III) is dissolved in 15M sulfuric acid solution, corresponding to a mole fraction of 0.55 sulfuric acid (Fig. 5.22). Measurements of the Raman spectra of sulfuric acid solutions, reviewed in Liler[2], have been used to determine the concentrations of dissociated sulfuric acid species as a function of total H_2SO_4 concentration (Fig. 6.1), and it was found that the concentration of HSO_4^-

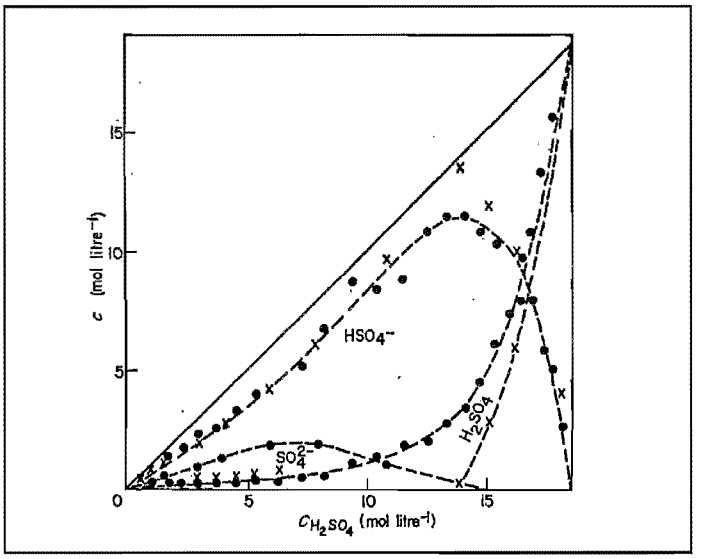

Figure 6.1 Concentrations of species in sulfuric acid/water mixtures from Raman spectra, (×) Young et al (1959); (•) Zarakhini and Vinnik (1963).[2]

reached a maximum in 13-14M H_2SO_4 solution. Since the maximum value of $\varepsilon_{Fe(III)}$ occurs at an acid concentration close to the maximum concentration of HSO_4^-, we believe that the dominant absorbing species is the Fe(III)-HSO_4^- complex. In this case, the primary photochemical process for Fe(III) in concentrated sulfuric acid solution is:

$$[Fe.HSO_4]^{2+} + h\nu \longrightarrow Fe^{2+} + HSO_4^{\cdot} \qquad (6.8)$$

The other Fe(III) species that may be present in the solution is $[FeSO_4]^+$, which would be photolysed to form:

$$[FeSO_4]^+ + h\nu \longrightarrow Fe^{2+} + SO_4^{-\cdot} \qquad (6.9)$$

$Fe^{3+}.H_2O$ is not expected to be present in the system, since virtually all of the water in 98wt% sulfuric acid is bound in acid hydrate complexes[3].

Benkelberg and Warneck have reported two photochemical processes in aqueous Fe(III) solutions[4]:

$$[Fe(OH)]^{2+}_{(aq)} + h\nu \longrightarrow Fe^{2+}_{(aq)} + {}^{\cdot}OH \qquad (1.50a)$$

$$[FeSO_4]^+_{(aq)} + h\nu \longrightarrow Fe^{2+}_{(aq)} + SO_4^{-\cdot} \qquad (1.51)$$

The reported quantum yields for both processes have the same wavelength-dependence over the range 280 to 370nm, with increased quantum yields at short wavelengths. However, the quantum yields for (1.50a) were approximately 50 times larger than for (1.51). To explain this, Benkelberg and Warneck suggested that the quantum yield was limited by the ability of the radicals to escape the solvent cage in which they were formed. In (1.50a), the geminate pair are free to diffuse apart. In (1.51), however, the photolysis products are subject to a Coulomb field attraction, making it more difficult for them to move apart and thus increasing the likelihood of recombination.

A similar argument can be applied to Fe(III) species in sulfuric acid. $[Fe.HSO_4]^{2+}$ in concentrated sulfuric acid is analagous to $[FeOH]^{2+}$ in water. One of the photolysis products is uncharged, and thus there is no Coulombic attraction preventing the photofragments from diffusing apart. However, the products of $[Fe.SO_4]^{+}$ photolysis carry opposite charges, and the quantum yield for the photolysis is expected to be small.

In summary, all of the sulfuric acid solutions that were irradiated at 248nm contained some initial Fe(III), including the Fe(II) solutions with nominal $[Fe(III)]_i = 0$. Fe(III) absorbs strongly at 248nm, with the most likely photochemical process being

$$[Fe.HSO_4]^{2+} + h\nu \longrightarrow Fe^{2+} + HSO_4^{\cdot} \qquad (6.8)$$

The K_a of the $HSO_4^{\cdot}$ radical is unknown. However, Polevoi et al's pulse radiolysis study of sulfuric acid[1] showed that the absorption spectrum of the sulfate radical in 98 wt% sulfuric acid is red-shifted compared to the $SO_4^{-\cdot}$ absorption spectra reported in more dilute acid or neutral solutions. This indicates that the protonated species, $HSO_4^{\cdot}$, is dominant in 98wt% sulfuric acid solutions, where our experiments were performed.

6.2.3 Photolysis of S(IV) Species

All of the Fe(II) solutions that were irradiated in Chapter 5 contained a small trace of dissolved SO_2 which was produced by reaction (6.7). In addition, it was found that increasing the SO_2 concentration in a solution increased the initial rate of Fe(III) formation (Fig. 5.34). The plot of Initial Rate vs [S(IV)] is linear, and shows that the reaction proceeds at an appreciable rate, even when [S(IV)] is extrapolated to zero. Thus, the main photochemical primary process leading to Fe(III) formation does not involve SO_2. However, the photolysis of SO_2 may contribute to the increased rate of Fe(III) formation observed when solutions containing comparable amounts of SO_2 and Fe(II) are irradiated.

The UV absorption spectrum of $SO_{2(aq)}$ consists of a single featureless absorbance at wavelengths below 260nm. Warneck et al[5], have reported that the primary photochemical processes for SO_2 in aqueous solution are

$$SO_3^{2-}{}_{(aq)} + h\nu \longrightarrow SO_3^{-\cdot} + e^-_{(aq)} \qquad (6.10)$$

$$HSO_3^-{}_{(aq)} + h\nu \longrightarrow SO_3^{-\cdot} + H^{\cdot} \qquad (6.11)$$

The quantum yield for (6.10) is 0.38 at 253.7nm, and for (6.11) is 0.19 at 213.9nm. The higher quantum yield for (6.10) may be attributed to Coulombic repulsion between the geminate pair, preventing recombination.

The UV absorption spectrum of SO_2 in concentrated sulfuric acid was reported in Chapter 5 (Fig. 5.19). Unlike the absorption spectrum in aqueous solution, there are two maxima present, occurring at 200nm and 280nm. This suggests that photochemical processes other than simple charge-transfer-to-solvent may occur. Possible reactions are:

$$HSO_3^- + h\nu \longrightarrow H^{\cdot} + SO_3^{-\cdot} \qquad (6.12)$$

$$SO_2.HSO_4^- + h\nu \longrightarrow H^{\cdot} + SO_2.\,SO_4^{-\cdot} \longrightarrow H^{\cdot} + SO_2 + SO_4^{-\cdot} \qquad (6.13a)$$

$$\longrightarrow H^{\cdot} + SO_3 + SO_3^{-\cdot} \qquad (6.13b)$$

$$SO_2.H_2SO_4 + h\nu \longrightarrow H^{\cdot} + SO_2.HSO_4^{\cdot} \longrightarrow H^{\cdot} + SO_2 + HSO_4^{\cdot} \qquad (6.14a)$$

$$\longrightarrow H^{\cdot} + SO_3 + HSO_3^{\cdot} \qquad (6.14b)$$

Reactions (6.13a) and (6.14a) result in the same products, as do (6.13b) and (6.14b), since the sulfoxy-radicals undergo rapid protonation in concentrated sulfuric acid. However, the pairs of reactions may not be entirely equivalent, since the partitioning between (6.13a) and (6.13b) may be different to that between (6.14a) and (6.14b). Without a greater knowledge of the speciation of dissolved S(IV) in concentrated sulfuric acid, it is not possible to decide which of (6.12), (6.13) or (6.14) will occur during the photolysis of SO_2 in concentrated sulfuric acid.

An alternative possibility is that SO_2 forms a complex with Fe(III), similar to that observed in aqueous solution, which is photodissociated in a reaction analagous to (1.52).

$$[FeSO_3]^+_{(aq)} + h\nu \longrightarrow Fe^{2+} + SO_3^{-\cdot} \qquad (1.52)$$

At present, it is not possible to determine which of the possible SO_2 photolysis reactions actually occurs in sulfuric acid solution. Although this problem is worthy of further investigation, it has not been pursued as part of this thesis, as SO_2 photolysis is not required by any of the mechanisms that are proposed for the photochemical oxidation of Fe(II).

6.3 Proposed Reaction Mechanisms

6.3.1 Photolysis of Fe(III) Solutions

We start with the simplest case, the irradiation of a sulfuric acid solution that initially contains Fe(III) only. In this solution, $[Fe.HSO_4]^{2+}$ is photolysed according to (6.8) to form Fe^{2+} and $HSO_4^{\cdot}$. Possible reactions of $HSO_4^{\cdot}$ are listed in Table 6.2. A complete list of the reactions discussed in this chapter is found in Table 6.4 on Page 207. Rate constants for the equivalent reactions of $SO_4^{-\cdot}$ in aqueous solution are taken from HALIPP[6], and are used as a guide to which reactions are likely to be rapid. These are, however, treated with caution, since the reactivity of a species can be altered significantly by protonation.

Reaction	k/dm^{3}mol^{-1}s^{-1}	No.
$HSO_4^{\cdot} + Fe^{2+} \longrightarrow HSO_4^- + Fe^{3+}$	$(3 - 4.8)\times10^8$	(6.15)
$HSO_4^{\cdot} + H_2O \longrightarrow H_2SO_4 + {}^{\cdot}OH$	9 - 12	(6.16)
$HSO_4^{\cdot} + H_2SO_4 \longrightarrow H_2SO_4 + HSO_4^{\cdot}$	unknown	(6.17)
$HSO_4^{\cdot} + HSO_4^{\cdot} \longrightarrow H_2S_2O_8$	$(1.6 - 4.5)\times10^8$ in H_2O 7.6×10^8 in 10M H_2SO_4	(6.18)
$HSO_4^{\cdot} + {}^{\cdot}OH \longrightarrow H_2SO_5$	9×10^9	(6.19)
$HSO_4^{\cdot} + S_2O_8^{2-} \longrightarrow HS_2O_8^{\cdot} + SO_4^{2-}$	6.1×10^5	(6.20)

Table 6.2 Reactions of $HSO_4^{\cdot}$ radical in concentrated sulfuric acid. Rate constants are for the equivalent reactions of $SO_4^{\cdot-}$ in aqueous solution

Reactions (6.15) – (6.18) involve the most common species in the irradiated solution. There are no plausible reactions between $HSO_4^{\cdot}$ and Fe^{3+}. Reaction (6.16) is too slow to be significant in our system, and (6.17) merely results in transfer of the radical from one sulfuric acid molecule to the next. This leaves reactions (6.15) and (6.18). Since the amounts of Fe^{2+} and $HSO_4^{\cdot}$ produced by (6.8) are equal, neither (6.15) or (6.18) will dominate, and the overall reaction:

$$2[FeHSO_4]^{2+}{}_{(H2SO4)} + h\nu \longrightarrow 2Fe^{2+}{}_{(H2SO4)} + H_2S_2O_{8(H2SO4)} \qquad (6.21)$$

will result. The quantum yield for production of Fe^{2+} will be low, and the reaction will be inhibited by any Fe^{2+} that is initially present. $H_2S_2O_8$ absorbs light at 248nm and thus some of the product will be photolysed – reversing the effect of (6.18) and re-forming $HSO_4^{\cdot}$. This does not compromise the proposed reaction mechanism, but will affect the steady-state concentration of $HSO_4^{\cdot}$ attained during the photolysis.

The reverse reaction should occur after the irradiation is stopped, since $H_2S_2O_8$ is, of course, a powerful oxidising agent capable of oxidising Fe^{2+} to Fe^{3+}; during experiments however, the concentration of Fe^{3+} was not observed to rise after irradiation ceased. This can be explained by proposing that the reaction is too slow to be observed using the experimental method described in Chapter 5. The mechanism

proposed by Mariano[7] for this reaction in 5mol.L^{-1} sulfuric acid solution involves $HS_2O_8^-$, rather than $H_2S_2O_8$:

$$HS_2O_8^- + Fe^{2+} \longrightarrow HSO_4^- + SO_4^{\cdot-} + Fe^{3+} \quad (6.22)$$

$$SO_4^{\cdot-} + Fe^{2+} \longrightarrow SO_4^{2-} + Fe^{3+} \quad (6.15a)$$

$$HS_2O_8^- + 2Fe^{2+} \longrightarrow HSO_4^- + SO_4^{2-} + 2Fe^{3+}$$

If the reaction requires $HS_2O_8^-$, rather than $H_2S_2O_8$, then its rate would be limited in 98wt% sulfuric acid due to the extremely low concentration of the deprotonated species.

6.3.2 Photolysis of Fe(II) Solutions

6.3.2.1 Fe(III) Absorption as Primary Process

Next, we consider the reactions that occur in photolysed Fe(II) solutions. Since there is a small amount of Fe(III) initially present due to reaction (6.7), the most likely primary photochemical process is reaction (6.8). The $HSO_4^{\cdot}$ radical produced by (6.8) will react according to (6.15)-(6.20), as discussed in 6.3.1; since the concentration of Fe(II) is much greater than the concentration of $HSO_4^{\cdot}$, the predominant reaction will be (6.15) – the reoxidation of Fe^{2+} by $HSO_4^{\cdot}$. However, another reaction is also possible – the reaction of $HSO_4^{\cdot}$ with dissolved SO_2, which will be present in the solution due to (6.7):

$$HSO_4^{\cdot} + HSO_3^- \longrightarrow HSO_4^- + HSO_3^{\cdot} \quad (6.23)$$

($k_{6.23} = 7\times10^8$L.mol^{-1}s^{-1} in aqueous solution) This reaction is fast enough for (6.23) to compete with (6.15), despite the high concentration of Fe(II).

Once $HSO_3^{\cdot}$ is formed, it will react rapidly with any dissolved oxygen in the solution:

$$HSO_3^{\cdot} + O_2 \longrightarrow HSO_5^{\cdot} \quad (6.5)$$

($k_{6.5} = 2\times10^9$ L.mol^{-1}s^{-1} in aqueous solution, which is close to the rate for a purely diffusion limited reaction) The product, $HSO_5^{\cdot}$ reacts with Fe^{2+} according to:

$$HSO_5^{\cdot} + Fe^{2+}.H_2SO_4 \longrightarrow HSO_5^- + Fe^{3+}.H_2SO_4 \quad (6.24)$$

($k_{6.24}$ = 4×10^7 $L.mol^{-1}.s^{-1}$ for the analagous reaction between $SO_5^{-\cdot}$ and $Fe^{2+}.H_2O$ in aqueous solution). The product of the reaction, HSO_5^-, is peroxymonosulfate anion, which a powerful oxidising agent. Fe^{2+} is oxidised according to:

$$HSO_5^- + Fe^{2+}.H_2SO_4 + H^+ \longrightarrow HSO_4^{\cdot} + FeHSO_4^{2+} + H_2O \qquad (6.25)$$

This produces $HSO_4^{\cdot}$, and completes the chain reaction consisting of reactions (6.23)-(6.25) and (6.5):

$$HSO_4^{\cdot} + HSO_3^- \longrightarrow HSO_4^- + HSO_3^{\cdot} \qquad (6.23)$$

$$HSO_3^{\cdot} + O_2 \longrightarrow HSO_5^{\cdot} \qquad (6.5)$$

$$HSO_5^{\cdot} + Fe^{2+}.H_2SO_4 \longrightarrow HSO_5^- + Fe^{3+}.H_2SO_4 \qquad (6.24)$$

$$HSO_5^- + Fe^{2+}.H_2SO_4 + H^+ \longrightarrow HSO_4^{\cdot} + FeHSO_4^{2+} + H_2O \qquad (6.25)$$

$$HSO_3^- + O_2 + 2Fe^{2+} + H_2SO_4 + H^+ \xrightarrow{Fe^{3+},\, h\nu} 2HSO_4^- + 2Fe^{3+} + H_2O \qquad (I)$$

The chain length of (I) will be determined by competition between (6.15) and (6.23), and is approximately equal to $k_{6.23}[HSO_3^-]/k_{6.15}[Fe(II)]$. Typical initial concentrations of these species during the photolysis of "Fe(II) only" solutions were [Fe(II)] = 1×10^{-4}M and $[HSO_3^-] = 5\times10^{-6}$, if we assume that HSO_3^- is present due to (6.7) and the initial concentration of HSO_3^- is $\frac{1}{2}[Fe(III)]_i$. Using the rate constants for the analagous reactions in aqueous solution, this gives an initial chain length of 3×10^{-4}. As the reaction proceeds, $[HSO_3^-]$ will decrease significantly while [Fe(II)] remains approximately constant and the chain length will drop to zero.

The chain length of (I) can be increased by the branching reaction (6.26a):

$$HSO_5^{\cdot} + HSO_3^- \longrightarrow HSO_5^- + HSO_3^{\cdot} \qquad (6.26a)$$

($k_{(6.26a)} = 8.1\times10^3$ $L.mol^{-1}s^{-1}$ in aqueous solution), which competes effectively with:

$$HSO_5^{\cdot} + HSO_3^- \longrightarrow HSO_4^- + HSO_4^{\cdot} \qquad (6.26b)$$

($k_{6.26b)} = 340$ $L.mol^{-1}s^{-1}$ in aqueous solution). Additional chain termination steps exist, including the direct oxidation of Fe^{2+} by $HSO_3^{\cdot}$, competing with (6.5):

$$HSO_3^{\cdot} + Fe^{2+}_{(H2SO4)} \longrightarrow HSO_3^- + Fe^{3+}_{(H2SO4)} \qquad (6.27)$$

(rate constant unknown), and all the possible fast bi-molecular reactions involving pairs of radical ions.

The reactions that comprise reaction scheme (I) form the basis of the reaction mechanism that we reported in our first publication of these results[8]. However, further work has revealed some serious difficulties with using reaction scheme (I) to explain our experimental observations. The scheme is limited in that it can only produce Fe(III) while there is both O_2 and HSO_3^- available in the system. When all of the O_2 is consumed, reaction (6.5) can no longer occur and instead, $HSO_3^\cdot$ must react with Fe^{2+} (6.27). The reaction cycle now consists of (6.8), followed by either (6.15) or (6.23) and (6.27), and results in no net change in the concentration of Fe(III).

Likewise, when all of the HSO_3^- is consumed, (6.23) cannot occur, and the only possible reaction for $HSO_4^\cdot$ produced by (6.8) is the re-oxidation of Fe^{2+} by (6.15), again resulting in no net change in [Fe(III)].

Thus, reaction scheme (I) will cease to be effective when either $[HSO_3^-]$ or $[O_2]$ is zero. This is inconsistent with experimental observations, where the observed increase in [Fe(III)] is more than twice the initial $[HSO_3^-]$ concentration (See, for instance, Fig. 5.28, where $\Delta[Fe(III)] > 3\times10^{-5}$, but the maximum initial concentration of HSO_3^- was 8×10^{-6}M). In addition, considerable effort was made to remove dissolved O_2 from the system. The concentration of dissolved oxygen in the degassed solution was measured at $(6\text{-}9)\times10^{-5}$M using an electrochemical probe (Section 5.4.11). However, the probe was not designed for use in concentrated sulfuric acid, and we believe that the true value of $[O_2]$ was much lower. We have come to the conclusion that Scheme (I) alone is insufficient to account for our experimental observations. However, it will proceed until either O_2 or HSO_3^- is fully consumed, and is responsible for a significant proportion of the initial reaction that is observed. To account for the continued production of Fe(III) during a prolonged irradiation, we are required to consider other primary photochemical processes.

6.3.2.2 Fe(II) Absorption as Primary Process

Although the absorption by Fe(II) species in concentrated sulfuric acid is weak at 248nm, we believe that it is an important primary process. Absorption by Fe(II) produces Fe^{3+} and $HSO_3^{\cdot}$ according to (6.6):

$$Fe^{2+} + H_2SO_4 + H^+ + h\nu \longrightarrow Fe^{3+} + HSO_3^{\cdot} + H_2O \qquad (6.6)$$

$HSO_3^{\cdot}$ from (6.6) can either react with Fe^{2+} directly according to (6.27), or it can react with dissolved oxygen according to (6.5), followed by (6.24), (6.25) and (6.23).

Thus, absorption by Fe(II) can lead to either:

$$Fe^{2+} + H_2SO_4 + H^+ + h\nu \longrightarrow Fe^{3+} + HSO_3^{\cdot} + H_2O \qquad (6.6)$$
$$HSO_3^{\cdot} + Fe^{2+}.H_2SO_4 \longrightarrow HSO_3^- + Fe^{3+}.H_2SO_4 \qquad (6.27)$$
$$2\,Fe^{2+} + H_2SO_4 + H^+ \xrightarrow{h\nu} 2Fe^{3+} + HSO_3^- + H_2O \qquad (II)$$

or a radical chain oxidation initiated by $HSO_3^{\cdot}$ radicals generated by (6.6):

$$HSO_3^{\cdot} + O_2 \longrightarrow HSO_5^{\cdot} \qquad (6.5)$$
$$HSO_5^{\cdot} + Fe^{2+}.H_2SO_4 \longrightarrow HSO_5^- + Fe^{3+}.H_2SO_4 \qquad (6.24)$$
$$HSO_5^- + Fe^{2+}.H_2SO_4 + H^+ \longrightarrow HSO_4^{\cdot} + FeHSO_4^{2+} + H_2O \qquad (6.25)$$
$$HSO_4^{\cdot} + HSO_3^- \longrightarrow HSO_4^- + HSO_3^{\cdot} \qquad (6.23)$$
$$2Fe^{2+} + H_2SO_4 + H^+ + HSO_3^- + O_2 \xrightarrow{h\nu} 2Fe^{3+} + H_2O + 2HSO_4^- \qquad (III)$$

Reaction scheme (III) requires HSO_3^- to be present in order to complete the chain. Since HSO_3^- is produced by scheme (II), the two reaction schemes are coupled, resulting in:

$$2\,Fe^{2+} + H_2SO_4 + H^+ \longrightarrow 2Fe^{3+} + HSO_3^- + H_2O \qquad (II)$$
$$2Fe^{2+} + H_2SO_4 + H^+ + HSO_3^- + O_2 \longrightarrow 2Fe^{3+} + H_2O + 2HSO_4^- \qquad (III)$$
$$4Fe^{2+} + 2H_2SO_4 + 2H^+ + O_2 \xrightarrow{h\nu} 4Fe^{3+} + 2HSO_4^- + 2H_2O \qquad (IV)$$

This scheme provides a path by which all of the O_2 in solution will react, even when the initial concentration of HSO_3^- is minimal. Once all of the available O_2 is consumed, Scheme (II) remains in effect, and will continue to produce Fe(III) and

SO_2, accounting for the experimental observation that Fe(III) formation continues throughout the irradiation.

Reaction schemes (II) and (IV) are self-inhibiting, due to absorption of light by the product, Fe(III). This acts as an internal filter and slows the reaction by reducing the intensity of light available for Fe(II) photolysis. Consequently, the photolysis rate will become immeasurably slow when the concentration of Fe(III) is high.

Although several important quantities are unknown, the experimental results indicate that absorption by Fe(II) is a plausible primary process, despite the low value of the molar extinction coefficient. If we assume that the primary absorption process is (6.6), then the rate of formation of Fe(III) is given by:

$$\frac{d[Fe(III)]}{dt} = \frac{\Phi \times I_{abs,Fe(II)}}{V \times N_A} \tag{6.28}$$

where Φ is the total quantum yield of the production of Fe(III), ie the number of Fe(III) ions produced per photon absorbed by Fe(II)

$I_{abs,\ Fe(II)}$ is the amount of light absorbed by Fe(II) per second, measured in photons.s^{-1}

V is the volume of the irradiated sample (= 0.0057 L)

N_A is Avogadro's Number, (= 6.022×10^{23} mol^{-1})

The amount of light absorbed by Fe(II) per second ($I_{abs,Fe(II)}$) is given by:

$$I_{abs,Fe(II)} = I_{0,Fe(II)}\left(1-10^{-\varepsilon_{Fe(II)}\times[Fe(II)]\times l}\right)$$

$$= I_{0,Fe(II)}\left(2.303\times\varepsilon_{Fe(II)}\times[Fe(II)]\times l\right) \tag{6.29}$$

provided that ($\varepsilon_{Fe(II)} \times [Fe(II)] \times l$) is <<1, which is true in all of our experiments due to the extremely small value of $\varepsilon_{Fe(II)}$. $I_{0,Fe(II)}$ is the intensity of the 248nm light incident on Fe(II) in the sample, measured in photons per second, $\varepsilon_{Fe(II)}$ is the molar extinction coefficient of Fe(II) at 248nm, [Fe(II)] is the concentration of Fe(II) and l is the pathlength of the cell (= 2.1cm).

The product of the reaction, Fe(III), absorbs strongly at 248nm and acts as an "inner filter", reducing the amount of light available to be absorbed by Fe(II). Thus, I_0 in equation (6.29) decreases as the reaction progresses. Since the absorption of light by Fe(III) is much greater than the absorption by Fe(II), the effective value of I_0 is determined by the amount of light transmitted by Fe(III):

$$I_{0,Fe(II)} = I_{trans,Fe(III)} = I_{0,cell}\left(10^{-\varepsilon_{Fe(III)}\times[Fe(III)]\times l}\right) \tag{6.30}$$

where $I_{0,cell}$ is the intensity of light incident on the cell (photons.s^{-1})

$\varepsilon_{Fe(III)}$ is the molar extinction coefficient of Fe(III) at 248nm

(=6136 L.mol^{-1}cm^{-1})

[Fe(III)] is the concentration of Fe(III)

l is the pathlength of the cell (= 2.1 cm)

Combining (6.28), (6.29) and (6.30), we have:

$$\frac{d[Fe(III)]}{dt} = \frac{\Phi\times I_{0,cell}\left(10^{-\varepsilon_{Fe(III)}\times[Fe(III)]\times l}\right)\left(2.303\times\varepsilon_{Fe(II)}\times[Fe(II)]\times l\right)}{V\times N_A}$$

$$= \left(\frac{2.303\times l\times I_{0,cell}\times\Phi\times\varepsilon_{Fe(II)}}{N_A\times V}\right)\times\frac{[Fe(II)]}{10^{\varepsilon_{Fe(III)}\times[Fe(III)]\times l}} \tag{6.31}$$

Equation (6.31) indicates that a plot of d[Fe(III)]/dt vs [Fe(II)]/($10^{\varepsilon Fe(III)\times[Fe(III)]\times l}$) will be linear if the primary process is absorption by Fe(II). The gradient will contain information about the quantum yield of the reaction and the molar extinction coefficient of Fe(II).

Figure 6.3 shows the graph of d[Fe(III)]/dt vs [Fe(II)]/($10^{\varepsilon Fe(III)\times[Fe(III)]\times l}$) for a typical irradiation of a Fe(II) solution. The initial concentration of Fe(II) was 8.9×10^{-4}M, the solution was deoxygenated, and there was no added SO_2 or Fe(III). The solution was irradiated with 0.8W of light, which corresponds to $I_{0,cell} = 1.0\times10^{18}$ photons.s^{-1}.

Two distinct regions are noted in the plot. During the initial stages of the reaction, the observed rate of the reaction is greater than predicted by (6.31). During this period equation (6.31) is not applicable, since absorption by Fe(III) initiates the reaction and gives rise to a net increase in [Fe(III)] via Scheme (I), with a possible contribution

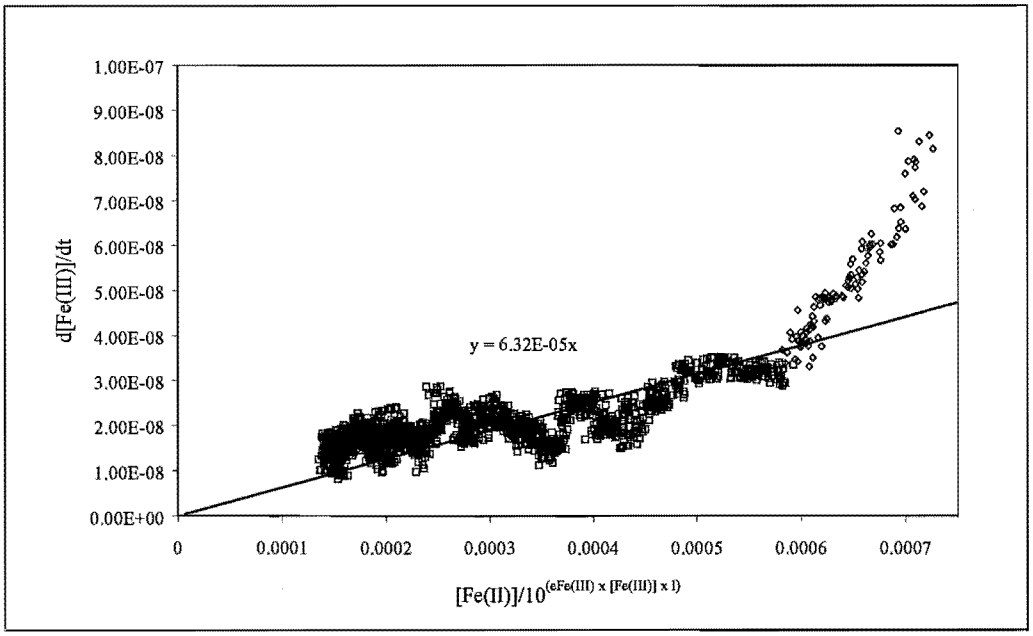

Figure 6.3 Rate equation (6.30) is tested by plotting d[Fe(III)]/dt vs $[Fe(II)]/10^{\varepsilon Fe(III) \times [Fe(III)] \times l}$ for a typical irradiated Fe(II) solution

from Schemes (III) and (IV). This continues for the first 200s of the reaction, until all dissolved oxygen in the sample is consumed. The linear portion of the graph corresponds to the reaction from 200s to 2600s, during which period Fe(III) is produced by Fe(II) absorption, via Scheme (II).

The gradient of the plot indicates that $\Phi \times \varepsilon_{Fe(II),\,248nm}$ is approximately 5×10^{-2} $L.mol^{-1}.cm^{-1}$ from 200s to 2600s. Since $\varepsilon_{Fe(II),\,248nm}$ is unknown, it is not possible to determine the actual quantum yield. However, this result confirms that absorption by Fe(II) can give rise to the observed Fe(III) production, despite a low value of $\varepsilon_{Fe(II),\,248nm}$, without requiring the quantum yield to be greater than unity.

6.3.2.3 *Fe(II) Photolysis with SO_2 Added*

The final situation that must be considered is photolysis of Fe(II) in the presence of additional SO_2. A number of possible photochemical processes involving solvated SO_2 have been proposed (reactions (6.12), (6.13a,b), (6.14a,b) and (1.52)) but it is

unknown which of these occur in concentrated sulfuric acid solution. The possible photolysis products are $SO_3^{-\cdot}$, $SO_4^{-\cdot}$ and $H^{\cdot}$.

The possible reactions of $SO_3^{-\cdot}$ and $SO_4^{-\cdot}$ have already been discussed, and either species will result in Fe^{2+} oxidation. Reaction (1.52) will be followed by (6.27), leading to no net change in [Fe(III)] unless O_2 is present, in which case the $SO_3^{\cdot}$ radicals can enter into the chain oxidation described in Scheme (III).

$H^{\cdot}$ from reactions (6.12), (6.13a,b) or (6.14a,b) is a reducing agent, and is converted to H^+ by reaction with Fe^{3+}:

$$H^{\cdot} + Fe^{3+} \longrightarrow H^+ + Fe^{2+} \qquad (6.32)$$

which will reverse the oxidation of Fe^{2+} by $SO_3^{-\cdot}$ or $SO_4^{-\cdot}$. If O_2 is present, the hydrogen atom may be converted to $HO_2^{\cdot}$, which in turn will produce $OH^{\cdot}$ by, for example:

$$HO_2^{\cdot} + HSO_3^- \longrightarrow OH^{\cdot} + HSO_4^- \qquad (6.33)$$

($k_{6.33}$ unknown) and the $OH^{\cdot}$ will oxidise any available species, such as S(IV) or Fe(II).

Thus, it appears that adding SO_2 to the irradiated solution will only affect the formation of Fe(III) while there is dissolved oxygen present. This is consistent with our observation that the initial reaction rate is increased when SO_2 is added, but that the effect of $[SO_2]$ is negligible at longer irradiation times, after all the O_2 has been consumed. (Fig. 5.33)

6.3.2.4 *Summary of Reaction Mechanism for Photochemical Oxidation of Fe(II)*

When Fe(II) in concentrated sulfuric acid solution is irradiated with 248nm light, Fe(III) and HSO_3^- are formed by Scheme (II) (resulting from Fe(II) absorption):

$$2\,Fe^{2+} + H_2SO_4 + H^+ \xrightarrow{h\nu} 2Fe^{3+} + HSO_3^- + H_2O \qquad (II)$$

If the solution also contains both dissolved oxygen and HSO_3^-, the reaction will then proceed by Scheme (I) (resulting from Fe(III) absorption):

$$HSO_3^- + O_2 + 2Fe^{2+} + H_2SO_4 + H^+ \xrightarrow{Fe^{3+},\, h\nu} 2HSO_4^- + 2Fe^{3+} + H_2O \qquad (I)$$

If the solution contains dissolved oxygen but no HSO_3^-, the reaction will proceed by Scheme (IV) (resulting from Fe(II) absorption):

$$4Fe^{2+} + 2H_2SO_4 + 2H^+ + O_2 \xrightarrow{h\nu} 4Fe^{3+} + 2HSO_4^- + 2H_2O \qquad (IV)$$

When all dissolved oxygen is consumed, the reaction will continue to produce Fe(III) by Scheme (II). The rate of the reaction will become progressively slower, since the product Fe(III) will absorb the light required for Fe(II) photolysis.

6.4 Suggestions for Future Work

Several reaction schemes have been proposed for the photochemical oxidation of Fe(II) to Fe(III) in concentrated sulfuric acid solution. There is significant interaction between these schemes, especially during the early stages of the reaction where both HSO_3^- and O_2 are present in solution. However, it has been difficult to model this early portion of the reaction due to uncertainty regarding the concentration of dissolved oxygen in the system. A rapid, reliable method for determining the concentration of dissolved oxygen in concentrated sulfuric acid would be valuable for further study of this system. Experiments should also be performed using more thoroughly deoxygenated sulfuric acid solutions.

Future experimental study of the reaction should also monitor the concentration of species other than Fe(III). A study of the changes in $[HSO_3^-]$ during the course of the irradiation would be particularly interesting, as the proposed mechanism involves HSO_3^- being consumed during the early stages of the reaction via reaction schemes (I), (III) and (IV), but being produced later in the irradiation, when $[O_2] = 0$, via scheme (II). The concentrations of Fe(III) and HSO_3^- can be simultaneously determined if the transmission of the solution is measured at multiple wavelengths

during irradiation. Similarly, $H_2S_2O_8$ has been proposed as a major product of Fe(III) photo-reduction, and should be readily detected using spectrophotometric measurements.

The molar absorption coefficients of Fe(II) in concentrated H_2SO_4 must be determined before it is possible to report a quantum yield for the important reaction (6.6).

Finally, computer modelling of the early stages of the reaction should be used to determine whether the proposed reaction mechanism is capable of reproducing the observed Fe(III) production. Preliminary attempts have shown that Scheme (I) alone is unable to reproduce the experimental results. Further modelling should include Schemes (II), (III) and (IV).

6.5 Conclusion: Significance of Fe(II)/(III) Photochemistry for the Cloud Chemistry of Venus

It is fitting to conclude this thesis by considering the role of Fe(II)/(III) photochemistry in the cloud chemistry of Venus. The composition of the Venus clouds was discussed in Section 1.24, where it was concluded that the clouds included concentrated sulfuric acid aerosols containing approximately 1% dissolved Fe. The experimental technique used to confirm the presence of iron in the clouds, x-ray fluorescence spectroscopy, is unable to determine the oxidation state of the Fe, although it has been assumed that Fe(III) is the dominant species. In addition to Fe(III), the clouds will contain dissolved SO_2, which is produced by thermal reactions in the lower atmosphere.

In this environment, photolysis of Fe(III) will produce $HSO_4^{\cdot}$ radicals by reaction (6.8), which will in turn react with HSO_3^- to form $HSO_3^{\cdot}$ via (6.23). This provides a sink for molecular oxygen via the very rapid reaction (6.5). If O_2 is present in significant concentrations below the cloud layer – as indicated by the gas

chromatograph measurements from Pioneer Venus (Section 1.2.3) – then the occurrence of reaction (6.5) in the upper cloud layers can account for the very low mixing ratio of O_2 observed in the upper atmosphere. In addition, (6.5) provides an additional sink for O_2 produced by CO_2 photolysis in the upper atmosphere. Reaction (6.5), followed by either (6.24) or (6.26a) gives rise to HSO_5^-, which is stable and able to persist in solution for long enough to become involved in slow oxidation reactions such as

$$HSO_5^- + CO \longrightarrow HSO_4^- + CO_2 \qquad (6.34)$$

Thus, the photochemistry of Fe(III) salts in concentrated sulfuric acid provides a viable mechanism for the regeneration of CO_2 from CO and O_2.

Without detailed atmospheric modelling that includes transport processes, it is not possible to decide how significant the reactions discussed in this chapter are to Venus. What is clear from these findings is that heterogeneous chemistry has the potential to play an important role in the atmosphere of Venus, just as it does on Earth. In order to improve on current models of the upper atmosphere of Venus, it will be necessary to incorporate liquid-phase reactions such as those discussed in this thesis.

Reaction	k/dm^{3}mol^{-1}s^{-1} (in aqueous solution)	No.
H_2SO_4 -------> $H_2SO_4^+ + e^-$	pulse radiolysis	(6.1a)
-------> $H_2SO_4^*$		(6.1b)
$H_2SO_4^+ + H_2SO_4 \longrightarrow H_3SO_4^+ + HSO_4^\cdot$	fast	(6.2)
$e^- + H_2SO_4 \longrightarrow H_2SO_4^- \xrightarrow{H_3O^+} 2H_2O + HSO_3^\cdot$	fast	(6.3)
$e^- + H_2SO_4 \longrightarrow H_2O + SO_3^{-\cdot}$	fast	(6.4a)
$\longrightarrow OH^- + HSO_3^\cdot$	fast	(6.4b)
$HSO_3^\cdot + O_2 \longrightarrow HSO_5^\cdot$	$(2.5\pm0.1)\times10^9$	(6.5)
$Fe^{2+} + H_2SO_4 + H^+ + h\nu \longrightarrow Fe^{3+} + HSO_3^\cdot + H_2O$	ϕ unknown	(6.6)
$2Fe^{2+} + H_2SO_4 + 2H^+ \rightleftharpoons 2Fe^{3+} + SO_2 + 2H_2O$	$K = 5.4\times10^{-21}$	(6.7)
$[Fe.HSO_4]^{2+} + h\nu \longrightarrow Fe^{2+} + HSO_4^\cdot$	ϕ unknown	(6.8)
$[FeSO_4]^+ + h\nu \longrightarrow Fe^{2+} + SO_4^{-\cdot}$	$\phi = 0.0079$ at 280nm	(6.9)
$SO_3^{2-}{}_{(aq)} + h\nu \longrightarrow SO_3^{-\cdot} + e^-$	$\phi = 0.38$ at 253.7nm	(6.10)
$HSO_3^-{}_{(aq)} + h\nu \longrightarrow SO_3^{-\cdot} + H$	$\phi = 0.19$ at 213.9nm	(6.11)
$HSO_3^-{}_{(acid)} + h\nu \longrightarrow H + SO_3^{-\cdot}$	ϕ unknown	(6.12)
$SO_2.HSO_4^- + h\nu \longrightarrow H + SO_2.SO_4^{-\cdot} \longrightarrow H + SO_2 + SO_4^{-\cdot}$	ϕ unknown	(6.13a)
$\longrightarrow H + SO_3 + SO_3^{-\cdot}$	ϕ unknown	(6.13b)
$SO_2.H_2SO_4 + h\nu \longrightarrow H + SO_2.HSO_4^\cdot \longrightarrow H + SO_2 + HSO_4^\cdot$	ϕ unknown	(6.14a)
$\longrightarrow H + SO_3 + HSO_3^\cdot$	ϕ unknown	(6.14b)
$HSO_4^\cdot + Fe^{2+} \longrightarrow HSO_4^- + Fe^{3+}$	$(3-4.8)\times10^8$	(6.15)
$HSO_4^\cdot + H_2O \longrightarrow H_2SO_4 + {}^\cdot OH$	9 – 12	(6.16)
$HSO_4^\cdot + H_2SO_4 \longrightarrow H_2SO_4 + HSO_4^\cdot$	unknown	(6.17)
$HSO_4^\cdot + HSO_4^\cdot \longrightarrow H_2S_2O_8$	$(1.6 - 4.5)\times10^8$ in H_2O	(6.18)
	7.6×10^8 in 10M H_2SO_4	
$HSO_4^\cdot + {}^\cdot OH \longrightarrow H_2SO_5$	$(9.0\pm0.4)\times10^9$	(6.19)
$HSO_4^\cdot + S_2O_8^{2-} \longrightarrow HS_2O_8^\cdot + SO_4^{2-}$	$(6.1\pm0.6)\times10^5$	(6.20)
$2[FeHSO_4]^{2+}{}_{(H2SO4)} + h\nu \longrightarrow 2Fe^{2+}{}_{(H2SO4)} + H_2S_2O_{8(H2SO4)}$	ϕ unknown	(6.21)
$HS_2O_8^- + Fe^{2+} \longrightarrow HSO_4^- + SO_4^- + Fe^{3+}$	unknown	(6.22)
$HSO_4^\cdot + HSO_3^- \longrightarrow HSO_4^- + HSO_3^\cdot$	$(6.8\pm0.1)\times10^8$	(6.23)
$HSO_5^\cdot + Fe^{2+}.H_2SO_4 \longrightarrow HSO_5^- + Fe^{3+}.H_2SO_4$	$(4\pm2)\times10^7$	(6.24)
$HSO_5^- + Fe^{2+}.H_2SO_4 + H^+ \longrightarrow HSO_4^\cdot + FeHSO_4^{2+} + H_2O$	unknown	(6.25)
$HSO_5^\cdot + HSO_3^- \longrightarrow HSO_5^- + HSO_3^\cdot$	$(8.1\pm0.3)\times10^3$	(6.26a)
$\longrightarrow HSO_4^- + HSO_4^\cdot$	$(3.4\pm0.13)\times10^2$	(6.26b)
$HSO_3^\cdot + Fe^{2+}.H_2SO_4 \longrightarrow HSO_3^- + Fe^{3+}.H_2SO_4$	unknown	(6.27)
$H^\cdot + Fe^{3+} \longrightarrow H^+ + Fe^{2+}$	unknown	(6.32)
$HO_2^\cdot + HSO_3^- \longrightarrow OH^\cdot + HSO_4^-$	unknown	(6.33)
$HSO_5^- + CO \longrightarrow HSO_4^- + CO_2$	unknown	(6.34)

Table 6.4 Summary of reactions discussed in Chapter 6, with rate constants or quantum yields for the analogous reactions in aqueous solution (where known).

References

Chapter 1

[1] A. Seiff, Models of Venus's atmospheric structure, *in "Venus" (D. Hunten, L. Colin, T. Donahue and V. Moroz, eds)*, 1983, University of Arizona Press, Tucson, p1045-8

[2] V.A. Krasnopolsky, *Photochemistry of the Atmospheres of Mars and Venus*, (1986) Springer-Verlag, Berlin.

[3] R. Knollenberg and D. Hunten, The Microphysics of the Clouds of Venus: Results of the Pioneer Venus Particle Size Spectrometer Experiment, *Journal of Geophysical Research*, 1980, **85**, 8039-58

[4] Y.L. Yung and W.B. DeMore, *Photochemistry of Planetary Atmospheres*, (1999) Oxford University Press, New York.

[5] J. Trauger and J. Lunine, Spectroscopy of Molecular Oxygen in the Atmospheres of Venus and Mars, *Icarus*, 1983, **55**, 272-81

[6] G.T. Sill, Sulfuric Acid in the Venus Clouds, *Communications of the Lunar and Planetary Laboratory*, 1972, **171**, 191

[7] A.T. Young, Are the Clouds of Venus Sulfuric Acid?, *Icarus*, 1973, **18**, 564

[8] V.A. Krasnopolsky, Chemical Composition of Venus Clouds, *Planetary and Space Science*, 1985, **33**, 109-17

[9] V.A. Krasnopolsky and J.B. Pollack, H_2O-H_2SO_4 System In Venus' Clouds and OCS, CO and H_2SO_4 Profiles in Venus' Troposphere, *Icarus*, 1994, **109**, 58

[10] V.A. Krasnopolsky, Vega Mission Results and Chemical Composition of Venusian Clouds, *Icarus*, 1989, **80**, 202-10

[11] U. von Zahn, S. Kumar, H. Niemann and R. Prinn, Composition of the Venus Atmosphere, *in "Venus" (D. Hunten, L. Colin, T. Donahue and V. Moroz, eds)*, 1983, University of Arizona Press, Tucson, p299

[12] G.P. Kuiper, Identification of the Venus Cloud Layer, *Communications of the Lunar and Planetary Laboratory*. 1968, **6**(100) p229, and **101** (1969))

[13] J.S. Lewis, Venus: atmospheric and lithospheric composition. *Earth and Planetary Science Letters*, 1970, **10**, 73-80

[14] L.V. Zasova, V.A Krasnopolsky, V.I Moroz, Vertical Distribution of SO2 in Upper Cloud Layer of Venus and Origin of U.V.-Absorption. *Advances in Space Research,* 1981, **1**(9), p13-6

[15] Y.A. Surkov, F.F. Kirnozov, V.I. Guryanov, V.N. Glazov, A.G. Dunchenko, S.S. Kurochkin, V.N. Rasputnyi, E.G. Kharitonova, L.P. Tatsii and V.L. Gimadov, Study of Aerosol in the Cloud Layer of Venus by the Venera-12 Spacecraft (Preliminary Results), *Kosmicheskie Issledovaniya. (Cosmic Research)*, 1982, **20**(3) 435-41

[16] Y.A. Surkov, F.F. Kirnozov, V.N. Glazov, A.G. Dunchenko and V.Vatrashkevich, New Data on Aerosol in the Cloud Layer of Venus. Preliminary Results of the study carried out with Venera-14, *Pis'ma Astronomicheskii Zhurnal (Astronomy Letters)*, 1982, **8**(11) 700-4

[17] I.V. Petryanov, B.M. Andreichikov, B.N. Korchuganov, E.I. Ovsyankin, B.I. Ogorodnikov, V.I. Skitovich and V.K. Khristianov, Iron in the Clouds of Venus, *Doklady Akademii nauk SSSR (Doklady Physics)*, 1981, **260**(4) 834-6

[18] B.M. Andreichikov, I.K. Akhmetshin, B.N. Korchuganov, L.M. Mukhin, B.I Ogorodnikov, I.V. Petryanov and V.I. Skitovich, X-ray Radiometric Analysis of Aerosols in the Venusian Clouds by Vega-1 and Vega-2, *Kosmicheskie Issledovaniya (Cosmic Research)*, 1987, **25**(5) 721-36

[19] R.G. Prinn, Photochemistry of HCl and Other Minor Constituents in the Atmosphere of Venus, *Journal of the Atmospheric Sciences*, 1971, **28**, 1058-67

[20] R. Prinn, Venus: Chemical and Dynamical Processes in the Stratosphere and Mesosphere, *Journal of the Atmospheric Sciences*, 1975, **32**, 1237-47

[21] V.A. Krasnopolsky and V. Parshev, Photochemistry of the Venus Atmosphere, *Kosmicheskie Issledovaniya (Cosmic Research)*, 1980, **19**, 261-78

[22] Y.L. Yung and W.B. DeMore, Photochemistry of the Stratosphere of Venus: Implications for Atmospheric Evolution, *Icarus*, 1982, **51**, 199

[23] P.Connes, J.F. Noxon, W.A. Traub and N.P. Carleton, $O_2(^1\Delta g)$ Emission in the Day and Night Airglow of Venus, *Astrophysical Journal*, 1979, **233**, L29

[24] M.J. McEwan and L.F. Phillips, *Chemistry of the Atmosphere*, 1975, Edward Arnold, London, UK, p249

[25] J. Lewis and F. Kreimendahl, Oxidation State of the Atmosphere and Crust of Venus from Pioneer Venus Observations, *Icarus*, 1980, **42**, p330-7

[26] I. Khodakovsky, Atmosphere-Surface Interactions on Venus and Implications for Atmospheric Evolution, *Planetary and Space Science*, 1982, **30**, 803-18

[27] R. Prinn, The Photochemistry of the Atmosphere of Venus, *in "The Photochemistry of Atmospheres" (ed. J. Levine)*, 1985, Academic Press, Orlando, p320-7

[28] *Transport and Chemical Transformation of Pollutants in the Troposphere, Vol. 2: Heterogeneous and Liquid-Phase Processes (ed. P.Warneck)*, 1996, Springer-Verlag, Berlin

[29] A.J. Elliot, D.R. McCracken, G.V. Buxton and N.D. Wood, Estimation of Rate Constants for Near-diffusion-controlled Reactions in Water at High Temperatures, *Journal of the Chemical Society, Faraday Transactions*, 1990, **86**(9), p1539-47

[30] E.A. Betterton and M.R. Hoffmann, Oxidation of Aqueous SO_2 by Peroxymonosulfate, , *Journal of Physical Chemistry*, 1988, **92**, 5962-5

[31] R.E. Connick, S. Lee and R. Adamic, Kinetics and Mechanism of the Oxidation of HSO_3^- by HSO_5^-, *Inorganic Chemistry*, 1993, **32**, 565-71

[32] H. Elias, U. Gotz and K. Wannowius, Kinetics and Mechanism of the Oxidation of Sulfur(IV) by Peroxomonosulfuric Acid Anion, *Atmospheric Environment*, 1994, **28**(3), p439-48

[33] U. Deister and P. Warneck, Photooxidation of SO_3^{2-} in Aqueous Solution, *Journal of Physical Chemistry,* 1990, **94**, 2191-8

[34] D.G. Karraker, The Kinetics of the Reaction Between Sulfurous Acid and Ferric Ion, *Journal of Physical Chemistry*, 1963, **67**, 871-4

[35] B.L. Tiwari, J. Kolbe and H.W. Hayden, Jr., Oxidation of Ferrous Sulfate in Acid Solution by a Mixture of Sulfur Dioxide and Oxygen, *Metallurgical Transactions B*, 1979, **10B**, p607-12

[36] T. Sato, T. Goto, T. Okabe and F. Lawson, The Oxidation of Iron(II) Sulfate with Sulfur Dioxide and Oxygen Mixtures, *Bulletin of the Chemical Society of Japan,* 1984, **57**, 2082-6

[37] J. Kraft and R. van Eldik, Kinetics and Mechanism of the Iron (III)-Catalyzed Autooxidation of Sulfur(IV) Oxides in Aqueous Solution. 1. Formation of Transient Iron (III)-Sulfur(IV) Complexes, *Inorganic Chemistry*, 1989, **28**, p2297-305

[38] J. Kraft and R. van Eldik, Kinetics and Mechanism of the Iron (III)-Catalyzed Autooxidation of Sulfur(IV) Oxides in Aqueous Solution. 2. Decomposition of Transient Iron (III)-Sulfur(IV) Complexes, *Inorganic Chemistry*, 1989, **28**, p2306-12

[39] K. Bal Reddy and R. van Eldik, Kinetics and Mechanism of the Sulfite-Induced Autooxidation of Fe(II) in Acidic Aqueous Solution, *Atmospheric Environment*, 1992, **26A**(4) p661-5

[40] W.J. McElroy and S.J. Waygood, Kinetics of the Reactions of the Sulfate Radical Ion with Sulfate, Peroxydisulfate, water and Iron(2+), *Journal of the Chemical Society, Faraday Transactions*, 1990, **86**(14), p2557-64

[41] G.V. Buxton, S. McGowan, G.A. Salmon, J.E. Williams and N.D. Wood, A Study of the Spectra and Reactivity of Oxysulfur-Radical Anions Involved in the Chain Oxidation of S(IV): A Pulse and γ-Radiolysis Study, *Atmospheric Environment*, 1996, **30**(14), p2483-93

[42] G.V. Buxton, T.N. Malone, G.A. Salmon, Reaction of $SO_4^{\cdot-}$ with Fe^{2+}, Mn^{2+} and Cu^{2+} in Aqueous Solution, *Journal of the Chemical Society, Faraday Transactions*, 1997, **93**(16) 2893-7

[43] J. Jortner and G. Stein, The Photochemical Evolution of Hydrogen from Aqueous Solutions of Ferrous Ions. Part I. The Reaction Mechanism at Low pH, *Journal of Physical Chemistry*, 1962, **66**, p1258-64

[44] L.J. Heidt, M.G. Mullin, W.B. Martin Jr. and A.M. Johnson Beatty, Gross and Net Quantum yields at 2537Å for Ferrous to Ferric in Aqueous Sulfuric Acid and the Accompanying Reduction of Water to Gaseous Hydrogen, *Journal of Physical Chemistry*, 1962, **66**, p336-41

[45] J. Jortner and G. Stein, The Photochemical Evolution of Hydrogen from Aqueous Solutions of Ferrous Ions. Part II. Effect of Changing pH, *Journal of Physical Chemistry*, 1962, **66**, p1264-71.

[46] P.L. Airey and F.S. Dainton, *Proceedings of the Royal Society of London. Series A: Mathematical and Physical Sciences*, 1966, **291**, p340

[47] S.R. Logan, Effects of Temperature and Wavelength on the Primary Process in the Photo-oxidation of Iron(II) Ion, *Journal of the Chemical Society, Faraday Transactions,* 1990, **86**(4), 615-7

[48] L. Vincze, B. Kraut, S. Papp, A Proposal for the Mechanism of the Photooxidation of Kinetically-Labile Transition Metal Complexes. Interpretation of Photoprocesses of FeSO4, Fe(ClO4)2 and feCl2 in Aqueous Acidic Solutions, *Inorganica Chimica Acta*, 1984, **85**, p89-96

[49] F. David and P.G. David, Photoredox Chemistry of Iron(III) Chloride and Iron(III) Perchlorate in Aqueous Media. A Comparative Study, , *Journal of Physical Chemistry*, 1976, **80**(6), p579-83

[50] B.C. Faust and J. Hoigné, Photolysis of Fe(III)-Hydroxy Complexes as Sources of OH Radicals in Clouds, Fog and Rain, *Atmospheric Environment,* 1990, **24A**(1), p 79-89

[51] H.J. Benkelberg and P. Warneck, Photodecomposition of Iron(III) Hydroxo and Sulfato Complexes in Aqueous Solution: Wavelength Dependence of OH and SO_4^- Quantum Yields, *Journal of Physical Chemistry*, 1995, **99**, 5214-21

Chapter 2

[1] C.T. Mills, Photo-oxidation of Carbon Monoxide in an Aerosol of Sulfuric Acid at 193nm, *M.Sc Thesis,* 1994, University of Canterbury, New Zealand

[2] C.T. Mills and L.F. Phillips, *Journal of Photochemistry and Photobiology A: Chemistry*, 1993, **74**, p7

[3] G.A. Rowland, Photochemical Reaction of Carbon Monoxide in a Sulfuric Acid Aerosol, *Honours Part III Research Project Report*, 1994, University of Canterbury, New Zealand

[4] K. Willeke and P.A. Baron, ed. *Aerosol Measurement: Principles, Techniques and Applications*, 1993, Van Nostrand Reinhold, New York

[5] E.Fajans and C.F. Goodeve, *Transactions of the Faraday Society*, 1936, **32**, p511

[6] J. Westergren, Determination of Size Distribution of Spherical Sulfuric Acid Aerosols by Light Scattering, *M.Sc. Thesis*, 1994, Chalmers University of Technology, Göteborg,

[7] J.W.T. Spinks and R.J. Woods, *An Introduction to Radiation Chemistry*, 1964, Wiley, New York

[8] S.G. Lias, J.E. Bartmess, J.F. Liebman, J.L. Holmes, R.D. Levin and W.G. Mallard, *Journal of Physical Chemistry: Reference Data*, 1988, **17**(Suppl 1)

[9] W.B. DeMore, S.P. Sander, D.M. Golden, R.F. Hampson, M.J. Kurylo, C.J. Howard, A.R. Ravishankara, C.E. Kolb and M.J. Molina, *Chemical Kinetic and Photochemical Data for Use in Stratospheric Modelling*, Evaluation Number 11, Jet Propulsion Laboratory, Pasadena, 1994

[10] L.F. Phillips, Surface Concentrations and Compound Formation in Aqueous Sulfuric Acid, *Australian Journal of Chemistry*, 1994, **47**, p91-9

[11] J.I. Gmitro and J. Vermeulen, *American Institute of Chemical Engineers Journal*, 1964, **10**, p740

Chapter 3

[1] W. John, The Characteristics of Environmental and Laboratory-Generated Aerosols, *in "Aerosol Measurement: Principles, Techniques and Applications"* (K. Willeke and P.A. Baron, eds), 1993, Van Nostrand Reinhold, New York

[2] W.C. Hinds, *Aerosol Technology: Properties , Behavior, and Measurement of Airborne Particles*, 1982, Wiley, New York, p271

[3] C.N. Davies, Evaporation of Airborne Droplets, *in "Fundamentals of Aerosol Science"* (D.T. Shaw, ed.), 1978, Wiley, New York

[4] Hinds, p44-5

[5] J. Westergren, Determination of Size Distribution of Spherical Sulfuric Acid Aerosols by Light Scattering, *M.Sc. Thesis*, Chalmers University of Technology, Göteborg, 1994

[6] L.F. Phillips, Surface Concentrations and Compound Formation in Aqueous Sulfuric Acid, *Australian Journal of Chemistry*, 1994, **47**, p91-99

[7] Hinds, p187-194

Chapter 4

[1] Morgan and Crist, The Photochemical Decomposition of Potassium Persulfate, *Journal of the American Chemical Society*, 1927, **49**, p338

[2] J.B. Burkholder, M. Mills and S. McKeen, Upper Limit for the UV Absorption Cross-Sections of H_2SO_4, *Geophysical Research Letters*, 2000, **27**(16), p2493-6

[3] J.M. Monger and O. Redlich, Peroxysulfuric Acid and Peroxyformic Acid. Equilibrium and Formation Rate, *Journal of Physical Chemistry*, 1956, **60**, p797-9

[4] C. Marsh and J.O. Edwards, The Free-Radical Decomposition of Peroxymonosulfate, *Progress in Reaction Kinetics,* 1989, **15**, p35-75

[5] R Savoie and P.A. Giguere, Les Spectres Infrarouges de L'Acide Sulfurique Et Des Oleums, *Canadian Journal of Chemistry*, 1960, **38**, 2467-2476

[6] J.L. Arnau and P.A. Giguere, Etude Spectroscopique des derives du peroxyde d'hydrogene. IV. L'acide de Caro, H_2SO_5, *Canadian Journal of Chemistry*, 1970, **48**, 3903-3910

[7] M.H. Mariano, Spectrophotometric Analysis of Sulfuric Solutions of Hydrogen Peroxide, Peroxymonosulfuric Acid and Peroxydisulfuric Acid, *Analytical Chemistry*, 1968 **40,** 1662-1667

[8] L. Brewer and J.B. Tellinghuisen; Detection of Iodine Atoms by an Atomic Fluorescence Technique, *Journal of Chemical Physics*, 1971, **54**(12), 5133-5138

[9] S.J. Wrenn, L.J. Butler, G.A. Rowland, C.J.H. Knox and L.F Phillips, The necessity for multiphoton processes in the 193-nm photochemistry of sulfuric acid aerosols, *Journal of Photochemistry and Photobiology A: Chemistry*, 1999, **129**, p101-4

[10] *Optical Effects Associated with Small Particles (P.W. Barber and R.K. Chang, eds)*, 1988, World Scientific, Singapore.

[11] V. Majidi and M.R. Joseph, Spectroscopic Applications of Laser-Induced Plasmas, *Critical Reviews in Analytical Chemistry*, 1992, **23**(3), p143-162

[12] R.K. Chang, J.H. Eickmans, W.F. Hseih, C.F. Wood, J.Z Zhang and J.B. Zheng, Laser-Induced Breakdown in Large TransparentWater Droplets, *Applied Optics*, 1988, **27**(12), p2377-85

[13] Y.G. Jin, H.C. Zhou, M. Suto and L.C. Lee, Fluorescence From Laser Excitation of H_2SO_4 Aerosols Produced by the Gas Reaction of SO_3 and H_2O, *Journal of Photochemistry and Photobiology A: Chemistry*, 1990, **52**, p255-70

Chapter 5

[1]G.V. Buxton, S. McGowan, G.A. Salmon, J.E. Williams and N.D. Wood; A study of the Spectra and Reactivity of Oxysulfur-Radical Anions involved in the Chain Oxidation of S(IV): A Pulse and γ-Radiolysis Study, *Atmospheric Environment*, 1996, **30**(14) 2483-93

[2] P.S. Polevoi, A.E. Khachaturov-Tavrizian and I.N. Ivanov, Pulse Radiolysis of Concentrated Sulfuric Acid, *Radiation Physical Chemistry*, 1990, **36**(2), p99-103

[3] *Transport and Chemical Transformation of Pollutants in the Troposphere, Vol. 2: Heterogeneous and Liquid-Phase Processes (ed. P.Warneck)*, 1996, Springer-Verlag, Berlin

[4] S.R Logan, Effects of Temperature and Wavelength on the Primary Process in the Photo-oxidation of Iron(II) Ion, *Journal of the Chemical Society Faraday Trans.*,1990, **86**(4), 615-7

[5] H. Elias, U. Götz and K. Wannowius; Kinetics and Mechanism of the Oxidation of Sulfur (IV) by Peroxomonosulfuric Acid Anion, *Atmospheric Environment*, 1994, **28**(3), 439-48

[6] P.W Atkins, *Physical Chemistry, 3rd Edition*, 1987, Oxford University Press, Oxford

[7] M. Liler, *Reaction Mechanisms in Sulfuric Acid*, 1971, Academic Press, London, p5

[8] K. Bal Reddy and R van Eldik; Kinetics and Mechanism of the Sulfite-Induced Autooxidation of Fe(II) in Acidic Aqueous Solution, *Atmospheric Environment*, 1992, **26A**, 661-5

Chapter 6

[1] P.S. Polevoi, A.E. Khachaturov-Tavrizian and I.N. Ivanov, Pulse Radiolysis of Concentrated Sulfuric Acid, *Radiation Physical Chemistry*, 1990, **36**(2) p99-130

[2] M. Liler, *Reaction Mechanisms in Sulfuric Acid*, 1971, Academic Press London and New York, p19

[3] L.F. Phillips, Surface Concentrations and Compound Formation in Aqueous Sulfuric Acid, *Australian Journal of Chemistry*, 1994, **47**, p91-99

[4] H.J. Benkelberg and P. Warneck, Photodecomposition of Iron(III) Hydroxo and Sulfato Complexes in Aqueous Solution: Wavelength Dependence of OH and SO_4^- Quantum Yields, *Journal of Physical Chemistry*, 1995, **99**, 5214-21

[5] P. Warneck, H.-J. Benkelberg, U. Deister, M. Fischer, A. Schäfer and J. Ziajka, Chain Oxidation Mechanisms of S(IV) in Aqueous Solution: Application of Radical Scavenger Techniques, in *Transport and Chemical Transformation of Pollutants in the Troposphere, Vol. 2: Heterogeneous and Liquid-Phase Processes (HALIPP) (ed. P.Warneck)*, 1996, Springer-Verlag, Berlin

[6] *(HALIPP)*, p38-41

[7] M.H. Mariano, Spectrophotometric Analysis of Sulfuric Solutions of Hydrogen Peroxide, Peroxymonosulfuric Acid and Peroxydisulfuric Acid, *Analytical Chemistry*, 1968 **40,** 1662-1667

[8] G.A. Rowland and L.F. Phillips, Cloud photochemistry and its effect on the composition of the upper atmosphere of Venus, *Geophysical Research Letters*, 2000, **27**, 3301-4